RELATING PROTEIN STRUCTURE TO FUNCTION: HOW PROTEIN DYNAMICS MAXIMIZES ENERGY GAINED BY ELECTRON TRANSFER IN AN ANAEROBIC ENERGY CONSERVATION MECHANISM

by

Luke Montgomery Berry

A dissertation submitted in partial fulfillment
of the requirements for the degree

of

Doctor of Philosophy

in

Biochemistry

MONTANA STATE UNIVERSITY
Bozeman, Montana

April 2019

ACKNOWLEDGMENTS

I would like to thank Dr. Brian Bothner for allowing me to join his lab, and whose continuous support, guidance, and encouragement made this work possible. I would also like the thank Dr. Bothner for the opportunity to work with the biological electron transfer and catalysis (BETCy) energy frontiers research center. The work done by this group was crucial in the characterization of a new form of energy conservation. Working with this group not only gave me valuable research experience, but also provided the experience or working with multiple collaborators who specialize in different techniques allowing me to sharpen my scientific communication skills.

I would also like to acknowledge my graduate committee Dr. Valerie Copie, Dr. Jennifer DuBois, and Dr. Martin Lawrence for supporting me throughout my graduate career. I would also like to thank Dr. Lance Seefeldt, Dr. John Peters, and Dr. Micheal Adams for their many collaborations with the BETCy project. I would like to extend a special thanks to Dr. Jonathan Hilmer, Dr. Ganesh Bala, and Jesse Thomas for mentoring me in the use of mass spectrometry, and for understanding my panic when a new error message appears. Finally I would like to extend a special thanks to the Bothner Lab members, specifically Alex Brown, Angela Patterson, Katie Steward, Jenna Mattice, Rachel Rawle, and Mohammed Refai. Not only did they help me run experiments when two hands were not enough, but they also supported me during minor breakdowns and when a second opinion is needed.

I would like to express my deepest gratitude to all of my family and friends who have provided constant support during my time at Montana State University.

ABSTRACT

Reduced ferredoxin (Fd) plays a critical role in anaerobic metabolism by acting as an alternative source of energy to adenosine triphosphate (ATP). The reduction potential of Fd is low (-450 mV) making it difficult to reduce individually. However, it has recently been discovered that a unique mechanism known as electron bifurcation allows anaerobic organisms to reduce Fd without suffering a loss of energy. Electron bifurcation was originally discovered in complex III of the electron transport chain, and increased the efficiency of the proton motive force without an overall change in the electron flow, minimizing energy loss. EB accomplishes this is by coupling a favorable (exergonic) and unfavorable (endergonic) reduction reaction. The exergonic reaction produces a singly reduced cofactor with a sufficiently negative reduction potential to allow the endergonic process to proceed. This allows anaerobic organisms to couple the formation of NADH, with the reduction of Fd. A detail of interest in the bifurcating mechanism is how these enzymes regulate the flow of electrons down the exergonic and endergonic branches to prevent multiple electrons from traveling down the exergonic branch. It is hypothesized that changes in the protein conformation alter the distance between cofactors altering the rate of electron transfer. To fully understand how changes in a protein's conformation regulates electron transfer in electron bifurcation we used a suite of in-solution techniques, such as H/D exchange and chemical cross-linking coupled to mass spectrometry to characterize the structure and dynamics of the model bifurcating enzyme, NADH-dependent ferredoxin-NADP$^+$ oxidoreductase (Nfn), during the different steps of electron bifurcation. Additionally we also set out to use these techniques to characterize the structure and dynamics of the nitrogenase systems in order to obtain biophysical evidence of negative cooperativity in the various nitrogenase systems.

TABLE OF CONTENTS

1. INTRODUCTION 1

Abstract 1
Electron Transfer, the Key to Energy Conservation 2
Representative Models of Electron Bifurcation as an Energy Conservation Mechanism in the Absence of Oxygen 6
    The NADH-dependent Ferredoxin-NADP$^+$ Oxidoreductase System 8
    The Electron Transfer Flavoprotein System 9
    The [FeFe]-Hydrogenase System 10
Regulation of Electron Transfer in the Bifurcating Systems 11
    Marcus Theory of Electron Transfer 11
    Mechanisms of Allosteric Communication 11
Relating Protein Dynamics to Allosteric Pathways 15
    Computational Methods to Identify Allosteric Pathways 15
    In-Solution Methods to Relate a Protein's Structure and Function 17
Summary 22
References Cited 23

2. HYDROGEN DEUTERIUM EXCHANGE MASS SPECTROMETRY OF OXYGEN SENSITIVE PROTEINS 30

Contributions of Authors and Co-Authors 30
Manuscript Information 31
Abstract 32
Background 33
Materials and Reagents 34
Equipment 36
Software 36
Procedure 37
Data Analysis 46
Notes 49
Recipes 51
References Cited 51

TABLE OF CONTENTS CONTINUED

3. H/D EXCHANGE MASS SPECTROMETRY AND STATISTICAL COUPLING ANALYSIS REVEAL A ROLE FOR ALLOSTERY IN A FERREDOXIN DEPENDENT BIFURCATING TRANSHYDROGENASE CATALYTIC CYCLE..........................53

Contributions of Authors and Co-Authors..53
Manuscript Information 55
Abstract 56
Abbreviations...57
Introduction..57
Materials and Methods..62
    Protein Purification 62
    Native Mass Spectrometry 63
    HDX-MS Analysis...63
    HDX-MS Clustering 65
    Generation of Nfn and Related Paralog Database 65
    Statistical Coupling Analysis 66
    Network Analysis...66
Results...67
    Evidence of Long Distance Communication in *Pf* Nfn 67
    SCA Analysis of Nfn 73
    Network Analysis of HDX-MS and SCA Data 75
Discussion..78
References Cited 82
Acknowledgments 85
Supplementary Material..86

4. COMBINING IN-SOLUTION AND COMPUTATIONAL METHODS TO CHARACTERIZE THE STRUCTURE-FUNCTION RELATIONSHIP OF THE NITROGNEASE SYSTEMS 104

Contributions of Authors and Co-Authors..104
Manuscript Information 106
Abstract 107
Abbreviations...108
Introduction..108
Materials and Methods..112
    Protein Expression and Purification...112
    Sequence Alignment and Homology Model Generation 112

    Chemical Cross-Linking Mass Spectrometry Experiments 113
    H/D Exchange Mass Spectrometry Experiments..114
    Normal Mode Analysis 115
  Results and Discussion 116
    Development and Validation of the AnfDGK Homology Model........................116
    Structural Comparison of the AnfDGK and NifDK Complexes 117
    The AnfG Subunit Binding Site...119
    AnfG Subunit Interactions Network 122
    Correlation of Interaction Networks in AnfDGK 125
    AnfDGK Protein Complex Dynamics 126
    Bimodal Peptides Reveal Asymmetry in Protein Dynamics 127
  Conclusions...128
  References Cited 131
  Supplementary Material..138

5. IRON PROTEIN DOCKING EFFECTS ON MOFE PROTEIN DYNAMICS: FUNCTION OF NEGATIVE COOPERATIVITY AND THE REGULATION OF ELECTRON TRANSFER.......................................143

  Contributions of Authors and Co-Authors..143
  Manuscript Information 145
  Abstract 146
  Introduction...147
  Materials and Methods...152
    Protein Purification 152
    Quench Flow H/D Exchange 152
    Bench Top H/D Exchange 153
    LC-MS Analysis of Deuterated MoFeP..153
    HDX-MS Analysis...154
  Results and Discussion 155
    Effects of FeP Binding on the Deuterium Uptake of MoFeP 155
    Structural Asymmetry of the MoFeP...160
    MoFe Dynamics on a Catalytic Timescale 163
  Conclusions...169
  References Cited 172
  Supplementary Material..177

TABLE OF CONTENTS CONTINUED

6. SUMMARY AND CONCLUSIONS 183

Abstract 183
Electron Bifurcation: A New Mechanism of Energy Conservation 184
Detailing the Structure and Dynamics of the NADH-Dependent Ferredoxin-NADP$^+$ Oxidoreductase 187
Characterizing the Similarities and Differences in The Structure-Function Relationship of the Nitrogenase Systems 193
Negative Cooperativity and the Regulation of Electron Transfer 198
Final Remarks 202
References Cited 203

CUMULATIVE REFERENCES CITED 209

LIST OF FIGURES

Figure Page

1.1 Schematic Overview of Cellular Respiration 3
1.2 Simplified Schematic of the Q Cycle in Complex III.......................................5
1.3 Schematic Representation of Model Bifurcating Enzymes 8
1.4 Schematics of the MWC and KNF Allosteric Models....................................13
1.5 Schematic of the Modern View of Allostery 15
1.6 Schematic of SL-MS General Workflow...18
1.7 Schematic of XL-MS General Workflow 19
1.8 Schematic of HDX-MS General Workflow...20
2.1 HDX-MS Sample Prep and Workflow 40
2.2 Example of Typical HDX-MS data 46
2.3 HDX-MS Data Mapped onto a Protein Structure 49
3.1 Schematic of the Electron Bifurcation and Confurcation Reactions in Nfn 60
3.2 Native Mass Spectra of the Nfn Complex 68
3.3 Histograms of Deuterium Incorporation After Three Hours in Key Regions of Nfn...71
3.4 Co-evolving Residues Putatively Involved in Allosteric Communication...75
3.5 Network Analysis of HDX-MS and SCA Data 77
4.1 Catalytic Cycle of the Mo-Dependent Nitrognease System 109
4.2 Comparison of the AnfDGK and NifDK Protein Dynamics 119

LIST OF FIGURES CONTINUED

Figure Page

4.3 Chemical Cross-Linking of AnfDGK Complex 121

4.4 Normal Mode Analysis of the AnfDGK Complex 123

4.5 XL-MS and HDX-MS Data Showing
Dynamic Behavior of the AnfDGK Complex 127

5.1 FeP Cycle Overview 148

5.2 Butterfly Plots of the QF-HDX-MS Data 156

5.3 MoFeP Bimodal Peptides 161

5.4 Structural Heat Maps of the MoFeP on the Catalytic Timescale 164

6.1 Simplified Schematic of the Q Cycle in Complex III....................................184

6.2 Schematic Representation of Model Bifurcating Enzymes 186

6.3 Histograms of Deuterium Incorporation
After Three Hours in Key Regions of Nfn...189

6.4 Co-evolving Residues Putatively
Involved in Allosteric Communication..187

6.5 XL-MS and HDX-MS Data Showing
Dynamic Behavior of the AnfDGK Complex 194

6.6 Normal Mode Analysis of the AnfDGK Complex 196

6.7 Butterfly Plots of the QF-HDX-MS Data 199

6.8 Structural Heat Maps of MoFeP on the Catalytic Timescale 201

CHAPTER ONE

INTRODUCTION

Abstract

Cellular energy conservation can be broken down into the exergonic electron transfer events between two chemical species. Cells have evolved to use the energy released from exergonic electron transfers in endergonic reactions. The most common example of this coupling reaction is cellular respiration which utilizes the downhill transfer of electrons to synthesize adenosine triphosphate (ATP), which is used as an energetic currency. Anaerobic organisms are not able to produce large amounts of ATP by traditional means because of the need for oxygen. It was originally unknown how these organisms thrive despite the supposed limit to energy. However, recent studies have uncovered a new mechanism of energy conservation in anaerobic organisms through the process known as electron bifurcation. Electron bifurcation involves the simultaneous coupling of exergonic and endergonic reduction reactions in order to provide anaerobic organisms with highly reduced species in the form of ferredoxin (Fd), supplying energy for reactions like nitrogen fixation. Several enzymes that perform electron bifurcation have been identified and the bifurcation mechanisms have been characterized to different extents. Biophysical techniques, such as H/D deuterium exchange coupled to mass spectrometry, are becoming increasingly popular in the study of electron bifurcation. These techniques are capable of characterizing the structure and dynamics of a protein system on the time scale of catalysis. In the case of electron bifurcation, biophysical techniques can characterize how protein dynamics regulates electron transfer down the exergonic and endergonic branches of electron bifurcation.

Electron Transfer, the Key to Energy Conservation

Cellular energy conservation can be broken down into the transfer of electrons between chemical species[1,2,3]. The movement of electrons between two species is known as an oxidation-reduction reaction (redox). In redox reactions electrons are transferred from an electron donor (reducing agent) to an acceptor (oxidizing agent), and results in the loss of an electron by the donor (oxidation) and the gain of an electron by the acceptor (reduction). The likelihood of an atomic species to donate or accept an electron is determined by its reduction potential[4,5]. The more positive a potential, the more likely it is the species will accept an electron, whereas the more negative a reduction potential the less likely it is to accept an electron. Electron transfer from a species with a low potential to a high potential is a spontaneous reaction (exergonic), however the opposite transfer is a non-spontaneous reaction (endergonic). The coupling of exergonic reduction reactions with endergonic reduction reactions is a key characteristic of cellular energy conservation, and allows the endergonic reaction to harness the energy released from the exergonic reaction, minimizing energy loss as heat[6,7,8].

Cellular respiration is the most characterized example of electron transfer events within cellular energy conservation[1,2,8]. Cellular respiration generates adenosine triphosphate (ATP), which acts as an energetic currency for the cell. The hydrolysis of ATP is a highly exergonic process (-316 mV), and this energy can be harnessed by endergonic processes. ATP synthesis occurs through a combination of substrate level phosphorylation (SLP) and oxidative phosphorylation (**Fig 1.1**)[1]. SLP includes glycolysis and the Kreb's cycle, where a substrate (like glucose) is oxidized to produce ATP and the intracellular electron carriers NADH (nicotinamide adenine dinucleotide) and FADH$_2$ (flavin adenine dinucleotide)[1,9]. Only a small amount of ATP is produced during SLP (two from glycolysis and two from the Kreb's cycle). The primary function of SLP is to generate a supply of the electron carriers NADH and FADH$_2$ that can participate in oxidative phosphorylation.

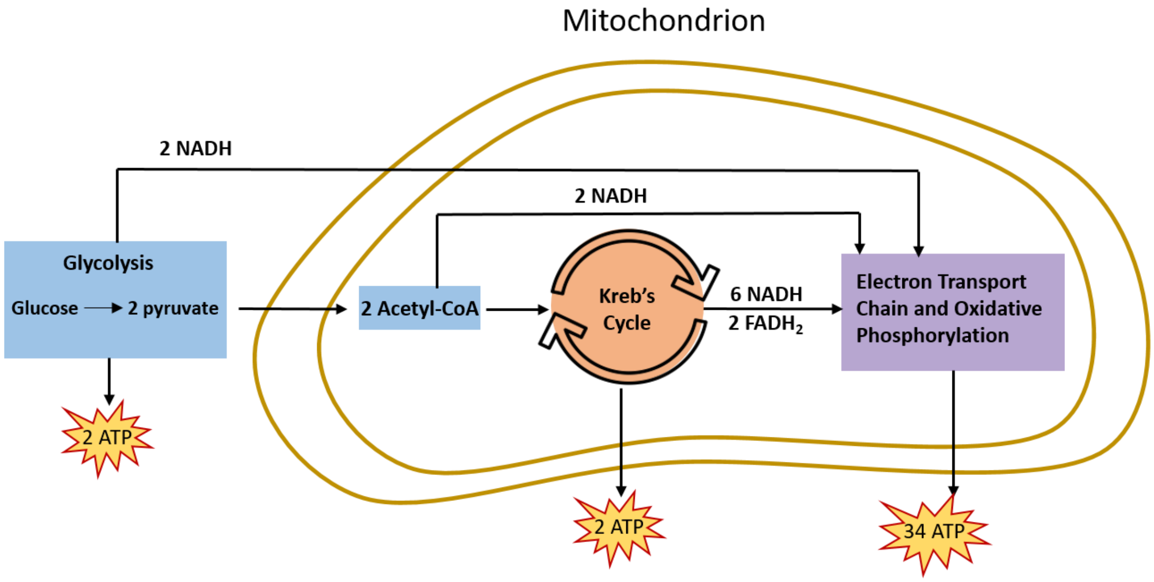

Figure 1.1 Overview of cellular respiration. From left to right: glycolysis begins in the cytosol, where glucose is converted to two molecules of pyruvate, while also producing ATP and NADH. Pyruvate enters the mitochondria and is converted to acetyl-CoA, producing two more molecules of NADH. Acetyl-CoA enters the Kreb's cycle, where more ATP and NADH are synthesized, as well as FADH$_2$. The final step of cellular respiration is the electron transport chain which uses the oxidation of NADH and FADH$_2$ to transport protons across the mitochondrial membrane. The protons then flow back into the mitochondria through ATP synthase triggering a conformational change that synthesizes ATP.

The electron transport chain (ETC) uses the electrons from NADH and FADH$_2$ to produce a proton gradient that synthesizes ATP. The ETC includes four integral membrane proteins (complexes I-IV) that couple the oxidation of NADH and $FADH_2$ with the transport of protons across a membrane[1,2,9,10]. Electrons travel through each of the complexes until arriving at complex IV where oxygen acts as the terminal electron acceptor because of its high reduction potential (816 mV), forming water[9]. Once a sufficient gradient of protons has been established, they will travel across the membrane by traveling through the enzyme ATP synthase (**Fig 1.1**). Each proton that passes through ATP synthase causes a conformational change forming ATP from adenosine diphosphate (ADP) with inorganic phosphate (Pi).

Studies on cellular respiration revealed a unique mechanism of moving electrons located in the cytochrome bc_1 complex (complex III in the ETC)[10,11]. Complex III oxidizes ubiquinol (QH_2) to ubiquinone reducing the Q_0 cofactor in the process (**Fig 1.2**).

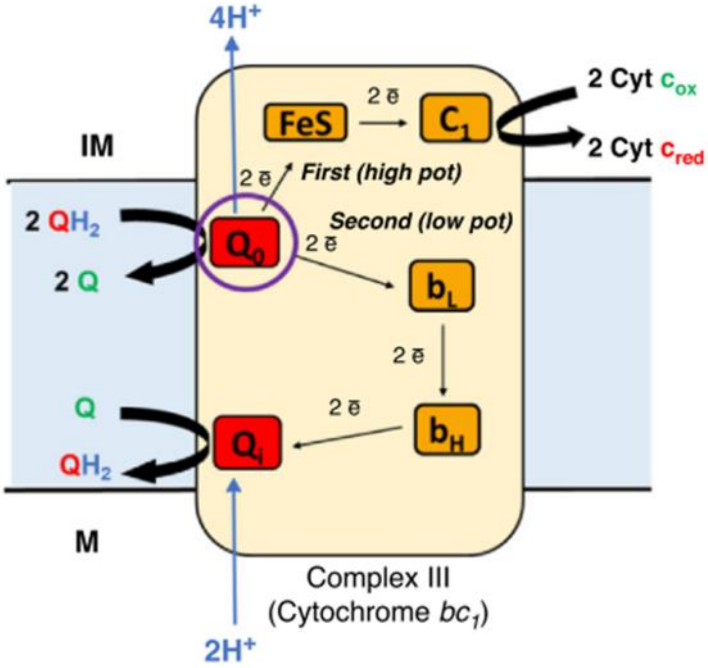

Figure 1.2 Simplified complex III in the ETC. Ubiquinone (Q) accepts electrons from complex I and II, forming the reduced Ubiquinol (QH_2). QH_2 is oxidized to Q, transferring a total of four electrons to Q_0 which bifurcates to the FeS and b_L heme and four protons are transferred into the inner membrane. The 2 electrons from the FeS are transferred to C_1, which reduces cytochrome c. From b_L, the electrons reduce the b_H heme, and then reduce Q_i, which in turn reduces a Q to QH_2, thus regenerating the Q cycle. This figure was adapted from Peters et al, 2018[10].

The electrons at the Q_0 cofactor travel in two different branches, one to a FeS cluster, and another to the b_L heme. The electron at the FeS is transferred to the cytochrome c_1 subunit, which then reduces cytochrome c. The electron at the b_L heme is transferred to the b_H heme, and then to the Q_i site where a ubiquinone molecule is bound. This process, known as the Q cycle, repeats to maintain a supply of QH_2 while simultaneously transporting electrons across the membrane. The Q cycle accomplishes this be coupling the favorable reduction of cytochrome c with the unfavorable reduction of ubiquinone [10,11]. The transferring of electrons down two energetically different pathways is known as electron bifurcation (EB) [6,12]. In EB a fully reduced cofactor, designated as the bifurcating center, transfers an electron down an exergonic pathway, resulting in an unstable intermediate. The unstable intermediate has a reduction potential that can travel down another pathway to form an endergonic reduction reaction[6,12]. In the Q cycle, the Q_0 site acts as the bifurcating center, and forms an unstable semiquinone intermediate after an electron is transferred to the FeS cluster. The unstable Q_0 site then has sufficient reduction potential to send an electron to the b_L heme. The use of EB in the Q cycle increases the efficiency of generating a proton motive force without an overall change in the electron flow, and minimizing energy loss [10,11,13].

Representative Models of Electron Bifurcation as an Energy Conservation Mechanism in the Absence of Oxygen

Oxygen is an ideal terminal electron acceptor because of its high reduction potential (816 mV), allowing the transport of multiple protons across the membrane with the transfer of a single electron on the ETC[9]. Anaerobic organisms thrive in the absence of oxygen, and without oxygen anaerobic organisms have to use a different species as the terminal electron acceptor[14]. These alternatives have a much lower reduction potential decreasing the efficiency of ATP synthesis, limiting the availability of ATP for reactions like CO_2 reduction and nitrogen fixation [10,12,14]. To counteract the lack of ATP, anaerobic organisms use other low potential electron carriers like ferredoxin (Fd)[12,15,16]. Fd is a small molecular weight protein that contain an FeS cluster[6,10,17]. Fd has a low reduction potential (~-420 mV) making it a challenge to reduce individually[6,15,16,18]. To efficiently produce large amounts of reduced Fd anaerobic organisms use EB to couple the endergonic reduction of Fd with the exergonic reduction of other compounds, such as NADH. The discovery of EB outside of the ETC has reshaped the understanding of anaerobic metabolism, and led to the establishment of EB as a new mechanism of energy conservation[6,8,10,12,19,20].

Three EB enzymes have been the main focus in studies to detail the mechanism of electron bifurcation: the NADH-dependent Ferredoxin-NADP$^+$ Oxidoreductase (Nfn) from *Pyrococcus furiosus* (**Fig 1.3A**), the electron transfer flavoprotein (Etf) from *Pyrobaculum aerophilum* (**Fig 1.3B**), and [FeFe]-Hydrogenase (Hyd) from *Thermotoga maritima* (**Fig 1.3C**) [6,10,16,21–25]. These three enzymes showcase the different ways the EB reaction is used to reduce Fd. The biggest difference between each enzyme are the cofactors that are responsible for transferring electrons down the exergonic and endergonic branches. The Hyd enzyme contains a high number of metal clusters, and a single FMN molecule, Etf contains three FAD molecules and two metal clusters, and Nfn contains two FAD molecules and three metal clusters. Upon initial discovery of these enzymes it was thought that the organic cofactors (FAD or FMN) were exclusively the site of bifurcation[6,10,16,21–25]. This hypothesis was supported by the bifurcation mechanism characterized in Nfn.

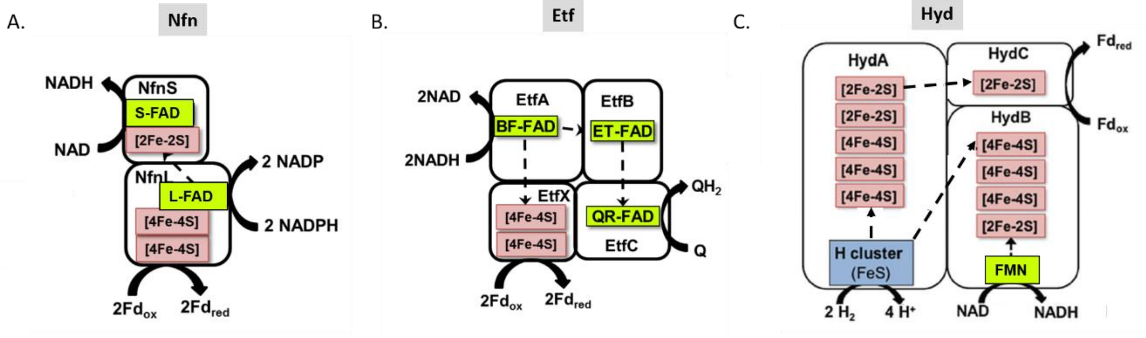

Figure 1.3 Schematic representation of the three model bifurcating enzymes Nfn (**A**), Etf (**B**), and Hyd (**C**). Each schematic details the cofactor and ligand binding sites, while also depicting the hypothesized electron flow for the bifurcating reactions in Nfn, Etf, and Hyd.

The NADH-dependent Ferredoxin-NADP$^+$ Oxidoreductase System Nfn is a heterodimer complex with a large (Nfn-L) and small (Nfn-S) subunit, and catalyzes the simultaneous reduction of NAD$^+$ and Fd through the oxidation of NADPH (Eq1)[6,10,21,26,27].

$$2NADPH + NAD^+ + Fd_{ox} \rightarrow 2NADP^+ + NADH + Fd_{red} + H^+ \qquad (1)$$

Nfn-S contains an FAD (S-FAD) [2Fe-2S], and Nfn-L contains another FAD (L-FAD), as well as two [4Fe-4S] clusters designated as proximal (p[4Fe-4S]) and distal (d[4Fe-4S]) to L-FAD (**Fig 1.3A**)[6,10,21,26,27]. Extensive research has been done to characterize the bifurcation reaction in Nfn, and has determined that L-FAD is the bifurcating center. The bifurcation is initiated with the oxidation of NADPH at Nfn-L, which reduces L-FAD to a hydroquinone state. The first electron reduces NAD$^+$ to NADH by transferring from L-FAD to [2Fe-2S], and then to S-FAD. The chain of cofactors leading to the reduction of NAD$^+$ is designated as the exergonic branch of bifurcation. The loss of an electron oxidizes the bifurcating flavin (L-FAD) from a hydroquinone state to a highly reduced and unstable semiquinone state[6,21]. The unstable semiquinone has enough energy to send an electron down the endergonic branch through the p[4Fe-4S] and d[4Fe-4S] cluster where Fd is reduced[6,21,27].

The Electron Transfer Flavoprotein System The theory that organic cofactors are exclusively the site of bifurcation was further supported by studies on the Etf complex. Etf catalyzes the oxidation of NADH and the simultaneous reduction of Fd and Q (Eq2)[18,22,24,28,29].

$$2NADH + Q + Fd_{ox} \rightarrow 2NAD^{+} + QH_{2} + Fd_{red} \qquad (2)$$

ETF contains three FAD molecules, with one located in the A, B, and C subunits, and two [4Fe-4S] clusters located in EtfX (**Fig 1.3B**). The bifurcation reaction begins in EtfA where NADH is oxidized at the bifurcating flavin (BF-FAD), reducing it to a hydroquinone state. Similar to Nfn, the first electron is transferred to the exergonic branch. The electron is first transferred to the FAD in EtfB (ET-FAD), which is then transferred to the FAD in EtfC (QR-FAD). The reduced QR-FAD is hypothesized to reduce Q to QH_2[18,22,24,28,29]. The first electron transfer event results in an unstable semiquinone at BF-FAD. The remaining electron is then hypothesized to travel down the endergonic path through EtfX, and the 2[4Fe-4S] clusters, reducing Fd. Studies on Etf complexes has suggested that some Etfs are membrane associated and involved in providing Fd or Fld to the nitrogenase systems responsible for reducing atmospheric nitrogen (N_2).

The [FeFe]-Hydrogenase System The final model enzyme Hyd, has provided evidence that inorganic cofactors, such as metal clusters, are capable of acting as sites of bifurcation. Hyd contains three subunits (ABC), several metal clusters, and a single FMN molecule [15,19,23,25]. HydA contains 2[2Fe-2S] cluster, 3[4Fe-4S] clusters, and a unique metal cluster termed the H-cluster. HydB contains 3[4Fe-4S] clusters, a [2Fe-2S] cluster, and a single FMN molecule, and HydC contains a single [2Fe-2S] cluster (**Fig 1.3C**). The Hyd system is hypothesized to catalyze the oxidation of H_2 to reduce NAD^+ and Fd (Eq3) [15,19,23,25].

$$2H_2 + 2NAD^+ + Fd_{ox} \rightarrow 2H^+ + 2NADH + Fd_{red} \tag{3}$$

It was originally thought that the FMN was the site of bifurcation, however only a single flavin binding motif is observed in the sequence of Hyd from *Thermotoga maritima*, and this is expected to be the site of NADH/NAD^+ binding[10]. The current hypothesis is thought that the H-cluster, the site of reversible hydrogen reduction, is the site of bifurcation in the Hyd complex. This is supported by a similar single subunit hydrogenase from *Clostridium pasteurianum* that does not bifurcate, but uses a similar array of FeS clusters to transport electrons from the H-cluster to the site of Fd binding[10,23]. The proposed pathway of bifurcation in Hyd is that hydrogen gas (H_2) is oxidized and an electrons is first transported to HydB where NAD^+ is reduced. The remaining electron then travels down the array of FeS clusters in HydA, then on to HydC where Fd is reduced.

Regulation of Electron Transfer in the Bifurcating Systems

Marcus Theory of Electron Transfer Each of the model bifurcating enzymes details the many ways anaerobic organisms have evolved to use EB to reduce ferredoxin. One area that remains of interest is how the enzymes regulate electron flow to prevent multiple electrons traveling down the exergonic pathway. The modern theory of electron transfer, developed by Rudolph A. Marcus, explains how an electrons environment influences the rate of electron transfer[3–5]. The two factors that influence electron transfer are the energy gap law, and the sensitivity of electron tunneling to the distance between donor and acceptor. The energy gap law intertwines the kinetics and thermodynamics of electron transfer, making them dependent on one another[30–32]. The donor-acceptor distance influences the rate of electron transfer between an electron donor and acceptor, and as the distance between the two species increases the rate of electron transfer decreases. The Marcus theory of electron transfer can be applied to proteins, which use a combination of the energy gap law and donor-acceptor distance to regulate the transfer of electrons between cofactors[30–32]. The Marcus theory of electron transfer can be applied to the bifurcating systems to understand the role protein structure plays in controlling electron transfer down the exergonic and endergonic branches.

Mechanisms of Allosteric Communication An emerging hypothesis on the regulation of electron transfer is that allostery plays a role in regulating which bifurcation branch the electron travels down. At its most basic level allostery can be defined as the transmission of a signal between two different binding sites. The allosteric signal is triggered by the binding of an effector molecule that can induce a conformational change.

The effects of the conformational change vary depending on the protein or effector that binds, and can enhance the binding of a ligand, increase the affinity between two protein subunits, or inhibit protein activity[33,34]. The discovery of allostery led to the development of two models that describe the basic mechanism of allosteric regulation. The first was the Monod-Wyman-Changeux (MWC) model which is also known as the concerted model (**Fig 1.4A**)[33]. The MWC model assumes that a protein complex is at equilibrium between a tense (T) and relaxed (R) state, where the T state is considered inactive and the R state active. When an effector binds to either state, the equilibrium is shifted to that state, altering the binding constant for a ligand.

The other model, Koshland-Nemethy-Filmer (KNF, or sequential), is another way of describing allosteric regulation within proteins[33]. The KNF model, similar to the MWC model, assumes that there are two protein states. However the KNF model differs with the assumption that each subunit in a multimeric protein goes through a conformational change independently (**Fig 1.4B**). This means that the binding of ligand at one subunit does not induce a conformational change at the other subunits, but increases the likelihood that the remaining subunits will undergo a conformational change. Each ligand binding event increases the probability that the remaining subunits will undergo a conformational change and bind a ligand. Ligand or effector binding increasing or decreasing the probability of binding at other subunits is known as cooperativity[33]. The KNF model demonstrates the basic concept behind positive cooperativity, where the likelihood of ligand binding increases as more ligands bind. In negative cooperativity, the binding of a negative effector decreases the probability of the remaining subunits binding a ligand.

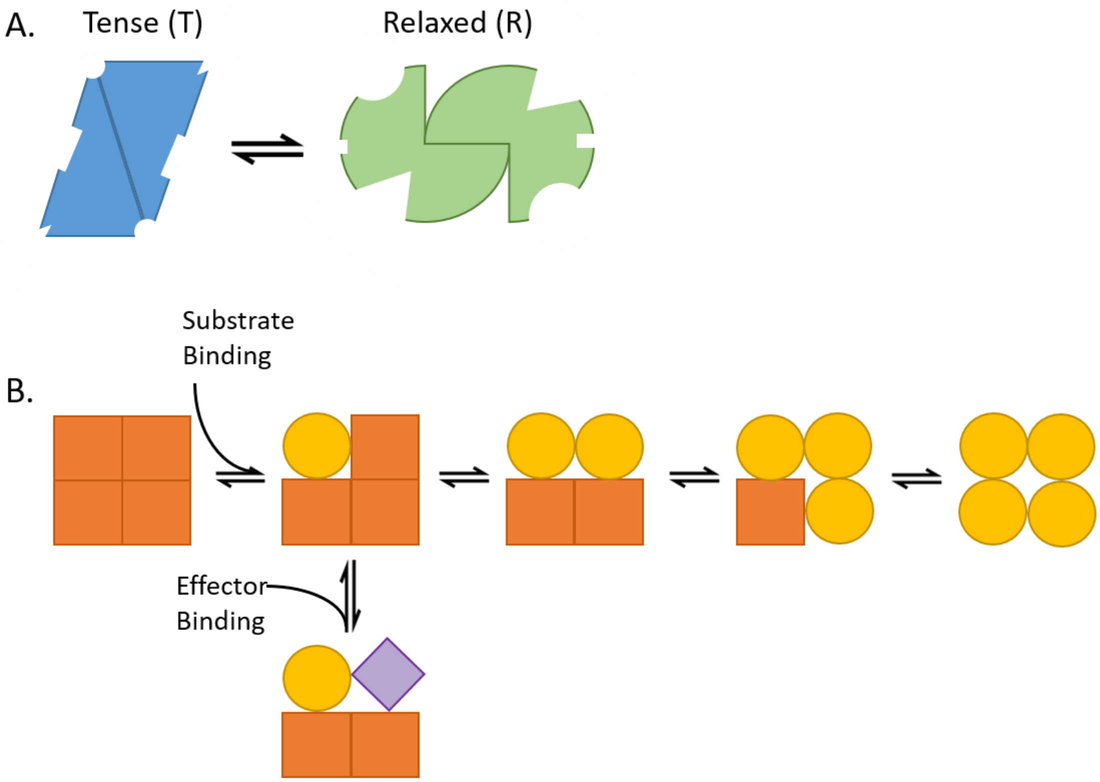

Figure 1.4 Schematic representation of the classical models of allostery. **(A)** The MWC model depicts the equilibrium between the tense and relaxed state of a protein. Both states have different binding sites available for effector and ligand binding. The binding of an effector molecule shifts the equilibrium between the T and R state allowing the protein to become active or inactive. **(B)** the KNF model of allostery depicts that the binding of a ligand to a single subunit of a multimeric protein increases the likelihood of the other subunits binding a ligand. Additionally, the binding of an effector molecule can increase the likelihood of ligand binding, or decrease the likelihood. The KNF model influenced the modern understanding of cooperativity.

The creation of the MWC and KNF models, has led to the identification of allosteric mechanisms in several protein systems. One insight gained from these studies is that the structural conformations available to a protein cannot be categorized into an active or inactive state[35,36]. Instead proteins adopt an ensemble of different conformations that are in equilibrium with one another, and this equilibrium can shift when an effector molecule binds. Initially allosteric regulation was expected to cause conformational changes that result in a distinctive shape to a protein's structure. While this is true for some proteins, it is becoming more apparent that the majority of proteins undergo much subtler conformational changes [37–39]. While much is known about the effects allostery can have on a protein, how the allosteric signal is sent from the effector binding site to the rest of the protein is still unknown[39,40]. The most common hypothesis is that proteins contain a conserved allosteric pathway that is responsible for transmitting the signal[39–42]. It is thought that a local stress event at the effector binding site causes a conformational change that is propagated from the allosteric site to the substrate or ligand binding site (**Fig 1.5**). In other words an effector molecule effects interacts with local amino acid residues by forming new bonds, altering the local interactions between amino acid residues. Alterations to amino acid residue interactions effects the enthalpy and entropy of the protein backbone, which has to be balanced by other residues[39–42]. Balancing the enthalpy and entropy of the protein backbone causes a cascade of changes from the effector binding site to the ligand binding site, as well as the rest of the protein[39–42].

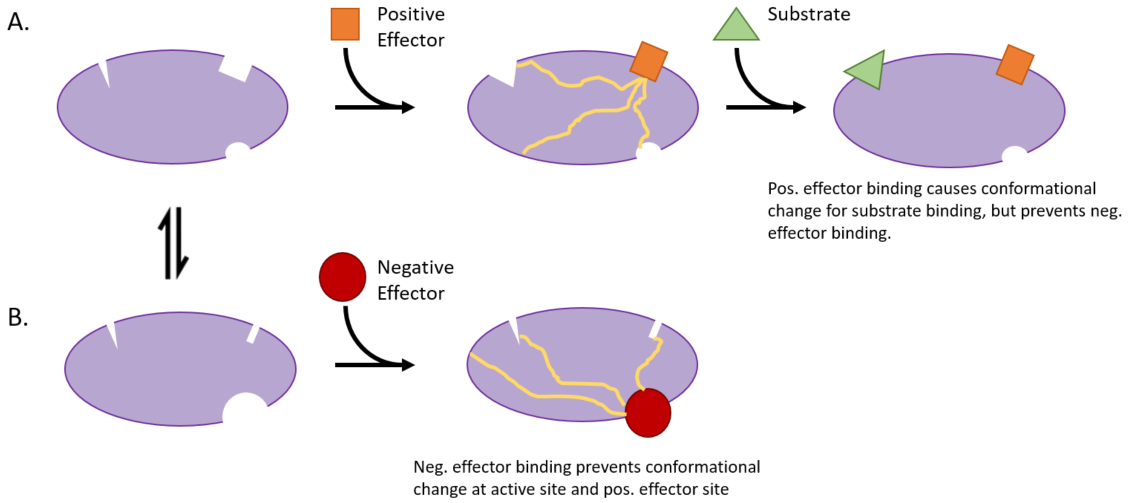

Figure 1.5 Modern view of allostery. Two protein conformations (**A**) and (**B**) are part of an ensemble of conformations that are in equilibrium with one another. (**A**) Depiction of a conformation that binds a positive effector molecule. The binding of the positive effector sends a signal from the binding site to other sites across the protein (gold lines). The binding of the positive effector activates the substrate binding site, while preventing negative effector molecules from binding. (**B**) Another protein conformation within the ensemble. With this conformation a negative effector molecule is able to bind to the protein. Binding of the negative effector sends a signal to other binding sites within the protein, preventing substrate and positive effector binding.

Relating Protein Dynamics to Allosteric Pathways

Computational Methods to Identify Allosteric Pathways

The discovery of allosteric pathways led to the development of several methods that can be used to identify these pathways. Several of these methods are computational and use simulations of a protein's 3D structure, or sequence alignments to identify evolutionarily conserved regions. One method is statistical coupling analysis (SCA) which uses the sequence of a protein of interest to do a multiple sequence alignment of 100+ homologous proteins[43–45]. Each residue is compared with the sequences of the homologous proteins, and when a mutation is found in a homologous protein, the remaining amino acid residues in that sequence are compared to the sequence of interest in order to identify another mutation. If another mutated residue is found, these residues are considered to be co-evolving. Co-evolving residues are evolutionarily conserved, meaning the mutation of one residue causes the other to mutate as well. For instance, if a residue were to mutate to a Lys in the interior of the protein, another residue would need to mutate to a negatively charged amino acid, in order to neutralize the charge and maintain protein structure. Co-evolving residues can serve as sites of potential mutagenesis experiments to test that activity of the protein, and build pathway of communication that traverses the protein structure.

An increasingly popular computational technique for the identification of allosteric pathways within a protein is normal mode analysis (NMA). Proteins adopt an ensemble of microstates that are in a dynamic equilibrium. NMA examines each microstate, and calculates the displacement of each amino acid residue and how this displacement effects the other residues in the protein structure. The calculations first determine the normal modes of a protein, and each normal mode is related to the thermal motions of the protein when all residues are oscillating at the same frequency[46–49]. The average of all normal modes determines the displacement of each amino acid residue, which are displayed as displacement vectors to indicate which residues have an in-phase (positive correlation) or out-of-phase (negative correlation) displacement. The displacement vectors can be illustrated in the form of a covariance matrix that shows the correlation of every residue in a protein. Examining specific regions, such as ligand binding sites, can reveal which parts of the protein have an in-phase displacement, and build a pathway of positively correlated residues that connect different sites of interest.

Additionally, areas with an out-of-phase correlation can be used to determine pathways of negative cooperativity[50]. This is especially helpful for large multi-subunit protein complexes.

In-Solution Methods to Relate a Protein's Structure and Function Computational methods can characterize protein dynamics on a global scale, however, experimental techniques are need to fully detail the structure-function relationship influences protein activity via allosteric pathways. Solution phase experimental techniques compliment computational methods by providing high resolution data on protein movements. A popular technique is surface labeling coupled to mass spectrometry (SL-MS), which uses a reagent to chemically modify specific amino side chains (**Fig 1.6**) [51–54]. After labeling, proteins are then digested by a protease to produce peptides, which are then analyzed by MS. MS identifies which residues have been labeled based on the change in the mass-to-charge ratio (m/z). The labeled residues can be used to characterize the surface topology of a protein. Experiments of SL-MS can also be used to identify protein-protein interactions and how ligand binding effects the surface of the protein.

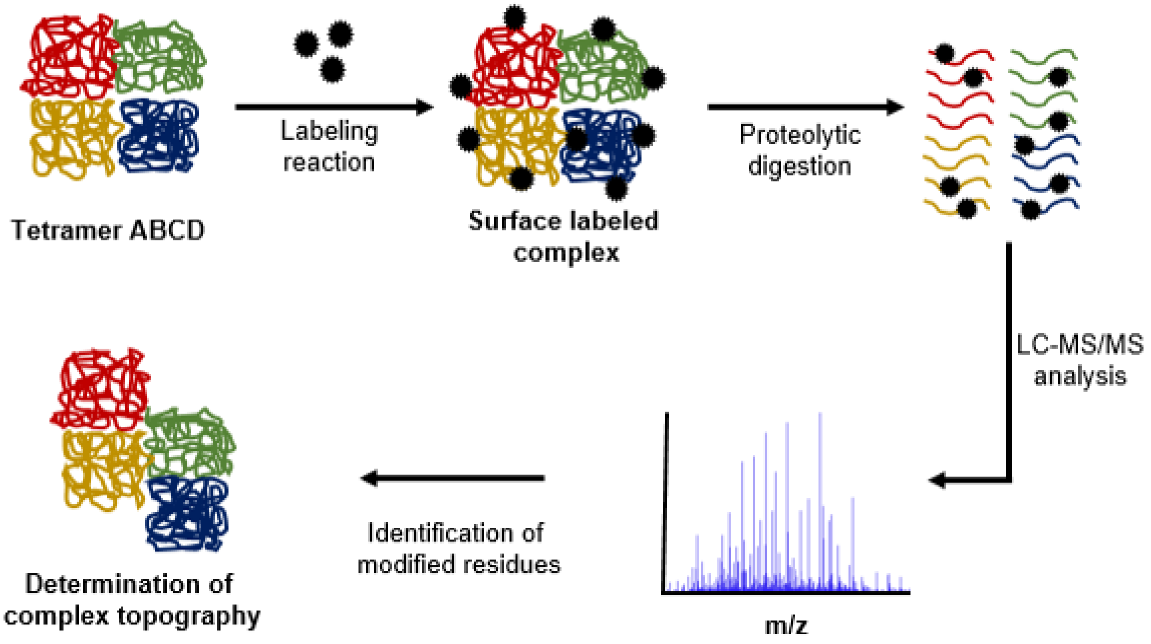

Figure 1.6 Schematic representing a general workflow of SL-MS. A protein of interest is incubated with a surface labeling reagent. The labeled protein is digested with a protease, and the peptides are then analyzed with LC-MS/MS. The MS data is used to identify the location of each of the surface labels. Once identified, this information can build a topology map of a protein complex. SL-MS can also be used in the presence of ligands, cofactors and even other protein subunits to determine how the addition of these components alters a protein's topography. Figure adapted from Tokimina-Lukaszewska et al. 2018[51].

Similar to SL-MS, chemical cross-linking coupled to MS (XL-MS) uses a reagent that targets specific amino acid side chains and connects two reactive groups with a carbon linker that can vary in distance (**Fig 1.7**)[51,55–58]. The cross-linker can react with two side chains simultaneously within a single subunit or between multiple subunits depending on the length of the cross-linker. After labeling protein digestion, followed by MS analysis is used to identify the cross-linked peptides with a cross-link map that can be used to build a 3D model of a protein. XL-MS can also be done in the presence of different ligands to identify changes in protein structure based on the changes in a cross-link map. While SL-MS and XL-MS can provide information on a protein structure, they are limited by the size of the reagents which can only label the surface of a protein.

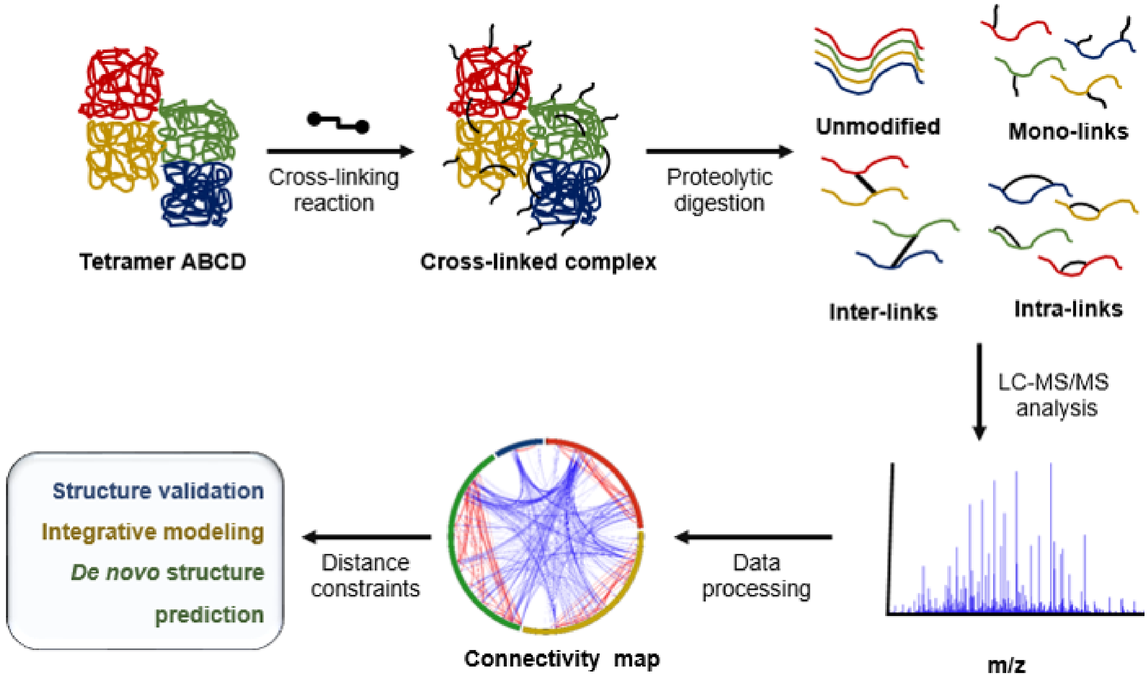

Figure 1.7 Schematic representing a general workflow of XL-MS. First a protein of interest (tetramer ABCD) is added to a solution of cross-linking reagents. The cross-linked complex is then exposed to a protease, such as trypsin, which digests the complex into peptides. These peptides can then be analyzed via LC-MS/MS to identify which peptides are cross-linked and the location of the cross-link. The LC-MS/MS data can be compiled into connectivity maps, which can reveal the inter- and intra-connectivity of each subunit. Finally, distance constraints can be factored in to perform structure validation, integrative modeling, and even structure predication with the cross-linking data. Figure adapted from Tokimina-Lukaszewska et al. 2018[51].

A technique that can provide high resolution information on a protein's structure and dynamics is H/D exchange coupled to mass spectrometry (HDX-MS) (**Fig 1.8**) [51,59–62]. Proteins have three types of hydrogens that are considered "exchangeable": carbon-hydrogen bonds, amine hydrogens on amino acid side chains, and amide hydrogens located on the peptide backbone. Of these three the only type that exchanges spontaneously and on a time scale that can be measured are the amide hydrogens located on the peptide backbone. The hydrogens exchange through an acid or based catalyzed reaction depending on the pH of the system[62]. By replacing the solvent system with deuterated water (D_2O) the amide hydrogens will exchange with the deuterium ions. As deuterium exchange occurs the mass of a protein will increase making MS an ideal technique to determine how much deuterium is incorporated into a protein by comparing the mass of a deuterated and non-deuterated protein.

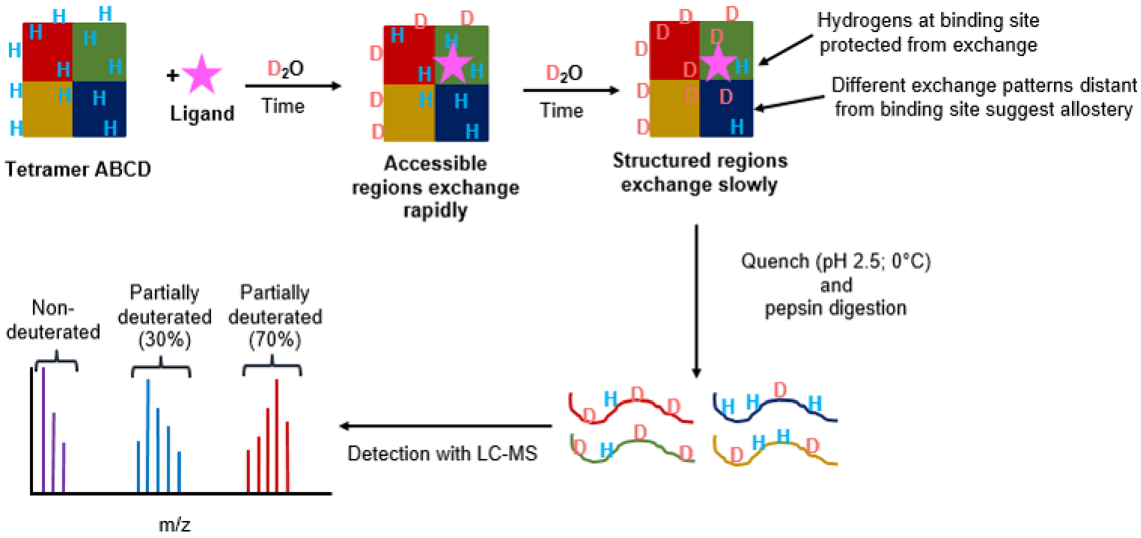

Figure 1.8 Schematic representing a general workflow of HDX-MS. First a protein, along with a ligand, is diluted into a solution containing D_2O. Accessible amide hydrogens (solvent exposed) will exchange rapidly, while amide hydrogens located in the interior of the protein will exchange at a slower rate. Additionally, the presence of a ligand will alter the exchange rate of amide hydrogens, typically by inducing a conformational change. The deuterated protein is placed in a low pH, low temperature solution to quench the reaction and digest the protein. The peptides are then analyzed via LC-MS and the amount of deuterium incorporated is calculated by comparing the deuterated peptides with non-deuterated peptides. Figure adapted from Tokimina-Lukaszewska et al. 2018[51].

Several factors can influence the rate of exchange on the peptide backbone. The most influential being secondary structural elements (alpha helices and beta sheets) which are stabilized by hydrogen bonds between an amide hydrogens and carbonyl oxygen [63–67]. The stability of the secondary structures effects the availability of amide hydrogens for deuterium exchange. Fast local unfolding breaks hydrogen bonds causing amide hydrogens to exchange quickly, whereas slower unfolding will need longer before the amide hydrogens are accessible to the deuterated solvent. The tertiary structure will also have an effect on exchange, with a protein's solvent accessible surface exchanging rapidly, and the interior of the protein will exchange slower. In addition to the structure of a single protein influencing the rate of exchange, protein-protein and protein-ligand interactions will also have an effect[63–67]. The quaternary interactions between proteins will decrease the accessibility of amide hydrogens, thus decreasing the exchange rate, or preventing exchange entirely by stabilizing the secondary structures at the protein-protein interface. Similar to protein-protein interactions, the binding of a ligand can alter the exchange rate based on the interactions that are formed. This aspect of HDX can be used to characterize a protein's structure and dynamics in the presence of ligands, cofactors and other subunits. Any changes in the deuterium incorporation rate can be used to determine how a protein's structure and dynamics change during catalysis, and how those changes relate to the mechanism[60,68–71]. Additionally, allosteric mechanisms can also be identified, and related to a protein's mechanism to build a pathway of communication, and determine the function of allostery within a protein system[72,73].

In general there are two types of HDX-MS experiments: intact HDX-MS and peptide level HDX-MS. Intact HDX-MS involves exposing a protein of interest to a deuterated solvent (between pH 7.0 and 8.0) by a 1:10 dilution in order to ensure that deuterium is the predominant species. From there a time course is collected and each sample is quenched by dropping the pH to 2.5, where the exchange reaction occurs at its slowest rate[62]. The protein mass can be obtained with MS, and by comparing the deuterated mass to the non-deuterated mass the amount of deuterium incorporated at each time point can be determined. Intact HDX-MS can only reveal global information on the rate of deuterium exchange, but with peptide level HDX-MS more local and higher resolution information on deuterium incorporation can be revealed. The only difference in peptide level HDX-MS is that during the quench step of the reaction, the protein of interest is exposed to pepsin, a non-specific protease active at low pH. Deuterated peptides reveal more local information about the rate of exchange within a protein.

Summary

The discovery of electron bifurcation in complex III of the ETC has led to the identification of several more bifurcating enzymes in anaerobic organisms. The function of these enzymes is to provide highly reduced species in the form of Fd and Fld to Anaerobic organisms. Fd and Fld can provide the energy necessary for reactions like hydrogen reduction, CO_2 reduction, and N_2 fixation. The reduction of Fd requires a large amount of energy (-450 mV), and in order to prevent the loss of excess energy anaerobes couple an exergonic reduction with the endergonic reduction of Fd. Studies on three model bifurcating enzymes (Nfn, Etf, and Hyd) showcase the diversity anaerobes have evolved to produce reduced Fd. Additionally these enzymes have provided evidence that inorganic cofactors as well as organic cofactors can be the site of electron bifurcation. An area that remains of interest is how the protein structure influences the transfer of electrons through the complex in order to prevent multiple electrons traveling down the exergonic branch.

It is hypothesized that electron bifurcating enzymes are controlled by an allosteric mechanism. This mechanism is proposed to influence how the substrate binding sites, the bifurcating center, and the Fd binding site influences the flow of electrons by utilizing subtle structural changes to remove key cofactors out of efficient electron transfer distance. The enclosed thesis details the study of this mechanism through the combined use of SL-MS, XL-MS, and HDX-MS to identify conformational changes at different steps of the bifurcating reactions. Additionally, SCA and NMA will be used to identify pathways of communication within the bifurcating enzymes. Together the computational and in-solution techniques will be used to build a model for the transmission of allosteric signals through bifurcating enzymes, and how these signals promote or prevent the transfer of electrons down the exergonic and endergonic branch.

References Cited

1. Fernie, A. R., Carrari, F. & Sweetlove, L. J. Respiratory metabolism: Glycolysis, the TCA cycle and mitochondrial electron transport. *Curr. Opin. Plant Biol.* **7,** 254–261 (2004).

2. Hatefi, Y. The Mitochondrial Electron Transport and Oxidative Phosphorylation System. *Ann. Rev. Biochem.* **54,** 1015–69 (1985).

3. Marcus, R. A., Sutin, N. & Stojek, Z. Electron transfers in chemistry and biology.

J. Phys. Chem. **67,** 504 (2002).

4. Marcus, R. A. On the theory of electrochemical and chemical electron transfer processes. *Can. J. Chem.* **37,** (1958).

5. Marcus, R. A. On the theory of oxidation-reduction reactions involving electron transfer. I. *J. Chem. Phys.* **24,** 966–978 (1956).

6. Peters, J. W., Miller, A. F., Jones, A. K., King, P. W. & Adams, M. W. W. Electron bifurcation. *Curr. Opin. Chem. Biol.* **31,** 146–152 (2016).

7. Kemeny, G. Energy Transfer Mechanisms in Mitochondria. *Quantum* **71,** 3669–3671 (1974).

8. Martin, W. F. Hydrogen, metals, bifurcating electrons, and proton gradients: The early evolution of biological energy conservation. *FEBS Lett.* **586,** 485–493 (2012).

9. Gnaiger, E., Steinlechner, R., Mendez, G., Eberl, T. & Margreiter, R. Control of Mitochondrial Respiration By Oxygen. *J Bioenerg. Biomembr.* **27,** 583–596 (1995).

10. Peters, J. W. *et al.* A new era for electron bifurcation. *Curr. Opin. Chem. Biol.* **47,** 32–38 (2018).

11. Mitchell, P. The Protonmotive Q Cycle: A General Formulation. *FEBS Lett.* **59,** 137–139 (1975).

12. Metcalf, W. W. Classic spotlight: Electron bifurcation, a unifying concept for energy conservation in anaerobes. *J. Bacteriol.* **198,** 1358–1358 (2016).

13. Chowdhury, N. P. *et al.* Studies on the mechanism of electron bifurcation catalyzed by electron transferring flavoprotein (Etf) and butyryl-CoA dehydrogenase (Bcd) of acidaminococcus fermentans. *J. Biol. Chem.* **289,** 5145–5157 (2014).

14. Thauer, R. K., Jungermann, K. & Decker, K. Energy conservation in chemotrophic anaerobic bacteria. *Bacteriol. Rev.* **41,** 100–180 (1977).

15. Buckel, W. & Thauer, R. K. Flavin-based electron bifurcation, ferredoxin, flavodoxin, and anaerobic respiration with protons (Ech) or NAD+(Rnf) as electron acceptors: A historical review. *Front. Microbiol.* **9,** (2018).

16. Buckel, W. & Thauer, R. K. Energy conservation via electron bifurcating

ferredoxin reduction and proton/Na+ translocating ferredoxin oxidation. *Biochim. Biophys. Acta - Bioenerg.* **1827,** 94–113 (2013).

17. Peters, J. W., Beratan, D. N., Schut, G. J. & Adams, M. W. W. On the nature of organic and inorganic centers that bifurcate electrons, coupling exergonic and endergonic oxidation-reduction reactions. *Chem. Commun.* **54,** 4091–4099 (2018).

18. Herrmann, G., Jayamani, E., Mai, G. & Buckel, W. Energy conservation via electron-transferring flavoprotein in anaerobic bacteria. *J. Bacteriol.* **190,** 784–791 (2008).

19. Buckel, W. & Thauer, R. K. Energy conservation via electron bifurcating ferredoxin reduction and proton/Na+ translocating ferredoxin oxidation. *Biochim. Biophys. Acta - Bioenerg.* **1827,** 94–113 (2013).

20. Buckel, W. & Thauer, R. K. Flavin-Based Electron Bifurcation, A New Mechanism of Biological Energy Coupling. *Chem. Rev.* **118,** 3862–3886 (2018).

21. Lubner, C. E. *et al.* Mechanistic insights into energy conservation by flavin-based electron bifurcation. *Nat. Chem. Biol.* **13,** 655–659 (2017).

22. Schut, G. J. *et al.* The catalytic mechanism of electron bifurcating electron transfer flavoproteins (ETFs) involves an intermediary complex with NAD $^{+}$. *J. Biol. Chem.* jbc.RA118.005653 (2018). doi:10.1074/jbc.RA118.005653

23. Schut, G. J. & Adams, M. W. W. The iron-hydrogenase of Thermotoga maritima utilizes ferredoxin and NADH synergistically: A new perspective on anaerobic hydrogen production. *J. Bacteriol.* **191,** 4451–4457 (2009).

24. Costas, A. M. G. *et al.* Defining electron bifurcation in the electron-transferring flavoprotein family. *J. Bacteriol.* **199,** (2017).

25. Schuchmann, K. & Müller, V. A bacterial electron-bifurcating hydrogenase. *J. Biol. Chem.* **287,** 31165–31171 (2012).

26. Demmer, J. K., Rupprecht, F. A., Eisinger, M. L., Ermler, U. & Langer, J. D. Ligand binding and conformational dynamics in a flavin-based electron-bifurcating enzyme complex revealed by Hydrogen–Deuterium Exchange Mass Spectrometry. *FEBS Lett.* **590,** 4472–4479 (2016).

27. Berry, L. *et al.* H/D exchange mass spectrometry and statistical coupling analysis reveal a role for allostery in a ferredoxin-dependent bifurcating transhydrogenase catalytic cycle. *Biochim. Biophys. Acta - Gen. Subj.* **1862,** 9–17 (2018).

28. Diessel Duan, H. *et al.* Distinct properties underlie flavin-based electron bifurcation in a novel electron transfer flavoprotein FixAB from Rhodopseudomonas palustris. *J. Biol. Chem.* **293,** 4688–4701 (2018).

29. Demmer, J. K., Pal Chowdhury, N., Selmer, T., Ermler, U. & Buckel, W. The semiquinone swing in the bifurcating electron transferring flavoprotein/butyryl-CoA dehydrogenase complex from Clostridium difficile. *Nat. Commun.* **8,** (2017).

30. Beratan, D. N. *et al.* Steering electrons on moving pathways. *Acc. Chem. Res.* **42,** 1669–1678 (2009).

31. Peters, J. W., Beratan, D. N., Schut, G. J. & Adams, M. W. W. On the nature of organic and inorganic centers that bifurcate electrons, coupling exergonic and endergonic oxidation-reduction reactions. *Chem. Commun.* **54,** 4091–4099 (2018).

32. Beratan, D. N. *et al.* Charge transfer in dynamical biosystems, or the treachery of (static) images. *Acc. Chem. Res.* **48,** 474–481 (2015).

33. Cui, Q. & Karplus, M. Allostery and Cooperativity revisited. *Protein Sci.* **17,** 1295–1307 (2008).

34. Motlagh, H. N. & Hilser, V. J. Agonism/antagonism switching in allosteric ensembles. *Proc. Natl. Acad. Sci.* **109,** 4134–4139 (2012).

35. Motlagh, H. N., Wrabl, J. O., Li, J. & Hilser, V. J. The ensemble nature of allostery. *Nature* **508,** 331–339 (2014).

36. Hilser, V. J., Wrabl, J. O. & Motlagh, H. N. Structural and Energetic Basis of Allostery. *Annu. Rev. Biophys.* **41,** 585–609 (2012).

37. Mitternacht, S. & Berezovsky, I. N. Coherent conformational degrees of freedom as a structural basis for allosteric communication. *PLoS Comput. Biol.* **7,** (2011).

38. Daily, M. D. & Gray, J. J. Allosteric communication occurs via networks of tertiary and quaternary motions in proteins. *PLoS Comput. Biol.* **5,** (2009).

39. del Sol, A., Tsai, C. J., Ma, B. & Nussinov, R. The Origin of Allosteric Functional Modulation: Multiple Pre-existing Pathways. *Structure* **17,** 1042–1050 (2009).

40. Goodey, N. M. & Benkovic, S. J. Allosteric regulation and catalysis emerge via a common route. *Nat. Chem. Biol.* **4,** 474–482 (2008).

41. Tsai, C., Sol, A. & Nussinov, R. Allostery: Absence of a change in shape does not imply that allostery is not at play. *J. Mol. Biol.* **378,** 1–11 (2008).

42. Tsai, C. J., Del Sol, A. & Nussinov, R. Protein allostery, signal transmission and dynamics: A classification scheme of allosteric mechanisms. *Mol. Biosyst.* **5,** 207–216 (2009).

43. Reynolds, K. A., McLaughlin, R. N. & Ranganathan, R. Hot spots for allosteric regulation on protein surfaces. *Cell* **147,** 1564–1575 (2011).

44. Lockless, S. W. & Ranganathan, R. Evolutionarily conserved pathways of energetic connectivity in protein families. *Science (80-.).* **286,** 295–299 (1999).

45. Halabi, N., Rivoire, O., Leibler, S. & Ranganathan, R. Protein Sectors: Evolutionary Units of Three-Dimensional Structure. *Cell* **138,** 774–786 (2009).

46. Dobbins, S. E., Lesk, V. I. & Sternberg, M. J. E. Insights into protein flexibility: The relationship between normal modes and conformational change upon protein-protein docking. *Proc. Natl. Acad. Sci.* **105,** 10390–10395 (2008).

47. Fuglebakk, E., Tiwari, S. P. & Reuter, N. Comparing the intrinsic dynamics of multiple protein structures using elastic network models. *Biochim. Biophys. Acta - Gen. Subj.* **1850,** 911–922 (2015).

48. Bahar, I. Normal Mode Analysis of Biomolecular Structures: Functional Mechanisms of Membrane Proteins. *Lang. Dev. crossroads* **110,** 49–59 (1983).

49. Tirion, M. M. Large amplitude elastic motions in proteins from a single-parameter, atomic analysis. *Phys. Rev. Lett.* **77,** 1905–1908 (1996).

50. Danyal, K. *et al.* Negative cooperativity in the nitrogenase Fe protein electron delivery cycle. *Proc. Natl. Acad. Sci.* **113,** E5783–E5791 (2016).

51. Tokmina-Lukaszewska, M. *et al.* The role of mass spectrometry in structural studies of flavin-based electron bifurcating enzymes. *Front. Microbiol.* **9,** (2018).

52. Steiner, R. F., Albaugh, S., Fenselau, C., Murphy, C. & Vestling, M. A mass spectrometry method for mapping the interface topography of interacting proteins, illustrated by the melittin-calmodulin system. *Anal. Biochem.* **196,** 120–125 (1991).

53. Glocker, M. O., Borchers, C., Fiedler, W., Suckau, D. & Przybylski, M. Molecular Characterization of Surface Topology in Protein Tertiary Structures by Amino-Acylation and Mass Spectrometric Peptide Mapping. *Bioconjug. Chem.* **5,** 583–590 (1994).

54. Suckau, D., Mak, M. & Przybylski, M. Protein surface topology-probing by selective chemical modification and mass spectrometric peptide mapping. *Proc. Natl. Acad. Sci. U. S. A.* **89,** 5630–4 (1992).

55. Young, M. M. *et al.* High throughput protein fold identification by using experimental constraints derived from intramolecular cross-links and mass spectrometry. *Proc. Natl. Acad. Sci.* **97,** 5802–5806 (2000).

56. Herzog, F. *et al.* Structural Probing of a Protein Phosphatase 2A Network by Chemical Cross-Linking and Mass Spectrometry. *Science (80-.).* **337,** 1348–1352 (2012).

57. Kaake, R. M. *et al.* A New in Vivo Cross-linking Mass Spectrometry Platform to Define Protein–Protein Interactions in Living Cells. *Mol. Cell. Proteomics* **13,** 3533–3543 (2014).

58. Fernandez-Martinez, J. *et al.* Structure and Function of the Nuclear Pore Complex Cytoplasmic mRNA Export Platform. *Cell* **167,** 1215–1228.e25 (2016).

59. Engen, J. R. Analysis of protein conformation and dynamics by hydrogen/deuterium exchange MS. *Anal. Chem.* **81,** 7870–7875 (2009).

60. Konermann, L., Pan, J. & Liu, Y.-H. Hydrogen exchange mass spectrometry for studying protein structure and dynamics Introduction: protein folding, dynamics, and function. *Chem. Soc. Rev. Chem. Soc. Rev* **40,** 1224–1234 (2011).

61. Percy, A. J., Rey, M., Burns, K. M. & Schriemer, D. C. Probing protein interactions with hydrogen/deuterium exchange and mass spectrometry-A review. *Anal. Chim. Acta* **721,** 7–21 (2012).

62. Walters, B. T., Ricciuti, A., Mayne, L. & Englander, S. W. Minimizing back exchange in the hydrogen exchange-mass spectrometry experiment. *J. Am. Soc. Mass Spectrom.* **23,** 2132–2139 (2012).

63. Woodward, C. K. & Hilton, B. D. HYDROGEN EXCHANGE KINETICS AND INTERNAL MOTIONS IN PROTEINS AND NUCLEIC ACIDS. *Annu. Rev. Biophys. Bioeng.* **8,** 99–127 (1979).

64. Woodward, C., Simon, I. & Tüchsen, E. Hydrogen exchange and the dynamic structure of proteins. *Mol. Cell. Biochem.* (1982). doi:10.1007/BF00421225

65. Englander, S. W., Mayne, L., Bai, Y. & Sosnick, T. R. Hydrogen exchange: the modern legacy of Linderstrøm-Lang. *Protein Sci.* **6,** 1101–1109 (1997).

66. Englander, S. W. & Kallenbach, N. R. Hydrogen exchange and structural dynamics of proteins and nucleic acids. *Q. Rev. Biophys.* **16,** 521–655 (1983).

67. Jaswal, S. S. Biological insights from hydrogen exchange mass spectrometry. *Biochim. Biophys. acta Protein Proteomics* **1834,** 1188–201 (2013).

68. Trabjerg, E., Nazari, Z. E. & Rand, K. D. Conformational analysis of complex protein states by hydrogen/deuterium exchange mass spectrometry (HDX-MS): Challenges and emerging solutions. *TrAC - Trends Anal. Chem.* **106,** 125–138 (2018).

69. Berry, L. *et al.* H/D exchange mass spectrometry and statistical coupling analysis reveal a role for allostery in a ferredoxin-dependent bifurcating transhydrogenase catalytic cycle. *Biochim. Biophys. Acta - Gen. Subj.* **1862,** (2018).

70. Chalmers, M. J., Busby, S. A., Pascal, B. D., West, G. M. & Griffin, P. R. Differential hydrogen/deuterium exchange mass spectrometry analysis of protein-ligand interactions. *Expert Review of Proteomics* **8,** 43–59 (2011).

71. Van Erp, P. B. G. *et al.* Conformational Dynamics of DNA Binding and Cas3 Recruitment by the CRISPR RNA-Guided Cascade Complex. *ACS Chem. Biol.* **13,** (2018).

72. Engen, J. R. *et al.* Partial cooperative unfolding in proteins as observed by hydrogen exchange mass spectrometry. *International Reviews in Physical Chemistry* (2013). doi:10.1080/0144235X.2012.751175

73. Wei, H. *et al.* Using hydrogen/deuterium exchange mass spectrometry to study conformational changes in granulocyte colony stimulating factor upon PEGylation. *J. Am. Soc. Mass Spectrom.* (2012). doi:10.1007/s13361-011-0310-x

CHAPTER TWO

HYDROGEN DEUTERIUM EXCHANGE MASS SPECTROMETRY OF OXYGEN SENSITIVE PROTEINS

Contributions of Authors and Co-Authors

Manuscript in Chapter 2

Author: Luke Berry

Contributions: Developed protocols for the hydrogen deuterium exchange experiment, operation of the mass spectrometer, and the preparation of oxygen sensitive proteins. Wrote and edited manuscript.

Co-Author: Angela Patterson

Contributions: Developed protocols for the hydrogen deuterium exchange experiment and operation of the mass spectrometer. Reviewed manuscript during development.

Co-Author: Natasha Pence

Contributions: Developed protocol for the preparation of oxygen sensitive proteins, Reviewed manuscript during development.

Co-Author: John Peters

Contributions: Supervised the development of oxygen sensitive protein preparation protocol. Reviewed manuscript during development.

Co-Author: Brian Bothner

Contributions: Supervised the development of the hydrogen deuterium exchange and mass spectrometry protocols. Reviewed manuscript during development.

Manuscript Information

HYDROGEN DEUTERIUM EXCHANGE MASS SPECTROMETRY OF OXYGEN SENSITIVE PROTEINS

Authors: Luke Berry, Angela Patterson, Natasha Pence, John Peters, and Brian Bothner

Journal: Bio-protocols

Status of Manuscript:
___ Prepared for submission to a peer-reviewed journal
___ Officially submitted to a peer-reviewed journal
___ Accepted by a peer-reviewed journal
_x_ Published in a peer-reviewed journal

Published in Vol 8, Issue 06 of Bio-protocols on March 02, 2018
(DOI: 10.21769/BioProtoc.2769)

CHAPTER TWO

HYDROGEN DEUTERIUM EXCHANGE MASS SPECTROMETRY OF OXYGEN SENSITIVE PROTEINS

Abstract

The protocol detailed here describes a way to perform hydrogen deuterium exchange coupled to mass spectrometry (HDX-MS) on oxygen sensitive proteins. HDX-MS is a powerful tool for studying the protein structure-function relationship. Applying this technique to anaerobic proteins provides insight into the mechanism of proteins that perform oxygen sensitive chemistry. A problem when using HDX-MS to study anaerobic proteins is that there are many parts that require constant movement into and out of an anaerobic chamber. This can affect the seal, increasing the likelihood of oxygen exposure. Exposure to oxygen causes the cofactors bound to these proteins, a common example being FeS clusters, to no longer be interact with the amino acid residues responsible for coordinating the FeS clusters, causing irreversible inactivation of the protein and the loss of the FeS clusters. To counteract this, a double vial system was developed that allows the preparation of solutions and reaction mixtures anaerobically, but also allows these solutions to be moved to an aerobic environment while shielding the solutions from oxygen. Additionally, movement isn’t limited like it is in an anaerobic chamber, ensuring more consistent data, and fewer errors during the course of the reaction.

Background

Many oxygen sensitive proteins are required for organisms to thrive in an anoxic environment. Some of these proteins provide an alternative supply of energy to anaerobic microbes through a process known as Flavin-based electron bifurcation (FBEB) (Lubner *et al*., 2017). FBEB generates reduced ferredoxin, which can be oxidized to produce energy. Proteins that are capable of reducing ferredoxin are of great interest and have been the focus of recent studies using HDX-MS (Demmer *et al*., 2016; Lubner *et al*., 2017; Berry *et al*., 2018). HDX-MS is a powerful technique for investigating protein stability, dynamics, and ligand binding providing information about the relationship between structure and function. HDX-MS uses the intrinsic property of amide hydrogens to exchange with hydrogens in solution to track changes in the structure and dynamics of a protein/protein complex. By preparing buffers with heavy water (D_2O) instead of monoisotopic water (H_2O), amide hydrogens on a protein will exchange with the deuterium in solution. The rate of exchange for a given amino acid is influenced by the stability of hydrogen bonds in the secondary structure, as well as the tertiary and quaternary interactions within a single protein or protein complex. Using mass spectrometry, deuterium incorporation is determined by measuring the shift in isotope distribution between deuterated and non-deuterated samples. HDX-MS has been applied to a large number of proteins and protein complexes across a wide range of conditions. To successfully study these proteins with HDX-MS, it was imperative to establish a means of performing this reaction on the benchtop to avoid heavy traffic into and out of an anaerobic chamber which is time consuming and burdensome. The problem was then how to allow manipulation of the sample while keeping the protein sample anaerobic for an extended period of time in an aerobic environment. To solve this problem, the reaction mixture and protein stock solutions were placed into a double vial system that allowed addition and removal of sample while maintaining strict anaerobic conditions. The logic behind the setup was to create an airlock. Vials are placed under positive pressure with nitrogen gas with a screw cap vial, inside a larger crimp vial that contains reductant. With this double barrier system, small volumes of air can be trapped in the outer vial and do not contact the sample.

Materials and Reagents

1. Curwood Parafilm M^{TM} laboratory wrapping film (Fisher, catalog number: 13-374-10)
2. Onyx Monolithic C18 column, 100 mm x 2 mm (Phenomenex,catalog number: CH0-8467)
    a. Alternative columns (see notes for detailed explanation):
        i. Onyx Monolithic C18 column, 100 mm x 3 mm (Phenomenex, catalog number: CH0-8158)
3. Verex^{TM} vial kit, 9 mm, screw top, polpropylene, 300 µl + PTFE/silicone cap, blue, 1000/pk (Phenomenex, catalog number: AR0-9991-13)
4. Model 1701 and 1702 small RN syringes, 10 µl (26s gauge) and 25 µl (22s gauge), 2" needle point style 2 (VWR (Hamilton), catalog numbers: 60376-172 (80030) and 60376-183 (80230))
5. Clear glass serum vial with 20 mm crimp top finish, 10 ml, 100/case (Wheaton, catalog number: 225278)
6. Unlined aluminum open-top seals, 20 mm, 1000/case (Wheaton, catalog number: 224178-405)
7. 20 mm stopper, straight plug, ultra-pure (Wheaton, catalog number: W224100-405)
8. Costar Microcentrifuge Tubes 0.65 ml, 500/bag (Fisher, catalog number: 07-200-185/3208)
9. 200 µl Pipet Tips (VWR, catalog number: 53508-810)
10. 37% hydrochloric acid (=12.1 M) (EMD, catalog number: HX0603-3)
11. Ammonium acetate, >=99% (Sigma, catalog number: 09689-250G)
12. Sodium hydroxide (Fisher, catalog number: HX0603-3)
13. Purified NADH-dependent ferredoxin-NADP$^+$ oxidoreductase (Nfn) in 20 mM Tris, 150 mM NaCl buffer at pH 8 in H_20 (stock concentration 16.5 mg/ml) from the organism *Pyrococcus furiosus* (*Pf*).

   a. pH set with 1 M HCl

14. Purified ferredoxin (Fd) in 50 mM Ammonium Acetate buffer at pH 6.8 in H_20 (stock concentration 150 μM) from *Pf.*
    a. pH set with 1 M HCl
15. Deuterium oxide (Sigma-Aldrich, catalog number: 151882-100G)
16. Tris base (Calbiochem-Fisher, catalog number: 64-831-15KG)
17. Sodium chloride (Fisher Scientific, catalog number: BP358-212)
18. Sodium dithionite (Sigma-Aldrich, catalog number: 1065051000)
19. 99.5% Formic acid (ThermoFisher, catalog number: A117-50)
20. Pepsin from porcine gastric mucosa (Sigma-Aldrich, catalog number: P6887-1G)
21. Sodium acetate trihydrate (Fisher Scientific, catalog number: S607-500)
22. HPLC grade water (ThermoFisher, catalog number: W5-4)
23. HPLC grade acetonitrile (ThermoFisher, catalog number: A998N1-4)
24. Nanopure water (purified in-house using a Millipore Q-Gard 2 [EMD Millipore, catalog number: QGARD00D2]
25. Nicotinamide adenine dinucleotide (NAD^+, Cayman Chemical, catalog number: 16077-500mg)
26. Nicotinamide adenine dinucleotide (NADH, Cayman Chemical, catalog number: 16078-500mg)
27. Nicotinamide adenine dinucleotide phosphate ($NADP^+$, Cayman Chemical, catalog number: 10004675-50mg)
28. Nicotinamide adenine dinucleotide phosphate (NADPH, Cayman Chemical, catalog number: 9000743-25mg)
29. Liquid nitrogen
30. Tris base, NaCl buffer (pH 7.0) in deuterium oxide (see Recipes)
    a. pH set with 1 M HCl
31. Tris base, NaCl buffer (pH 7.0) in H_2O (see Recipes)
    a. pH set with 1 M HCl
32. Tris base, NaCl, sodium dithionite buffer (pH 7.0) in H_2O (see Recipes)
    a. pH set with 1 M HCl

Equipment

1. HPLC stack for separation of peptides generated via pepsin digestion (*e.g.*, 1290 Infinity series HPLC stack manufactured by Agilent Technologies) (Agilent Technologies, model: 1290 Infinity series)
2. LC/MS Q-TOF system for sample analysis/data acquisition (*e.g.*, 6538 UHD Accurate-Mass Q-TOF LC/MS manufactured by Agilent Technologies) (Agilent Technologies, model: 6538 UHD Accurate-Mass Q-TOF LC/MS)
3. Glove box capable of maintaining anaerobic conditions under positive inert gas pressure (*e.g.*, UNIlab Plus Glove Box Workstation manufactured by MBraun)
4. Milli-Q purification system (EMD Millipore, catalog number: QGARD00D2)
5. 20 mm Kebby standard crimper for aluminum seals (Med Lab Supply, catalog number: 20001-00-C01A)
6. Pipettes (10 µl and 100 µl) (Eppendorf, BioExpress, catalog numbers: P-3015-6 and P-3015-1)
7. Fisher Scientific isotemp 110 water bath (Fisher Scientific, catalog number: S63077Q)

Software

1. Microsoft Excel 2016 on Windows 7
2. UCSF Chimera v. 1.11.2
3. MassHunter Workstation Software Qualitative Analysis v. B.06.00 (Agilent Technologies)
4. HDExaminer v. 1.3.0 beta 6 (Sierra Analytics, Inc.)
5. MassHunter Workstation Software LC/MS Data Aqcuisition for 6200 series TOF/6500 series Q-TOF v. B.05.01 (Agilent Technologies)
6. Peptide Analysis Worksheet Freeware Edition (PAWs, ProteoMetrics – freeware edition)
7. SearchGUI v. 3.2.18 (Compomics)
8. Peptide Shaker v. 1.16.9 (Compomics)

Procedure

A. Reaction preparation

1. Before preparation of stock solutions and reaction mixtures, determine the number of time points. The number of time points dictates the volume of the reaction mixtures. For every time point, 10 µl must be available to add to the quench solution, plus an additional 10 µl for the 24 h/fully deuterated time point. For instance, in the HDX experiment of Nfn, five time points were measured (1 min, 3 min, 15 min, 60 min, 3 h, and 24 h) (Berry *et al.*, 2018). An additional 10 µl of reaction solution is included to prevent withdrawing the full reaction solution, thus bringing the total volume to 70 µl.

   Note: Time points are chosen to provide data on fast, medium, and slow exchanging residues. Data spanning multiple time scales facilitates a deeper interpretation of the results. While short time points can be very informative on protein dynamics, care should be taken to allow time to withdraw sample from the reaction chamber and quench in a reproducible manner.
2. Prepare stock solutions and reaction mixtures under anaerobic conditions, using an MBraun glove box fed by a nitrogen tank set to 40 PSI. The anaerobic atmosphere inside the glove box is maintained by keeping a positive nitrogen pressure. The exact gas flow will depend on the specific set up, however, the gas sensor monitoring conditions inside the glove box should register 0 ppm O_2 and H_2O and a positive pressure of 2 mbar.
3. Prepare two anaerobic aliquots of purified Nfn (stock concentration 16.5 mg/ml) in an MBraun glove box by adding 30 µl of Nfn into one verex vial, and 10 µl of Nfn into another verex vial. Purified Fd is then added to the 10 µl aliquot of Nfn in a 1:1 molar ratio. Using a double vial system, cap the Verex vials, and place inside a clear glass serum vial that contains 1 ml of degassed Tris-HCl buffer with sodium dithionite, and seal using a crimper. Remove sealed vials from the glove box, wrap in parafilm, and store at 4 °C prior to reaction initiation.

Note: Only 1 ml of reductant containing buffer is added to the glass serum vial. Any more volume causes the Verex vial to slightly float, making it difficult to withdraw sample at the designated time points.

4. Make deuterated buffers with 1 mM of each pyridine nucleotide in the following combinations: NAD^+, NADH, $NADP^+$, NADPH, NADH + $NADP^+$, and NADPH + NAD^+. Also prepare an additional stock of the same buffer without pyridine nucleotides to test the Nfn:Fd complex.

   Note: A 5 mL stock of deuterated buffer was made and subsequently aliquoted out with each nucleotide combination to make a 500 µL stock of each condition to use to set up reaction mixtures. For a condition run in triplicate, 500 µL should be sufficient volume to set up reaction mixtures. These volumes can/should change depending on the number of conditions and time points being tested.

5. Prepare reaction vials by first degassing the deuterated buffers using four-10 min cycles on a Schlenk line. The Schlenk line functions by alternating between a vacuum to remove the oxygen, and nitrogen to place the solutions under positive pressure. After degassing, transfer reaction solutions to the glove box.

6. Place 63 µl of each reaction buffer into three Verex vials, cap, place into clear glass serum vials, and seal using a crimper. This volume of buffer accommodates the volume for all time points while also leaving room for the addition of the protein. Seal the reaction vials, remove from the glove box, and store at room temperature prior to reaction initiation.

7. Prepare a quench solution for each time point, and keep the solutions on ice before and during the reaction. Prepare solutions in Costar microcentrifuge tubes by mixing 1% formic acid (45 µl) and porcine pepsin (15 µl of 1 mg/ml in 50 mM sodium acetate pH 4.5 (H_2O; pH set with 0.1 M HCl); final concentration: 0.2 mg/ml). This final concentration of pepsin gives sufficient coverage of the target proteins (~100%) in the limited digestion time. Prepare a separate quench solution with 10 µl of reaction buffer to test the pH of the solution. The target pH for HDX quenching is pH 2.5.

   Notes:

   a. *Quench solutions do not need to be prepared anaerobically because the reaction is over at this point.*
   b. *Pepsin digestion of the protein localizes the location of exchange onto certain regions of the protein while under low pH quench conditions.*

B. Hydrogen Deuterium exchange reaction

1. Begin the HDX reaction by adding protein via a 1:10 (v/v) dilution into the deuterated buffer using gastight Hamilton syringes (this results in a final Nfn concentration of 1.6 mg/ml). This ensures that D_2O is the dominant solvent species. A workflow depicting the HDX reaction steps is shown in **Figure 2.1**.

   Note: The reaction for Nfn is performed at 60 °C. Regulation of this temperature was through a Fisher Scientific isotemp 110 water bath. This temperature was chosen to simulate the high temperature conditions where the organism, Pyrococcus furiosus lives.
2. At specific time points (for this reaction: 1 min, 3 min, 15 min, 60 min, 3 h, and 24 h), remove 10 µl of the reaction mixture using a gas tight, Hamilton syringe, and add to the quench solution (pH 2.5, 0°C; Concentration of Nfn in quench solution: ~0.23 mg/ml).

   Notes:
   a. *This halts the exchange reaction, so any damage to the protein caused by low pH, temperature, or oxygen exposure will not impact data interpretation.*
   b. *Pepsin digestion is allowed to proceed for 2 min before flash freezing the solution in liquid nitrogen and storing at -80 °C.*

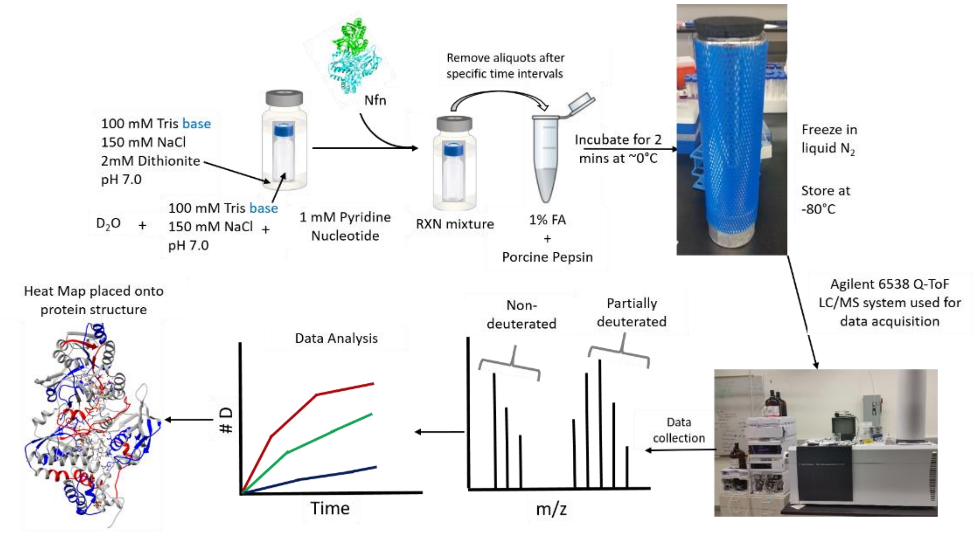

Figure 2.1. HDX-MS sample prep and workflow. Samples are kept anaerobic using a double vial system in which all reaction components are added to a small screw cap vial, which are sealed anaerobically in a slightly larger clear glass crimp vial. Protein is injected into the reaction mixture using gas tight Hamilton syringes to initiate the reaction. At designated time points, 10 µl of sample is extracted from the reaction mixture and added to an aerobic quench solution, containing formic acid and porcine pepsin. The acid not only locks in any deuterium that has exchanged onto the protein, but also serves to partially denature the protein complex, making it more accessible to pepsin digestion. Additional unfolding occurs upon exposure to oxygen. After 2 min of digestion, samples are flash frozen in liquid N$_2$ and stored at -80 °C until data acquisition on Agilent 6538 Q-TOF. After acquisition, data is processed to display deuterium uptake over time in the form of uptake curves. Deuterium incorporation can be localized onto the structure of a protein by mapping the deuterium incorporation onto a 3D structure of the protein (if one is available).

C. Data acquisition and processing

1. Conduct liquid chromatography using an Onyx monolithic C18 column with the following gradient of A (H_2O, 0.1% formic acid) and B (ACN, 0.1% formic acid) solvents over 10 min: 0.0-1.0 min, 5% B; 1.0-9.0 min, 5-45% B; 9.1-9.8 min, 95% B; 9.8-9.9 min, 5% B. Set the flow rate to 500 µl/min. Inject 10 µl, resulting in the injection of approximately 2.3 µg of protein onto the column. Keep the solvents cool (~0 °C) by storing the LC bottles on ice before and during data acquisition. Additionally, set the column compartment temperature to 1 °C and the auto-sampler

temperature to 4 °C to help maintain a low temperature in the samples prior to injection on the mass spectrometer.

Notes:

a. *Low temperatures in the HPLC stack helps minimize the amount of back exchange during chromatographic separation of peptides.*
b. *The HPLC stack used in this protocol does not allow lower temperatures in the auto-sampler and lower temperatures in the column compartment are not stable, which can result in variations in the data.*

2. For data acquisition on an Agilent 6538 Q-TOF operating with MassHunter Workstation Software, scans are collected at 2 Hz over a scan range 50-1,700 *m/z* in positive mode. Set electrospray settings to the following: nebulizer gas at 3.7 bar, drying gas at 8.0 L/min, drying temperature at 350 °C, ~~and~~ capillary voltage at 3.5 kV, and the acquisition mode was set to MS (seg).

   Note: Agilent Technologies supplies detailed information on its software for new users. For more information about different software options including masshunter, please refer to Agilent Technologies' website (Agilent Software: Software & Informatics)

3. Identify compounds in the mass spectra by molecular feature in Agilent MassHunter Qualitative Analysis using the following settings: Extraction algorithm target data type, Small molecules; Peak filters, ≥ 500 counts; Ion species, +H and +Na; Isotope grouping, peak spacing tolerance 0.0025 *m/z* + 7.0 ppm, isotope model: peptides; Charge state assignment limited to a maximum of 5.

   Note: This is also a good chance to review the data, and look in the mass spectra for signs that deuterium exchange took place (this can also be done during data acquisition). Find an isotope envelope of a peptide in the non-deuterated sample. Then look at the same retention time in the deuterated samples to see if the isotope distribution has shifted. If it has, the experiment worked, if not, it is crucial to determine why the exchange either didn't work, or why back exchange occurred causing a loss of deuterium ions. An example isotope comparison can be seen in ***Figure 2.2A****.*

4. Create compound lists for non-deuterated digests of the protein sample, and export as a compound summary CSV (.csv) and import into Microsoft Excel 2016.
5. Use the compound summary lists in a two-step process to identify peptides produced by pepsin digestion.

   Notes:

   a. *The first step identifies unique peptides detected with mass spectrometry. These are masses that only have one match with the sequence of Nfn, while also falling in the mass error tolerance.*
   b. *The second step determines the identity of masses containing multiple peptide matches within the error tolerance by collecting fragmentation data to sequence the peptide.*
6. Place the protein sequence into PAWs to create a theoretical cleavage map using pepsin cleavage sites and an error of 100 ppm to account for the non-specific nature of pepsin cleavage.

   Note: Pepsin cleavage sites are after the following residues: L, W, I, A, F, Y, N, T, C, V, S, Q, G, E, D, R, M, K, H, and P. Cleavage sites were chosen based on outputs provided by the program PeptideShaker.
7. PAWs identifies unique peptides for each of the subunits present in the protein complex of interest. Unique peptides are those who only have one match with the sequence of Nfn within the set error tolerance (100 ppm). Add each unique peptide to an Excel spreadsheet along with the corresponding sequence, charge, and retention time.

   Note: Exclude any masses with multiple matches within the error tolerance
8. Save the peptide list as a comma delimited (.csv) file.

D. Peptide fragmentation data acquisition and processing

1. Several peptides can have the same m/z, therefore in order to successfully identify these peptides fragmentation was data collected on the Agilent 6538 Q-TOF instrument. ~~Set c~~Collision energies for fragmentation were set as a gradient over the data acquisition scan range (50-1700 *m/z*) ranging from 4 V to 68 V.

Note: The HPLC and MS settings that were used are the same as discussed previously in Section C, steps 1 and 2 with the exception of the data acquisition mode, which is set to auto MS/MS (seg)..

2. Open the data files in the Masshunter Qualitative Analysis software to identify fragmentation features using the command ‘Find by Auto MS/MS’. Then export the data files as a Mascot Generic File (.mgf).
3. Use SearchGUI to identify peptides based on the fragmentation data.
   a. To set up SearchGUI, start by defining the protein sequence. For this experiment the sequence for the Nfn small and large subunits from *Pyrococcus furiosus* is used. SearchGUI will ask to make decoy sequences, which will help identify false positives.
   b. Next, set the search parameters for SearchGUI. For this experiment use the following settings: Digestion: Enzyme; Enzyme: Pepsin A; Specificity: Semi-Specific; Max Missed Cleavages: 5; Fragment Ion Types: b and y; Precursor *m/z* Tolerance: 20 ppm; Fragment *m/z* Tolerance: 20 ppm; Precursor Charge: 1-5; Isotopes: 0-1.
   c. Choose both the output folder, as well as the search engines. For this experiment, X!Tandem, MyriMatch and MS Amanda are chosen for the peptide search.
   d. Select PeptideShaker for post processing. PeptideShaker provides an easy to follow output of the fragment ion identifications, and provides the sequence, *m/z*, and retention time of the identified peptides.
   e. Combine the peptides identified from the fragmentation data ~~to~~ with the unique peptides identified in PAWs. The combined list of identified peptides is saved as a .csv file, and used as the input file for deuterium incorporation calculations.

E. Calculation of deuterium uptake using HDExaminer

1. Deuterium incorporation is calculated by measuring the shift in the centroid of the isotope distribution for a given peptide. While this can be done manually, it is extremely time consuming. Several programs are available that will calculate the

deuterium incorporation for HDX data. HDExaminer is a commercially available program by Sierra Analytics Inc. that accomplishes this.

Note: Sierra Analytics has several tutorial videos to show the features of HDExaminer and how to set up the program (HDExaminer: The Basics).

2. To set up HDExaminer, first add the sequence for the protein of interest and add a list of tested conditions on the 'proteins' page. This allows the program to calculate the deuterium incorporation in each condition.
3. Next, add the list of peptides under the 'peptides' page, and select the column which has the charge, sequence, and retention time of each peptide. Then add the peptides to the peptide pool.
4. Finally, on the 'analysis' page add the data files for each condition. All conditions will have the non-deuterated files, which are added first. Next add the fully deuterated data files (24 h time point), followed by the partially deuterated data files (1 min, 3 min, 15 min, 1 h, 3 h). To begin calculations automatically select the 'auto-calculate' box in the bottom right-hand corner of the screen, otherwise calculations will have to be initiated manually. A progress bar in the bottom right-hand corner indicates when calculations are underway.

   Note: Alternatively, the maximum number of deuterium can be calculated from the number of exchangeable amide hydrogens within the peptide sequence.
5. Once the calculations are complete, manually verify the calculations.
   a. Under the peptide tab of HDExaminer, each peptide has a dropdown menu showing the different conditions. Each condition has an additional dropdown menu showing the different charge states of the peptide based on the peptide pool.
   b. If HDExaminer successfully identifies the location of the peptide within the data files, clicking on a charge state shows the isotope distribution of the peptide in each data file on the left-hand side. The right-hand side shows the chromatogram for each data file and two red arrows indicate the retention time window containing the peptide isotope pattern.

   c. To verify the data, examine the retention time window for the peptides, they should be the same, or within a few seconds of one another for each data file. The search window can be adjusted by moving either of the red arrows. If the partially deuterated or fully deuterated data files are changed, the deuterium incorporation for only those files will be re-calculated. However, if the non-deuterated files search retention time is changed, the deuterium incorporation for all data files for that peptide will be re-calculated.
   d. Manually verifying the data ensures the same retention time search window is used for all data files for a peptide. This gives the most accurate measurement of the deuterium incorporation and helps minimize the error between replicates.
6. After manual verification, export the peptide pool results for each condition, this provides the peptide identification, search retention time and charge. This also provides the start and end retention time, amount of deuterium incorporated (#D), percent deuterium incorporated (%D), score and confidence for each time point and replicate.
7. The data provided in the peptide pool results can be used in a variety of ways.
   a. The easiest means of visualizing the data are uptake curves which show the #D incorporated into a peptide over time. Generate a curve for each peptide in order to compare the deuterium incorporation over time for each condition tested. **Figure 2.2B** displays an example of an uptake curve that shows a comparison of four conditions.
   b. An additional way to analyze the data is to calculate the %D incorporated and measure the percent difference to determine the relative change in accessibility to exchange between conditions. Calculate the %D by dividing the #D for a time point by the #D from the fully deuterated sample and multiply by 100. Then calculate the percent difference by subtracting the %D for two conditions. This allows comparisons in the deuterium incorporation between peptides of different length.
   c. Map the percent difference onto the structure of the protein (if available) to show the areas that are impacted by the different conditions. Mapping the

exchange data onto the structure can also reveal the presence of allostery, as well as which regions of the protein are communicating with one another to enact the allosteric mechanism.

Note: For a detailed explanation on mapping exchange data onto a protein structure, see Data Analysis.

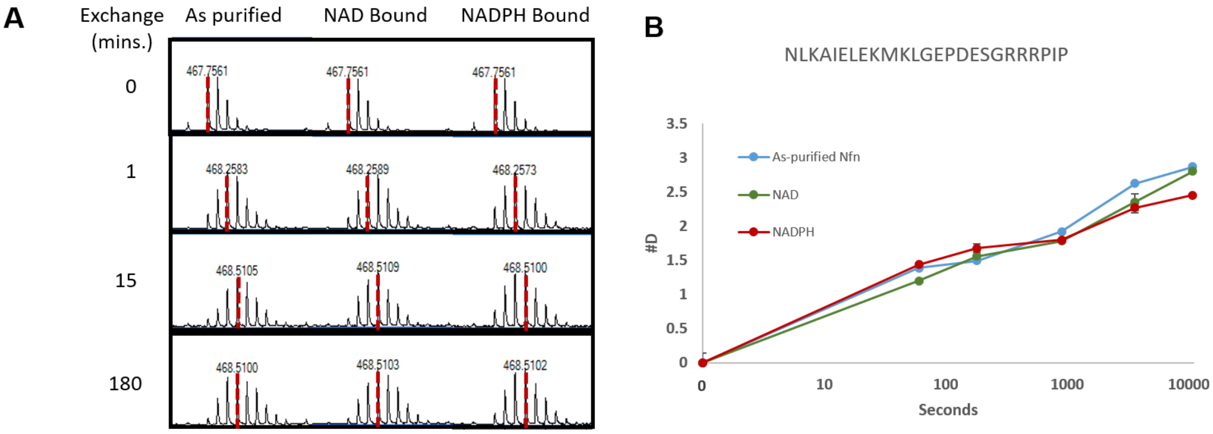

Figure 2.2. A) Example of the shift in isotope distribution for a peptide from Nfn-L. As the time for exchange increases (0-180 mins) the centroid shifts to the right due to the addition of deuterium, as indicated by the dashed red line. **B**) Uptake curves showing the deuterium incorporation for four tested conditions. This data is for residues 124-144 of Nfn-L, the amino acid sequence located above the uptake curve.

Data Analysis

1. Use MassHunter Qualitative Analysis to verify the data during data acquisition by examining the deuterated samples for evidence of exchange in the isotope distribution. This is done by comparing the deuterated samples to the non-deuterated samples. **Figure 2.2A** shows an example of this by displaying the isotope distribution for the non-deuterated, 1 min, 15 min, and 3 h time points. This allows for a comparison in the shift in the isotope distribution as more deuterium is incorporated between the tested conditions.

2. After calculation of the deuterium incorporation, use Microsoft Excel or a similar spreadsheet program to generate uptake curves to compare deuterium incorporation over time in the tested conditions within a peptide. **Figure 2.2B** shows an example uptake curve.
3. To compare deuterium incorporation between multiple peptides and/or conditions, convert the #D to %D and calculate the difference between two peptides. Additionally, the percent difference can be mapped onto a 3D structure of a protein using UCSF Chimera as shown in **Figure 2.3** (Pettersen *et al.*, 2004).
4. Generate a structure-based heat map of the HDX data in UCSF Chimera (Pettersen *et al.*, 2004).
    a. Create a txt file that lists the residue number and the %D that correlates to that residue in the following format:

    ```
    Attribute: nad_nadph-as_purified_nfn_3hrs_percent_deuterium
    match mode: 1-to-1
    recipient: residues

    :1.A	20
    :2.A	20
    :3.A	45
    :4.A	45
    :5.A	45
    ```

    The header names the attribute that will be displayed onto the model and defines that the residues are what will be colored according to the attribute (rather than atoms). The ':1.A' defines the residue number and chain name. A tab separates the value from the residue identifier. These columns can easily be generated in Excel or a similar spreadsheet program and either saved as a txt file or copy/pasted into a text file. If there is no data for a residue, leave empty space next to the residue identifier or completely remove the line.

b. Open the pdb protein structure file in Chimera. Go to Tools > Structure Analysis > Define Attribute. Select the .txt file generated in step a.

   Note: An error will open in a pop up window if data is listed for residues that are not resolved in the structure file. This error can be ignored.

c. Once the attribute is defined, the Render/Select by Attribute window opens. Use this window to determine which colors will represent which %D values.

   i. Residues that are listed in the txt file but do not have data associated with them will be colored according the highest %D color unless an additional color is added above this value.

   ii. To add additional color bars use Ctrl + left click in the histogram plot. Ctrl + left click on existing color bars to remove them.

   iii. Move color bars either by the mouse or by entering a value in the 'Value' box.

d. Click 'Apply' to color the protein structure according to the data file.

e. **Figure 2.3** shows an example of a colored structure.

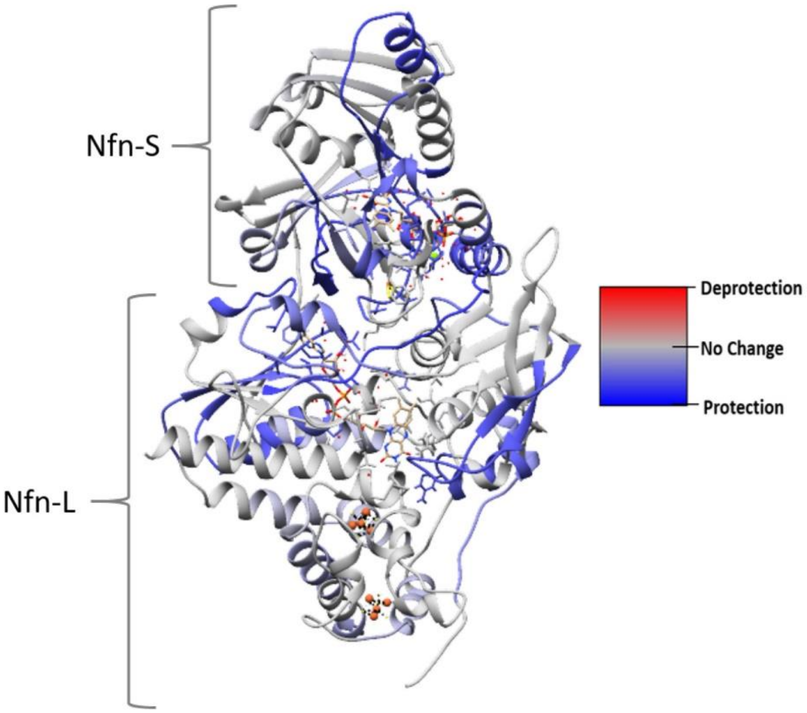

Figure 2.3. HDX-MS data mapped onto a protein structure. This structural heat map shows the influence of NADPH and NAD$^+$ binding on exchange of Nfn. H/D exchange data collected under two different conditions was mapped onto the protein structure using UCSF Chimera (see Notes). The heat map was calculated from the difference deuterium uptake in the as-purified and NADPH + NAD$^+$ bound reactions. Color code was set to red (100% difference, increased exchange), blue (-100% difference, protection), and gray (0% difference, no change). In this example, the NADPH + NAD$^+$ bound condition incorporates less deuterium than the as-purified protein.

<u>Notes</u>

1. The recommended alternative column for HPLC separation of peptides is the same as the one used in the protocol described here, however the internal diameter is 1 mm larger. This will influence the flow rate of solvent through the column, which can affect the elution of peptides from the column. It is highly recommended to test different flow rates and gradients to optimize separation of peptides prior to performing the exchange reaction.

2. The measured pH of the deuterated buffers must be corrected to pD by adding the correction factor (0.4 pH units) to the measured pH. For this experiment the tris base buffer prepared in D_2O had a measured pH of 7.0, therefore the pD of the buffer is 7.4 (Krezel *et al. 2004)*
3. Before beginning the exchange reaction, check that the quench solution with formic acid, pepsin, and reaction buffer is at pH 2.5 so back exchange does not occur during protein digestion.
4. Place HPLC solvents on ice, set the column compartment to 0 °C, and the auto-sampler to 4 °C to help reduce back exchange of the deuterated amides.
5. HDX-MS can be performed under a wide range of temperatures. While exchange rate does have a dependence on temperature, pH can affect it much more (Walters *et al.,* 2012). However, it should be noted that a comparative analysis between HDX-MS reactions run at different temperatures is difficult because of the change in exchange rate as the temperature is varied. HDX-MS is most commonly run at 25 °C (room temperature), however some cases are reported to run as low as 0°C and as high as 60 °C.
6. When planning an HDX-MS experiment, it is highly recommended that the starting concentration of the protein of interest be approximately 10 mg/ml, this ensures that approximately 1.5 μg of protein is injected onto the instrument.
   a. Lower amounts of protein injected onto the instrument will cause low intensity peptides to be detected, which in turn can prevent accurate deuterium incorporation calculations.
   b. A 1:10 dilution of protein into D_2O buffer is encouraged, it is possible to do less if a particular protein is not easy to obtain aliquots with a high concentration. It is then recommended to do some pilot experiments to ensure that deuterium incorporation is satisfactory, and the extra water present in the reaction is not causing back exchange of the deuterium ions.

Recipes

1. Tris base buffer in deuterium oxide (shelf life ~one week)

   100 mM Tris-HCl

   150 mM NaCl at pH 7.0
2. Tris base buffer in H_2O

   100 mM Tris-HCl

   150 mM NaCl at pH 7.0
3. Tris base buffer w/sodium dithionite

   100 mM Tris-HCl

   150 mM NaCl

   2 mM sodium dithionite at pH 7.0

References Cited

1. Berry, L., Poudel, S., Tokmina-Lukaszewska, M., Colman, D. R., Nguyen, D. M. N., Schut, G. J., Adams, M. W. W., Peters, J. W., Boyd, E. S. and Bothner, B. (2018). H/D exchange mass spectrometry and statistical coupling analysis reveal a role for allostery in a ferredoxin-dependent bifurcating transhydrogenase catalytic cycle. *Biochim Biophys Acta* 1862(1): 9-17.

2. Demmer, J. K., Rupprecht, F. A., Eisinger, M. L., Ermler, U. and Langer, J. D. (2016). Ligand binding and conformational dynamics in a flavin-based electron-bifurcating enzyme complex revealed by Hydrogen-Deuterium Exchange Mass Spectrometry. *FEBS Lett* 590(24): 4472-4479.

3. Lubner, C. E., Jennings, D. P., Mulder, D. W., Schut, G. J., Zadvornyy, O. A., Hoben, J. P., Tokmina-Lukaszewska, M., Berry, L., Nguyen, D. M., Lipscomb, G. L., Bothner, B., Jones, A. K., Miller, A. F., King, P. W., Adams, M. W. W. and Peters, J. W. (2017). Mechanistic insights into energy conservation by flavin-based electron bifurcation. *Nat Chem Biol* 13(6): 655-659.

4. Pettersen, E. F., Goddard, T. D., Huang, C. C., Couch, G. S., Greenblatt, D. M., Meng, E. C. and Ferrin, T. E. (2004). UCSF Chimera--a visualization system for exploratory research and analysis. *J Comput Chem* 25(13): 1605-1612.

5. Krezel, A. and Bal, W. (2004). A formula for correlating pK_a values determined in D_2O and H_2O. *J Inorg Biochem* 98:161-166.

6. Walters, B. T., Ricciuti, A., Mayne, L. and Englander, S. W. (2012). Minimizing back exchange in the hydrogen exchange-mass spectrometry experiment. *J Am Soc Mass Spectrom* 23(12): 2132-2139.

CHAPTER THREE

H/D EXCHANGE MASS SPECTROMETRY AND STATISTICAL COUPLING ANALYSIS REVEAL A ROLE FOR ALLOSTERY IN A FERREDOXIN-DEPENDENT BIFURCATING TRANSHYDROGENASE CATALYTIC CYCLE

Contributions of Authors and Co-Authors

Manuscript in Chapter 3

Author: Luke Berry

Contributions: Planned and performed the HDX experiment, including sample preparation, data acquisition, and analysis. Organized and wrote manuscript.

Co-Author: Saroj Poudel

Contributions: Performed SCA calculations, and analyzed results. Wrote sections of manuscript involving SCA data, and reviewed manuscript during development.

Co-Author: Monika Tokmina-Lukaszewska

Contributions: Performed native mass spectrometry on the Nfn protein. Reviewed manuscript during development.

Co-Author: Daniel R. Colman

Contributions: Assisted with SCA calculations and reviewed manuscript during development.

Co-Author: Diep M.N. Nguyen

Contributions: Purified protein samples and reviewed manuscript during development.

Co-Author: Gerrit J. Schut

Contributions: Purified protein samples and reviewed manuscript during development.

Co-Author: Michael W.W. Adams

Contributions: Supervised protein purification and reviewed manuscript during development.

Co-Author: John W. Peters

Contributions: Reviewed manuscript during development.

Co-Author: Eric S. Boyd

Contributions: Supervised SCA calculations and reviewed manuscript during development.

Co-Author: Brian Bothner

Contributions: Supervised mass spectrometry based techniques and reviewed manuscript during development.

Manuscript Information

H/D EXCHANGE MASS SPECTROMETRY AND STATISTICAL COUPLING ANALYSIS REVEAL A ROLE FOR ALLOSTERY IN A FERREDOXIN-DEPENDENT BIFURCATING TRANSHYDROGENASE CATALYTIC CYCLE

Authors: Luke Berry, Saroj Poudel, Monika Tokmina-Lukaszewska, Daniel R. Colman, Diep M.N. Nguyen, Gerrit J. Schut, Micheal W.W. Adams, John W. Peters, Eric S. Boyd, Brian Bothner

Journal: Biochimica et Biophysica Acta (BBA) – General Subjects

Status of Manuscript:
___ Prepared for submission to a peer-reviewed journal
___ Officially submitted to a peer-reviewed journal
___ Accepted by a peer-reviewed journal
_x_ Published in a peer-reviewed journal

Published in Vol 1862, Issue 1 of BBA – General Subjects in Janurary 2018
(DOI: 10.1016/j.bbagen.2017.10.002)

CHAPTER THREE

H/D EXCHANGE MASS SPECTROMETRY AND STATISTICAL COUPLING ANALYSIS REVEAL A ROLE FOR ALLOSTERY IN A FERREDOXIN-DEPENDENT BIFURCATING TRANSHYDROGENASE CATALYTIC CYCLE

Abstract

Recent investigations into ferredoxin-dependent transhydrogenases, a class of enzymes responsible for electron transport, have highlighted the biological importance of flavin-based electron bifurcation (FBEB). FBEB generates biomolecules with very low reduction potential by coupling the oxidation of an electron donor with intermediate potential to the reduction of high and low potential molecules. Bifurcating systems can generate biomolecules with very low reduction potentials, such as reduced ferredoxin (Fd), from species such as NADPH. Metabolic systems that use bifurcation are more efficient and confer a competitive advantage for the organisms that harbor them. Structural models are now available for two NADH-dependent ferredoxin-NADP$^+$ oxidoreductase (Nfn) complexes. These models, together with spectroscopic studies, have provided considerable insight into the catalytic process of FBEB. However, much about the mechanism and regulation of these multi-subunit proteins remains unclear. Using hydrogen/deuterium exchange mass spectrometry (HDX-MS) and statistical coupling analysis (SCA), we identified specific pathways of communication within the model FBEB system, Nfn from *Pyrococus furiosus*, under conditions at each step of the catalytic cycle. HDX-MS revealed evidence for allosteric coupling across protein subunits upon nucleotide and ferredoxin binding. SCA uncovered a network of co-evolving residues that can provide connectivity across the complex. Together, the HDX-MS and SCA data show that protein allostery occurs across the ensemble of iron-sulfur cofactors and ligand binding sites using specific pathways that connect domains allowing them to function as dynamically coordinated units.

Abbreviations

FBEB: Flavin-Based Electron Bifurcation

HDX-MS: H/D Exchange Mass Spectrometry

#D: Absolute number of deuterium incorporated

%D: Percentage of deuterium incorporated

SCA: Statistical Coupling Analysis

Nfn: NADH-dependent ferredoxin-NADP$^+$ oxidoreductase I

Nfn-S: Nfn Small Subunit

Nfn-L: Nfn Large Subunit

Fd$_{Ox}$: Oxidized Ferredoxin

Fd$_{Red}$: Reduced Ferredoxin

FAD: Flavin Adenine Dinucleotide

NAD$^+$/NADH: Nicotinamide Adenine Dinucleotide

NADP$^+$/NADPH: Nicotinamide Adenine Dinucleotide Phosphate

Tm: *Thermatoga maritima*

Pf: *Pyrococcus furiosus*

Introduction

NADH-dependent ferredoxin-NADP$^+$ oxidoreductase (Nfn) catalyzes the formation of reduced ferredoxin (Fd$_{Red}$), from the less energetic donor, nicotinamide adenine dinucleotide phosphate (NADP$^+$/NADPH), by coupling this reaction to the thermodynamically favorable reduction of nicotinamide adenine dinucleotide (NAD$^+$/NADH), through a process termed flavin-based electron bifurcation (FBEB)

[1,2]. FBEB modulates the energy metabolism within a cell by coupling the oxidation of an electron donor with an intermediate reduction potential to promote the reduction of two electron acceptors, one with a high reduction potential and one with a low potential. Doing so allows the formation of low potential, high-energy compounds, such as hydrogen gas and reduced Fd. Due to the relatively recent discovery of FBEB, the mechanism behind catalysis remains largely unresolved. However, crystal structures of the bifurcating enzyme Nfn were successfully obtained from *Thermotoga maritima* (*Tm*) [3] and *Pyrococcus furiousus* (*Pf*) [4] which enhances the ability to study the FBEB mechanism using this enzyme.

Nfn is a heterodimeric protein comprising a small (Nfn-S) and large (Nfn-L) subunit (**Fig 3.1A**) [4,5]. Each of these subunits have cofactors involved in the bifurcation reaction, including two flavin adenine dinucleotides (FAD), one in each subunit, a proximal [4Fe-4S] cluster (p[4Fe-4S]) in Nfn-L, a distal [4Fe-4S] cluster (d[4Fe-4S]) in Nfn-L, and one [2Fe-2S] cluster in Nfn-S. These cofactors allow Nfn to catalyze the formation of reduced Fd, from NADPH and NAD$^+$ (eq **1, Fig. 3.1B**). The enzyme can also catalyze the reverse confurcating reaction to form NADPH by oxidizing Fd and NADH (**Fig. 3.1C**); this is thought to be the physiological role of Nfn.

$$2\ \mathrm{NADPH} + \mathrm{NAD}^+ + \mathrm{Fd}_{\mathrm{Ox}} \rightleftharpoons 2\ \mathrm{NADP}^+ + \mathrm{NADH} + \mathrm{Fd}_{\mathrm{Red}}^{2-} + \mathrm{H}^+ \qquad (\mathbf{1})$$

Studies of Nfn purified from *Pf* and *Tm* have revealed that NAD$^+$/NADH binds to Nfn-S, and NADP$^+$/NADPH binds to Nfn-L, and Fd is predicted to bind to Nfn-L near the distal [4Fe-4S] cluster [4,6]. Recent studies have revealed that the bifurcation reaction proceeds by the formation of a highly unstable flavin anionic semiquinone (ASQ) that forms through the oxidation of NADPH, and this ASQ has sufficient energy to reduce Fd [4]. A key feature of bifurcating enzymes, specifically Nfn from *Pf*, that remains unknown is how energy is conserved during the exergonic reduction reaction, how this energy is then used to drive the endergonic reaction, and whether gating of electrons might be involved in either of these processes. Studying the effects of substrate binding on the structure and dynamics of Nfn may provide critical new information regarding the role of protein structure in modulating FBEB.

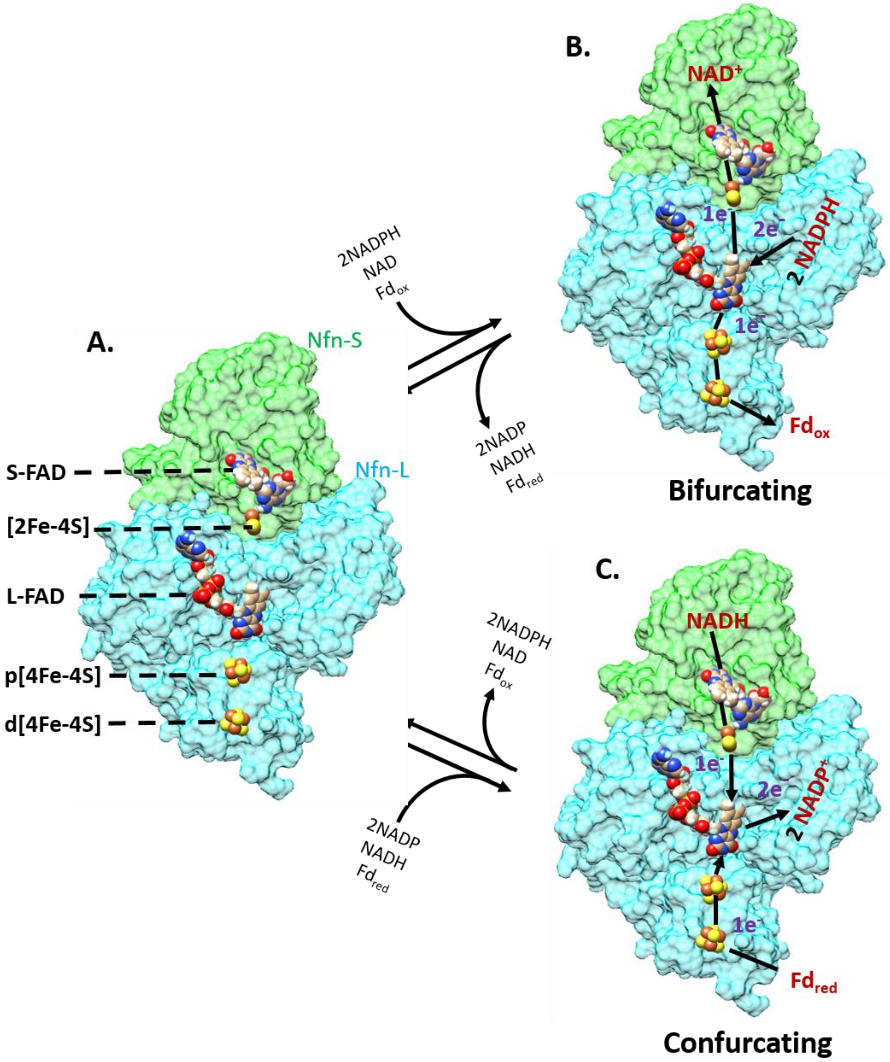

Figure 3.1 *Schematic representation of the electron bifurcation and confurcation reactions in Nfn*: (**A**). Surface rendered model of Nfn from *P. furiosus* (PDB ID: 5JCA) with the small subunit, Nfn-S, shown in green, and the large subunit, Nfn-L, shown in blue. Cofactors are spheres and their location within the complex is shown. Nfn-S contains a FAD (S-FAD) and a [2Fe-2S] cluster while Nfn-L contains a FAD (L-FAD) and two [4Fe-4S] clusters, one proximal (p[4Fe-4S]) and one distal (d[4Fe-4S]) to the FAD. (**B**). Schematic representation of the bifurcating reaction. During the bifurcation reaction, two NADPH bind to the large subunit and transfer electrons to L-FAD. One electron is then sent to the high potential branch and another to the low potential branch. These individual electrons then reduce NAD and Fd_{ox} to NADH and Fd_{red}. (**C**). The reverse reaction of electron bifurcation is termed electron confurcation and involves the oxidation of Fd_{red} and NADH to reduce NADP. The electrons follow the path indicated by black arrows (**B** and **C**).

While previous studies have described the structure and catalytic properties associated with Nfn [7,8], the finer mechanistic details of FBEB in this enzyme largely remain unknown. In a recent study of *Tm* Nfn using H/D exchange mass spectrometry (HDX-MS), it was shown that binding of the nucleotide NADP$^+$/NADPH to Nfn-L resulted in a subtle conformational change near the proposed Fd binding site [3], which suggested the possibility of long distance communication between the nucleotide and Fd binding sites. This observation was made possible through the application of the powerful technique, HDX-MS that tracks exchange of amide hydrogens in the protein backbone with water via a base-catalyzed reaction [9]. By replacing water (H_2O) with deuterated water (D_2O), the amide hydrogens that exchange will be replaced with deuterium which can be tracked using mass spectrometry. The tertiary and quaternary structure of a protein, as well as the stability of the hydrogen bonds within the secondary structural elements, influence the rate by which H/D exchange occurs [10,11]. This allows HDX-MS to reveal substrate/ligand binding sites, points of contact between subunits in a complex, and changes in dynamics even in peptides that participate in allosteric communication within a single protein, or an entire complex [12,13].

Conformational changes caused by ligand binding are increasingly being recognized as an intrinsic feature involved in the functionality of many proteins [14]. The ability of ligands to induce conformational changes at a site remote from the site of binding has been termed allostery [15]. However, the pathways of allosteric communication in a protein complex, or even a single protein are rarely known. One method that has proven useful for mapping allosteric pathways of connectivity and can provide mechanistic insights on protein regulation is Statistical Coupling Analysis (SCA). SCA is a method that identifies co-varying (co-evolving) suites of amino acid residues that exhibit evidence for energetic connectivity, which in turn has been suggested to be evidence for possible allosteric communication within the protein [15,16,17]. SCA quantifies how changes in the distribution of amino acids at one position influence changes in the amino acid distribution at another position. Energetic connectivity is then computed using a curated sequence alignment of homologs, within the context of a combined statistical and protein structural framework.

To investigate the potential role of allosteric communication in FBEB by *Pf* Nfn, we used SCA to identify potential pathways of communication within the enzyme complex and HDX-MS to study changes in the stability and dynamics of the protein complex when different substrates are present. Analyses were conducted on enzymes in the presence and absence of nucleotides and Fd_{Ox}. Our HDX-MS results reveal that ligand binding sites display protection from exchange when substrates are bound to a distant site, suggesting allosteric communication. SCA analyses identified 137 residues in Nfn that form an allosteric communication pathway, providing strong evidence supporting the role of ligand induced allosteric communication during FBEB. Additionally, changes in H/D suggests a role for protein dynamics and communication pathways in tuning electron transfer by influencing the protein microenvironment around the cofactors.

Materials and Methods

Protein Purification The *Pf* Nfn complex (Nfn-SL) and Fd were purified from *P. furiosus*, as previously described [4].

Native Mass Spectrometry Non-covalent mass spectrometry experiments were conducted on a SYNAPT G2-*Si* instrument (Waters) in a similar fashion as described previously [18]. Briefly, the Nfn complex sample was buffer exchanged to 200 mM ammonium acetate and pH 7 (Sigma) using 3 kDa molecular weight cutoff spin filters (Pall Corporation). Nfn was then infused from in-house prepared gold-coated borosilicate glass capillaries to the electrospray source at a protein concentration of 5 μM and a rate of roughly 90 nL/min. The instrument was tuned to enhance performance in the high mass-to-charge range. Settings were as follows: Source temperature 30°C, capillary voltage of 1.7 kV, trap bias voltage of 16 V, and argon flow in the collision cell (trap) of 7 mL/min. Transfer collision energy was held at 10 V while trap energy varied between 10–200 V. Data analysis was performed in the MassLynx software version 4.1 (Waters).

HDX-MS Analysis Nfn was subjected to HDX-MS analysis under eight conditions: 1) as-purified, 2) NADH bound, 3) NAD^+ bound, 4) $NADP^+$ bound, 5) NADPH bound, 6) NADH+$NADP^+$ bound, 7) NADPH+NAD^+ bound, and 8) Fd_{Ox} bound. Pyridine nucleotides were incubated with *Pf* Nfn at a final concentration of 1 mM. Nfn:Fd_{Ox} complex was formed by first making a 1:1 molar ratio of Nfn to Fd_{Ox} using 10 µL of Nfn (16.58 mg/mL) followed by incubation under anoxic conditions for 1 hr. at room temperature (~21°C) before initiating the reaction. The exchange reaction was initiated by a 10-fold dilution of Nfn with reaction buffer at 60°C. This temperature was chosen due to temperature limitations of the equipment available. Reaction buffer contained 100 mM Tris-HCl and 150 mM NaCl in D_2O (pD 7.0) with 1 mM of pyridine nucleotides (NAD$^+$, NADH, NADP$^+$, NADPH, NADPH+NADP$^+$, or NADH+NADP$^+$). Samples were removed and quenched to stop exchange after 1 min., 3 min., 15 min., 60 min., 3 hrs, and 24 hrs. At each time point, a 10 µL subsample was withdrawn from each reaction vial and placed into quenching/digestion solution containing 1% formic acid (FA, Sigma) and porcine pepsin (Sigma, 0.2 mg/mL final concentration) on ice. After a two min. incubation, the reaction mixture was frozen in liquid N_2 and stored at -80°C until it was subjected to liquid chromatography-mass spectrometry (LC-MS) analysis.

LC-MS analysis of Nfn peptide fragments was completed on a 1290 UPLC series chromatography stack (Agilent Technologies) coupled directly to a 6538 UHD Accurate-Mass Q-TOF LC/MS mass spectrometer (Agilent Technologies). Before electrospray-time of flight (ESI-TOF) analysis, peptides were separated on a reverse phase (RP) column (Phenomenex Onyx Monolithic C18 column, 100 x 2 mm) at 1°C using a flow rate of 500 µL/min. under the following conditions: 0.0-1.0 min., 5% B; 1.0-9.0 min., 5-45% B; 9.1-9.8 min., 95% B; 9.8-9.9 min., 5% B. Solvent A contained 0.1% FA in water (ThermoFisher) while solvent B contained 0.1% FA in acetonitrile (ACN, ThermoFisher). Data was acquired at 2 Hz over a scan range 50-1700 m/z in positive mode. Electrospray settings were: nebulizer at 3.7 bar, drying gas at 8.0 L/min., drying temperature at 350°C, and capillary voltage at 3.5 kV. Data dependent MS/MS, specifying a selection window of 4 m/z, was used to generate peptide sequence tags. Data processing was carried out in Agilent MassHunter Qualitative Analysis version 6.0. Peptide identification was performed using the peptide analysis worksheet (PAWs, ProteoMetrics LLC.). Deuterium uptake was determined by monitoring shifts of the centroid peptide isotopic distribution by using the program HDExaminer (Sierra Analytics Inc.). Measured values were then used to generate uptake curves to compare relative deuterium exchange in all conditions tested.

HDX-MS Clustering The percent deuterium (%D) incorporated at a given time point was calculated by dividing the number of deuterium atoms incorporated (#D) by the number of deuterium atoms incorporated after 24 hours. The percent difference between the deuterium uptake in the as-purified condition and the percent deuterium incorporated during experimental manipulation was calculated as published by Chalmers et al. [20]. Briefly, the %D of the as-purified condition (no substrate bound) was then subtracted from the %D of the nucleotide bound and Fd_{Ox} bound conditions. The difference was then plotted for peptides with sufficient deuterium incorporation at the early (60 sec.), middle (900 sec.), and late (10800 sec.) time points. A hierarchical clustering script in R (R version 3.0.0) was used to determine the number of trends present within the deuterium uptake profiles based on the slope of the treadline. For instance, linear treadlines with a positive slope were clustered together, whereas profiles with a polynomial treadline were clustered depending on if the treadline continually increased, continually decreased, if the parabola formed is positive or negative, or if there is no change throughout the time course (**Supp. Figs. 3.1-7**). The clustered profiles were then implemented in a network analysis (described below).

Generation of Nfn and Related Paralog Database A database of Nfn-S and Nfn-L homologs, compiled as part of our previous study [5], was used here. Briefly, the database was constructed by subjecting Nfn-S and Nfn-L from *Pf* (AAD36706 and AAD36707, respectively) to separate BLASTp queries against the National Center for Biotechnology Information (NCBI) complete genome database (n = 4586 genomes as of March 2016) specifying thresholds of >30% amino acid identity and >60% coverage. Only Nfn-S and Nfn-L sequences that were co-localized in the genome were retained for further analysis. Compiled Nfn-S and Nfn-L homologs were aligned with Clustal omega specifying default settings and were then manually screened to filter out non-Nfn sequences using residues previously suggested to be essential to protein function, as outlined in Demmer et al., 2016 [6, 20]. These steps resulted in a curated database of 467 Nfn-SL homologous sequences.

Statistical Coupling Analysis Aligned homologous sequences of both Nfn-S and Nfn-L (n=467) were concatenated using a custom python script (python version 2.7). The concatenated sequences were then curated to include only positions that contained a maximum gap frequency of 20%, resulting in a total of 750 positions (out of 1955 positions including gaps). The curated Nfn-SL sequences along with the *Pf* Nfn structure (PDB: 5JFC) were subjected to SCA analysis in matlab (matlab version 9.1) as previously described in Halabi *et al.* 2009 [17]. Chimera (version 3.2.0) was used to map and visualize the spatial location of positions that exhibited evidence for co-variance (co-evolution) in the *Pf* Nfn structure [21].

Network Analysis The matrix obtained by clustering the HDX-MS data was subjected to Pearson correlation using the correlation package in Cytoscape (version

3.2.0) [22]. The network was visualized with the force directed organic layout [23]. Each unique peptide was denoted as a node and the edges between nodes represent the degree of correlation between a given set of peptides (nodes). The network was further analyzed using the Network Analyzer plugin in Cytoscape to map the correlation information onto the network [24]. Network nodes were colored based on results from SCA analysis.

Results

Evidence of Long Distance Communication in *Pf* Nfn To investigate the role of structural dynamics in the mechanism of FBEB in Nfn, we applied HDX-MS to *Pf* Nfn poised at different steps in the catalytic cycle. Individual steps were simulated by adding pyridine nucleotides and Fd_{Ox} to oxidized Nfn in seven different combinations. Deuterium uptake over time was then compared in the as-purified Nfn enzyme with that observed when provided with pyridine nucleotides or Fd_{Ox}. Before beginning experiments, the as-purified Nfn complex from *Pf* was analyzed by native MS to confirm its composition. Native MS showed that *Pf* Nfn contains two FAD molecules, two [4Fe-4S] clusters, and one [2Fe-2S] cluster (**Fig. 3.2**). Based on native MS data collected at low collision energy, cofactor occupancy is estimated to be 100%. This analysis also provided assurance that pyridine nucleotides and Fd_{Ox} did not co-purify with the Nfn enzyme. A pepsin digestion of Nfn produced more than 200 peptides that could each be uniquely mapped to the amino acid sequence of *Pf* Nfn. From these 200 peptides, 97 and 125 were used as input to generate deuterium uptake curves for Nfn-S and Nfn-L, respectively. Sequence coverage was 100% for Nfn-S and 94% for Nfn-L for the peptides chosen (**Supp. Fig. 3.8**). These peptides were used to map specific regions of deuterium incorporation during HDX-MS.

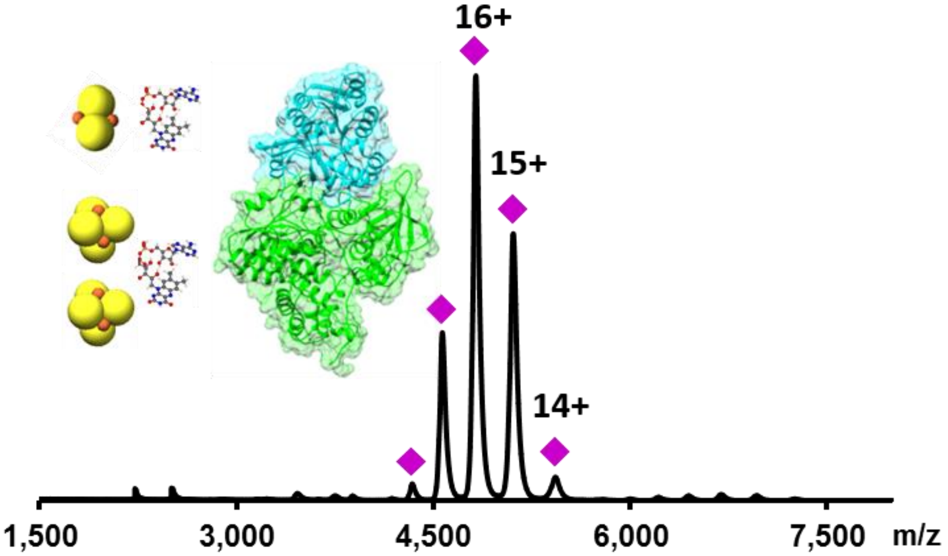

Figure 3.2. *Native Mass Spectra of the Nfn Complex*. Intact complex (magenta diamonds represent charge envelope centered on 16+ charge) contains two subunits (Nfn-S, blue and Nfn-L, green), two FAD, two [4Fe-4S] clusters and one [2Fe-2S] cluster. Mass of the complex based on deconvoluted signal is 86,407Da (calculated MW = 86,425Da).

Of the identified peptides, a subset from each subunit displayed significantly different levels of deuterium incorporation dependent on nucleotide binding. We reasoned that peptides displaying changes in dynamic behavior upon substrate binding are important in the mechanism underpinning FBEB and catalytic activity. Also, since the deuterium uptake in a number of peptides did not change under any of the conditions tested, we are confident that the observed changes are not an artifact of ligand binding [25]. Heat maps of the selected peptides show a global view of exchange in Nfn-S (**Supp.**

Fig. 9) and Nfn-L (**Supp. Fig. 3.10**) as a function of incubation time. The heat maps show that the as-purified state of Nfn had the most deuterium incorporation while the NADPH+NAD$^+$ bound form had the lowest deuterium incorporation. Uptake curves for each of the peptides provide a local view of the deuterium incorporation in each condition during the course of the reaction (**Supp. Fig. 3.11 and 3.12**).

To investigate the possible role of protein dynamics in the mechanism of FBEB, we focused additional analyses on peptides in close proximity to the cofactors and nucleotide binding sites. Six key peptides (two in Nfn-S and four in Nfn-L) were selected for a detailed analysis. All peptide residue numbers are relative to Nfn from *Pf*. The two peptides from Nfn-S (residues 131-139 and 210-226) are involved in NAD$^+$/NADH binding and S-FAD/[2Fe-2S] cluster coordination, respectively [4,6]. The other four peptides are located in Nfn-L; residues 43-64 ([4Fe-4S] cluster binding/near putative Fd docking site), 70-85 (control region), 245-262 (L-FAD binding domain), and 370-392 (stabilizing loop upon NADP$^+$/NADPH binding).

To visualize changes in the exchange profile of Nfn upon nucleotide and Fd binding, we created a histogram plot comparing HDX data for the 3 hr. time point. Nfn-S residues 131-139, involved in the NAD$^+$/NADH binding, showed a 30% decrease in deuterium incorporation when NADH or NAD$^+$ are bound, when compared to the as-purified condition (**Fig. 3.3A**). When the nucleotides NADP$^+$ or NADPH bind to Nfn-L, a decrease in deuterium incorporation of 10 and 20%, respectively, occurs at residues 131-139 of Nfn-S. This suggests that the binding of NADP$^+$ or NADPH to Nfn-L induces a change in the structure or stability of Nfn-S. When Fd is bound to Nfn-L, residues 131-

139 of Nfn-S incorporate 10% less deuterium than the as-purified condition. This indicates a change in the secondary structure stability in this region. The remaining conditions tested, NADH+NADP$^+$ and NADPH+NAD$^+$, both exchange less deuterium than the as-purified condition, with the NADH+NADP$^+$ condition exhibiting less exchange than the NADPH+NAD$^+$ condition. Residues 210-226 in Nfn-S exhibited a 20% and <10% decrease in deuterium incorporation when NADH+NADP$^+$ are both bound or when the nucleotides are individually bound to Nfn, respectively (**Fig. 3.3B**). Similarly, when NADPH+NAD$^+$ are both bound, there is a 30% decrease in exchange at residues 210-226 in Nfn-S, indicating that this condition has the greatest effect on the structure or stability of this peptide.

Of the four peptides that were closely examined in Nfn-L, residues 70-85 exhibited small changes in deuterium incorporation in all conditions (**Fig. 3.3E**) and thus can be considered as one of the control regions for the HDX experiments. Other control regions include residues 128-141 of Nfn-S, and residues 302-323 of Nfn-L (**Supp. Fig. 3.11E and Supp. Fig. 3.12M**). The remaining three peptides in Nfn-L (43-64, 245-262, and 370-392) displayed evidence of synergistic exchange dynamics during nucleotide binding (**Fig. 3.3C, D, and F**). Nfn-L residues 245-262, which are in close proximity to the L-FAD, exhibit high amounts of exchange in the as-purified, NADH bound, NADP$^+$ bound, NAD$^+$ bound, and NADPH bound conditions. The NADH and NADP$^+$ conditions exchanged 15% and 10% less deuterium relative to the as-purified condition, respectively, whereas NAD$^+$ and NADPH bound exchanged 20% and 25% less deuterium, respectively (**Fig. 3.3C**). The least amount of exchange was observed in this peptide when Fd_{Ox}, NADH+NADP$^+$, or NADPH+NAD$^+$, are bound. Relative to as-purified Nfn, a 45%, 30%, and 35% decrease in deuterium exchange was observed in the NADPH+NAD$^+$, NADH+NADP$^+$, and Fd bound states, respectively (**Fig. 3.3C**).

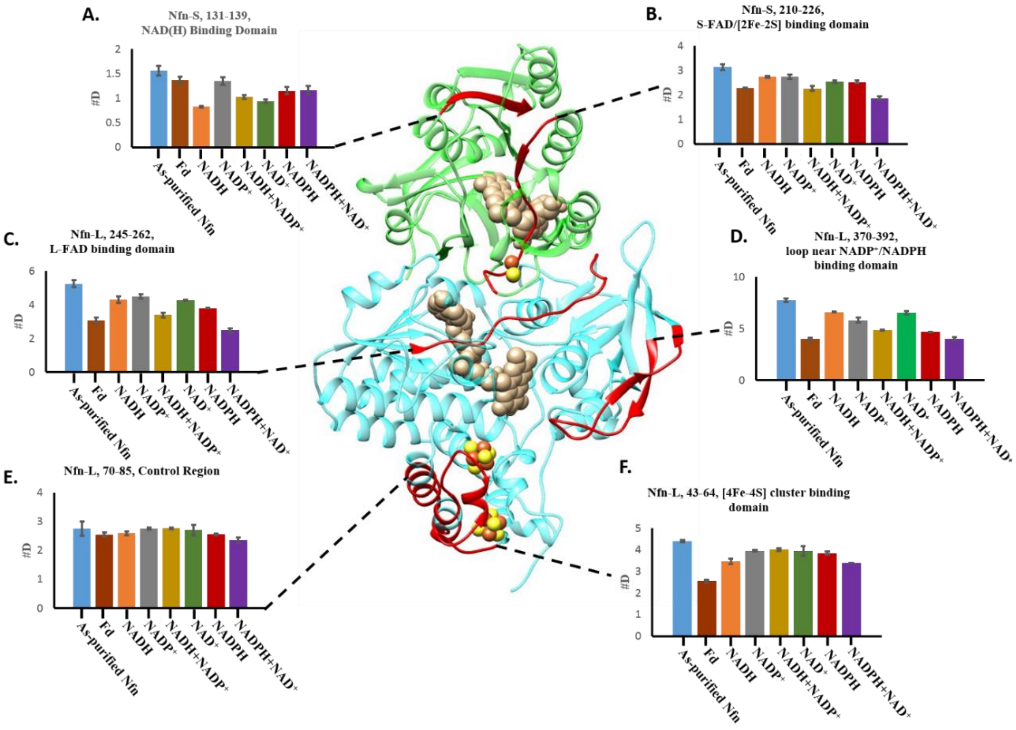

Figure 3.3. *Histograms of Deuterium Incorporation After Three Hours in Key Regions of Nfn*. Ribbon diagram depicts peptides of interest (**A-F**), as mapped in red, in the Nfn structure from *P. furiosus* (PDB ID: 5JCA). Each histogram plot shows exchange for the indicated peptide after 3 hrs of incubation in deuterated buffer. Each bar represents a different condition: Blue (as-purified Nfn), brown (Fd bound), orange (NADH bound), grey (NADP bound), gold (NADH+NADP bound), green (NAD bound), red (NADPH bound), and purple (NAD+NADPH bound). The peptides indicated are key regions that are thought to be involved in the electron bifurcation reaction. (**A**). Nfn-S (green ribbon structure) residues 131-139 involved in NAD(H) binding. (**B**). Residues 210-226 involved in coordinating the S-FAD and the [2Fe-2S] of Nfn-S are shown. (**C**). Nfn-L (blue ribbon structure) residues 245-262 are near the L-FAD. (**D**). Residues 370-392 are involved in NADP(H) binding. (**E**). Residues 70-85 act as a HDX-MS control region. (**F**). Residues 43-64 are involved in coordinating the two [4Fe-4S] clusters of Nfn-L. Error bars indicate the standard deviation of three replicates.

Residues 370-392 of Nfn-L are involved in a loop that becomes less flexible, and therefore less accessible to exchange, upon $NADP^+$/NADPH binding because of the interactions formed between the loop and the $NADP^+$/NADPH binding pocket [4]. Importantly, Fd_{Ox} and NADPH+NAD^+ binding results in a decrease of 40% in the amount of deuterium incorporated in this peptide. This indicates that residues 370-392 are the least accessible to exchange under these two conditions. Additionally when $NADP^+$, NADPH, and NADH+$NADP^+$ are bound to Nfn, a decrease in deuterium incorporation (20%, 30%, and 30%, respectively) is observed at residues 370-392, albeit not as much of a decrease when compared to Fd_{Ox}, or NADPH+NAD^+ bound conditions (40% decrease in both conditions). The remaining two conditions, with NADH or NAD^+ bound, display a 15% decrease in exchange at residues 370-392 relative to the as-purified condition. This is the opposite of the results in Nfn-S where a decrease of 10% and 20% is observed in residues 131-139 when $NADP^+$ or NADPH are bound to Nfn-L.

The fourth peptide of interest in Nfn-L (residues 43-64) is responsible for coordinating both [4Fe-4S] clusters, and is believed to be near the site of Fd binding to the large subunit [4]. Fd is expected to bind near the distal FeS cluster on the large subunit, close to 43-64 region [3,4]. It was observed that Fd_{Ox} binding to Nfn caused increased protection from exchange in residues 43-64 of Nfn-L. This observation is consistent with previous studies of protein-protein and protein-ligand interactions, in which a large decrease in exchange indicates a site of possible interaction between the two subjects of interest [26, 27].

SCA Analysis of Nfn Data generated from HDX-MS revealed evidence of long distance communication within the complex. To elucidate specific details about potential pathways of communication across Nfn, we utilized SCA. SCA can reveal energetically linked, or co-evolving, amino acid residues. A structure-based sequence alignment was constructed of 467 Nfn-like proteins. From this, a total of 137 co-evolving positions were identified of which 52 positions were in Nfn-S and 85 were in Nfn-L (**Supp. Table 3.1**). Of the 52 co-evolving residues identified in Nfn-S, 18 residues were within 10 Å of the S-FAD and another two were within 10 Å to the [2Fe-2S] cluster in Nfn-S. Of these 20 residues, six that were in close proximity to S-FAD were highly conserved (i.e., >80%) and one residue near the [2Fe-2S] cluster was also highly conserved (**Supp. Table 3.1**). In Nfn-L, 16 of the 85 residues were within 10 Å of the L-FAD, two residues were located within 10 Å of the proximal [4Fe-4S] cluster, and six residues were within 10 Å of the distal [4Fe-4S] cluster. Of the 16 residues that were near the L-FAD, two were highly conserved (**Supp. Table 3.31**).

Residues that were 100% conserved (a total of 50 residues) were not included in the SCA due to the lack of variation among homologous proteins used in the multiple sequence alignment. Twelve of the 100% conserved residues were identified in Nfn-S and 38 were identified in Nfn-L (**Supp. Table 3.2**). Of the 12 identified in Nfn-S, five are within 10 Å of the [2Fe-2S] cluster and six are within 10 Å of the S-FAD. In Nfn-L, five 100% conserved residues were located near the proximal [4Fe-4S] cluster, five were located near the distal [4Fe-4S] cluster, and 21 were located near the L-FAD.

To visualize and identify a putative communication pathway in Nfn, the combination of residues that were 100% conserved in our sequence dataset and those that exhibited evidence for co-evolution from SCA were mapped onto the *Pf* Nfn structure. A total of 14 residues were identified that were within 6 Å from one another or from the cofactors involved in electron transfer (**Fig. 3.4**); all of the residues identified were >70% conserved. Of the 14 residues, six were identified in Nfn-S, connecting the NAD(H) binding site to the L-FAD. Three of the six residues in Nfn-S are present in peptides identified via HDX-MS analysis: Glycine at position 138 within the 131-139 region peptide that interacts with NAD^+/NADH, G112 in peptide 95-113 that interacts with the S-FAD, and G226 that interacts with the [2Fe-2S] cluster. Likewise, eight of the 14 residues were identified in NfnL that connect the L-FAD to the $NADP^+$/NADPH and Fd binding sites. Two of these residues were detected by HDX-MS as being involved in deuterium exchange: Proline at position 252 (P252) in peptide 242-262 that interacts with L-FAD and cysteine at position 45 (C45) in peptide 43-64 that interacts with the distal [4Fe-4S] cluster and Fd.

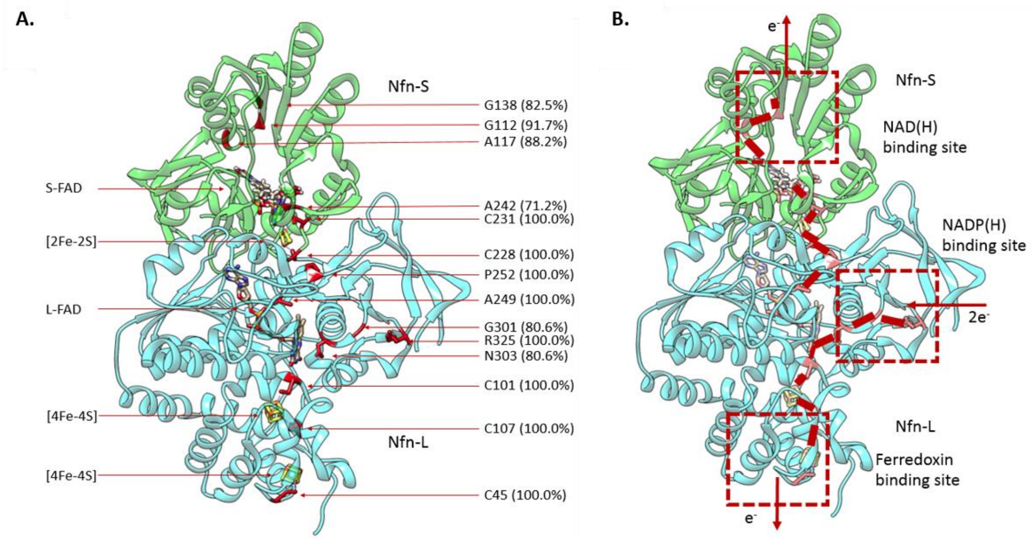

Figure 3.4. *Co-evolving residues putatively involved in allosteric communication.* (**A**). Structure of Nfn (PDB ID: 5JCA) with residues represented by red sticks that are potentially involved in allosteric communication. All the identified residues along the putative pathway were within 6Å of each other. Here, the small subunit of Nfn (i.e Nfn-S) is represented in green and the large subunit of Nfn (i.e. Nfn-L) is represented in cyan The residues identified in the allosteric communication pathway. Here, the first letter abbreviation is used to denote each residue while the number indicates the position in the structure of *P. furiosus* Nfn (PDB ID: 5JCA). The number in parentheses represents the percent conservation of this residue in our Nfn sequence database comprising 396 Nfn-like homologous sequences. (**B**). Potential pathway of electron transfer between the nucleotide binding and Fd binding sites.

Network Analysis of HDX-MS and SCA Data Protein function is an emergent property arising from the integration of functional units. We reasoned that the biophysical properties and evolutionary fingerprint could be combined to elucidate underlying modules that give rise to protein functionality. Peptides were clustered based on the percent difference in deuterium uptake between the as-purified and different pyridine nucleotide/Fd_{Ox} bound conditions. Thirty six of the mapped peptides from Nfn were used. These peptides all had significant deuterium incorporation (#D >1) and were proximal to key regions of the protein. We also selected several peptides in which little to no difference in exchange was observed between the tested conditions. The resulting matrix was analyzed by Pearson correlation and converted to a network map for visualization. This network was then overlayed with the SCA data which identified evidence for co-evolving residues within the designated peptides. Two networks were generated by separating the bifurcating and confurcating reactions in order to reveal pathways of connectivity (**Fig. 3.5A and Supp. Fig. 3.13A**). The bifurcating and confurcating reactions were separated based on the pyridine nucleotides needed to perform the reaction in a specified direction (see Equation 1). For instance, the bifurcating reaction uses NAD^+, NADPH, and Fd_{Ox}, whereas the confurcating reaction uses NADH, $NADP^+$, and Fd_{Red}. The HDX conditions involving one or both of the nucleotides that are required to drive reaction directionality were grouped together to create the network plots.

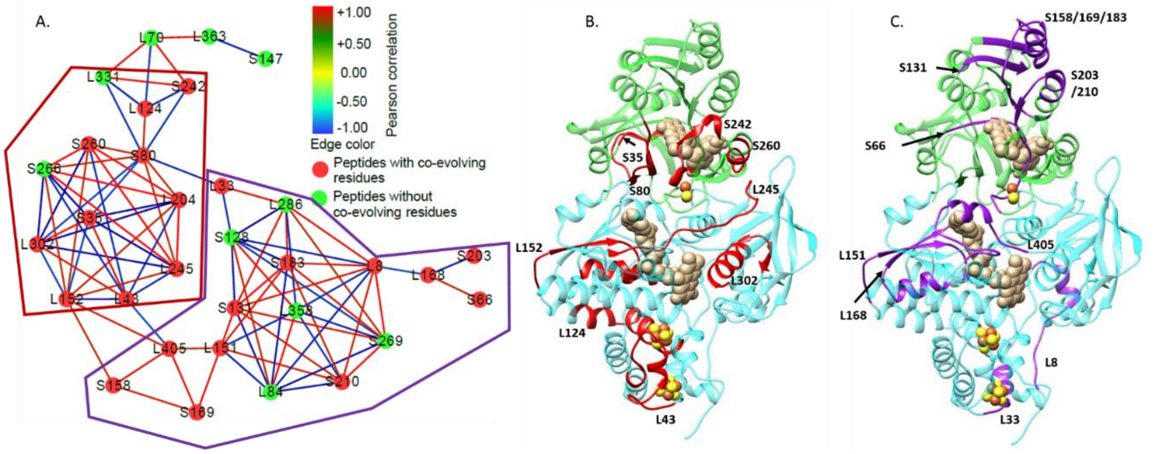

Figure 3.5. *Network analysis of HDX-MS and SCA data*. (**A**). Network plot generated from clustered HDX-MS data and co-evolving residues for the bifurcating conditions (NAD, NADPH, NADPH+NAD$^+$, and Fd).Each node represents a peptide analyzed in this study with HDX-MS. The node label indicates whether it is located on the large (Nfn-L) or small (Nfn-S) subunit and includes the residue number of the first amino acid in the sequence (residue numbering is defined by the sequence position in *P. furiosus* Nfn (PDB ID: 5JCA)). Red nodes indicate the presence of a residue that exhibits strong evidence for co-evolution, relative to other residues within the protein (see materials and methods). Edges connecting each node indicate the correlation between the deuterium uptake profiles of each peptide. A high correlation is indicated by red edges and a low correlation is indicated by blue edges. Nodes were grouped together qualitatively based on the degree of correlation between peptides and can be separated into two groups, indicated by the red and purple outlines. (**B).** The residues depicted by the red outline and which exhibit evidence for co-evolution were mapped in red on the structure of Nfn from *P. furiosus*. They are heavily centered around the cofactors of Nfn-S and Nfn-L.(**C**). The same has been done for the residues with the purple outline. These cofactors and the NAD$^+$/NADH binding site.

The bifurcation network revealed two distinct clusters of peptides based on HDX (**Fig. 3.5A**). One cluster corresponds to peptides that exhibit high levels of HDX exchange under conditions (NADPH, NAD$^+$, NADPH+NAD$^+$, and Fd_{Ox} bound) that promote bifurcation, while a second corresponds to peptides that exhibit high levels of correlation under conditions (NADP$^+$, NADH, NADH+NADP$^+$, and Fd_{Ox} bound) that promote confurcation (**Supp. Fig. 3.13**). In each of these conditions, peptides (i.e., network nodes) that contained at least one residue that exhibited evidence for co-evolution with other residues within the protein were highlighted in red whereas network nodes that did not exhibit evidence for co-evolution were highlighted in green. The peptides involved in the bifurcation direction were separated into the red or purple clusters and were then mapped onto the *Pf* Nfn structure (**Figs. 3.5B and 3.5C, respectively**). Mapping of the peptides that comprise the red cluster on the *Pf* Nfn structure reveals that they are heavily centered around the cofactors of Nfn-S and Nfn-L. In contrast, mapping of the peptides that comprise the purple cluster on the *Pf* Nfn structure reveals peptides that are more spread across the enzyme complex, including residues near the cofactors and the NAD^+/NADH binding site.

Discussion

The use of FBEB to improve metabolic efficiency in anaerobic organisms is of great interest because of the advantage provided in energy poor environments and potential application for biotechnology [1,4]. The key step in FBEB is the transfer of electrons from a molecule of medium reduction potential to one of lower potential (thermodynamically unfavorable) by coupling this with a transfer to a high potential acceptor (thermodynamically favorable). Our interest is in understanding the mechanism behind the splitting of electron pairs and how enzymes ensure that both electrons do not travel down the energetically favorable pathway. Current hypotheses include a “gating-step” in which a change in the reduction potential or distance between cofactors is involved. Two recent studies that used HDX to investigate Nfn homologs identified evidence in support of a role for conformational change during FBEB [4,6]. Here we have significantly deepened understanding of this mechanism using native mass spectrometry, HDX, in combination with SCA of *Pf* Nfn at each step of the catalytic cycle.

The first step in our analysis was to establish the subunit and cofactor stoichiometry of purified Nfn. Using native MS, it was determined that Nfn purified from *Pf* contained the predicted cofactors (2 [4Fe-4S] clusters, 1 [2Fe-2S], and 2 FADs) for the holo-enzyme complex (**Fig. 3.2**). This is the first native MS of an oxygen sensitive multisubunit protein complex. This opens the door for investigating other systems under strictly anaerobic conditions using this powerful technique.

Many proteins utilize long distance communication between binding sites and subunits to ensure efficient function [e.g., 14,15]. HDX-MS of *Pf* Nfn in the presence of different substrates and products revealed behavior consistent with allosteric regulation (**Fig. 3.3A-F**). The goal of this experiment was to track the conformational dynamics of Nfn as it progresses through the catalytic cycle to elucidate the functional role of protein motion. We hypothesized that these effects are involved in tuning the affinity of Nfn for substrate, or gating the electrons by effecting the protein microenvironment.

The transfer of electrons within proteins is highly sensitive to distance, with very few examples in which there is more than 14 Å between sites [28]. Most of the cofactors within Nfn are within efficient electron transfer distance of one another (<14 Å), with the exception of the L-FAD and the [2Fe-2S] cluster of Nfn-S, which are separated by a distance of 14.1 Å, as revealed by the crystal structure of *Pf* Nfn [4]. It was previously hypothesized that Nfn undergoes a structural rearrangement that brings the L-FAD and the [2Fe-2S] cluster of Nfn-S together during catalysis [6, 29]. HDX-MS of *Pf* Nfn shows that residues 210-226 of Nfn-S are the most protected from deuterium exchange when NAD^+ and NADPH are simultaneously bound to the complex (**Fig. 3.3B**). This increase in protection is consistent with a structural rearrangement that brings the two cofactors closer together, improving the efficiency of electron transfer while decreasing the accessibility of several amide hydrogens to exchange. A similar effect is seen at residues 245-262 of Nfn-L, which are near the L-FAD binding site (**Fig. 3.3C**). This additional protection from deuterium exchange when NAD^+ and NADPH are present may act as a way of orienting the L-FAD in an orientation that is closer to the [2Fe-2S] cluster of Nfn-S. Demmer et al. performed HDX-MS experiments on Nfn purified from *Tm* and hypothesized that a rigid body movement in the small subunit brings the FAD of the large subunit and [2Fe-2S] cluster of the small subunit closer together in *Tm*Nfn [6]. These two cofactors are 15 Å apart in the crystal structure, however, upon binding of NADPH, the distance becomes ~13 Å [6]. Our analysis suggests that rather than a rigid body movement, a more sophisticated means of communication likely occurs within Nfn during catalysis.

To further test our hypothesis and to supplement our understanding of how long distance communication is accomplished in Nfn, SCA was used to identify co-evolving amino acids for use in predicting a pathway of communication (**Fig. 3.4**). We identified the presence of a pathway of amino acids that connects cofactors and ligand binding sites within and between subunits, providing a potential physical conduit for information transfer through Nfn. To test whether the pathway of co-evolving residues facilitate allostery, we combined our HDX data on protein dynamics with our SCA data on co-selection (co-evolution) of residues).

The percent change in deuterium uptake for each condition was used to cluster peptides based on HDX profiles generated using early, middle, and late time points. (**Supp. Figs. 3.1-7**). By grouping peptides with similar HDX profiles under bifurcating and confurcating reaction conditions, networks were generated. This network was then overlaid with the identity of the co-evolving residues and the extent that they are undergoing co-evolution. In the bifurcating conditions, peptides with co-evolving residues formed a sub-network together and are all highly correlated (**Fig. 3.5A**). When mapped onto the structure of Nfn, many of these peptides are localized near the cofactors of both Nfn-S and Nfn-L (**Fig. 3.5B**). The high correlation of the deuterium uptake profiles and the presence of co-evolving residues pinpoints a scaffold for communication around the cofactors involving these peptides. These subtle structural rearrangements in Nfn involve conformational switching at the Nfn-S and Nfn-L interface controlling the flow of electrons. A second network of peptides with correlated deuterium uptake and co-evolving residues is more distributed across Nfn (**Fig. 3.5C**). These peptides are located near the NAD^+/NADH, [2Fe-2S] cluster, and S-FAD binding site of Nfn-S, the L-FAD binding site, as well as the interface between Nfn-L and Nfn-S. This pathway suggests the presence of a signaling network throughout the complex. This network could function by acting as a sensor for pyridine nucleotides.

In this study we have made progress toward revealing the finer mechanistic details of FBEB by using HDX-MS and SCA techniques to reveal multiple pathways of communication within Nfn purified from *P. furiosus*. Our analysis of *Pf* Nfn suggests that Nfn is a precisely tuned catalyst that undergoes coordinated motions using networks of amino acids. We hypothesize that the connectivity illustrated by these networks allows Nfn to integrate input from multiple substrate and product concentrations making it an important factor in the gating of electrons. It was previously hypothesized that electron gating in Nfn occurred through a rigid body movement, [6]. Our in-depth analysis on the conformational dynamics of Nfn revealed physical networks that could utilize allosteric communication to trigger the conformational gating of electrons. Additionally the HDX-MS data collected on Nfn here suggests that a network of peptides displaying similar exchange behavior that also contain co-evolving residues are responsible for coordinating sophisticated movements within the complex upon nucleotide substrate and Fd binding. This suggests that the physical connectivity of the peptides plays a role in allostery, and helps the complex prepare to send electrons in either a bifurcating or confurcating direction, the connectivity of peptides also influences the gating of electrons, ensuring that an electron transfers down the high and low potential pathway. Additionally, it could also play a role in the transfer of protons, which occurs simultaneously with electron transfer during bifurcation [4]. With the identity of key amino acids involved in communication within Nfn, we can now focus our efforts on determining the specific role of each amino acid residue in the FBEB mechanism.

References Cited

1. W. Buckel, R.K. Thauer, Energy conservation via electron bifurcating ferredoxin reduction and proton/Na^+ translocating ferredoxin oxidation, BBA Bioenergetics 1827 (2013) 94-113.

2. G. Herrmann, E. Jayamani, G. Mai, W. Buckel, Energy conservation via electron-transferring flavoprotein in anaerobic bacteria, J. Bateriol. 190 (2008) 784-791.

3. J.K. Demmer, H. Huang, S. Wang, U. Demmer, R.K. Thauer, U. Ermler, Insights into Flavin-based FBEB via the NADH-dependent Reduced Ferredoxin:NADP Oxidoreductase Structure, The Journal of Biol. Chem. 290 (2015) 21985-21995.

4. C.E. Lubner, D.P. Jennings, D.W. Mulder, G.J. Schut, O.A. Zadvornyy, J.P. Hoben, M. Tokmina-Lukaszewska, L. Berry, D.M. Nguyen, G.L. Lipscomb, B. Bothner, A.K. Jones, A. Miller, P.W. King, M.W.W. Adams, J.W. Peters, Mechanistic insights into enegy conservation by flavin-based FBEB, Nat. Chem. Biol. (2017) DOI:10.1038/nchembio.2348

5. D.M.N. Nguyen, G.J. Schut, O.A. Zadvornyy, M. Tokmina-Lukaszewska, S. Poudel, G.L. Lipscomb, L.A. Adams, J.T. Dinsmore, W.J. Nixon, E. Boyd, B. Bothner, J.W. Peters, M.W.W. Adams, Two functionally distinct bifurcating NADP-dependent ferredoxin oxidoreductases maintain the primary redox balance of *Pyrococcus furiosus*, J. Biol. Chem. (2017).

6. J.K. Demmer, F.A. Rupprecht, M.L. Eisinger, U. Ermler, J.D. Langer, Ligand binding and conformational dynamics in a flavin-based electron-bifurcating enzyme complex revealed by Hydrogen-Deuterium Exchange Mass Spectrometry, FEBS Letters 590 (2016) 4472-4479.

7. J.K. Hurley, R. Morales, M. Martinez-Julvez, T.B. Brodie, M. Medina, C. Gomex-Morena, G. Tollin, Structure-Function relationships in *Anabaena* ferredoxin/ferredoxin:NADP$^+$ reductase electron transfer: insights from site-directed mutagenesis, transient absorption spectroscopy and X-ray Crystallography, BBA 1554 (2002) 5-21.

8. N.P. Chowdhury, A.M. Mowafy, J.K. Demmer, V. Upadhyay, S. Koelzer, E. Jayamani, J. Kahnt, M. Hornung, U. Demmer, U. Ermler, W. Buckel, Studies on the Mechanism of FBEB Catalyzed by Electron Transferring Flavoprotein (Etf) and Butyryl-CoA Dehydrogenase (Bcd) of *Acidaminococcus fermentans*, The Journal of Biol. Chem. 289 (2014) 5145-5157.

9. V. Katta, B.T. Chait, Conformation Changes in Proteins Probed by Hydrogen-exchange Electrospray-ionization Mass Spectrometry, Rapid Communications in Mass Spectrometry 5 (1991) 214-217.

10. L. Konermann, J. Pan, Y. Liu, Hydrogen exchange mass spectrometry for studying protein structure and dynamics, Chem. Soc. Rev. 40 (2011) 1224-1234.

11. S.R. Marcsisin, J.R. Engen, Hydrogen exchange mass spectrometry: what is it and what can it tell us? Anal. Bioanal. Chem. 397 (2010) 967-972.

12. J. Rumi-Masante, F.I. Rusinga, T.E. Lester, T.B. Dunlap, T.D. Williams. A.K. Dunker, D.D. Weis, T.P. Creamer, Structural Basis for Activation of Calcineurin by Calmdoulin, J. Mol. Biol. 415 (2012) 307-317.

13. J.R. Engen, T.E. Wales, S. Chen, E.M. Marzluff, K.M. Hassell, D.D. Weis, T.E. Smithgall, Partial cooperative unfolding in proteins as observed by hydrogen exchange mass spectrometry, Int. Rev. Phys. Chem., 32 (2013) 96-127.

14. N.M. Goodey, S.J. Benkovic, Allosteric regulation and catalysis emerge via a common route, Nat. Chem. Biol. 4 (2008) 474-482.

15. J.F. Swain, L.M. Gierasch, The changing landscape of protein allostery, Cur. Op. in Struc. Biol. 16 (2006) 102-108.

16. S.W. Lockless, R. Ranganathan, Evolutionary Conserved Pathways of Energetic Connectivity in Protein Families, Science 286 (1999) 295-299.

17. N. Halabi, O. Rivoire, S.Leibler, R. Ranganathan, Protein Sectors: Evolutionary Units of Three-Dimensional Structure, Cell 138 (2009) 774-786.

18. M. Luo, R. Jackson, S. Denny, M. Tokmina-Lukaszewska, K. Maksimchuk, W. Lin, B. Bothner, B. Wiedenheft, C. Beisel, The CRISPR RNA-guided surveillance complex in Escherichia coli accommodates extended RNA spacers. Nucleic Acids Research, (2016) 44 (15): 7385-7394.

19. M.J. Chalmers, B.D. Pascal, S. Willis, J. Zhang, S.J. Iturria, J.A. Dodge, P.R. Griffin, Methods for the analysis of high precision differential hydrogen-deuterium exchange data, Int. Journal of Mass Spec. 302 (2011) 59-68.

20. F. Sievers, A. Wilm, D. Dineen, T.J. Gibson, K. Karplus, W.Z. Li, R. Lopez, H. McWilliam, M. Remmert, J. Soding, J.D. Thompson, D.G. Higgins, Fast, scalable generation of high-quality protein multiple sequence alignments using Clustal Omega, Molecular Systems Biology, 7 (2011).

21. E.F. Petterson, T.D. Goddard, C.C. Huang, G.S. Couch, D.M. Greenblatt, E.C. Meng, T.E. Ferrin, UCSF Chimera—a visualization system for exploratory research and analysis, J. Comput. Chem. 25 (2004) 1605-1612.

22. P. Shannon, A. Markiel, O. Ozier, N.S. Baliga, J.T. Wang, D. Ramage, N. Amin, B. Schwikowski, T. Ideker, Cytoscape: A Software Environment for Integreated

Models of Biomolecular Interaction Networks, Genome Research, 13 (2003) 2498-2504.

23. M.E. Smoot, K. Ono, J. Ruscheinski, P. Wang, T. Ideker, Cytoscape 2.8: new features for data integration and network visualization, Bioinformatics, 27 (2011) 431-432.

24. Y. Assenov, F. Ramirez, S. SChelhorn, T. Lengauer, M. Albrecht, Computing topological parameters of biological networks, Bioinformatics, 24 (2008) 282-284.

25. J.K. Hilmer, A. Zlotnick, B. Bothner, Conformational Equilibria and rates of localized motion within Hepatitis B Virus capsids, J. Mol. Biol 375 (2008) 581-594.

26. S.S. Jaswal, Biological insights from hydrogen exchange mass spectrometry, BBA Proteins and Proteomics, 1834 (2013) 118-1201.

27. J.R. Engen, Analysis of Protein Conformation and Dynamics by Hydrogen/Deuterium Exchange MS, Anal. Chem. 81 (2009) 7870-7875.

28. C.C. Page, C.C. Moser, P.L. Dutton, Mechanism for electron transfer within and between proteins, Curr. Op. in Chem. Biol. 7 (2003) 551-556.

29. J.W. Peters, A. Miller, A.K. Jones, P.W. King, M.W.W. Adams, FBEB, Curr. Op. in Chem. Biol. 31 (2016) 146-152.6-152.

Acknowledgments

This work is supported as part of the Biological and Electron Transfer and Catalysis (BETCy) EFRC, an Energy Frontier Research Center funded by the U.S. Department of Energy, Office of Science (DE-SC0012518). We would like to thank Montana State University Microfabrication Facility for help in preparation of gold-coated borosilica capillaries for non-covalent mass spectrometry. The Mass Spectrometry Facility at MSU is supported in part by the Murdock Charitable Trust and an NIH IDEA program grant P20GM103474.

Supplementary Material A

Supplementary Table 3.1: A total of 137 residues that exhibited evidence for co-selection (co-evolution) were identified using the structure of Nfn from *P. furiosus* (PDB ID: 5JCA) and our aligned Nfn sequence alignment database. The column termed 'Region' denotes the location of a specific residue if that residue is within 10 Å of a given cofactor in the Nfn. "N/A" designates residues that are not within 10 Å of a cofactor in Nfn. The S-FAD represents the FAD present in Nfn-S while the L-FAD represents the FAD present in Nfn-L. The [2Fe-2S] represents the iron-sulfur cluster present in Nfn-S while d[4Fe-4S] represents the distal iron-sulfur cluster from L-FAD and p[4Fe-4S] represents the proximal iron-sulfur cluster near the L-FAD in Nfn-L. The column with '%conserved' indicates the degree of conservation of the residues. The residues highlighted bold denote high conservation (i.e. >80%).

Nfn-S	**Region**	**% conserved**	**Nfn-L**	**Region**	**% conserved**
M7	N/A	75.6	T11	N/A	9.4
F23	S-FAD	22.2	P12	N/A	57.1
Q38	**S-FAD**	**83.3**	R14	N/A	15.6
M41	S-FAD	9.0	V16	N/A	11.1
I55	S-FAD	74.6	D22	N/A	12.2
D57	N/A	74.4	**F23**	**N/A**	**87.2**
S64	N/A	10.0	**Y30**	**N/A**	**85.0**
T66	S-FAD	66.9	Q44	d[4Fe-4S]	54.9
I67	S-FAD	51.5	P46	d[4Fe-4S]	19.7
Q70	S-FAD	73.5	A50	d[4Fe-4S]	4.5
T76	**S-FAD**	**82.9**	V80	N/A	10.3
D90	**N/A**	**81.8**	N91	p[4Fe-4S]	65.8
L92	N/A	7.5	T97	p[4Fe-4S]	14.5
I101	N/A	51.7	G114	d[4Fe-4S]	73.1
G105	N/A	63.7	V116	N/A	12.8
V107	N/A	67.3	I120	d[4Fe-4S]	24.6

G112	**N/A**	**91.7**	N121	d[4Fe-4S]	11.3
G113	**S-FAD**	**91.5**	A162	L-FAD	20.1
A117	**S-FAD**	**88.2**	T168	L-FAD	69.4
E118	S-FAD	10.5	C169	N/A	45.9
Y120	N/A	62.2	D172	N/A	68.2
K124	N/A	60.0	**L173**	**N/A**	**87.6**
N131	N/A	65.2	K175	N/A	72.0
I136	N/A	75.0	Y178	N/A	59.0
G138	**N/A**	**82.5**	**K204**	**N/A**	**84.2**
R140	N/A	79.3	I206	N/A	67.1
F146	N/A	15.6	**V207**	**N/A**	**87.6**
K150	N/A	8.8	N224	L-FAD	78.4
L151	N/A	23.7	T230	L-FAD	65.2
T162	**N/A**	**94.0**	E234	N/A	22.4
N163	N/A	9.4	D241	N/A	56.6
D164	**N/A**	**94.4**	**A242**	**N/A**	**87.6**
G165	**N/A**	**94.9**	I245	L-FAD	61.3
Y167	N/A	45.7	T251	N/A	17.3
G171	**N/A**	**90.8**	I254	N/A	1.5
T173	N/A	3.0	Y255	N/A	0.9
T174	**N/A**	**83.8**	W257	N/A	2.4
V193	S-FAD	20.1	V260	N/A	3.0
I197	N/A	55.3	**N261**	**N/A**	**81.6**
M198	**N/A**	**88.9**	N263	N/A	59.2
M199	**N/A**	**92.5**	**G264**	**N/A**	**86.6**
T206	N/A	76.5	I265	N/A	20.3
T213	N/A	76.1	Y266	N/A	60.9
A215	N/A	16.0	**A268**	**L-FAD**	**88.0**
S216	**S-FAD**	**92.1**	F271	N/A	76.5
N218	**S-FAD**	**90.6**	K279	N/A	70.5
A242	[2Fe-2S]	71.2	Y281	N/A	62.2
V244	**[2Fe-2S]**	**87.4**	P284	N/A	66.7
E248	S-FAD	75.6	Y286	N/A	62.4
H252	N/A	71.8	A297	N/A	62.4
M260	S-FAD	43.8	**G301**	**N/A**	**80.6**
Y266	S-FAD	78.6	T304	L-FAD	32.9
			A308	L-FAD	79.5
			A309	**N/A**	**81.8**

			V319	N/A	71.6
			L322	N/A	6.2
			E329	**L-FAD**	**89.5**
			M330	N/A	62.0
			T331	L-FAD	8.1
			L350	**N/A**	**91.2**
			V351	N/A	10.5
			T352	N/A	2.8
			N363	N/A	22.4
			L369	N/A	20.7
			M372	**N/A**	**87.8**
			K373	N/A	12.2
			P385	**N/A**	**90.6**
			E390	N/A	15.0
			T391	N/A	13.5
			F392	N/A	62.4
			A402	L-FAD	70.9
			P407	N/A	77.4
			K409	N/A	7.1
			T414	N/A	48.5
			V415	L-FAD	5.1
			G424	**N/A**	**80.1**
			D429	N/A	64.3
			L432	N/A	16.6
			T434	**N/A**	**91.0**
			I446	L-FAD	11.3
			R447	L-FAD	24.1
			E449	L-FAD	10.9
			D458	L-FAD	24.6
			I466	**N/A**	**84.8**
			Y469	N/A	70.1

Supplementary Table 3.2: A total of 50 conserved residues (conserved in 100% of identified sequences) and their location within Nfn-SL are indicated. The single letter represents the identified residue position in the structure of Nfn from *P. furiosus* (PDB: 5JFC). The column with 'Region' denotes the general location of the residue relative to co-factors in the Nfn structure. S-FAD represents the FAD present in Nfn-S while L-FAD represents the FAD present in Nfn-L. The [2Fe-2S] represents the iron-sulfur cluster present in Nfn-S while d[4Fe-4S] represents the distal iron-sulfur cluster from L-FAD and p[4Fe-4S] represents the proximal iron-sulfur cluster from L-FAD in Nfn-L. "N/A" designates residues that are not within 10 Å of a cofactor in Nfn.

Nfn-S	**Region**	**Nfn-L**	**Region**
G93	N/A	R19	N/A
P94	S-FAD	V26	N/A
G96	S-FAD	E38	d[4Fe-4S]
G194	S-FAD	R41	d[4Fe-4S]
G226	[2Fe-2S]	C45	d[4Fe-4S]
M227	[2Fe-2S]	C52	d[4Fe-4S]
C228	[2Fe-2S]	C56	p[4Fe-4S]
G229	[2Fe-2S]	G98	L-FAD
C231	[2Fe-2S]	R99	L-FAD
G246	S-FAD	V100	L-FAD
P247	S-FAD	C101	p[4Fe-4S]
R262	S-FAD	C107	p[4Fe-4S]
		C111	p[4Fe-4S]
		G123	p[4Fe-4S]
		E126	p[4Fe-4S]
		G161	L-FAD
		G163	L-FAD
		P164	L-FAD
		G190	L-FAD
		G191	L-FAD
		V192	L-FAD
		G196	L-FAD
		P198	L-FAD
		F200	L-FAD
		P203	N/A
		G228	L-FAD

		G248	L-FAD
		A249	L-FAD
		P252	L-FAD
		G259	N/A
		L272	L-FAD
		G300	N/A
		G302	L-FAD
		N303	L-FAD
		D307	L-FAD
		R310	L-FAD
		R314	N/A
		R325	N/A

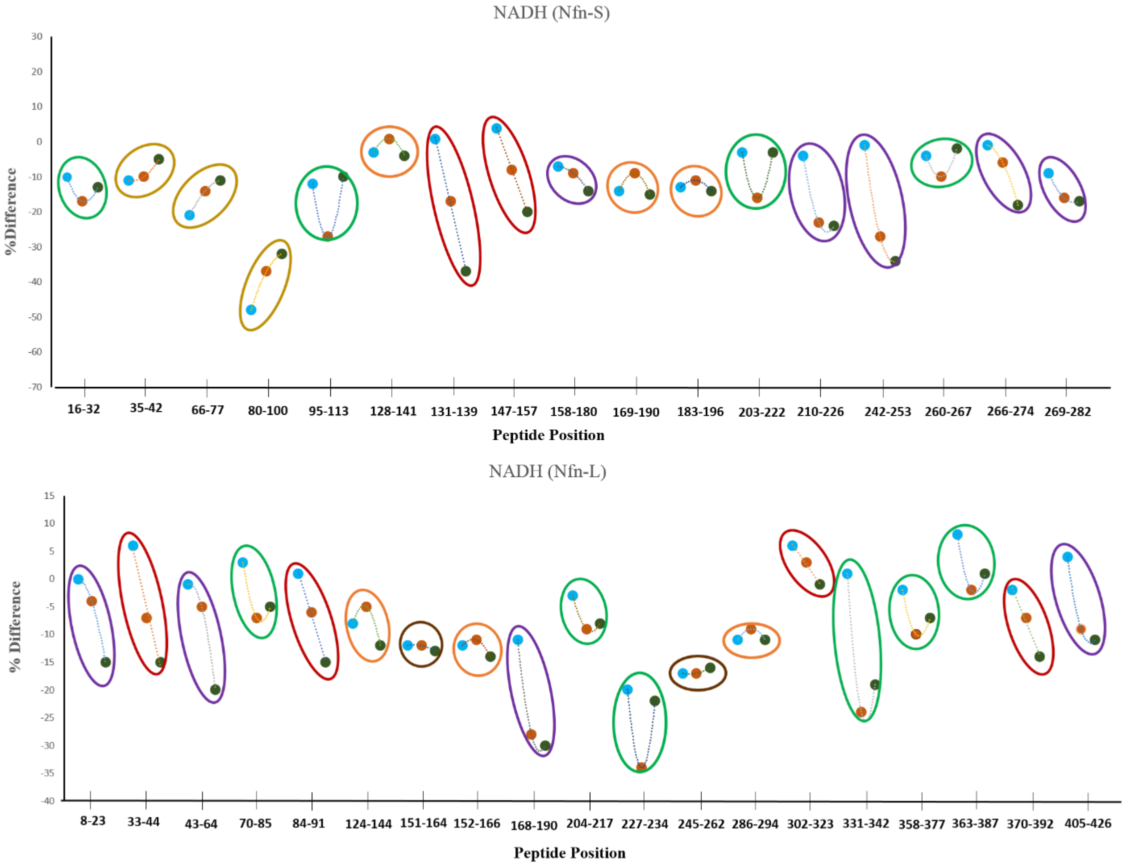

Supplementary Figure 3.1. *HDX comparison between the NADH bound form and the as purified form of Nfn.* The percent difference was calculated by subtracting the percent deuterium (%D) of the as purified Nfn condition from the %D of the NADH condition at the early (60 sec), middle (900 sec), and late (10800 sec). Each timepoint is represented by a specific color: Blue (60 sec), orange (900 sec), and green (10800 sec). The resulting percent difference was graphed for each peptide. The trend of the percent differences was examined at each peptide for use in clustering the data. A total of seven clusters were specified. Each profile is circled by a color denoting the specific cluster that a fragment belongs to. This was done in both Nfn-S (**A**) and Nfn-L (**B**) for all conditions.

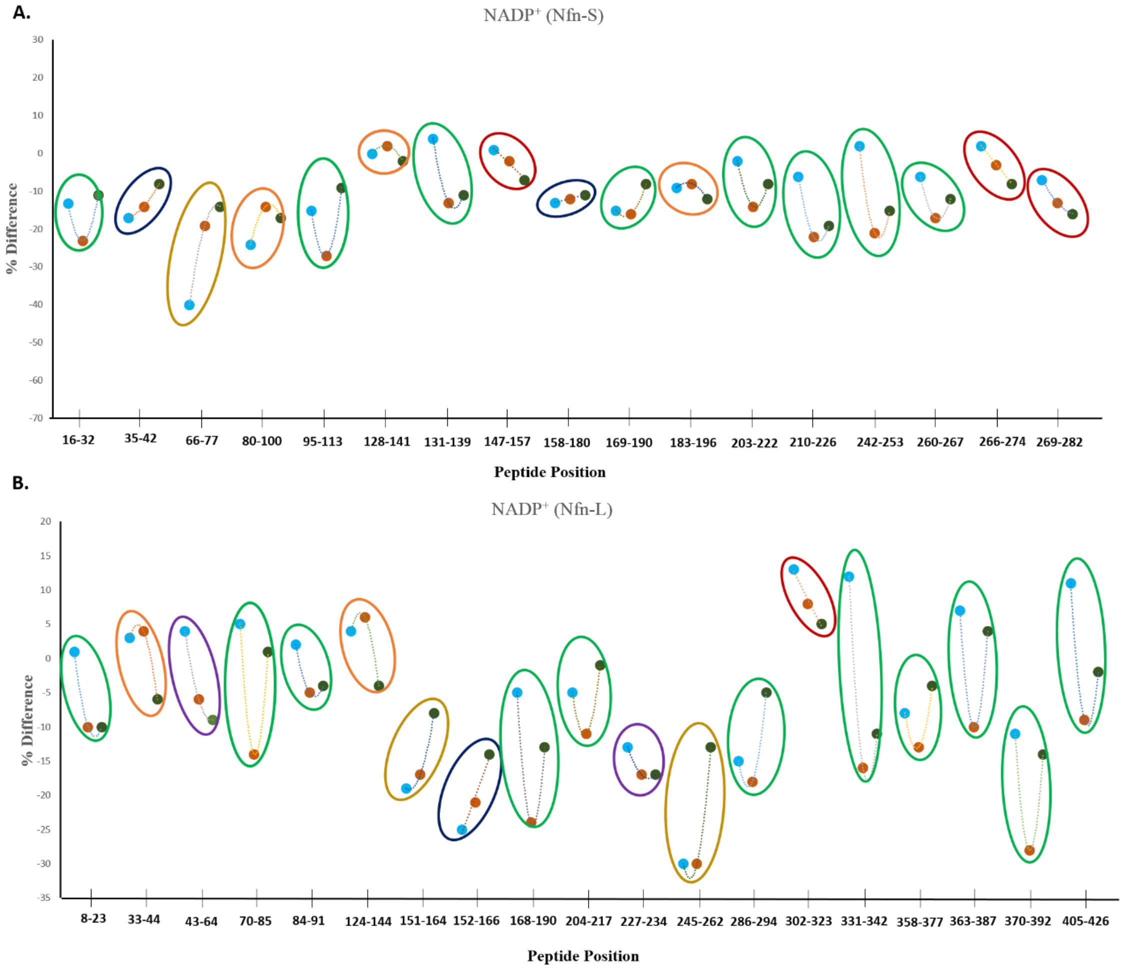

Supplementary Figure 3.2. *HDX comparison between the NADP$^+$ bound form and the as-purified form of Nfn.* The percent difference was calculated by subtracting the percent deuterium (%D) of the as-purified Nfn condition from the %D of the NADP$^+$ condition at the early (60 sec), middle (900 sec), and late (10800 sec). Each timepoint is represented by a specific color: Blue (60 sec), orange (900 sec), and green (10800 sec). The resulting percent difference was graphed for each peptide. The trend of the percent differences was examined at each peptide to cluster the data. A total of seven clusters were specified. Each profile is circled by a color denoting the specific cluster that a fragment belongs to. This was done for HDX exchange data obtained for both Nfn-S (**A**) and Nfn-L (**B**) for all conditions.

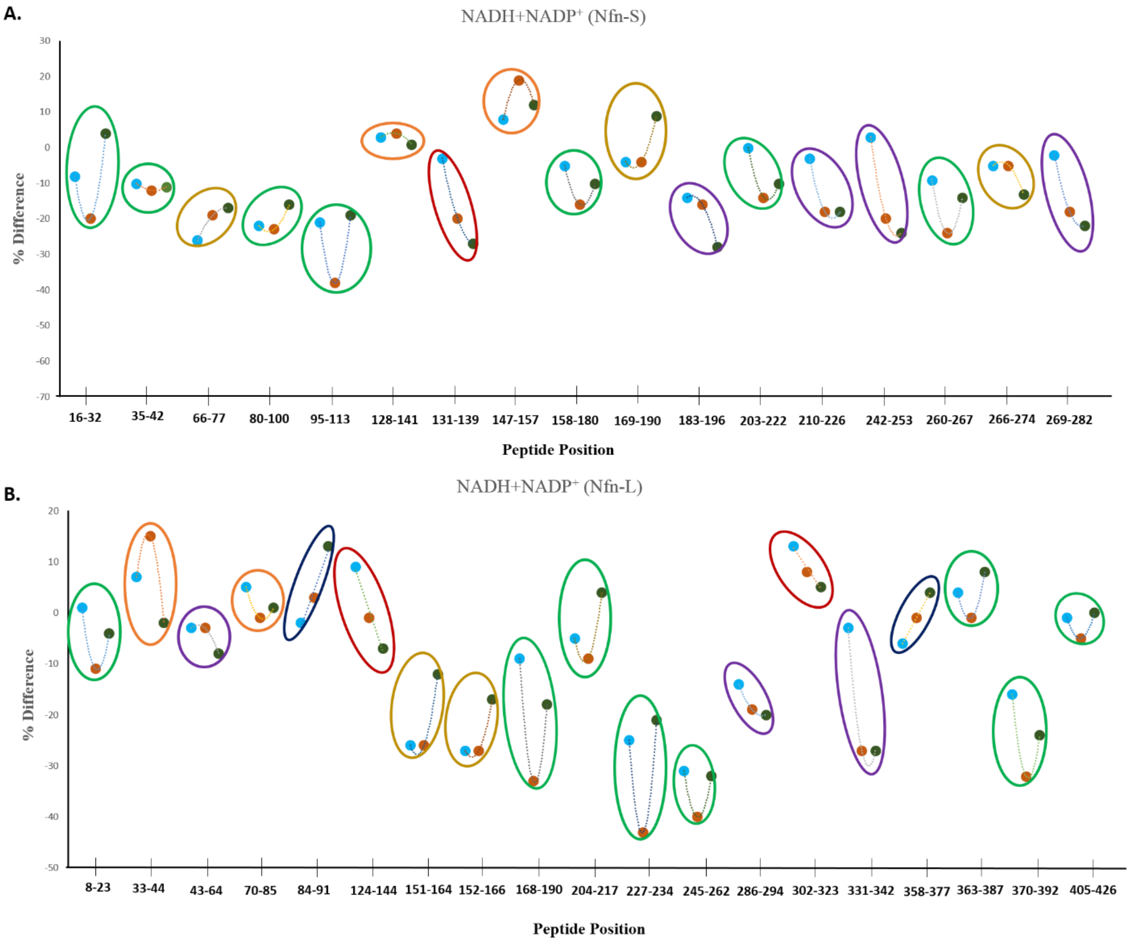

Supplementary Figure 3.3. *HDX comparison between the NADH+NADP$^+$ bound form and the as-purified form of Nfn.* The percent difference was calculated by subtracting the percent deuterium (%D) of the as-purified Nfn condition from the %D of the NADH+NADP$^+$ condition at the early (60 sec), middle (900 sec), and late (10800 sec). Each timepoint is represented by a specific color: Blue (60 sec), orange (900 sec), and green (10800 sec). The resulting percent difference was graphed for each peptide. The trend of the percent differences was examined at each peptide to cluster the data. A total of seven clusters were specified. Each profile is circled by a color denoting the specific cluster that a fragment belongs to. This was done for HDX exchange data obtained for both Nfn-S (**A**) and Nfn-L (**B**) for all conditions.

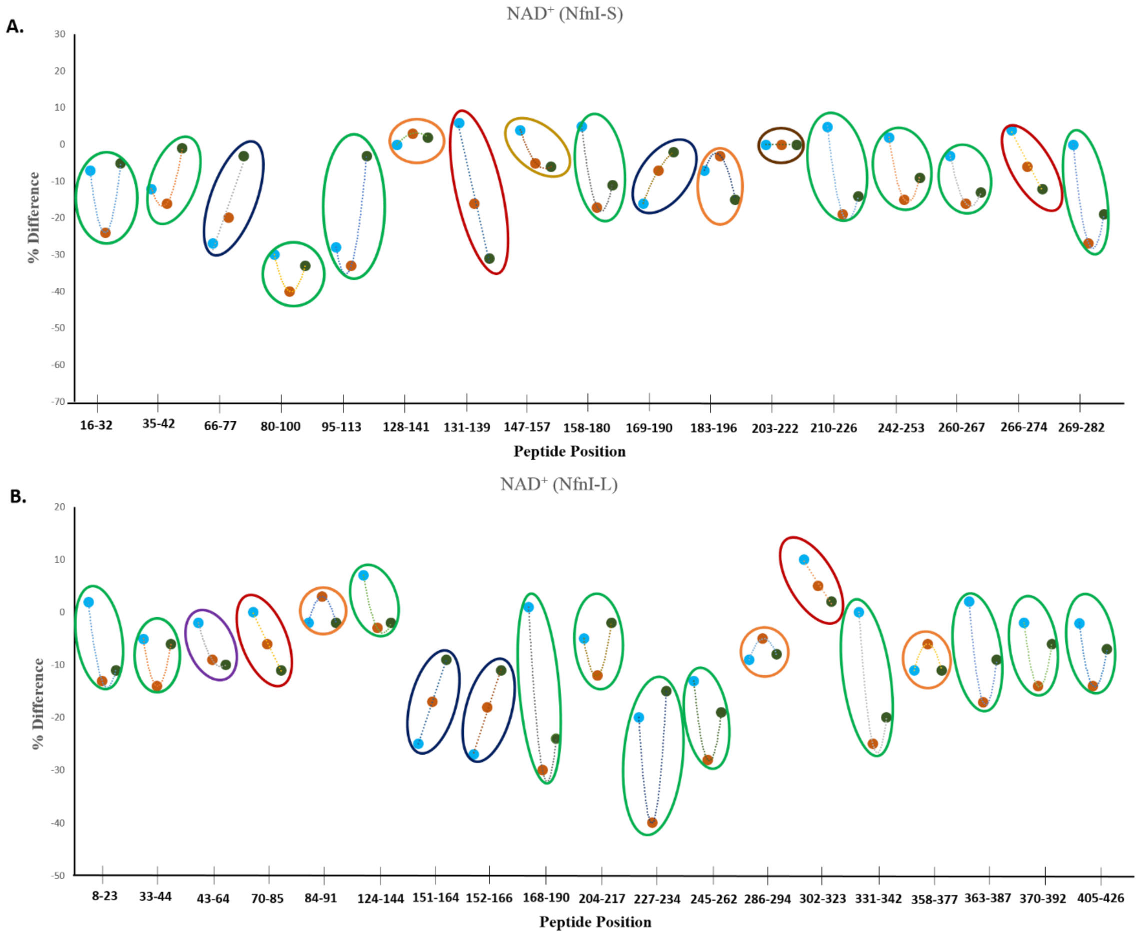

Supplementary Figure 3.4. *HDX comparison between the NAD$^+$ bound form and the as-purified form of Nfn.* The percent difference was calculated by subtracting the percent deuterium (%D) of the as-purified Nfn condition from the %D of the NAD condition at the early (60 sec), middle (900 sec), and late (10800 sec). Each timepoint is represented by a specific color: Blue (60 sec), orange (900 sec), and green (10800 sec). The resulting percent difference was graphed for each peptide. The trend of the percent differences was examined at each peptide to cluster the data together. A total of seven clusters were specified. Each profile is circled by a color denoting the specific cluster that a fragment belongs to. This was done for HDX exchange data obtained for both Nfn-S (**A**) and Nfn-L (**B**) for all conditions.

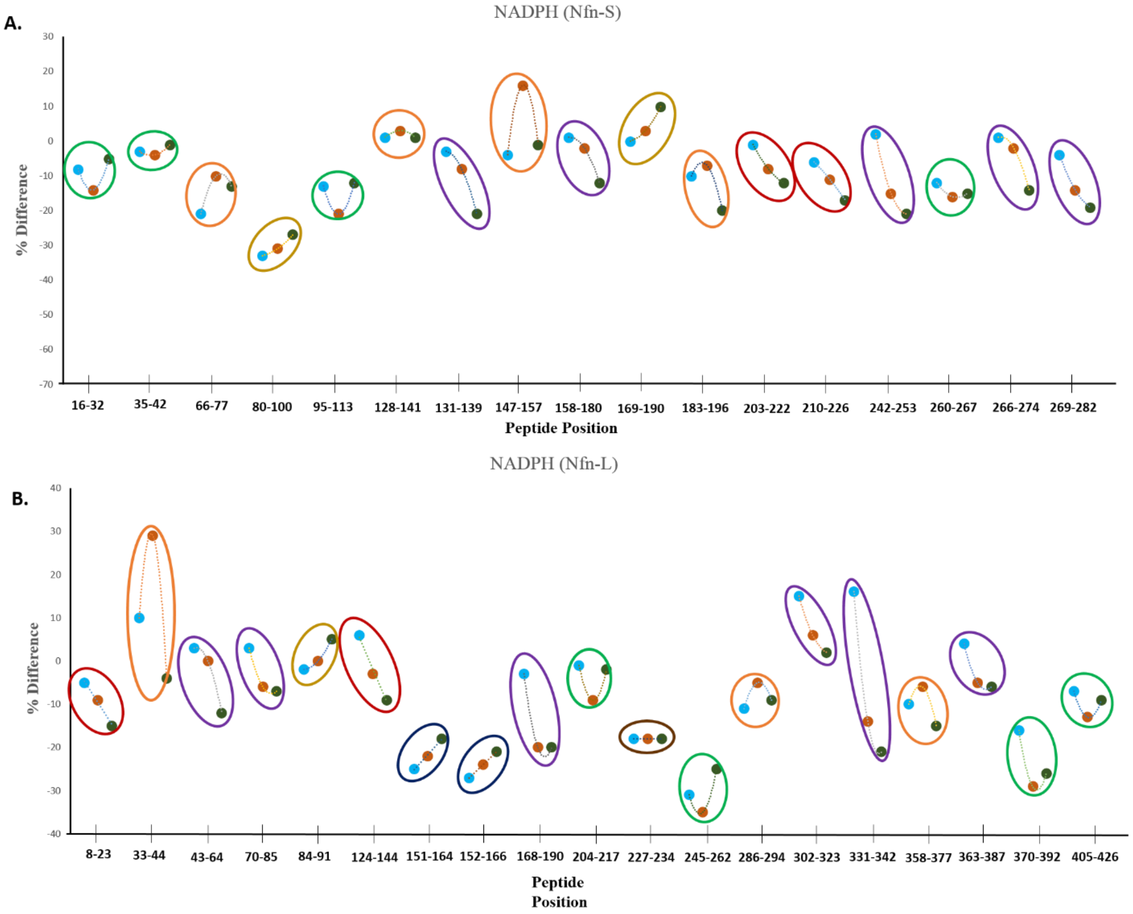

Supplementary Figure 3.5. *HDX comparison between the NADPH bound form and the as-purified form of Nfn.* The percent difference was calculated by subtracting the percent deuterium (%D) of the as-purified Nfn condition from the %D of the NADPH condition at the early (60 sec), middle (900 sec), and late (10800 sec). Each timepoint is represented by a specific color: Blue (60 sec), orange (900 sec), and green (10800 sec). The resulting percent difference was graphed for each peptide. The trend of the percent differences was examined at each peptide to cluster the data. A total of seven clusters were specified. Each profile is circled by a color denoting the specific cluster that a fragment belongs to. This was done for HDX exchange data obtained for both Nfn-S (**A**) and Nfn-L (**B**) for all conditions.

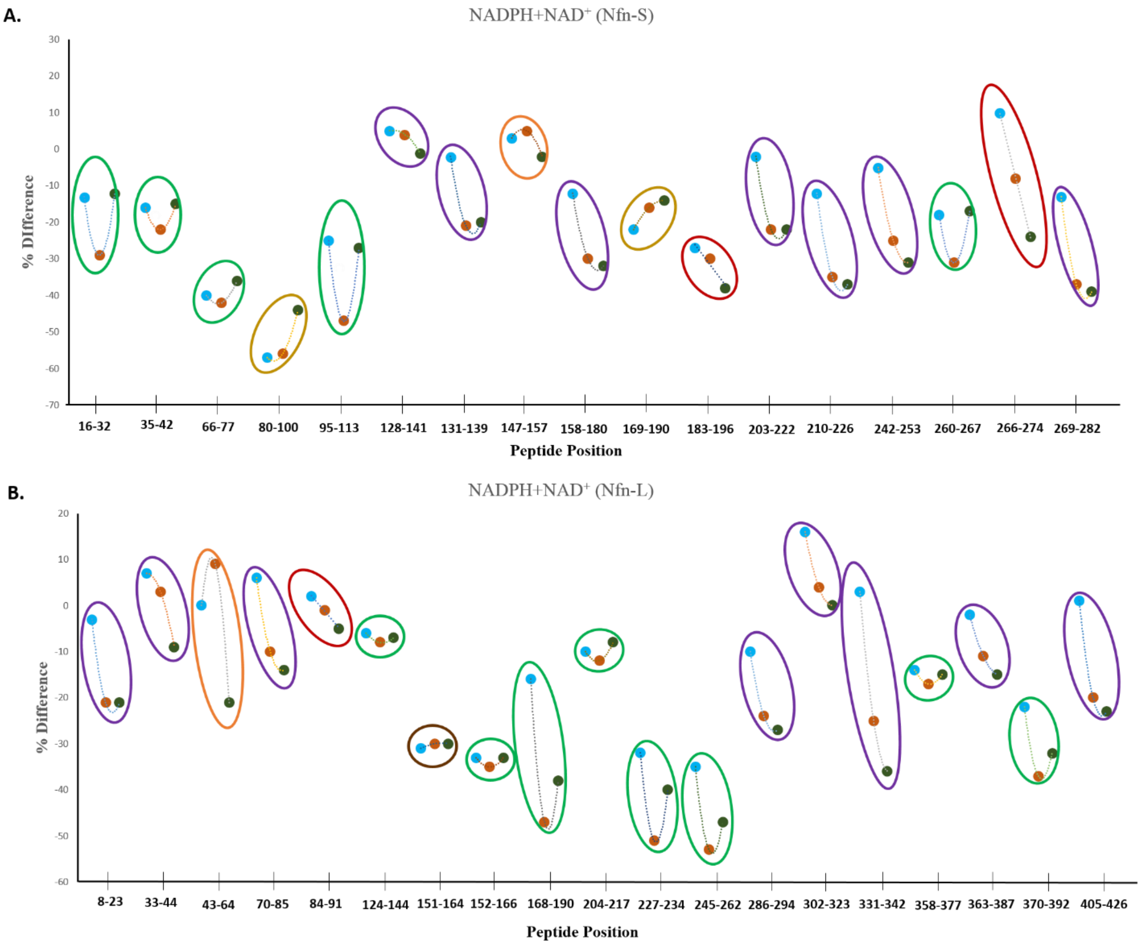

Supplementary Figure 3.6. *HDX comparison between the NAD+NADPH bound form and the as-purified form of Nfn.* The percent difference was calculated by subtracting the percent deuterium (%D) of the as-purified Nfn condition from the %D of the NAD+NADPH condition at the early (60 sec), middle (900 sec), and late (10800 sec). Each timepoint is represented by a specific color: Blue (60 sec), orange (900 sec), and green (10800 sec). The resulting percent difference was graphed for each peptide. The trend of the percent differences was examined at each peptide to cluster the data. A total of seven clusters were specified. Each profile is circled by a color denoting the specific cluster that a fragment belongs to. This was done for HDX exchange data obtained for both Nfn-S (**A**) and Nfn-L (**B**) for all conditions.

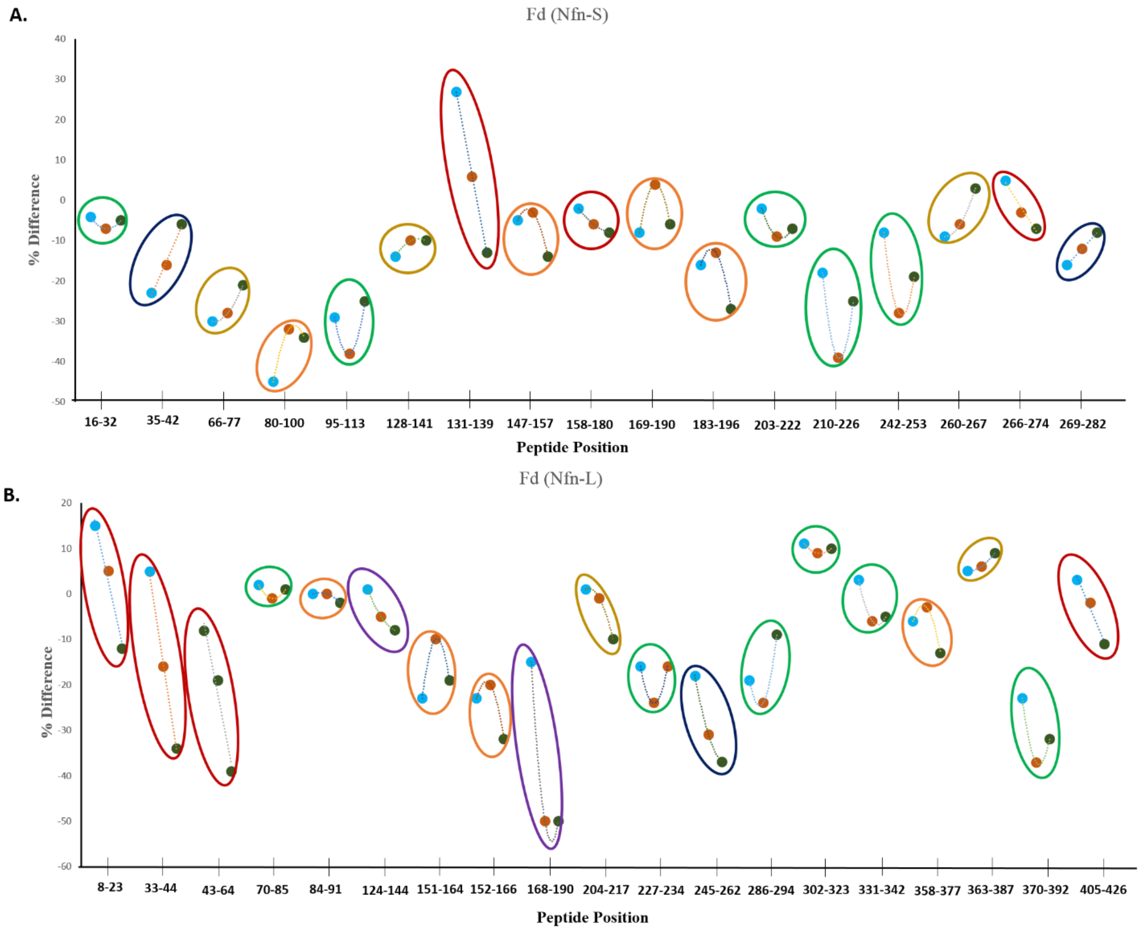

Supplementary Figure 3.7. *HDX comparison between the Fd bound form and the as-purified form of Nfn.* The percent difference was calculated by subtracting the percent deuterium (%D) of the as-purified Nfn condition from the %D of the Fd condition at the early (60 sec), middle (900 sec), and late (10800 sec). Each timepoint is represented by a specific color: Blue (60 sec), orange (900 sec), and green (10800 sec). The resulting percent difference was graphed for each peptide. The trend of the percent differences was examined at each peptide to cluster the data. A total of seven clusters were specified. Each profile is circled by a color denoting the specific cluster that a fragment belongs to. This was done for HDX exchange data obtained for both Nfn-S (**A**) and Nfn-L (**B**) for all conditions.

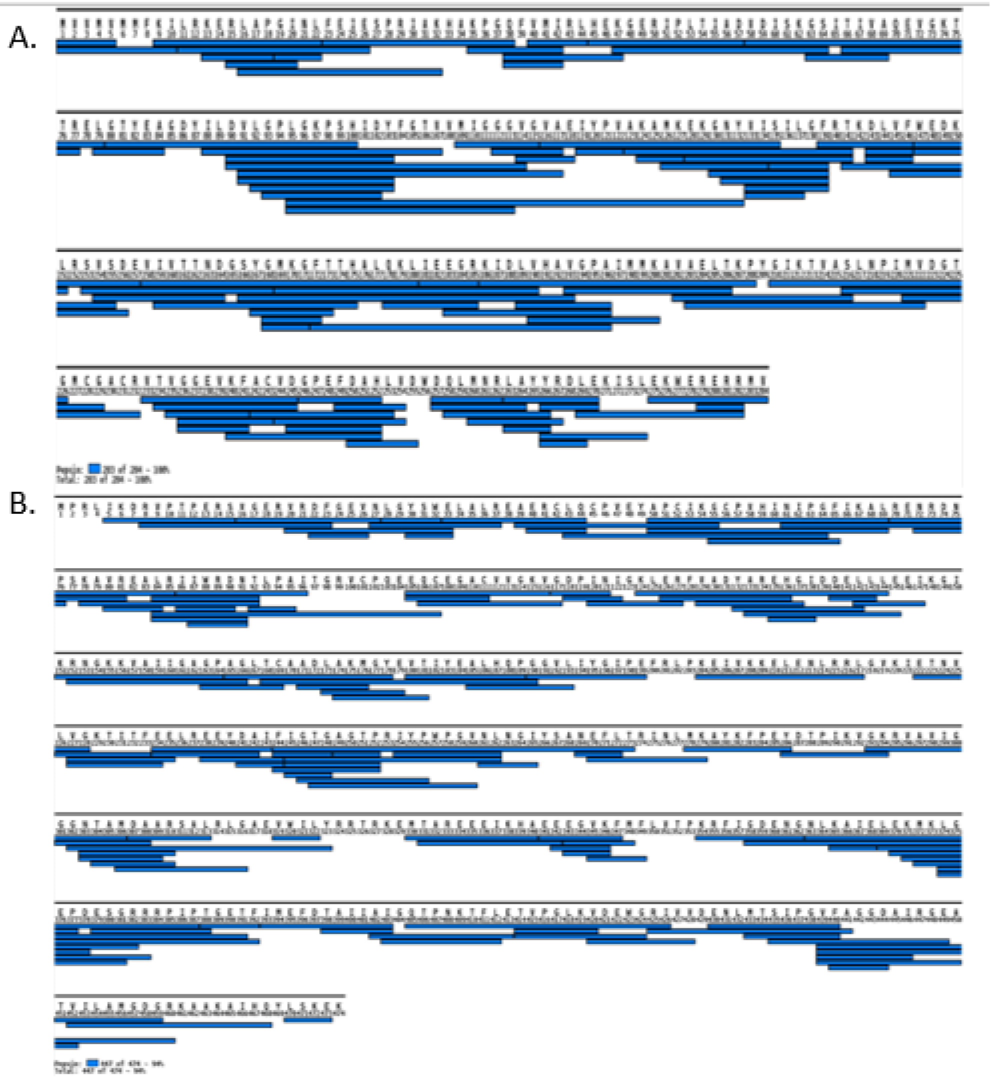

Supplementary Figure 3.8: *Peptide coverage maps of Nfn-S (A) and Nfn-L (B)*. Each peptide detected using mass spectrometry is indicated by a blue bar, with the amino acid position number relative to Nfn-SL from *P. furiosus* (PDB ID: 5JFC), as well as the one letter abbreviation located at the top of each row. The total percentage of coverage is indicated for each subunit at the bottom left corner of each panel.

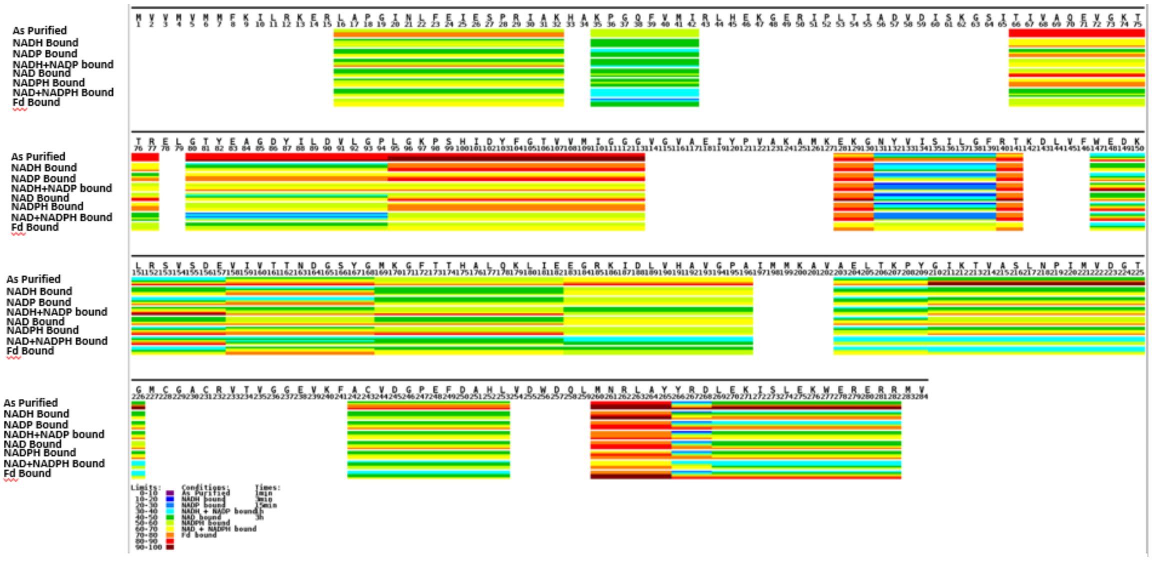

Supplementary Figure 3.9. *Heat Map of %D in Nfn-S depicting the percentage of deuterium exchanged for the protein at every time point and in all tested conditions*. The conditions tested (as-purified Nfn, NADH bound, NADP bound, NADH+NADP bound, NAD bound, NADPH bound, NAD+NADPH bound, and Fd bound) are displayed as separate rows and the percent deuterium uptake is indicated by differing colors with purple representing 0-10% exchange and dark red representing 90-100% exchange (keys are present beneath each heat map). Each condition's block is then further divided into rows indicating each tested time point.

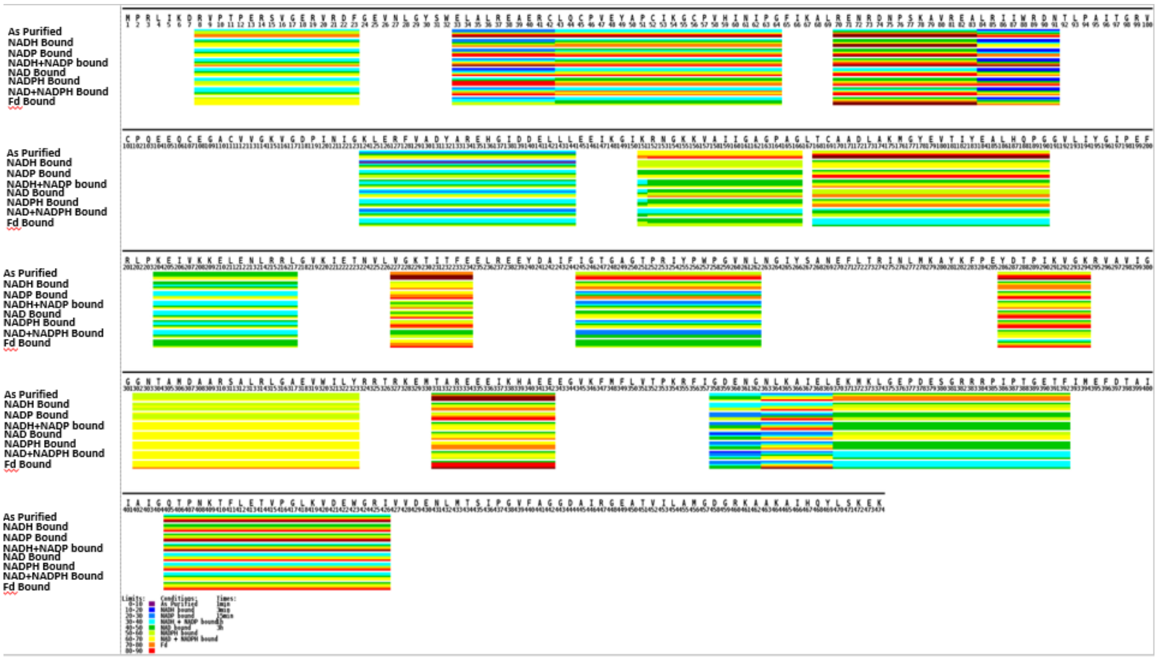

Supplementary Figure 3.10. *Heat Map of %D in Nfn-L shows the percentage of deuterium exchanged for the protein at every time point and in all tested conditions*. The conditions tested (as-purified Nfn, NADH bound, NADP bound, NADH+NADP bound, NAD bound, NADPH bound, NAD+NADPH bound, and Fd bound) are displayed as separate rows and the percent deuterium uptake is indicated by differing colors with purple representing 0-10% exchange and dark red representing 90-100% exchange (keys are present beneath each heat map). Each condition’s block is then further divided into rows indicating each tested time point.

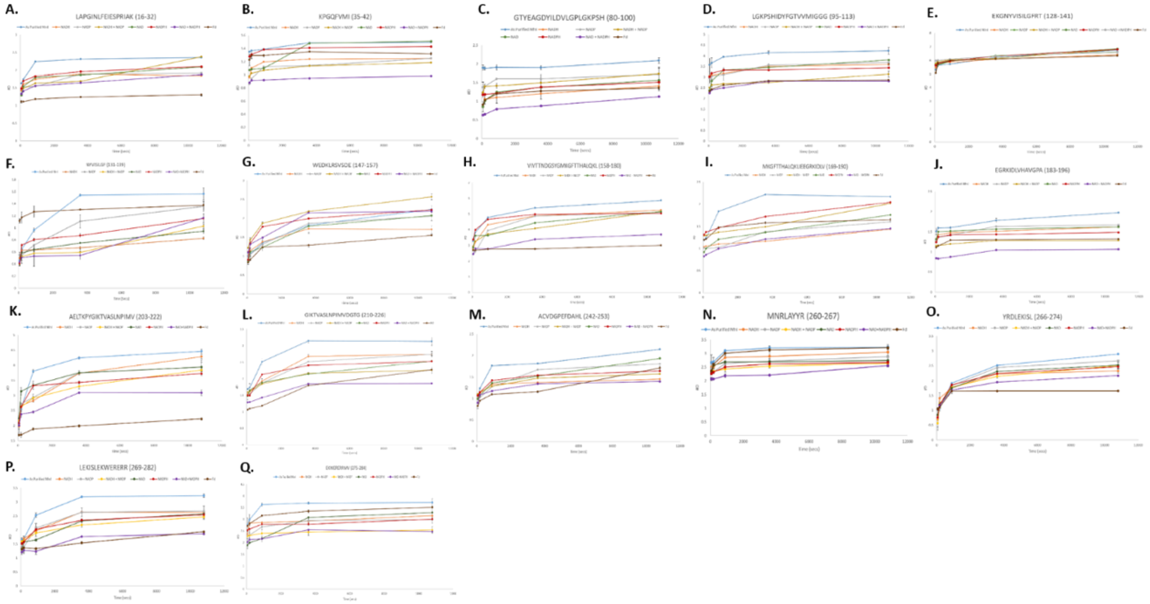

Supplementary Figure 3.11. *NfnS Uptake Curves*. Uptake curves in Nfn-S near key regions predicted to be involved in electron bifurcation. Each curve shows the absolute number of deuterium (#D) atoms on the y-axis, and the time in seconds in the x-axis for the region of Nfn-S indicated at the top of each graph for the five main time points in seconds (60, 180, 900, 3600, 10800). All eight conditions are displayed on each graph in the following colors: blue (as-purified), orange (NADH bound), grey (NADP bound), gold (NADH+NADP bound), green (NAD bound), red (NADPH bound), purple (NAD+NADPH bound), and brown (Fd bound).

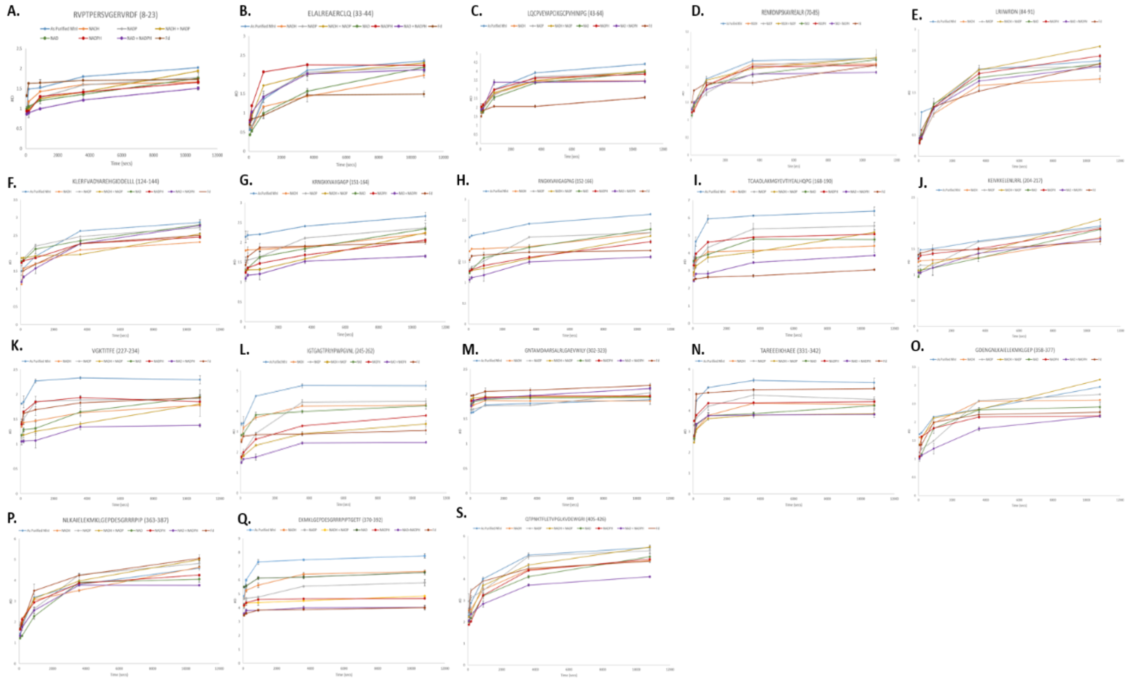

Supplementary Figure 3.12. *NfnL Uptake Curves*. Uptake curves in NfnL near key regions believed to be involved in electron bifurcation. Each curve shows the absolute number of deuterium (#D) on the y-axis, and the time in seconds in the x-axis for the region of NfnL indicated at the top of each graph for the five main time points in seconds (60, 180, 900, 3600, 10800). All eight conditions are displayed on each graph in the following colors: blue (as-purified), orange (NADH bound), grey (NADP bound), gold (NADH+NADP bound), green (NAD bound), red (NADPH bound), purple (NAD+NADPH bound), and brown (Fd bound).

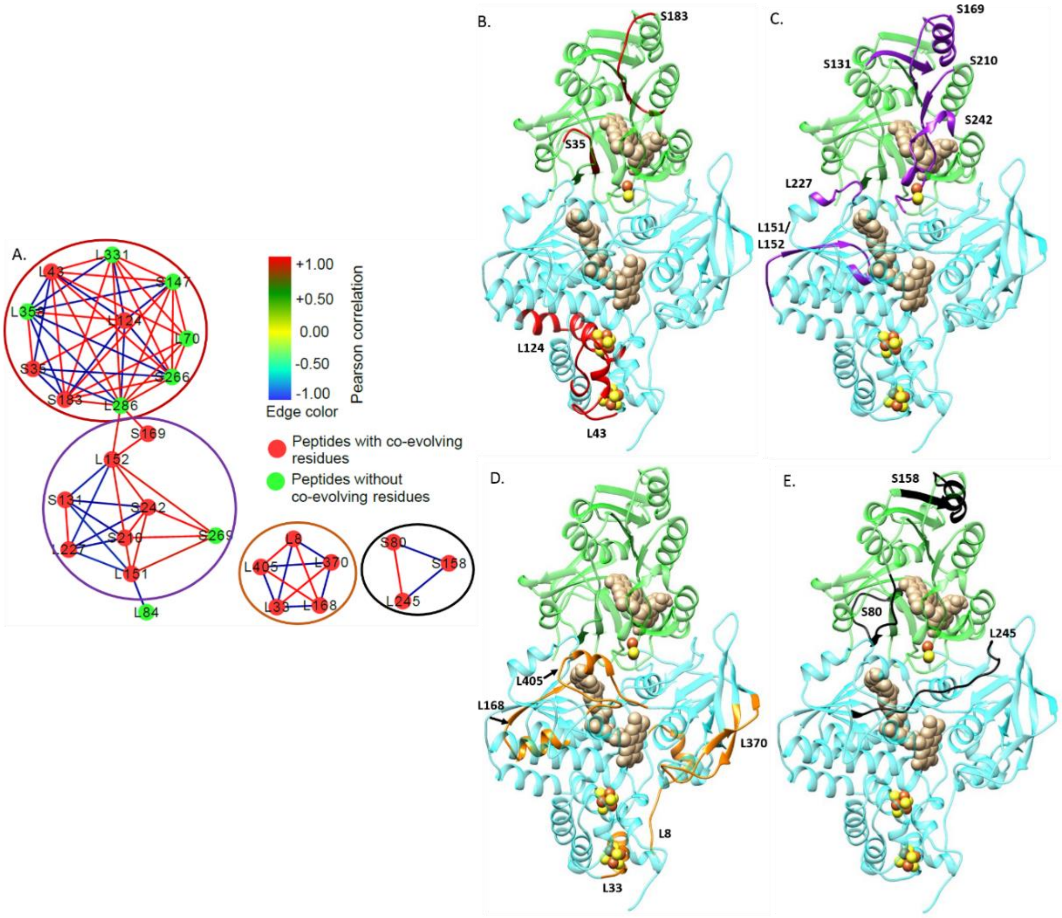

Supplementary Figure 3.13. *Network analysis of HDX-MS data and co-evolving residues*. (**A).** Network plot generated from clustered HDX-MS data and co-evolving residues for the confurcating conditions (NADH, NADP, and NADH+NADP). Each node represents a peptide analyzed in this study with HDX-MS. The node label indicates whether it is located on the large (Nfn-L) or small (Nfn-S) subunit and includes the residue number of the first amino acid in the sequence (residue numbering is defined by the sequence position in *P. furiosus* Nfn (PDB ID: 5JCA)). Red nodes indicate the presence of a residue that exhibits strong evidence for co-evolution, relative to other residues within the protein, and the green nodes indicate a lack of co-evolution. Edges connecting each node indicate the correlation between the deuterium uptake profile of each peptide. A high correlation is indicated by red edges and a low correlation is indicated by blue edges. Nodes were qualitatively grouped together based on the degree of correlation between peptides and can be separated into four groups, indicated by the red, purple, orange and black outlines in the same manner that was used to form groups of connected peptides in Figure 5. These residues were then mapped onto the structure of *Pf* Nfn using the following colors (which match the outline: red (**B**), purple (**C**), orange (**D**) and black (**E**).

CHAPTER FOUR

COMBINING IN-SOLUTION AND COMPUTATIONAL METHODS TO CHARACTERIZE THE STRUCTURE-FUNCTION RELATIONSHIP OF THE NITROGENGASE SYSTEMS

Contributions of Authors and Co-Authors

Manuscript in Chapter 4

Author: Luke Berry

Contributions: Performed HDX-MS experiment and analyzed data. Developed covariance matrix of the normal mode analysis data and assisted in data analysis. Organized and wrote manuscript.

Author: Monika Tokmina-Lukaszewska

Contributions: Performed the chemical cross-linking experiment and analyzed data. Led the analysis of the normal mode analysis data. Organized and wrote manuscript.

Co-Author: Derek F. Harris

Contributions: Expressed and purified protein samples. Reviewed manuscript during development.

Co-Author: Oleg A. Zadvornyy

Contributions: Reviewed manuscript during development.

Co-Author: Simone Raugei

Contributions: Performed normal mode analysis calculations. Reviewed manuscript during development.

Co-Author: John W. Peters

Contributions: Reviewed manuscript during development.

Co-Author: Lance C. Seefeldt

Contributions: Supervised the protein purification protocol. Reviewed manuscript during development.

Co-Author: Brian Bothner

Contributions: Supervised the hydrogen deuterium exchange experiment, chemical cross-linking experiment, and mass spectrometry operation. Reviewed manuscript during development.

Manuscript Information

COMBINING IN-SOLUTION AND COMPUTATIONAL METHODS TO CHARACTERIZE THE STRUCTURE-FUNCTION RELATIONSHIP OF THE NITROGENGASE SYSTEMS

Authors: Luke Berry, Monika Tokmina-Lukaszewska, Derek F. Harris, Oleg A. Zadvornyy, Simone Raugei, John W. Peters, Lance C. Seefeldt, Brian Bothner

Journal: To be determined

Status of Manuscript:
_x_ Prepared for submission to a peer-reviewed journal
___ Officially submitted to a peer-reviewed journal
___ Accepted by a peer-reviewed journal
___ Published in a peer-reviewed journal

CHAPTER FOUR

COMBINING IN-SOLUTION AND COMPUTATIONAL METHODS TO CHARACTERIZE THE STRUCTURE-FUNCTION RELATIONSHIP OF THE NITROGENGASE SYSTEMS

Abstract

Nitrogenases have the ability to catalyze the reduction of nitrogen gas, arguably one of the most difficult chemical reactions, under ambient temperatures and pressures. A comprehensive model detailing how electron transfer is orchestrated by these multi-subunit enzymes has yet to be presented. There are three classes of nitrogenases, each distinguished by a unique transition metal at the site of nitrogen reduction. While the quaternary structures are largely similar, there are differences in the structure of the complexes, indicating differences in the mechanism of nitrogen reduction. Several studies of the Mo-dependent and V-dependent nitrogenases have revealed intricate details on the mechanism of nitrogen reduction, however little is known about the Fe-dependent system. Additionally the catalytic component of the Fe-dependent and V-dependnet nitrogenases contains an additional subunit, termed the G subunit, that is necessary for nitrogen reduction, but the exact role in catalysis is unknown. To fully understand the structure-function relationship of the nitrogenase systems the Fe-dependent system needs to be characterized. To address the current gap in knowledge, we used a suite of biophysical approaches to generate structural models and probe the behavior of the Fe-dependent nitrogenase system in-solution and *in silico*. Chemical cross-linking and hydrogen deuterium exchange coupled to mass spectrometry identified the binding site of the G subunit and revealed unique structural dynamics of the catalytic component of the Fe-dependent nitrogenase system (AnfDGK). This investigation was supported with normal mode analysis (NMA) which provided evidence for the role of the AnfG subunit in the catalytic activity of the Fe-dependent nitrogenase. Analysis of a covariance matrix produced with the NMA data revealed the presence of highly correlated networks involving the cofactors necessary for nitrogen reduction and revealed pathways of long distance communication between the two halves of the AnfDGK protein. Our analysis suggests, that the dynamic energy landscape and structural flexibility of the AnfDGK protein defines the catalytic activity of the Fe-dependent nitrogenase through a similar mechanism observed in the catalytic component of the Mo-dependent nitrogenase.

Abbreviations

NifDK: MoFe protein of the Molybdenum-dependent nitrogenase

VnfDGK: VFe protein of the Vanadium-dependent nitrogenase

AnfDGK: FeFe protein of the Iron-dependent nitrogenase

XL-MS: Chemical cross-linking mass spectrometry

HDX-MS: Hydrogen/deuterium exchange mass spectrometry

#D: Absolute number of deuterium incorporated

%D: Percentage of deuterium incorporated

NMA: Normal Mode Analysis

Introduction

In nature, the conversion of nitrogen gas (N_2) into its bioavailable form, ammonia (NH_3), is carried out by a group of microorganisms to as diazotrophs. This reaction is facilitated by a class of enzymes called nitrogenases, which use protons, electrons and the hydrolysis of ATP to control the cleavage of the N-N triple bond[1]. The industrial version of this reaction, the Haber-Bosch process[2–4], uses high temperature and pressure, but the nitrogenase systems are capable of biological nitrogen fixation at ambient temperature and pressure[5–7]. In the organism *Azotobacter vinelandii* three forms of the nitrogenase system have been identified, each featuring a different transition metal in the active site: the Mo-dependent, V-dependent, and the Fe-dependent nitrogneases[1,8,9]. The Mo-dependent system was the first discovered and is the most studied of all three nitrogenases, and will be used as an example to introduce the composition and general mechanism of the nitrogenases (**Fig. 4.1**). The Mo-dependent nitrogenase is a two component system which contains the MoFe protein (NifDK) and Fe protein (NifH). The active form of NifH is a homodimer bridged by a single 4Fe-4S cluster and contains two nucleotide binding sites, one per monomer. NifDK is a tetramer composed of two heterodimers (abbreviated as D_1K_1 and D_2K_2), each contains two unique cofactors: an [8Fe-7S] cluster (P-cluster) and a [7Fe-9S-1Mo-1C-homocitrate] cofactor (FeMo-co).

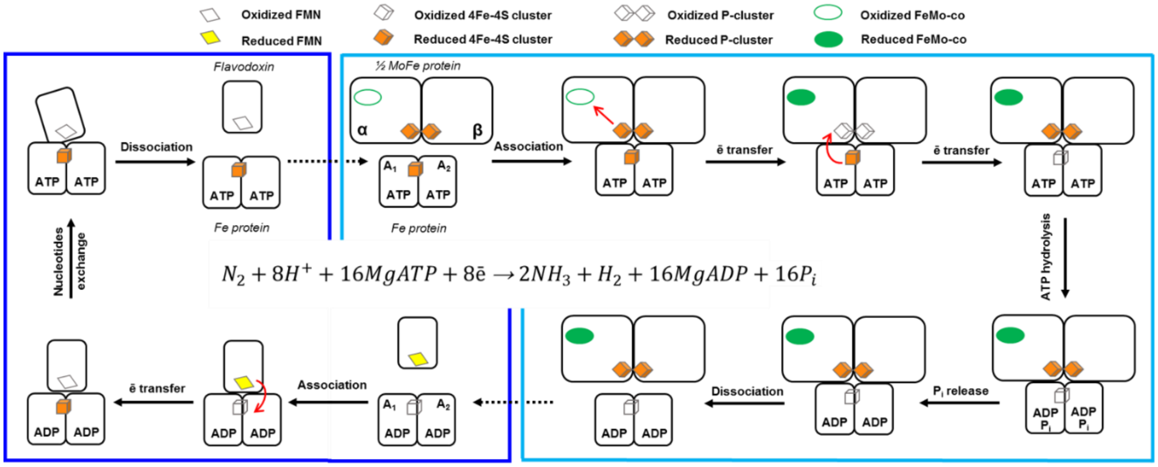

Figure 4.1. Catalytic cycle of the Mo-dependent nitrogenase system. The Mo-nitrogenase is a two component system which contains MoFe protein (NifDK) and Fe protein (NifH). The active form of Fe protein is a homodimer (abbreviated as A_1A_2) bridged by a single 4Fe-4S cluster and contains two nucleotide binding sites, one per monomer. The MoFe protein is a tetramer composed of two heterodimers (abbreviated as $\alpha_1\beta_1\alpha_2\beta_2$) which contains two unique cofactors: P-cluster (8Fe-7S) and FeMo-cofactor (7Fe-9S-1Mo-1C homocitrate cofactor), one per each half. The P-cluster is located at the αβ interface and is responsible for electron transfer from the Fe protein to the FeMo-cofactor. FeMo-cofactor occupies a space in the α subunit and it serves as the active site of the nitrogenase system. The catalytic process requires multistep, synchronized interactions between Fe protein and MoFe protein (called the Fe protein cycle), and Fe protein and flavodoxin. The nitrogenase Fe protein cycle involves transient associations between the reduced, MgATP-bound Fe protein and the MoFe protein and includes electron transfer, ATP hydrolysis, release of P_i, and dissociation of the oxidized, MgADP-bound Fe protein from the MoFe protein. To complete the cycle, Fe protein needs to be re-charged (4Fe-4S cluster is reduced) by accepting electrons from flavodoxin.

The P-cluster is located at the DK interface and facilitates electron transfer from NifH to the FeMo-cofactor. The FeMo-co occupies space in the D subunit and it serves as the active site of the nitrogenase system. The catalytic process requires multistep, synchronized interactions between NifH and NifDK (called the Fe protein cycle), and NifH and the intracellular electron carrier, flavodoxin (Fld). The Fe protein cycle involves transient associations between the reduced, MgATP-bound NifH and the NifDK protein. After NifH binding, electron transfer, ATP hydrolysis, release of P_i, and dissociation of the oxidized, MgADP-bound Fe protein from the NifDK protein occur transferring an electron from NifH to the FeMo-co[10,11]. NifH is then regenerated accepting an electron from Fld, and exchanging ADP for ATP[1,12–14].

The expression and activity of the different nitrogenases is dependent on environmental factors, such as the availability of Mo and V[15]. In the absence of Mo and V, *A.vinelandii* expresses the Fe-dependent nitrogenase[16]. Conversly in the presence of Mo and V expression of the Fe-dependent nitrogenase suppressed[17]. The Fe-dependent nitrogenase system is comprised of the electron delivery Fe protein (AnfH) and the catalytic component FeFe protein (AnfDGK), which contains only Fe at the catalytic site ([7Fe-9S-1Fe-1C-homocitrate];FeFe-co)[16,18–21]. While the residues involved in the AnfH-AnfDGK complex formation as well as the P-cluster and FeFe-co coordination sphere are conserved in both the Fe- and Mo-dependent nitrogenase systems, the AnfDGK contains an additional G subunit, one per heterotrimer[16,19,22,23]. This additional subunit is also present in the catalytic component of the V-dependent nitrogenase (VnfDGK). The catalytic function of the G subunit is not known, however, it is necessary for Fe- and V-dependent nitrogenase catalytic function, and plays a critical role in substrate specificity of VnfDGK[15,24]. A unique aspect of the nitrogenase system is the ability to catalyze the reduction of N_2 to NH_3 while simultaneously catalyzing the formation of hydrogen (H_2). The allocation of the electrons among substrates is different for each enzyme, and based on the stoichiometry of the products the Mo-dependent nitrogenase is an excellent nitrogen fixing system, while the Fe-dependent nitrogenase is better at hydrogen production[8,19,25–27].

It has been implicated by several structural and functional studies of the nitrogenase systems that mechanistic insights from one system are applicable to all classes[8,18,21,28–32]. Therefore, the identification of the G subunit location and its role in the Fe-dependent nitrogenase system is a critical piece of information needed to understand the structural and functional disparities between the different nitrogenase systems. Using a combined approach of structure based alignments and chemical cross-linking coupled to mass spectrometry (XL-MS) we developed and validated a homology model of the AnfDGK complex. Additionally, the XL-MS data was combined with hydrogen/deuterium exchange coupled to mass spectrometry (HDX-MS) experiments, to detail that the AnfG subunit interacts primarily with the AnfD subunit, and to characterize the structural and dynamic differences between the NifDK and AnfDGK proteins. XL-MS and HDX-MS analysis also determined the presence of long-distance interactions and correlated motions that serve to propagate conformational change across the complex indicating that Fe-dependent nitrogenase catalytic activity is under allosteric regulation. Incorporating structural dynamic calculations with normal mode analysis

(NMA) provided evidence for a functional connection between AnfG and the P-cluster, AnfH binding site and AnfK$_1$-K$_2$ subunit interface which reveals the influence of the AnfG subunit on the catalytic activity of the Fe-dependent nitrogenase. Correlated in- and out-of-phase motions identified from NMA coupled with the presence of bimodal peptides in the HDX-MS data provided evidence for negative cooperativity playing a role in controlling the electron flow in the Fe-dependent nitrogenase in a mechanism similar to the Mo-dependent nitrogenase.

Materials and Methods

Protein Expression and Purification AnfDGK was expressed in *A.vinelandii* strain DJ1255. Cells were grown at 30°C in Burk N-free medium with Na_2MoO_4 omitted in a custom-built 100 L fermenter with stirring and aeration to an OD_{600} of 1.8-2.0 [33]. AnfDGK complex was isolated and purified according to previously described methods [18,34–36]. Protein identification and sample purity was done as previously described [37] using a maXis Impact UHR-QTOF instrument (Bruker Daltonics) interfaced with a Dionex 3000 nano-uHPLC (Thermo-Fisher) followed by data analysis in SearchGUI/Peptide Shaker versions 3.2.20/1.14.16 [38].

Sequence Alignment and Homology Model Generation Protein homology models were generated by Phyre^2 a protein fold recognition server and individual Anf subunits were overlaid on a structure of recently published crystal structure of the VnfDGK from *A. vinelandii*[21,39]. Subunit alignment (“best-aligning pair of chains between reference and match structure” in match maker option) and molecular graphics were generated using the UCSF Chimera[40]. Side chain clashes in the obtained AnfDGK model were resolved by a single course of energy minimization performed in Chimera. The final homology model of the AnfDGK complex was used in the structural analysis presented in this manuscript.

Chemical Cross-Linking Mass Spectrometry Experiments AnfDGK sample was cross-linked in a similar fashion to the protocol previously described[41]. Briefly, 20 µM AnfDGK complex was chemically cross-linked with 1mM bis(sulfosuccinimidyl)suberate (BS3) (Thermo-Fisher) in 50 mM HEPES/150 mM NaCl buffer pH 7.2 at room temperature for one hour. The reaction was quenched with 120 mM Tris base (final concentration). After a 15 minutes incubation, the resulting mixture was separated by SDS-PAGE (4-20% linear gradient mini gel, Bio-Rad) and stained with Coomassie Brilliant Blue (Thermo-Fisher). The entire lane between 10-250 kDa (according to the broad range marker migration profile) was digested with trypsin (Promega) according to a standard protocol recommended by the manufacturer (protease:complex molar ratio of 1:50, overnight). Proteins were identified as described[37] using a maXis Impact UHR-QTOF instrument (Bruker Daltonics) interfaced with a Dionex 3000 nano-uHPLC (Thermo-Fisher). Cross-linked species were identified with Spectrum Identification Machine (SIM)[42] with dynamic data base reduction enabled and precursor/fragment ion tolerance set to 20 ppm. The resulting data output was imported into XLink Analyzer for analysis and visualization of the cross-linking data in the context of the proteins' three-dimensional structures[43]. Cross-links complying with the assigned 30 Å distance cutoff were visualized in CX-Circos[44].

H/D Exchange Mass Spectrometry Experiments The exchange reaction was initiated by a 10-fold dilution of AnfDGK (10.6 mg/mL) and NifDK (11.7 mg/mL) into the reaction buffer at room temperature under anaerobic conditions [45,46]. The reaction buffer contained 50 mM Tris-HCl, 100 mM NaCl, and 2 mM dithionite in D_2O (pD 7.0). Samples were removed and quenched to stop exchange after 1 minute, 5 minutes, 15 minutes, 60 minutes, 3 hours, and 24 hours. At each time point, a 10 µL subsample was withdrawn from each reaction vial and placed into quench/digestion solution containing 1% formic acid (Sigma) and porcine pepsin (Sigma, 0.2 mg/mL final concentration) on ice. After two minutes incubation, the reaction mixture was frozen in liquid N_2 and stored at -80 °C until it was subjected to liquid chromatography-mass spectrometry (LC-MS) analysis.

LC-MS analysis of AnfDGK and NifDK peptide fragments was completed on a 1290 UPLC series chromatography stack (Agilent Technologies) coupled directly to a 6538 UHD Accurate-Mass Q-TOF LC-MS mass spectrometer (Agilent Technologies) as previously described[46,47]. Data processing was carried out in MassHunter Qualitative Analysis version 6.0 (Agilent Technologies). Peptide identification was performed using the Peptide Analysis Worksheet (PAWs, ProteoMetrics, LLC.). Deuterium uptake was determined by monitoring shifts of the centroid peptide isotopic distribution by using the program HDExaminer (Sierra Analytics, Inc.). Measured values were then used to generate uptake curves to compare relative deuterium exchange in all conditions tested. To generate the heat maps, the percent deuterium (%D) incorporated at a given time point was calculated by dividing the number of deuterium atoms incorporated (#D) by the number of deuterium atoms incorporated after 24 hours. Overlapping peptides were resolved as described by Pascal *et al* [48]. The %D for each detected peptide in the Nif and Anf proteins were aligned based on the sequence alignment generated in Phyre^2 [39]. The percent difference in deuterium incorporation was then calculated by subtracting the %D of Anf from the %D of Nif for the final (10800 seconds) time point. The resulting numbers were aligned to the Anf sequence for the D and K subunits. Positions that did not have a %D in both sequences were assigned a value of zero. The percent difference of deuterium incorporation between the AnfDGK and NifDK was rendered on the AnfDGK homology model in Chimera[40] using the following values: blue = -100 for minimum deuterium exchange, gray = 0 for no change, and red = 100 for maximum deuterium exchange.

Normal Mode Analysis To define a conformation of the AnfDGK complex a normal mode vibrational analysis based on the anisotropic Gaussian network model was performed as previously described [49]. In addition, the detailed description of elastic network model and analysis can be found in Tirioin and Atilgan *et al*. [50,51]. To calculate the normal modes of vibration (displacement vectors) and their frequency the temperature factors provided in PDB of AnfDGK homology model acquired based on VnfDGK template (PDB ID: 5N6Y[21]) were used. Covariance matrix was visualized in R 3.4 language and environment for statistical computing and graphics[52] using the corrplot package[53].

Results and Discussion

Development and Validation of the AnfDGK Homology Model

Our first step in developing a functional model encompassing the three forms of nitrogenase was to construct a structural model of the AnfDGK complex. To begin our analysis we generated homology models for individual subunits using the Phyre^2, protein fold recognition server[54]. Phyre^2 uses the primary sequence of a protein of interest in order to develop a three-dimensional structural model. This process begins with a multiple sequence alignment against proteins with known structural models. The sequence alignment is followed by secondary and tertiary structure predictions. The homology models of the AnfG, AnfD, and AnfK subunits were generated with 100% confidence and 84%, 89% and 99% sequence coverage, respectively. The top hit for each subunit was the corresponding chain from the VnfDGK complex (41%, 55%, and 58% sequence identity for Anf G, D, and K subunits, respectively). The second highest hit for the AnfDK subunits was the corresponding subunits from the NifDK with 33% and 31% sequence identity for the D and K subunits, respectively. **Supp. Fig. 4.1** presents independent secondary structure prediction for the AnfDGK proteins and a sequence alignment for the catalytic components of all three nitrogenases. Next, we overlaid the energy minimized homology models of individual Anf subunits on the highest scoring protein template, VnfDGK (PDB ID: 5N6Y, [21]). To obtain a final homology model of AnfDGK and performed an energy minimization calculation to resolve remaining amino acid side chain clashes.

In order to evaluate the homology model of the AnfDGK complex we applied the XL-MS protocol using BS3 (bis(sulfosuccinimidyl)suberate) as the cross-linking reagent. BS3 reacts with primary amines, as well as hydroxyl groups but at a slower rate, to form stable covalent bonds. Inter-subunit cross-links provide useful information on protein binding interfaces, and intra-subunit cross-links can reveal the architecture of a single subunit. This makes XL-MS an excellent validation tool for the generated homology models. In our experiments we found a modest number of intra-subunit cross-links for AnfG. We attribute this to two factors: (1) spatial distribution of residues available to BS3 permits few intra-connections to be formed and (2) protein/complex dynamics favor formation of dead-end cross-links rather than allowing for a complete bridge. The calculated distance for all intra-subunit crosslinks are below 17.2 Å. This stays well within the 30 Å distance threshold for BS3[55] supporting the fit of our AnfDGK homology model with its template, VnfDGK.

Structural Comparison of the AnfDGK and NifDK Complexes The analysis of protein dynamics in the context of structure is a powerful tool for understanding the structure-function relationship. While it has been established that the overall mechanism of N_2 binding and reduction within AnfDGK and NifDK is the same[18], the overall rates of reduction and product stoichiometry differ greatly. To elucidate the factors controlling the allocation of electrons to substrates and the protein component contribution to catalysis, we used peptide level HDX-MS to contrast the structure and dynamics of the AnfDGK and NifDK complexes. We were able to achieve 98-100% sequence coverage for AnfDGK (**Supp. Fig. 4.2**) and NifDK (**Supp. Fig. 4.3**) using pepsin digestion. To directly compare the percent deuterium incorporation (%D) over time, a carefully constructed structural-based alignment of the Nif and Anf protein sequences was made. From this, exchange kinetics were used to make heat maps (**Supp. Fig. 4.4** and **Supp. Fig. 4.5**) showing the global %D for the D and K subunits. The % difference after three hours of exchange was then mapped onto the AnfDGK homology model (**Fig. 4.2A**). The protein regions highlighted in red indicate greater deuterium incorporation (deprotection) in the AnfDK subunits and regions highlighted in blue indicate a lower amount of deuterium incorporation (protection). There are several peptides located near the P-cluster and the FeFe-co showing higher amount of deuterium incorporation in the AnfDK subunits. Three peptides on the AnfD subunit showing deprotection near the P-cluster were residues 69-89, 93-122, and 131-161 (**Fig. 4.2B**). Residues 69-89 are located adjacent to the P-cluster, whereas the remaining residues are closer to the surface of AnfD where it is predicted that the Fe protein docks to transfer an electron to the P-cluster. Additional regions showing deprotection were near the FeFe-co and include residues 24-41, 211-224, and 334-359 (**Fig. 4.2C**). The increased exchange in the residues near the FeFe-cofactor is smaller in magnitude than was observed near the P-cluster. The region showing the most protection on the AnfDGK in comparison to NifDK include residues 283-309 of the AnfD subunit (**Fig. 4.2D**) and residues 277-293, 307-322 and 455-462 of the AnfK subunit. The rate of exchange is largely influenced by a protein's structure[56–58] as such this dramatic difference in exchange rate can best be explained by the presence of protein-protein interactions, which stabilizes the secondary structure at the site of interaction causing a decrease in exchange.

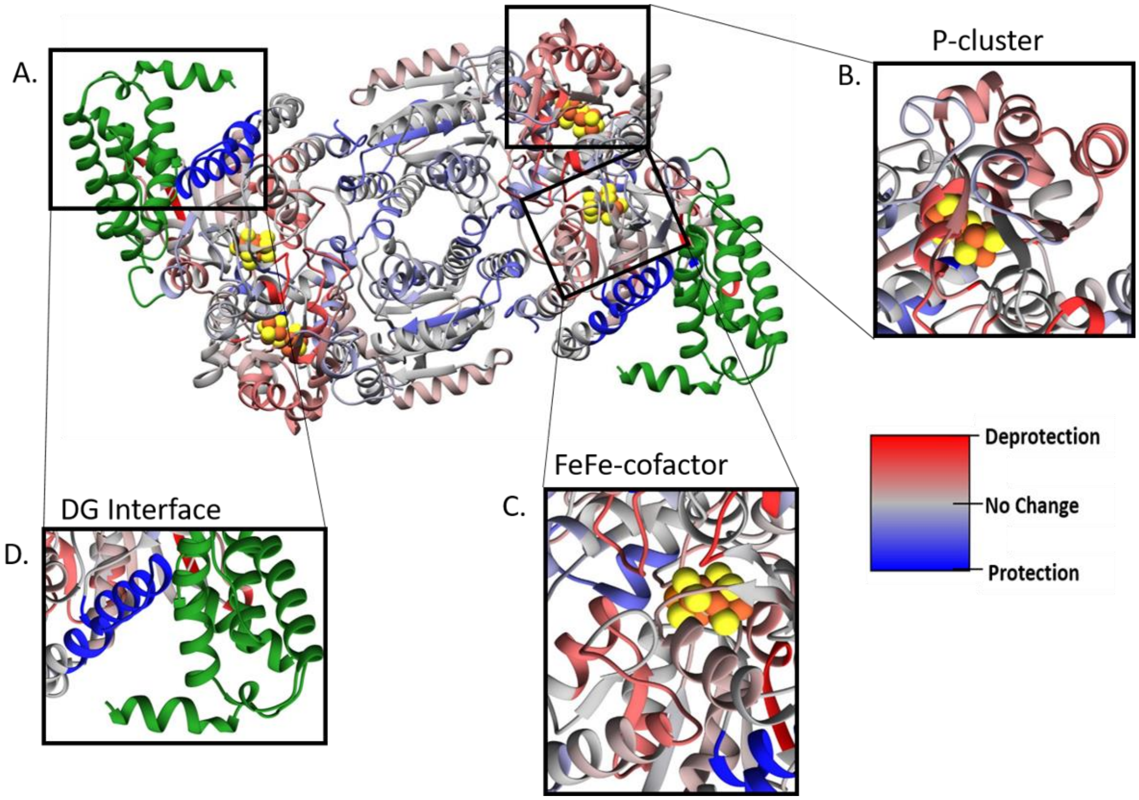

Figure 4.2. Comparison of the AnfDGK and NifDK Protein Dynamics. (A) HD Exchange kinetics for AnfDGK and NifDK were used to measure differences in dynamics. Differences in exchange at three hours at the level of peptides was mapped on to the structural model. The protein regions highlighted in gray indicate areas where no differences between Nif and Anf proteins were detected. The protein regions highlighted in red/blue indicate where deprotection or protection occurred in the Anf protein, indicating indicated the differences in accessibility of the amide hydrogens. (B) Inset shows P-cluster environment, (C) inset shows FeFe-co environment and (D) Inset shows AnfD-G interface.

<u>The AnfG Subunit Binding Site</u> To elucidate the binding site of the G subunit on the AnfDK, we applied XL-MS protocol. Samples of purified AnfDGK complex were reacted with the BS3 cross-linker and then separated using one-dimensional SDS PAGE gel electrophoresis. Bands from the gel between 10-250 kDa (based on molecular weight markers) were excised, digested with trypsin and peptides were identified using liquid chromatography tandem mass spectrometry (LC-MS/MS). The BS3 linker arm is 11.4 Å

in length, but allows for the connection of residues within 24 Å in its fully extended conformation (Euclidean distance measured between alpha carbons of the protein backbone). However, XL-MS studies on proteins of known structure frequently report cross-links between Lys residues that exceed this distance and fall in the range of 26-30 Å. This is explained by the flexibility of the protein backbone in-solution[55]. In our analysis we used a 30 Å cutoff distance and considered only those matching the highest level of confidence based on MS/MS peptide sequence data.

Based on the connectivity map (cross-link density, **Figure 4.3A**) the full-length of the G subunit engages in interactions with AnfD. Seven out of nine Lys residues and seven out of eleven Ser residues were involved in interactions with three distant regions of the D subunit. There are several connections within residues 285-339, connections within the N-terminal region (residues 22-24), and connections with residue 431 (**Figure 4.3B).** This data matches with the HDX-MS results where regions 282-291, 298-309, and 327-333 of AnfD exhibit high amounts of protection relative to the NifD subunit. Localized and extensive cross-linking, along with protection of the AnfD subunit confirms the AnfG biding site.

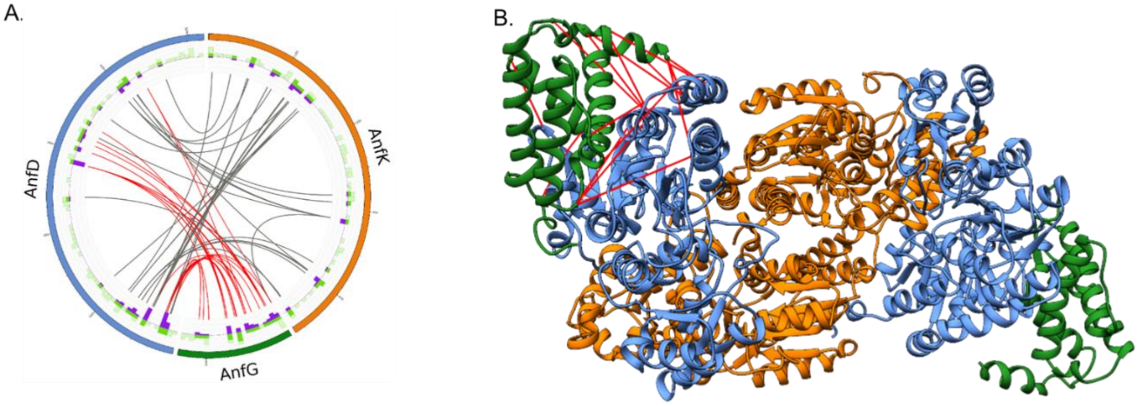

Figure 4.3. Chemical cross-linking of AnfDGK complex. (**A**) Multi-layers circular plot presenting interactions within AnfDGK complex captured by BS3 cross-linker. The most outer layer represents protein sequence: AnfG in dark green, AnfD in blue and AnfK in orange; Green and purple histograms show location of BS3 target residues (Lys, Ser) and density of cross-links, respectively; gray lines represent connections between subunits (inter-subunit cross-links), red lines highlight interactions between AnfD and AnfG subunits. Cross-links maintaining less than 30 Å threshold (measured from Cα to Cα) are displayed. (**B**) Inter-subunit cross-links (red dash line) between the D and G subunits mapped onto the homology model of AnfDGK generated in Phyre^2 based on VnfDGK template (PDB ID: 5N6Y), color-coding the same as on panel A.

To further investigate the binding of AnfG, we turned to the identification of dead-end cross-links. This type of cross-link occurs when a single residue reacts with the cross-linker. In this case, a second residue is not available with which to form an inter-peptide link. In such cases, the BS3 cross-linker serves as a surface labeling reagent. Dead-end cross-links provide valuable information by identifying regions that are not near subunit interfaces. In the AnfG subunit, six Ser residues (Ser2, Ser5, Ser70, Ser72, Ser122, and Ser128) and five Lys residues (Lys11, Lys13, Lys56, Lys57, and Lys111) in AnfG modified by the hydrolyzed BS3 cross-linker. Interestingly, most of these residues are involved in complete, inter-or intra-subunit cross-links with the exception of Ser122, Ser128 and Lys111. Such diversity suggests the presence of dynamic protein regions which may include rigid body movements or more subtle structural rearrangements related to allosteric tuning.

AnfG Subunit Interactions Network NMA provides a way to study protein dynamics across structural modules facilitating and local conformational analysis, including correlative motion of distant residues, such as allosteric movements[59,60].To obtain information about the global dynamics of the AnfDGK complex and identify networks of interactions between subunits, NMA was performed. From this data we calculated off-diagonal elements of the covariance matrix based on eigenvalues and eigenvectors of a large number of modes[61–63]. Since the covariance matrix is normalized, the diagonal is equal to one, and the off-diagonal term represents the motional correlation between the normal mode pairs, referred to as the correlation coefficient (values between -1 and 1)[64]. **Fig. 4.4A** shows the covariance matrix generated from the NMA of backbone atoms displacements for our model of the AnfDGK complex. Although the AnfDGK complex is structurally symmetric, the NMA results indicate that the two halves of the complex are functionally asymmetric. Prominent asymmetric motions in the complex were observed at the AnfG subunit binding site, P-cluster and FeFe-co coordination spheres, AnfH binding site, and the heterotrimer interface (defined here as AnfK$_1$-K$_2$ interactions).

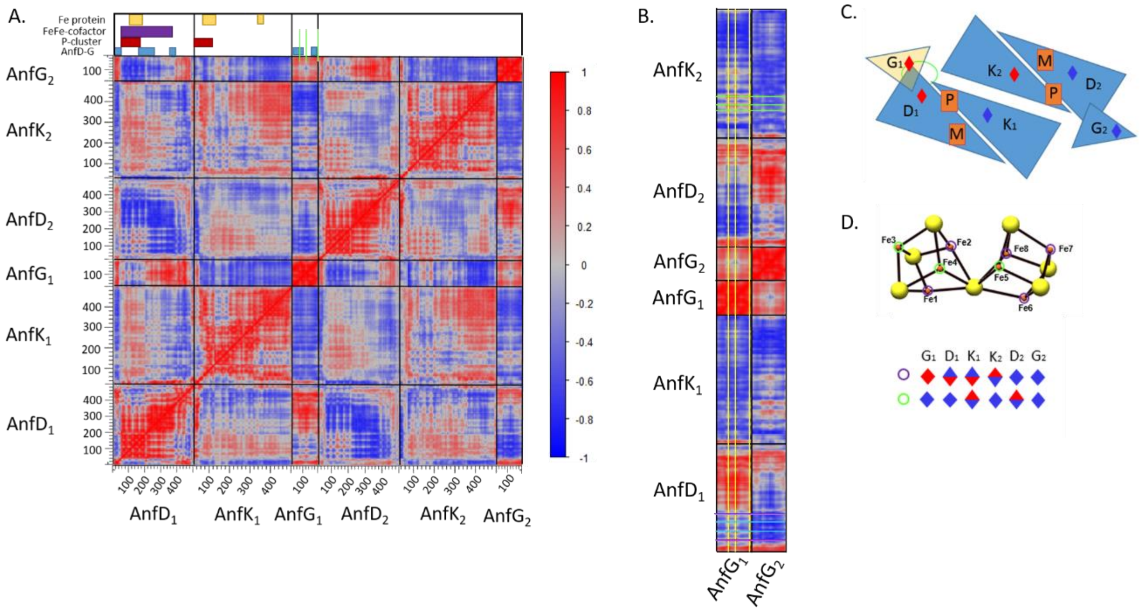

Figure 4.4. Normal mode analysis of the AnfDGK complex. (**A**) Covariance matrix shows the displacement of amino acid residues in Fe-nitrogenase complex. Regions of correlated (in-phase) and anti-correlated (out-of-phase) motions are shown in red and blue, respectively. Axis labels represent approximation of residue numbers at that location. Colored bars at the top represent specific regions of interest within the complex: AnfD-G interactions (blue), P-cluster site (red), FeFe-cofactor (purple), and Fe protein binding site (gold). (**B**) AnfG interaction network. Yellow lines correspond to three main interaction points between AnfG and AnfD. They are positively (movement it the same phase) correlated with the AnfD P-cluster environment (cyan lines), Fe protein binding site (purple lines) and AnfK-K interface (green lines). (**C**) Schematic model highlighting correlations within AnfG interaction network. Red and blue diamonds correspond to regions in- and out-of-phase, respectively. (**D**) The P-cluster interaction network. Green and purple circles distinguish parts of the first coordination sphere showing the same trends of the correlated motions. Red (in-phase) and blue (out-of-phase) triangles correspond only to the differences in the correlated motions between individual subunits. Top/bottom triangle refers to difference in N/C-terminal part of the subunit.

Initial analysis of the covariance matrix led to a more detailed investigation of the AnfG subunit interactions network (**Fig. 4.4B**). The covariance matrix shows that on a global scale most of the residues in AnfG_1 and AnfG_2 experience a similar displacement vector when comparing the G subunits to each other (**Fig. 4.4B**, AnfG_1 vs AnfG_2 or

$AnfG_2$ vs $AnfG_1$ comparison). Examining the displacement of amino acid residues in AnfG that interact with AnfD, and comparing the displacement in the $AnfG_1$ and $AnfG_2$ revealed that the only major differences in displacement were at residues 34-42, 71-86, 117-132 of AnfG, with the most pronounced difference located in the 71-86 region (**Fig. 4.4B, yellow lines**). These regions all showed an out-of-phase correlation, indicating a negative displacement. Since these regions exhibit different correlation patterns in the $AnfG_1$ and $AnfG_2$ subunit, we focused on investigating correlations at points of contact in the entire AnfDGK complex. Further investigation of functionally relevant regions, such as the P-cluster and FeFe-co coordination spheres, and the displacement in relation to the AnfD-G interactions (**Fig. 4.4B, yellow lines**) revealed long distance changes in the AnfDGK complex that originate at the AnfD-G interface. For instance, investigation of residues in the AnfD subunit that coordinate the P-cluster (**Fig. 4.4B, blue lines**) revealed that where these regions intersect with the AnfG docking regions (**Fig. 4.4B, intersection of yellow and blue lines**) high intensity positive displacement is occurring in the $AnfD_1$ vs $AnfG_1$ comparison, whereas negative displacement is occurring in the $AnfD_1$ vs $AnfG_2$ comparison. A similar pattern is also observed in the comparison of the AnfH docking site AnfD (**Fig 4.4B, purple lines**). While AnfG does not interact directly with AnfK, examination of the amino acid displacement of the AnfG residues involved in AnfD-G interactions revealed an unexpected behavior. Residues in AnfK involved in the AnfK-K interface showed a negative amino acid displacement vector at the intersection of AnfG and AnfK when compared to the “homologous” halves ($AnfG_1$ to $AnfK_1$) (**Fig. 4.4B, green lines**). However, when examining the “heterologous” halves ($AnfG_1$ to $AnfK_2$), these regions show a distinct positive displacement, indicating that the AnfK$_2$ residues involved in forming the AnfK-K interface highly correlated with residues of AnfG$_1$ that form the AnfD-G interface (**Fig. 4.4B, intersection of green and yellow lines**). This is an unexpected trend in displacement, because it is expected the AnfDGK trimers interact in a concerted manner. Meaning AnfD$_1$G$_1$K$_1$ are expected to have highly correlated motions. Instead this observation indicates that AnfD$_1$G$_1$K$_2$ are experiencing correlated motions.

Correlation of Interaction Networks in AnfDGK Analysis of the covariance matrix has led to the establishment of multiple interaction networks that vary in size, interconnectivity, and complexity. For example, there is a clear relationship between the AnfG subunit, and the P-cluster, AnfH binding site, and the AnfK-K interface (**Fig. 4.4B**). While this network represents a unique pattern of motions between the AnfDGK halves (**Figure 4.4C**), patterns involving coordination spheres of the P-cluster and FeFe-co patterns are more complex, with multiple, asymmetric motions (**Figure 4.4D**). For instance, the first coordination sphere of the P-cluster is divided into two pattern groups, circled in green and purple in **Figure 4.4D**. Green circles indicate displacement patterns similar to AnfG, but are limited only to the N-terminus of the AnfD and AnfK subunits. These protein regions are spatially adjacent in the complex and form interactions with AnfH. The pattern highlighted with purple circles shows a more complex part of the P-cluster network, where multiple trends can be found in both AnfD and AnfK with inverted trends observed in the AnfG$_1$ and AnfG$_2$ subunits.

AnfDGK Protein Complex Dynamics Longer cross-links (47 - 61 Å) support the notion that the AnfDGK complex is highly dynamic and capable of adopting multiple conformations in solution. This behavior was recently observed in the Mo-dependent nitrogenase[65]. This study concluded that during the pre-steady-state phase of electron delivery, wide spread conformational changes occur to gate electron transfer within each half through a mechanism of negative cooperativity that promotes electron transfer in one half but suppresses it in the other. One of the hallmarks of the cross-links between AnfD and AnfG subunits that exceed the distance constraint is that nearly all are located in loop regions of AnfD with the exception of Lys406, Lys413 and Lys414 of AnfD which are part of the same (**Fig. 4.5A**). This contrasts with the AnfG subunit, where BS3 bridged residues are in long helical regions with the exception of Ser70, Ser97, and Lys130 of AnfG which are located in loop regions. These cross-linking results highlights the AnfD-G interface in AnfG (Lys130 and Ser70), the P-cluster binding site in AnfD (Ser43, Ser45, Lys55), the binding site of the FeFe-co in AnfD (Ser45, Lys87, Lys55, Ser260, Lys329, Lys406), and the predicted AnfH binding site in AnfD (Lys113 and Lys116). The presence of the longer cross-links indicate that there is more freedom in the binding of the G subunit than the crystal structure of the VnfDGK complex would suggest [21].

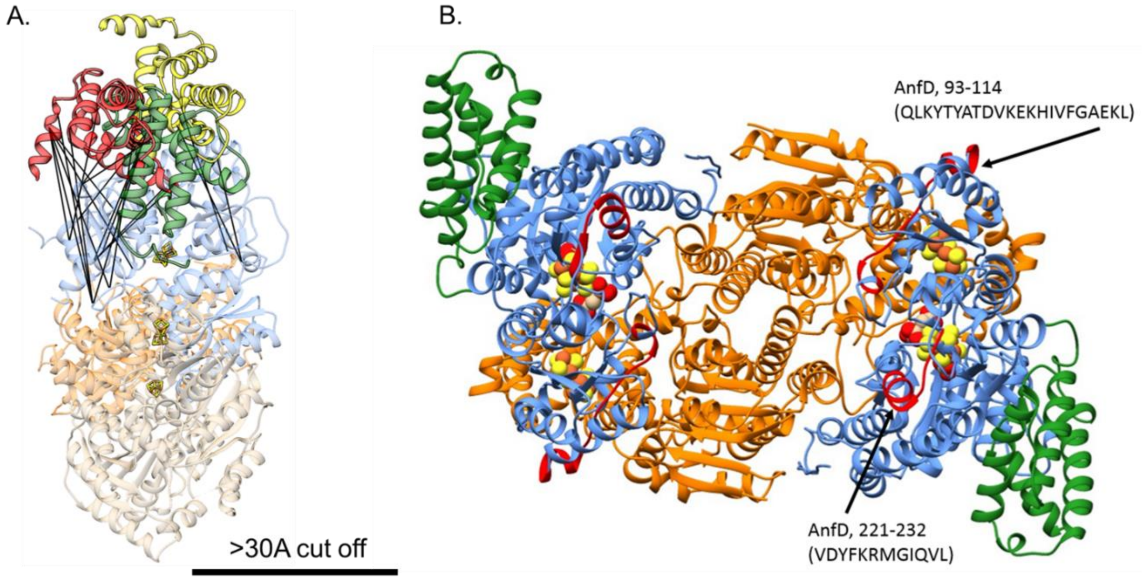

Figure 4.5. Presence of bimodal peptides and long distance cross-links is consistent with the FeFe protein multiple conformations in solution. (**A**) Long distance cross-links between AnfD and AnfG are located mostly in the loop regions and a short helix on AnfD. By rotating the position of AnfG into two alternative positions, as could occur during the Fe protein cycle, all distance constraints can be met. This suggests that the crystal structure of the VFe protein caught only one conformation within the ensemble of FeFe protein. AnfG subunits in red and yellow project alternate docking orientations on AnfD subunit. (**B**) Peptides with bimodal behavior (in red) were found on AnfD and AnfK subunits near P-cluster and FeFe-cofactor.

Bimodal Peptides Reveal Asymmetry in Protein Dynamics A deeper examination of the HDX-MS data revealed that specific regions of the complex had exchange kinetics consistent with bimodal deuterium incorporation rates. The isotope distributions of peptides from the AnfDGK complex exhibited deuterated distributions with a greater with than was expected. Bimodal distribution manifests as two separate isotope distributions for a single peptide, which typically overlap causing a widening of the deuterated isotope distribution[66,67]. In the case of the AnfD subunit, two peptides had bimodal deuterium incorporation, 93-114 and 221-232 (**Fig. 4.5B**). Residues 93-114 of the AnfD subunit interacts with the "homologous" AnfK subunit, and is also in close proximity to the P-cluster and FeFe-co. Additionally, this peptide also interacts with the N-terminus of the heterologous AnfK subunit. Examining the covariance matrix for this region (**Fig. 4.4A**) reveals a largely positive correlation with the homologous half ($AnfD_1G_1K_1$), and a negative correlation with the $AnfD_2G_2$ subunits, however the $AnfK_2$ subunit shows a positive correlation. The other bimodal peptide, residues 221-232 of the AnfD subunit, forms part of the surface of the AnfD subunit, and while it does not interact with it directly, adjacent residues also interact with the heterologous AnfK subunit, similar to residues 93-114 of the AnfD subunit. Examining this region in the covariance matrix shows a similar patter to residues 93-114. Amino acid displacement of this peptide is positively correlated with the rest of the $AnfD_1$ subunit and with the $AnfG_1$ subunit. While there is some positive correlation with $AnfK_1$, there is a much more intense pattern of positive correlation in the $AnfK_2$ subunit (**Fig. 4.4A**). The presence of the bimodal peptides, and the correlation of the residues involved with the rest of the complex provides further evidence that there is an asymmetric communication pathway in the AnfDGK complex.

Conclusions

According to numerous studies the efficiency of reducing N_2 compared to other electron acceptors such as H_2 is different for each of the nitrogenase classes[8,18,19,25–27]. One of the main differences between the catalytic components of the Mo-dependent nitrogenase and the V-/Fe-dependent nitrogenase is the presence of the G subunit. The crystal structure of the VnfDGK complex has established that VnfG binds to the VnfD subunit[21]. Additionally it has been previously determined that the G subunit is important for catalytic activity[15,24]. Our XL-MS and HDX-MS experiments confirmed that the AnfG subunit binds in an analogous position to the VnfG subunit of the VnfDGK complex (**Fig. 4.2** and **Fig. 4.3**). Additionally, insights on the nature of the AnfG interaction emerged. First, we identified a significant number of high confidence cross-links longer than 30 Å when using the BS3 cross-linking reagent (**Fig. 4.5A**). When examining these cross-links on the homology model of the AnfDGK complex we observed that the cross-linked regions were either part of long loops or short helices, elements of the secondary structure often involved in protein-protein interactions. Second, detailed examination of the deuterium incorporation in the AnfDGK and NifDK revealed the presence of bimodal pepitides in the AnfDGK complex, indicating that these regions are adopting two different conformations simultaneously during the course of the exchange reaction (**Fig. 4.5B**). The presence of extra-long cross-links and peptides with bimodal exchange behavior suggest that the AnfDGK complex is a highly dynamic complex, adopting multiple conformations simultaneously. This highly dynamic behavior can also be interpreted to mean that the AnfDGK complex adopts an asymmetric conformation, where each AnfDGK trimer is in a different conformation. This behavior has been observed in the NifDK complex of the Mo-dependent nitrogenase, and has been implicated in allosteric regulation of electron transfer through negative cooperativity[68,69]. This behavior was first identified in NifDK pre-steady-state kinetic measurements and was further confirmed using NMA of the NifDK complex. Following the line of reasoning of this previous study, we also employed NMA of the AnfDGK homology model. This revealed that at several regions of the AnfDGK complex, such as the P-cluster binding site, AnfH binding site, AnfD-G interface, and the AnfK-K interface there is a distinct asymmetric displacement correlation pattern. However this was not the asymmetrical behavior that was expected where the $AnfD_1G_1K_1$ trimer is adopting a similar conformation, and the $AnfD_2G_2K_2$ trimer is adopting another. Instead the behavior we observed indicated that $AnfD_1G_1K_2$ subunits are adopting a similar conformation, as seen by the positive correlation at the functionally relevant regions (**Fig. 4.4B**).

To fully understand the unique dynamics observed in the AnfDGK complex, we developed an ensemble allosteric model (EAM). The framework of the EAM is unique in that it views allostery in terms of ensembles that are dictated by the intrinsic stabilities of conformations for each cooperative substructure (i.e., domain) in the protein and the interactions between domains[70]. The EAM can also be used to investigate the effects of a thermodynamic architecture of a protein, which describes how energy changes in one part of a protein are manifested at distal sites. This describes the propogation of a signal that is initiated by the binding of a ligand which effects the thermodynamic landscape and how the conformational equilibria in the different regions of the protein are poised prior to ligand binding[71,72]. Investigation of crystal structures of the NifDK and VnfDGK complexes, as well as our homology model of the AnfDGK complex reveal very little structural differences. This does not exclude an allosteric mechanism in the nitrognease systems, instead it indicates that the process is regulated by thermodynamics, rather than protein dynamics. This suggests that conformational changes result in subtle protein movements rather than large scale rigid body movements. This domain tunability can be modulated by many factors such as mutations, covalent modification, protons and cofactors and change in pH. This important feature of an EAM is that the energy landscape can be poised to respond in a "functionally pluripotent manner"[73,74]. Our *in silico* and in solution experiments strongly suggest that dynamic energy landscape defines catalytic activity of Fe-dependent nitrogenase.

References Cited

1. Burgess, B. K. & Lowe, D. J. Mechanism of Molybdenum Nitrogenase. *Chem. Rev.* **96,** 2983–3012 (1996).

2. Smil, V. *Enriching the earth : Fritz Haber, Carl Bosch, and the transformation of world food production*. (MIT Press, 2001).

3. Haber, F. Über die Darstellung des Ammoniaks aus Stickstoff und Wasserstoff. *Naturwissenschaften* **10,** 1041–1049 (1922).

4. Haber, F. Bemerkung zu vorstehender Notiz. *Naturwissenschaften* **11,** 339–340 (1923).

5. Raymond, J., Siefert, J. L., Staples, C. R. & Blankenship, R. E. The Natural History of Nitrogen Fixation. *Mol. Biol. Evol.* **21,** 541–554 (2004).

6. Burris, R. H. & Roberts, G. P. Biological Nitrogen Fixation. *Annu. Rev. Nutr.* **13,** 317–335 (1993).

7. Gruber, N. & Galloway, J. N. An Earth-system perspective of the global nitrogen cycle. *Nature* **451,** 293–296 (2008).

8. Eady, R. R. Structure-function relationships of alternative nitrogenases. *Chem. Rev.* **96,** 3013–3030 (1996).

9. Hu, Y., Lee, C. C. & Ribbe, M. W. Vanadium nitrogenase: A two-hit wonder? *Dalt. Trans.* **41,** 1118–1127 (2012).

10. Yang, Z. Y. *et al.* Evidence That the Pi Release Event Is the Rate-Limiting Step in the Nitrogenase Catalytic Cycle. *Biochemistry* **55,** 3625–3635 (2016).

11. Seefeldt, L. C., Hoffman, B. M. & Dean, D. R. Electron transfer in nitrogenase catalysis. *Curr. Opin. Chem. Biol.* **16,** 19–25 (2012).

12. Hageman, R. V & Burris, R. H. Nitrogenase and nitrogenase reductase associate and dissociate with each catalytic cycle. *Proc. Natl. Acad. Sci. U. S. A.* **75,** 2699–702 (1978).

13. Seefeldt, L. C., Hoffman, B. M. & Dean, D. R. Mechanism of Mo-dependent nitrogenase. *Annu. Rev. Biochem.* **78,** 701–722 (2009).

14. Hoffman, B. M., Lukoyanov, D., Yang, Z. Y., Dean, D. R. & Seefeldt, L. C. Mechanism of nitrogen fixation by nitrogenase: The next stage. *Chemical Reviews* **114,** 4041–4062 (2014).

15. Schneider, K. & Müller, A. Iron-Only Nitrogenase: Exceptional Catalytic, Structural and Spectroscopic Features. in *Catalysts for Nitrogen Fixation* 281–307 (Springer Netherlands, 2004). doi:10.1007/978-1-4020-3611-8_11

16. Chisnell, J. R., Premakumar, R. & Bishop, P. E. Purification of a second alternative nitrogenase from a nifHDK deletion strain of Azotobacter vinelandii. *J. Bacteriol.* **170,** 27–33 (1988).

17. Luque, F. & Pau, R. N. Transcriptional regulation by metals of structural genes for Azotobacter vinelandii nitrogenases. *Mol. Gen. Genet.* **227,** 481–7 (1991).

18. Harris, D. F. *et al.* Mechanism of N_2 Reduction Catalyzed by Fe-Nitrogenase Involves Reductive Elimination of H_2. *Biochemistry* **57,** 701–710 (2018).

19. Schneider, K., Gollan, U., Dröttboom, M., Selsemeier-Voigt, S. & Müller, A. Comparative biochemical characterization of the iron-only nitrogenase and the molybdenum nitrogenase from Rhodobacter capsulatus. *Eur. J. Biochem.* **244,** 789–800 (1997).

20. Siemann, S., Schneider, K., Dröttboom, M. & Müller, A. The Fe-only nitrogenase and the Mo nitrogenase from Rhodobacter capsulatus: a comparative study on the redox properties of the metal clusters present in the dinitrogenase components. *Eur. J. Biochem.* **269,** 1650–1661 (2002).

21. Sippel, D. & Einsle, O. The structure of vanadium nitrogenase reveals an unusual bridging ligand. *Nat. Chem. Biol.* **13,** 956–960 (2017).

22. Joerger, R. D., Jacobson, M. R., Premakumar, R., Wolfinger, E. D. & Bishop, P. E. Nucleotide sequence and mutational analysis of the structural genes (anfHDGK) for the second alternative nitrogenase from Azotobacter vinelandii. *J. Bacteriol.* **171,** 1075–1086 (1989).

23. Schüddekopf, K., Hennecke, S., Liese, U., Kutsche, M. & Klipp, W. Characterization of anf genes specific for the alternative nitrogenase and identification of nif genes required for both nitrogenases in Rhodobacter capsulatus. *Mol. Microbiol.* **8,** 673–684 (1993).

24. Waugh, S. I. *et al.* The genes encoding the delta subunits of dinitrogenases 2 and 3 are required for Mo-independent diazotrophic growth by Azotobacter vinelandii. *J. Bacteriol.* **177,** 1505–1510 (1995).

25. Hales, B. J., Case, E. E., Morningstar, J. E., Dzeda, M. F. & Mauterer, L. A. Isolation of a New Vanadium-Containing Nitrogenase from Azotobacter vinelandii. *Biochemistry* **25,** 7251–7255 (1986).

26. Dilworth, M. J., Eldridge, M. E. & Eady, R. R. The molybdenum and vanadium nitrogenases of Azotobacter chroococcum: effect of elevated temperature on N2 reduction. *Biochem. J.* **289 (Pt 2,** 395–400 (1993).

27. Eady, R. R., Robson, R. L., Richardson, T. H., Miller, R. W. & Hawkins, M. The vanadium nitrogenase of Azotobacter chroococcum. Purification and properties of the VFe protein. *Biochem. J.* **244,** 197–207 (1987).

28. Hales, B. J. Alternative nitrogenase. *Adv. Inorg. Biochem.* **8,** 165–198 (1990).

29. Chan, M. K., Kim, J. & Rees, D. C. The nitrogenase FeMo-cofactor and P-cluster pair: 2.2 A resolution structures. *Science* **260,** 792–794 (1993).

30. Kim, J. & Rees, D. C. Structural models for the metal centers in the nitrogenase molybdenum-iron protein. *Science* **257,** 1677–1682 (1992).

31. Rees, D. C. & Howard, J. B. Structural bioenergetics and energy transduction mechanisms. *J. Mol. Biol.* **293,** 343–350 (1999).

32. Georgiadis, M. M. *et al.* Crystallographic structure of the nitrogenase iron protein from Azotobacter vinelandii. *Science* **257,** 1653–1659 (1992).

33. Toukdarian, A. & Kennedy, C. Regulation of nitrogen metabolism in Azotobacter vinelandii: isolation of ntr and glnA genes and construction of ntr mutants. *EMBO J.* **5,** 399–407 (1986).

34. Christiansen, J., Goodwin, P. J., Lanzilotta, W. N., Lance C. Seefeldt, A. & Dennis R. Dean. Catalytic and Biophysical Properties of a Nitrogenase Apo-MoFe Protein Produced by a nifB-Deletion Mutant of Azotobacter vinelandii†. *Biochemistry* **37,** 12611–12623 (1998).

35. Burgess, B. K., Jacobs, D. B. & Stiefel, E. I. Large-scale purification of high activity Azotobacter vinelandii nitrogenase. *Biochim. Biophys. Acta - Enzymol.* **614,** 196–209 (1980).

36. Peters, J. W., Fisher, K. & Dean, D. R. Identification of a nitrogenase protein-protein interaction site defined by residues 59 through 67 within the Azotobacter vinelandii Fe protein. *J. Biol. Chem.* **269,** 28076–28083 (1994).

37. Yang, Z. Y. *et al.* Evidence That the Pi Release Event Is the Rate-Limiting Step in the Nitrogenase Catalytic Cycle. *Biochemistry* **55,** 3625–3635 (2016).

38. Vaudel, M. *et al.* PeptideShaker enables reanalysis of MS-derived proteomics data sets: To the editor. *Nat. Biotechnol.* **33,** 22–24 (2015).

39. Kelley, L. A., Mezulis, S., Yates, C. M., Wass, M. N. & Sternberg, M. J. E. The Phyre2 web portal for protein modeling, prediction and analysis. *Nat. Protoc.* **10,** 845–858 (2015).

40. Pettersen, E. F. *et al.* UCSF Chimera - A visualization system for exploratory research and analysis. *J. Comput. Chem.* **25,** 1605–1612 (2004).

41. Ledbetter, R. N. *et al.* The Electron Bifurcating FixABCX Protein Complex from Azotobacter vinelandii: Generation of Low-Potential Reducing Equivalents for Nitrogenase Catalysis. *Biochemistry* **56,** 4177–4190 (2017).

42. Lima, D. B. *et al.* SIM-XL: A powerful and user-friendly tool for peptide cross-linking analysis. *J. Proteomics* **129,** 51–55 (2014).

43. Kosinski, J. *et al.* Xlink analyzer: Software for analysis and visualization of cross-linking data in the context of three-dimensional structures. *J. Struct. Biol.* **189,** 177–183 (2015).

44. Wang, J., Shi, Y. & Chait, B. T. CX-Circos: a Web-based Tool for Visualization and Analysis of Chemical Cross-linking Data. in *Proceedings of the 64th ASMS Conference on Mass Spectrometry and Allied Topics* (2016).

45. Berry, L. *et al.* H/D exchange mass spectrometry and statistical coupling analysis reveal a role for allostery in a ferredoxin-dependent bifurcating transhydrogenase catalytic cycle. *Biochim. Biophys. Acta - Gen. Subj.* **1862,** (2018).

46. Berry, L., Patterson, A., Pence, N., Peters, J. W. & Bothner, B. Hydrogen Deuterium Exchange Mass Spectrometry of Oxygen Sensitive Proteins. *Bioprotocols* **8,** 1–16 (2018).

47. Berry, L. *et al.* H/D exchange mass spectrometry and statistical coupling analysis reveal a role for allostery in a ferredoxin-dependent bifurcating transhydrogenase catalytic cycle. *Biochim. Biophys. Acta - Gen. Subj.* **1862,** 9–17 (2018).

48. Pascal, B. D., Chalmers, M. J., Busby, S. A. & Griffin, P. R. HD Desktop: An Integrated Platform for the Analysis and Visualization of H/D Exchange Data. *J. Am. Soc. Mass Spectrom.* (2009). doi:10.1016/j.jasms.2008.11.019

49. Smith, D., Danyal, K., Raugei, S. & Seefeldt, L. C. Substrate channel in nitrogenase revealed by a molecular dynamics approach. *Biochemistry* **53,** 2278–2285 (2014).

50. Tirion, M. M. Large amplitude elastic motions in proteins from a single-parameter, atomic analysis. *Phys. Rev. Lett.* **77,** 1905–1908 (1996).

51. Atilgan, A. R. *et al.* Anisotropy of fluctuation dynamics of proteins with an elastic network model. *Biophys. J.* **80,** 505–515 (2001).

52. R Development Core Team. R Development Core Team, 2017. (2017).

53. Wei, T. & Simko, V. R package ‘corrplot’: Visualization of a Correlation Matrix (Version 0.84). (2017).

54. Kelly, L. A., Mezulis, S., Yates, C., Wass, M. & Sternberg, M. The Phyre2 web portal for protein modelling, prediction, and analysis. *Nat. Protoc.* **10,** 845–858 (2015).

55. Merkley, E. D. *et al.* Distance restraints from crosslinking mass spectrometry: Mining a molecular dynamics simulation database to evaluate lysine-lysine distances. *Protein Sci.* **23,** 747–759 (2014).

56. Konermann, L., Pan, J. & Liu, Y. H. Hydrogen exchange mass spectrometry for studying protein structure and dynamics. *Chem. Soc. Rev.* **40,** 1224–1234 (2011).

57. Engen, J. R. *et al.* Partial cooperative unfolding in proteins as observed by hydrogen exchange mass spectrometry. *International Reviews in Physical Chemistry* **32,** 96–127 (2013).

58. Engen, J. R. Analysis of protein conformation and dynamics by

hydrogen/deuterium exchange MS. *Anal. Chem.* **81,** 7870–7875 (2009).

59. Wako, H. & Endo, S. Normal mode analysis as a method to derive protein dynamics information from the Protein Data Bank. *Biophys. Rev.* **9,** 877–893 (2017).

60. Na, H., ben-Avraham, D. & Tirion, M. M. Slow Normal Modes of Proteins are Accurately Reproduced across Different Platforms. 1–31 (2018).

61. Brooks III, C. L., Karplus, M. B. & Pettitt, M. *Proteins: A Theoretical Perspective of Dynamics, Structure, and Thermodynamics*. (J. Wiley, 1988).

62. Hayward, S. *Normal mode analysis of biological molecules*. (M. Dekker,Inc, 2001).

63. Mizuguchi, K., Kidera, A. & Gō, N. Collective motions in proteins investigated by X-ray diffuse scattering. *Proteins Struct. Funct. Genet.* **18,** 34–48 (1994).

64. Van Wynsberghe, A. W. & Cui, Q. Interpreting Correlated Motions Using Normal Mode Analysis. *Structure* **14,** 1647–1653 (2006).

65. Danyal, K. *et al.* Negative cooperativity in the nitrogenase Fe protein electron delivery cycle. *Proc. Natl. Acad. Sci.* **113,** E5783–E5791 (2016).

66. Weis, D. D., Wales, T. E., Engen, J. R., Hotchko, M. & Ten Eyck, L. F. Identification and Characterization of EX1 Kinetics in H/D Exchange Mass Spectrometry by Peak Width Analysis. *J. Am. Soc. Mass Spectrom.* (2006). doi:10.1016/j.jasms.2006.05.014

67. Guttman, M., Weis, D. D., Engen, J. R. & Lee, K. K. Analysis of overlapped and noisy hydrogen/deuterium exchange mass spectra. *J. Am. Soc. Mass Spectrom.* (2013). doi:10.1007/s13361-013-0727-5

68. Danyal, K. *et al.* Negative cooperativity in the nitrogenase Fe protein electron delivery cycle. *Proc. Natl. Acad. Sci.* **113,** E5783–E5791 (2016).

69. Maritano, S., Fairhurst, S. A. & Eady, R. R. Long-range interactions between the Fe protein binding sites of the MoFe protein of nitrogenase. *J. Biol. Inorg. Chem.* **6,** 590–600 (2001).

70. Wyman, J. *On allosteric models in Current topics in cellular regulation. Volume 6*. (Elsevier, 1972).

71. Goodey, N. M. & Benkovic, S. J. Allosteric regulation and catalysis emerge via a

common route. *Nat. Chem. Biol.* **4,** 474–482 (2008).

72. Cui, Q. & Karplus, M. Allostery and Cooperativity revisited. *Protein Sci.* **17,** 1295–1307 (2008).

73. Motlagh, H. N. & Hilser, V. J. Agonism/antagonism switching in allosteric ensembles. *Proc. Natl. Acad. Sci. U. S. A.* **109,** 4134–4139 (2012).

74. Hilser, V. J. & Thompson, E. B. Intrinsic disorder as a mechanism to optimize allosteric coupling in proteins. *Proc. Natl. Acad. Sci. U. S. A.* **104,** 8311–8315 (2007).

Supplementary Material B

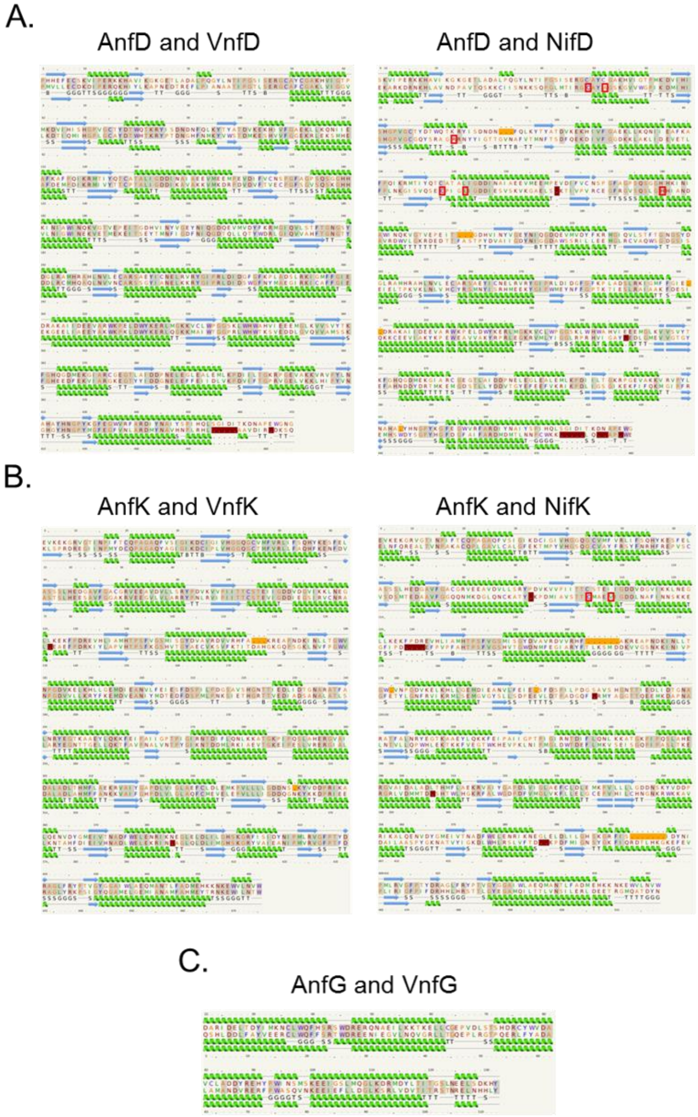

Supplementary Figure 4.1. Structure-based sequence alignments of nitrogenase subunits. AnfDGK protein subunits were aligned with homologous nitrogenase subunits from the MoFe and VFe protein using Phyre^2. (**A**) Alignment of the D subunits (**B**) Alignment of the K subunits (**C**) Alignment of the G subunit. Each alignment includes the following information (from top to bottom): Anf sequence amino acid position, predicted secondary structure of Anf, Anf sequence, template sequence (Nif or Vnf), template known secondary structure, template predicted secondary structure, template sequence amino acid position. Red and orange blocks within the sequence indicate an insertion or deletion of the sequence relative to the template sequence (Nif or Vnf). Red boxes indicate catalytic residues identified from the Catalytic Site Atlas. G, 3-turn helix; I, 5-turn helix; T, hydrogen bonded turn; B, residue in isolated beta-bridge; S, bend.

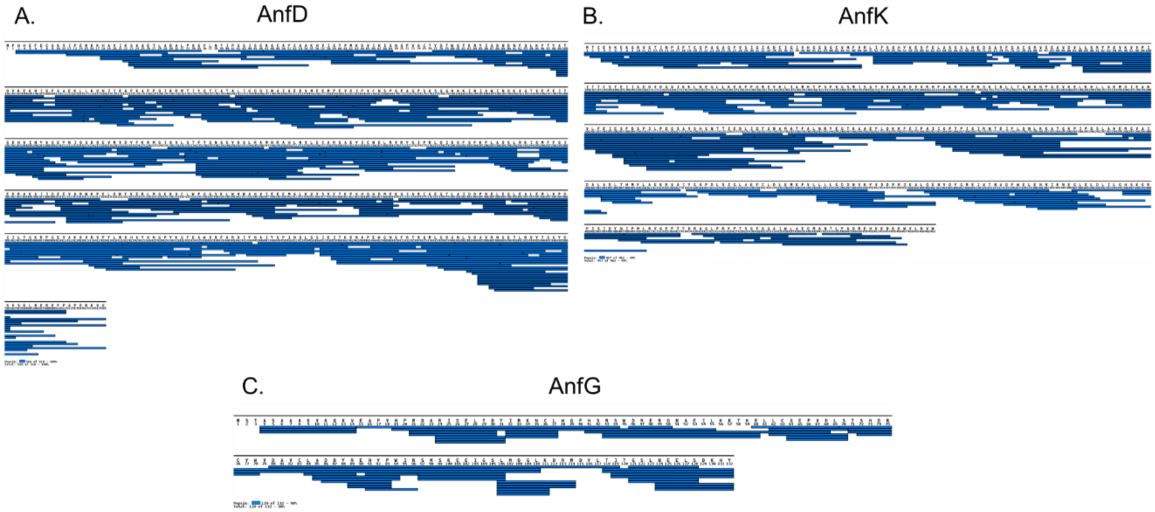

Supplementary Figure 4.2. AnfDGK pepsin digestion coverage map. Each bar (in blue) represent single peptic peptide identified in LC-MS/MS protocol. The maximized sequence coverage allows for reaching near single amide resolution and obtaining comprehensive structural information.

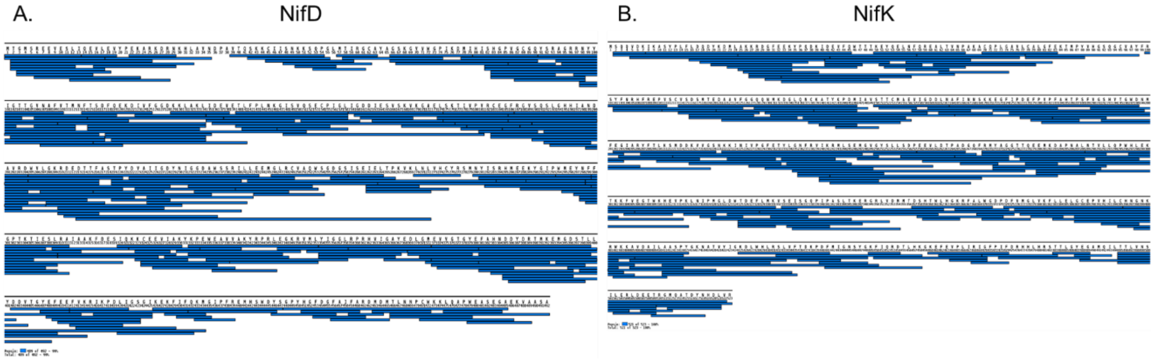

Supplementary Figure 4.3. NifDK pepsin digestion coverage map. Each bar (in blue) represent single peptic peptide identified in LC-MS/MS protocol. The maximized sequence coverage allows for reaching near single amide resolution and obtaining comprehensive structural information.

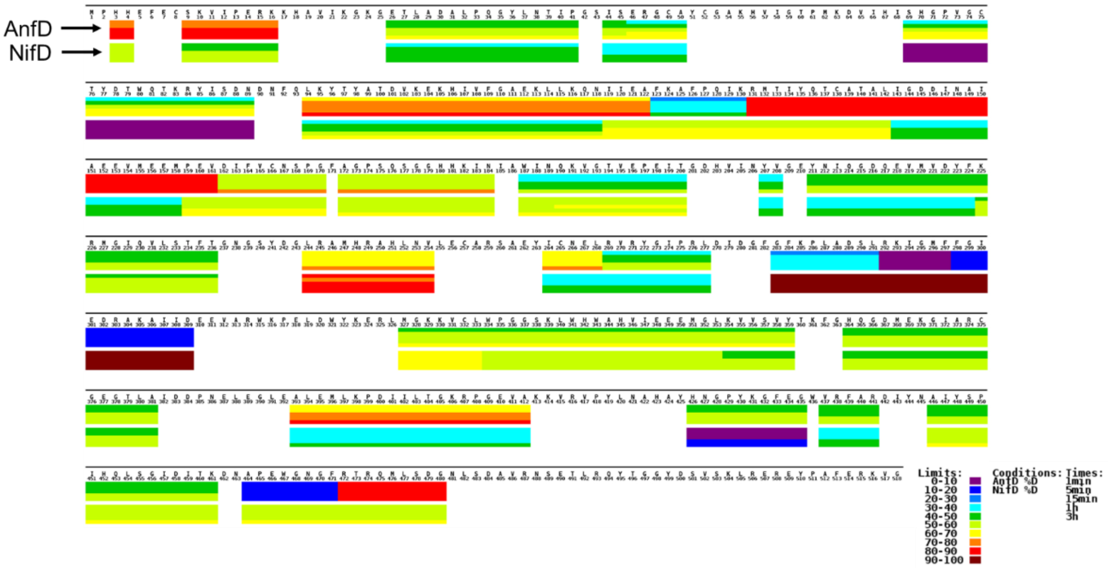

Supplementary Figure 4.4. AnfD and NifD subunits heat maps. Side by side comparison of the percent of deuterium (%D) incorporation into the AnfD (top) and NifD (bottom) protein structure over 1 min, 5 min, 15 min, 1 hr, and 3 hrs time course. To generate the heat maps the AnfD and NifD protein sequences were aligned and the AnfD protein sequence was used as the template. The gradient of the heat maps goes from purple (0-10 %D) to dark red (90-100 %D).

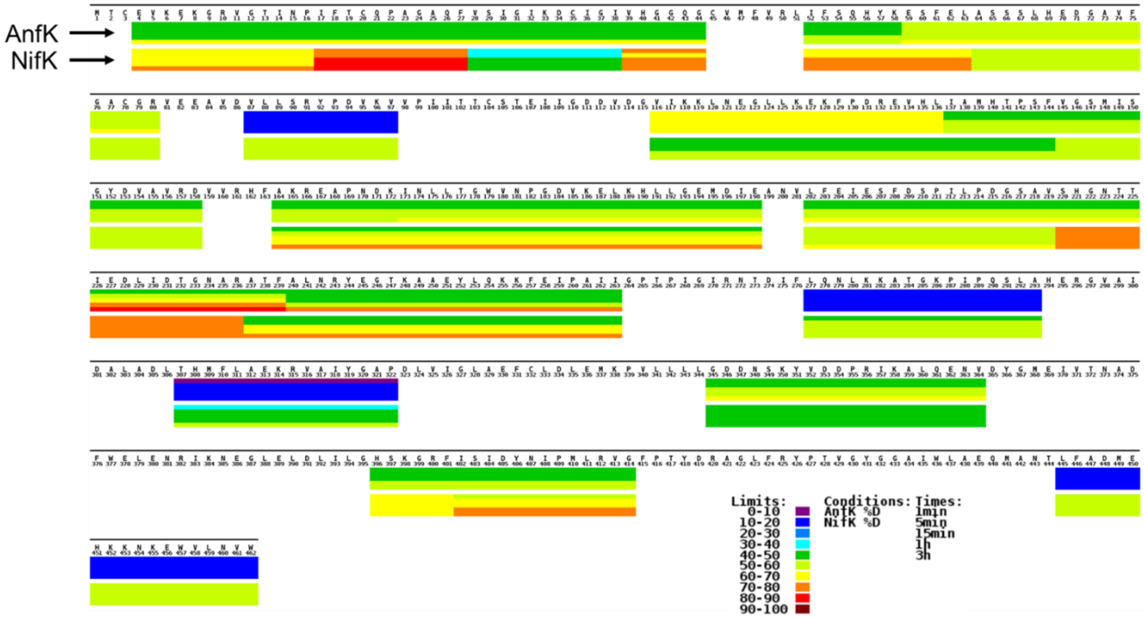

Supplementary Figure 4.5. AnfK and NifK subunits heat maps. Side by side comparison of the percent of deuterium (%D) incorporation into the AnfK (top) and NifK (bottom) protein structure over 1 min, 5 min, 15 min, 1 hr, and 3 hrs time course. To generate the heat maps the AnfK and NifK protein sequences were aligned and the AnfK protein sequence was used as the template. The gradient of the heat maps goes from purple (0-10 %D) to dark red (90-100 %D).

CHAPTER FIVE

IRON PROTEIN DOCKING EFFECTS ON MOFE PROTEIN DYNAMICS: FUNCTION OF NEGATIVE COOPERATIVITY AND THE REGULATION OF ELECTRON TRASFER

Contributions of Authors and Co-Authors

Manuscript in Chapter 5

Author: Luke Berry

Contributions: Planned and performed the HDX experiment. Operated mass spectrometer for data acquisition. Analyzed HDX-MS data Organized and wrote manuscript

Co-Author: Hayden Kallas

Contributions: Planned and performed the HDX experiment. Expressed and purified protein samples. Operated the quench flow apparatus. Reviewed manuscript during development.

Co-Author: Derek F. Harris

Contributions: Expressed and purified protein samples. Reviewed manuscript during development.

Co-Author: Monika Tokmina-Lukaszewska

Contributions: Reviewed manuscript during development.

Co-Author: Simone Raugei

Contributions: Performed normal mode analysis calculations. Reviewed manuscript during development.

Co-Author: Lance C. Seefeldt

Contributions: Supervised the quench flow experiment and protein purification protocols. Reviewed manuscript during development.

Co-Author: Brian Bothner

Contributions: Supervised the hydrogen deuterium exchange experiment and mass spectrometry operation. Reviewed manuscript during development.

Manuscript Information

IRON PROTEIN DOCKING EFFECTS ON MOFE PROTEIN DYNAMICS: FUNCTION OF NEGATIVE COOPERATIVITY AND THE REGULATION OF ELECTRON TRASFER

Authors: Luke Berry, Hayden Kallas, Derek F. Harris, Monika Tokmina-Lukaszewska, Simone Raugei, Lance C. Seefeldt, and Brian Bothner

Journal: To be determined

Status of Manuscript:
_x_ Prepared for submission to a peer-reviewed journal
___ Officially submitted to a peer-reviewed journal
___ Accepted by a peer-reviewed journal
___ Published in a peer-reviewed journal

CHAPTER FIVE

IRON PROTEIN DOCKING EFFECTS ON MOFE PROTEIN DYNAMICS: FUNCTION OF NEGATIVE COOPERATIVITY AND THE REGULATION OF ELECTRON TRASFER

Abstract

The reduction of atmospheric nitrogen (N_2) to ammonia (NH_3) is facilitated by the nitrogenase systems. Of the three classes of nitrogenases, the Mo-dependent system is the most studied. The Mo-dependent nitrogenase uses two protein complexes to reduce N_2, the MoFe protein (MoFeP) and the Fe protein (FeP). The FeP transiently associates with each αβ dimer of the MoFeP and undergoes the process known as the FeP cycle to transfer electrons to the active site of the MoFeP, the FeMo-cofactor. The MoFeP contains two αβ dimers, which are both active and participate in the FeP cycle. It was previously thought that the αβ dimers acted independently, however recent kinetic measurements during the presteady state phase of electron transfer suggests that the αβ dimers do not undergo the FeP cycle independently. Instead, the docking of FeP at one αβ dimer partially suppresses the FeP cycle in the other. This reveals a mechanism of negative cooperativity in the Mo-dependent nitrogenase, however the exact function of the allosteric mechanism remains unknown. Quench flow H/D exchange coupled to mass spectrometry (QF-HDX-MS) is a technique that can measure how much deuterium a protein incorporates on the millisecond time scale. Using this technique on the MoFeP complex in the presence and absence of FeP biophysical evidence for negative cooperativity can be obtained. In this study QF-HDX-MS is used to detail the effects asymmetric FeP docking has on the MoFeP, and how these changes relate to the function and pathway of an allosteric signal between the two αβ dimers of MoFeP.

Introduction

The biological reduction of nitrogen gas (N_2) to ammonia (NH_3) is facilitated by the nitrogenase systems. There are three classes of nitrogenase: the Mo-dependent, V-dependent, and Fe-dependent, each characterized by the unique transition metal found in the active site of the catalytic component[1–3]. Of the three nitrogenases, the most studied is the Mo-dependent nitrogenase system which is composed of the MoFe protein (MoFeP) and Fe protein (FeP) [1,3–6]. The MoFeP is a tetramer containing two alpha and two beta subunits that form symmetric αβ dimers. Each dimer contains an [8Fe-7S] cluster, called the P-cluster, and an FeMo-cofactor (FeMo-co; [7Fe-(S-Mo-C-*R*-homocitrate])[1,3–6]. The P-cluster is located at the interface of the alpha and beta subunits, while FeMo-co is located within the alpha subunit[4,7]. The FeP is a homodimer containing two ATP/ADP-binding sites (one in each subunit), and a single [4Fe-4S] cluster that bridges the subunits[8,9]. Nitrogen catalysis is initiated by an ATP-bound, one electron reduced FeP interacting with an αβ dimer of the MoFeP, near the P-cluster[10]. FeP binding triggers a sequence of events known as the “FeP cycle” and culminates with the transfer of an electron to the FeMo-co and the hydrolysis of the ATP molecules bound to FeP[3,11–15]. A schematic of the FeP cycle is shown in **Fig 5.1**.

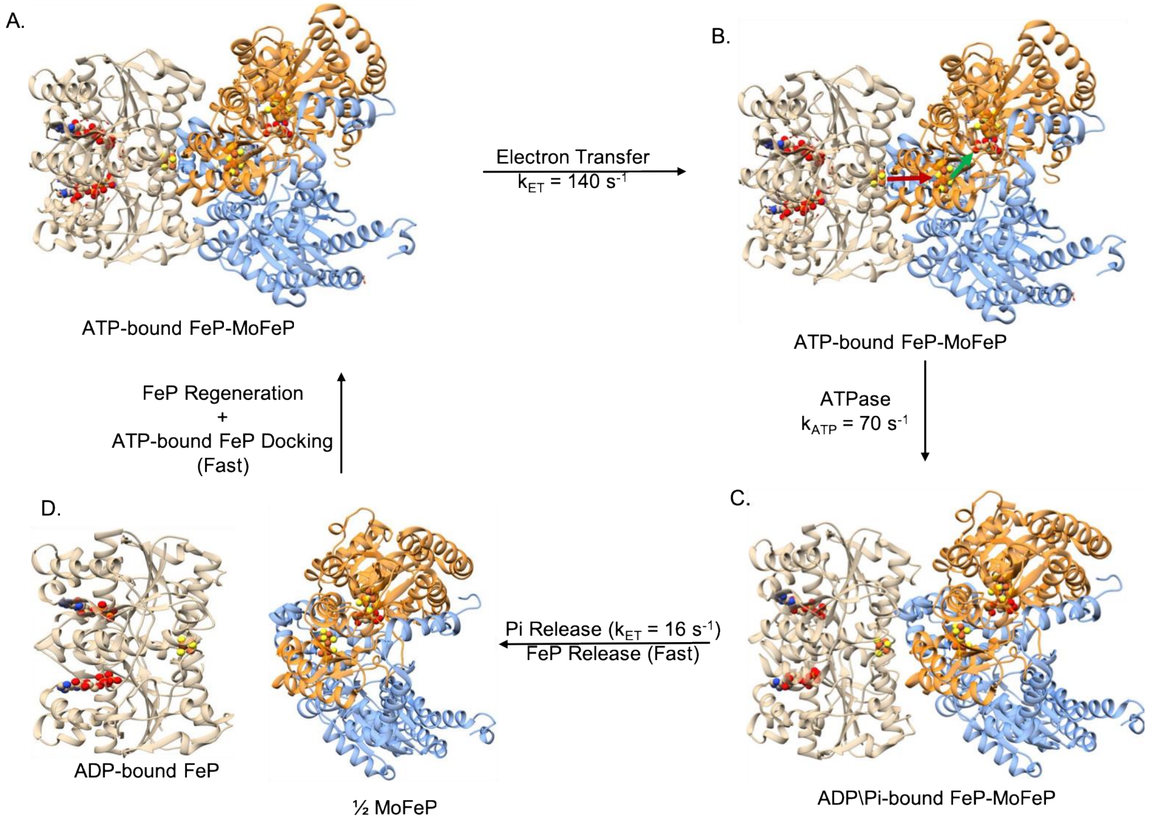

Figure 5.1. Schematic showing the steps of the FeP cycle using structures of FeP and MoFeP. ATP binding to FeP places FeP in a conformation that binds to MoFeP quickly (**A**). After FeP docking electron transfer occurs ($k_{ET} = 140\ s^{-1}$), supposedly through the deficit-spending model (**B**) with an electron first going from the P-cluster to FeMo-co (**B, green arrow**) and then an electron transferring from the [4Fe-4S] cluster of FeP to the P-cluster of MoFeP (**B, red arrow**). After electron transfer ATP hydrolysis occurs ($k_{ATP} = 70\ s^{-1}$) form the ADP/Pi bound FeP-MoFeP complex (**C**), ATP hydrolysis causes a conformational change in FeP, lowering the affinity between FeP and MoFeP. Pi release ($k_{Pi} = 16\ s^{-1}$) causes another conformational change, lowering the affinity of FeP docking, causing the release of FeP from MoFeP, making FeP available for regeneration, and the repeat of the FeP cycle (**D**). Protein structures used were the AMP-PCP bound FeP-MoFeP complex for the ATP-bound FeP-MoFeP complexes (PDB ID:4WZB) and the ADP bound FeP-MoFeP complex for the ADP/Pi bound FeP-MoFeP complex (PDB ID: 2AFI).

The characterization of the FeP cycle has led to the discovery of the rate and order of each of the steps. After FeP binding an electron is transferred from the [4Fe-4S] cluster of

FeP to the MoFeP with an observed rate constant of $k_{ET} = 140\ s^{-1}$ [8,16]. The order of electron transfer (ET) is hypothesized to occur through a two-step process known as deficit-spending ET. This involves a conformationally gated ET from the P-cluster to the FeMo-co, quickly followed by ET from the FeP to the P-cluster[17–19]. The remainder of the FeP cycle involves the hydrolysis of ATP ($k_{ATP} = 70\ s^{-1}$) and the release of inorganic phosphate (Pi, $k_{Pi} = 16\ s^{-1}$). The ADP-bound, oxidized FeP dissociates from the MoFeP, allowing the regeneration of ATP-bound reduced FeP to allow the FeP cycle to continue[8,16,20,21].

The FeP cycle needs to occur a total of eight times per αβ dimer to provide the electrons and protons necessary for N_2 reduction to NH_3 (**Eq. 1**)[1,3,4,6,22].

$$N_2 + 8e^- + 8H^+ + 16ATP \rightarrow 2NH_3 + H_2 + 16ADP + 16\ Pi \qquad \textbf{(1)}$$

It was originally thought that the FeP cycle occurred in each αβ dimer independently. Thus allowing ET, and eventually N_2 reduction, to occur at one αβ dimer, unhindered by the other dimer[12]. A recent kinetic study uncovered evidence that ET at one αβ dimer suppresses ET during the FeP cycle when using FeP and MoFeP from different organisms[23]. This study concluded that the slower rate of ET observed in the MoFeP-FeP complex is the result of a mechanism of negative cooperativity to regulate ET between the αβ halves. The hypothesis of negative cooperativity was further investigated in a study using quantitative kinetic measurements during the pre-steady state of the FeP cycle and calculations of protein motions between the MoFeP and FeP structures to determine if evidence for the same mechanism is present in the MoFeP-FeP complex when using FeP and MoFeP from the same organism[24]. This study also concluded that a mechanism of negative cooperativity is present within the Mo-dependent nitrogenase, through a two-branch kinetic scheme. This scheme assumes that ET at one αβ dimer of the MoFeP induces a conformational change that allosterically suppresses ET at the other αβ dimer, but still allows ET to occur[24]. Despite the kinetic and computational evidence that supports the existence of negative cooperativity in the Mo-dependent nitrogenase, the role of allosteric regulation in N_2 reduction is not known.

To fully understand the role of negative cooperativity in the Mo-dependent nitrogenase biophysical evidence detailing changes in the structure and dynamics of the MoFeP during the FeP cycle is needed. H/D exchange coupled to mass spectrometry (HDX-MS) is a powerful technique that measures the accessibility of hydrogens on the peptide backbone[25–30]. Amide hydrogens will exchange with hydrogens in solution, and by replacing the solvent system with deuterated water (D_2O) the change in mass can be used to determine how much deuterium is incorporated at a given time[31]. Several factors can influence the rate of exchange on the peptide backbone The most influential being the secondary structures (alpha helices and beta sheets) which are stabilized by hydrogen bonds between an amide hydrogens and carbonyl oxygen[32–34]. The stability of the secondary structures effects the availability of amide hydrogens for deuterium exchange. Fast local unfolding breaks hydrogen bonds causing amide hydrogens to exchange quickly, whereas slower unfolding takes longer before the amide hydrogens are accessible for exchange[35]. The tertiary interactions in a protein can also influence the rate of exchange with amide hydrogens on the surface of a protein exchanging much faster, and amide hydrogen in the interior of the protein exchanging at a slower rate[34].

Additionally, protein-protein and protein-ligand interactions can influence the rate of exchange, which can be used to determine the site of protein-protein interactions and ligand binding[36,37]. A benefit of HDX-MS is that changes in deuterium exchange are not only observed at the site of perturbation, but can be seen throughout the entire protein structure. This change in deuterium incorporation can be used to identify the mechanistic role of changes in structure and dynamics, and even identify pathways of allosteric communication in a protein[36,38–40].

Quench flow HDX-MS (QF-HDX-MS) is an ideal technique to determine the mode of action for allosteric communication in the MoFeP. The addition of a quench flow apparatus allows the measurement of deuterium incorporation on the millisecond time scale[41]. Using QF-HDX-MS the structure and dynamics of the MoFeP can be determined on a time scale relevant to catalysis, specifically during the different stages of the FeP cycle. To accomplish this three conditions were tested with QF-HDX-MS: MoFeP in the absence of FeP (MoFe), MoFeP and ATP-bound FeP mixed in a 1:1 mol ratio (MoFe:FeP 1:1), and MoFeP and ATP-bound FeP mixed in a 1:2 mol ratio (MoFe:FeP 1:2). These conditions were deuterated and quenched after 10ms, 30ms, 60ms, and 80ms of exchange via quenchflow. Later timepoints (2 min, 4min, 15 min, 1 hr, and 24 hrs) were initiated and quenched as anaerobic benchtop reactions. In this study the structure and dynamics of MoFeP when FeP is present or absent is used to further confirm the presence of allosteric regulation in the Mo-dependent nitrogenase system. Additionally, differences in deuterium uptake between the FeP bound conditions will be used to determine the changes in the MoFeP structure and dynamics when one equivalent

(MoFe:FeP 1:1 condition) or two equivalents (MoFe:FeP 1:2) of FeP are present. Differences in the FeP bound conditions will reveal the effects asymmetric FeP binding has on the MoFeP structure, and how these effects relate to an allosteric signal passing between the αβ dimers to suppress ET.

Materials and Methods

Protein Purification Nitrogenase proteins were expressed in *Azotobacter vinelandii* strains DJ995 (Polyhistidine-tagged MoFe protein) and DJ884 (wild-type Fe Protein). Cells were grown and proteins purified as previously described[42,43]. Proteins were concentrated using an Amicon (EMD Millipore, Billerica,MA) anaerobic pressure concentrator with appropriate molecular weight cutoff membranes. Protein purities were assessed by SDS-PAGE analysis with Coomassie Blue stain used for protein detection. Protein concentration was determined by Biuret assay against a Bovine Serum Albumin standard.

Quench Flow H/D Exchange QF-HDX experiments were conducted using a quench flow (Kintek) in a Coy chamber (Grass Lake, MI) under Argon. Three solutions were prepared for the drive syringes: deuterated buffer (50 mM Tris, 12 mM dithionite, pD 7.4), non-deuterated buffer (50 mM Tris, 12 mM dithionite, pH 7.4), and quench solution (3% formic acid; FA, Sigma). All buffers were degassed for use anaerobically. Dilution buffer (15 mM ATP and 8 mM $MgCl_2$) was also prepared to dilute protein samples prior to rapid mixing in both H_2O and D_2O. MoFeP samples were diluted using non-deuterated buffers, and FeP diluted using deuterated buffers. This ensured that the

MoFeP was not exposed to deuterated buffer prior to rapid mixing in the quench flow apparatus. Quench flow reactions were conducted anaerobically under positive Ar pressure. The 10 ms, 30 ms, 60 ms, and 80 ms time points were collected in duplicate for the MoFe, MoFe:FeP 1:1 and MoFe:FeP 1:2 conditions, and flash frozen after quench. Samples were subject to protease digestion via porcine pepsin (0.2 mg/mL final concentration, Sigma) for two minutes prior to injection onto the LC-MS system.

Bench Top H/D Exchange Longer time points (2 min, 4 min, 15 min, 1 hr, and 24 hrs) were performed as a bench top reaction using the protocol described previously, however pepsin digestion did not occur with quench[44]. Instead samples were subject to protease digestion via porcine pepsin (0.2 mg/mL final concentration, Sigma) for two minutes prior to injection onto the LC-MS system.

LC-MS Analysis of Deuterated MoFeP LC-MS analysis of the MoFeP was completed on a 1290 UPLC series chromatography stack (Agilent Technologies) coupled directly to a 6538 UHD Accurate-Mass Q-TOF LC/MS mass spectrometer (Agilent Technologies). Before electrospray-time of flight (ESI-TOF) analysis, peptides were separated on a reverse phase (RP) column (Phenomenex Onyx Monolithic C18 column, 100 x 2 mm) at 1°C using a flow rate of 500 µL/min. under the following conditions: 0.0-1.0 min., 5% B; 1.0-9.0 min., 5-45% B; 9.1-9.8 min., 95% B; 9.8-9.9 min., 5% B. Solvent A contained 0.1% FA in water (ThermoFisher) while solvent B contained 0.1% FA in acetonitrile (ACN, ThermoFisher). Data was acquired at 2 Hz over a scan range 50-1700 m/z in positive mode. Electrospray settings were: nebulizer at 3.7 bar, drying gas at 8.0

L/min., drying temperature at 350°C, and capillary voltage at 3.5 kV. MS/MS of non-deuterated protein digests, specifying a selection window of 4 m/z, was used to generate peptide sequence tags. Data processing was carried out in Agilent MassHunter Qualitative Analysis version 6.0. Non-deuterated peptide identification was performed using the peptide analysis worksheet for single level MS (PAWs, ProteoMetrics LLC.) and Peptide Shaker (Compomics, version 1.16.15) for MS/MS.

HDX-MS Analysis Initial digests of the MoFeP led to the identification of 107 peptides in the alpha subunit and 152 in the beta subunit, generating 99% and 100% sequence coverage respectively (**Supp Fig 5.1 and 5.2**). Deuterium uptake was determined by monitoring shifts of the centroid peptide isotopic distribution by using the program HDExaminer (Sierra Analytics Inc., Version 2.4.1). Measured values were then used to generate uptake curves to compare relative deuterium exchange in all conditions tested. A total of 37 peptides from alpha and 26 peptides in beta showed high confidence deuterium incorporation scores (Score: >0.70). The heat maps showing the global deuterium incorporation can be found in **Supp. Fig 5.3 and 5.4** for the alpha and beta subunits respectively. Peptide coverage and deuterium heat maps were generated using the MSTools web based platform[45]. Butterfly plots were generated using the percent deuterium (%D) incorporated at each time point, for all deuterated peptides. The %D was calculated by using the number of deuterium (#D) incorporated after 24 hours of exchange as the maximum amount of deuterium. The %D of the FeP bound conditions was inverted by multiplying by -1. Butterfly plots using the three conditions were generated in Microsoft Excel.

Bimodal peptides were determined using the program HDExaminer (Sierra Analytics Inc.). Peptides with low unimodal scores (<70%) were subjected to bimodal deuteration calculations, and those having high scores (>90%) were designated as bimodal peptides and mapped onto a crystal structure of the MoFeP (PDB ID: 4WZB) using UCSF Chimera (version 1.12)[18,46].

Structural heat maps were generated using the percent difference in exchange between the MoFe condition and the FeP bound conditions. Percent difference was calculated by subtracting the %D incorporated in the MoFe condition from the %D incorporated in the FeP bound conditions. The resulting numbers were mapped onto the structures of the MoFeP (PDB ID:4WZB and 2AFI) using UCSF Chimera (version 1.12)[18,46].

Results and Discussion

Effects of FeP Binding on the Deuterium Uptake of MoFeP The results of the QF-HDX-MS experiment were used to calculate the percent deuterium (%D) incorporated using the amount of deuterium incorporated after 24 hours as the maximum number of deuterium for that peptide. The percent deuterium (%D) of the 63 peptides (37 from the α subunit and 26 from the β subunit) with high confidence deuterium calculation scores (>70%) at four time points (10 ms, 80 ms, 2 min, and 1 hr) were calculated and plotted using a butterfly plot to show the comparison between the FeP bound states (MoFe:FeP 1:1 and MoFe:FeP 1:2) and unbound MoFeP (MoFe) (**Fig 5.2**).

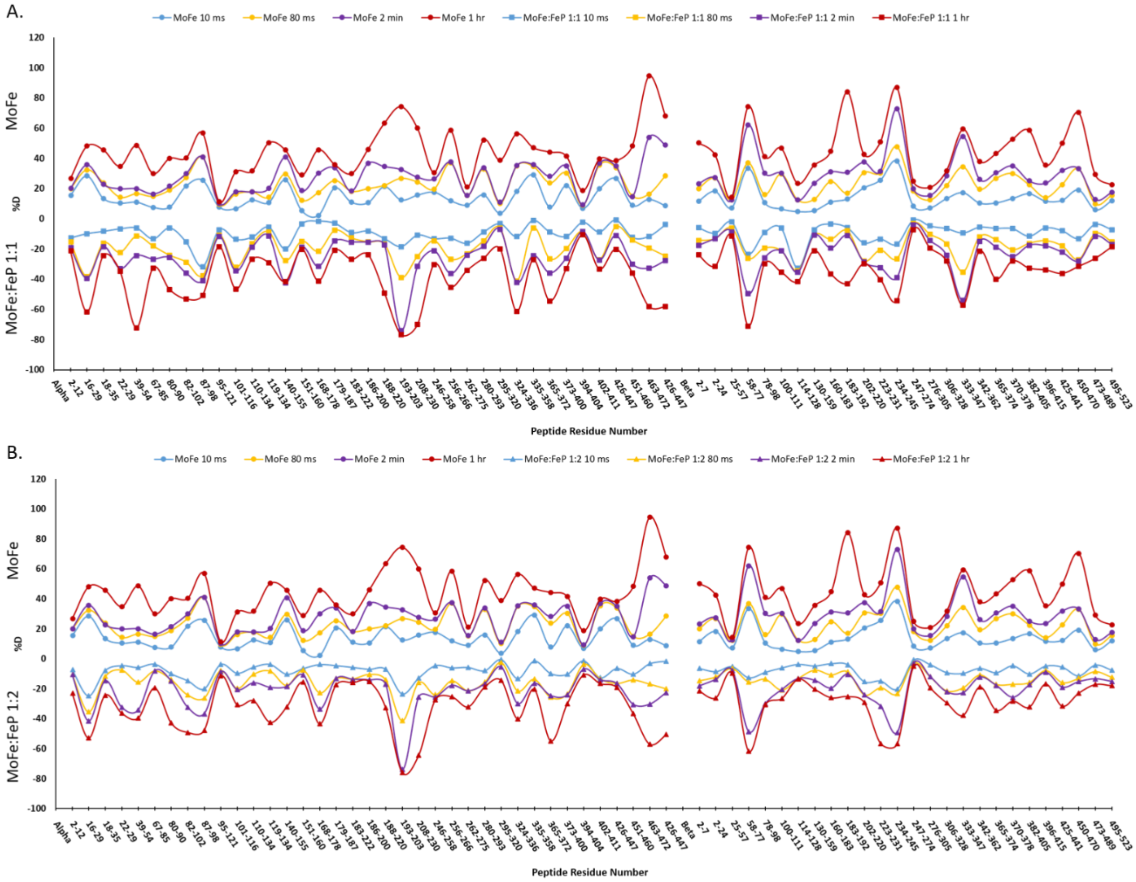

Figure 5.2. Butterfly plots showing the percent deuterium incorporated (%D) at four time points (10 ms, 80 ms, 2 min, 1 hr) for each of the peptides with high confidence scores from the α (left) and β (right) subunits of the MoFe protein. **A.** Comparison of the MoFe (positive values) and MoFe:FeP 1:1 conditions (negative values). **B.** Comparison of the MoFe (positive values) and MoFe:FeP 1:2 conditions (negative values).

Only four time points were used for simplicity, plots with the %D of all time points is shown as **Supp. Fig. 5.5**. In general, the MoFe condition exhibits the fastest rate of exchange, and incorporates the most deuterium when compared to the MoFe:FeP 1:1 (**Fig 5.2A**) and MoFe:FeP 1:2 (**Fig 5.2B**) conditions. Regions of interest in all three conditions can be identified quickly using the butterfly plots. This includes regions that show an increase in exchange when FeP is present (α39-54 and β223-231), a decrease in exchange when FeP is present (α151-160 and β130-159), or no change (α95-121 and β25-57). To validate the effectiveness of the QF-HDX-MS reaction, regions showing a decrease in exchange at the early time points were needed. One such region is the β160-183 peptide, which is located on the surface of the β subunit of the MoFeP, and forms part of the surface that interacts with FeP. In the absence of FeP this region exchanges 11% of the maximum possible deuterium at 10 ms. In the MoFe:FeP 1:1 and MoFe:FeP 1:2 conditions, this number decreases to 3%. This trend continues through the full time course, with the MoFe condition incorporating 42%D, MoFe:FeP 1:1 incorporating 36%D, and MoFe:FeP 1:2 incorporating 26%D. Decreases in deuterium incorporation in the presence of additional protein subunits are the result of protein-protein interactions stabilizing secondary structures. More stable secondary structures result in a decreased rate of local unfolding events and causes the amide hydrogens to become less accessible to exchange. With the MoFeP, this effect increases as more FeP is added to the reaction. The decreased exchange in the MoFeP when FeP is bound indicates that the complexes observed at all time points of the QF-HDX-MS experiment are the one FeP bound (MoFe:FeP 1:1) and two FeP bound (MoFe:FeP 1:2) complexes.

Peptides at functionally relevant regions can reveal the effects FeP binding has on the dynamics of MoFeP, and how these changes can influence electron transfer. For instance, α87-98 is involved in coordinating the P-cluster through αCys88 and the FeMo-co through αArg96, and forms part of the protein environment responsible for transporting electrons between the two cofactors. Upon the addition of a single equivalent of FeP (MoFe:FeP 1:1) the α87-98 peptides incorporates 31%D by the 10 ms time point, whereas the MoFe condition incorporates 25%D by 10 ms (**Fig 5.2A**, blue trace). In the MoFe:FeP 1:2 condition, 20%D is incorporated at a similar rate of exchange to the MoFe condition. The increased rate of exchange in the MoFe:FeP 1:1 condition suggests that this region becomes more dynamic in the presence of FeP, allowing more exchange to occur. In the presence of two equivalents of FeP, a decrease in the rate of exchange is not observed, instead MoFeP exchanges deuterium in a similar manner to the MoFe condition. Mechanistically, the increase in exchange when one equivalent of FeP is present is to change the position of the P-cluster. Because the increase in exchange is not observed in the MoFe:FeP 1:2 condition it can be inferred that with one equivalent of FeP present the change in exchange is not at the site of FeP binding, but instead is reporting on the half of the MoFeP without FeP bound. This change likely functions to increase the distance between the P-cluster and FeMo-co, reducing the rate of electron transfer.

To provide further support for the unique exchange pattern observed in the α87-98 region, the β114-128 region was examined more closely. This region is close to the FeP binding site in a crystal structure of the MoFe-FeP complex (PDB ID:4WZB) and is expected to be protected from exchange in the presence of FeP. Because of its location the β114-128 region is likely involved in the recognition and coordination of FeP. In the MoFe condition, β114-128 shows a slow rate of exchange incorporating 4%D after 10 ms. In the MoFe:FeP 1:2 condition the amount of deuterium incorporated is also low, incorporating 3%D after 10 ms of exchange. Despite the presence of FeP at both halves of the MoFeP, a difference in deuterium incorporation is not observed. Similar to α87-98, β114-128 exchanges quickly in the MoFe:FeP 1:1 condition, incorporating 32%

deuterium after 10 ms. The higher deuterium incorporation in the MoFe:FeP 1:1 condition shows that the β114-128 region behaves in a similar manner to the α87-98 region. At these regions, FeP binding causes the free half of MoFeP to adopt a conformation more available to exchange. The fact that this behavior is not observed in the MoFe:FeP 1:2 condition suggests that FeP is capable of binding to both halves, and causing the structure to stabilize resulting in a lower rate of exchange. Instead of decreasing the FeP binding affinity the increase in exchange instead effects the protein environment near the cofactors, which would affect the rate of electron transfer between cofactors. This unique exchange pattern observed in the MoFe:FeP 1:1 condition suggests that the MoFeP adopts an asymmetric conformation in the presence of one equivalent of FeP. This is consistent with previous studies on the MoFeP that found evidence that negative cooperativity regulates electron transfer.

<u>Structural Asymmetry of the MoFeP</u> To fully understand the asymmetrical nature of the MoFeP and how this asymmetry influences electron transfer, we sought more evidence to support asymmetry in the MoFeP complex. HDX reactions are extremely sensitive to a protein's conformation and can detect if a protein of interest is occupying multiple conformations simultaneously. Typically, the deuterated isotope distribution of a peptide maintains a constant width as more deuterium is incorporated, but the centroid mass-to-charge ratio (m/z) gradually increases as more deuterium is added onto the peptide. If multiple conformations are present and exchanging at different rates, the isotope distribution for a given peptide will become much wider because of the presence of overlapping isotope distributions and are known as bimodal peptides[47,48]. In the

MoFeP, asymmetric binding of the FeP is hypothesized to cause the two halves of the MoFeP to adopt a different conformation. The site of FeP binding will have one conformation, while the FeP free half is expected to adopt a different conformation that suppresses electron transfer. This makes the MoFeP an ideal target for bimodal peptides, specifically in the MoFe:FeP 1:1 condition. Bimodal peptides here would provide further evidence that MoFeP adopts an asymmetric conformation during the asymmetrical binding of FeP.

The QF-HDX-MS data collected on the MoFeP in the MoFe, MoFe:FeP 1:1, and MoFe:FeP 1:2 conditions were examined for bimodal peptides. The list of peptides used in the deuterium incorporation calculations includes 107 peptides from the α subunit, and 152 from the β subunit. Several peptides showed potential bimodal distributions, primarily in the MoFe:FeP 1:1 condition, but also the MoFe and MoFe:FeP 1:2 condition. Three peptides exhibited isotope distributions consistent with bimodal exchange: α82-109, α208-230, and α186-200 (**Fig 5.3**). The α102-117 peptide is located in the interior of the protein, and forms interactions between the α_1 and β_2 subunits, and only exhibits bimodal behavior in the MoFe:FeP 1:1 condition at 10 ms (**Fig 5.3A**). Additionally, this region contains αThr104, which is hypothesized to form a substrate channel allow N_2 to binding to the FeMo-co (**Fig 5.3A, inset**).

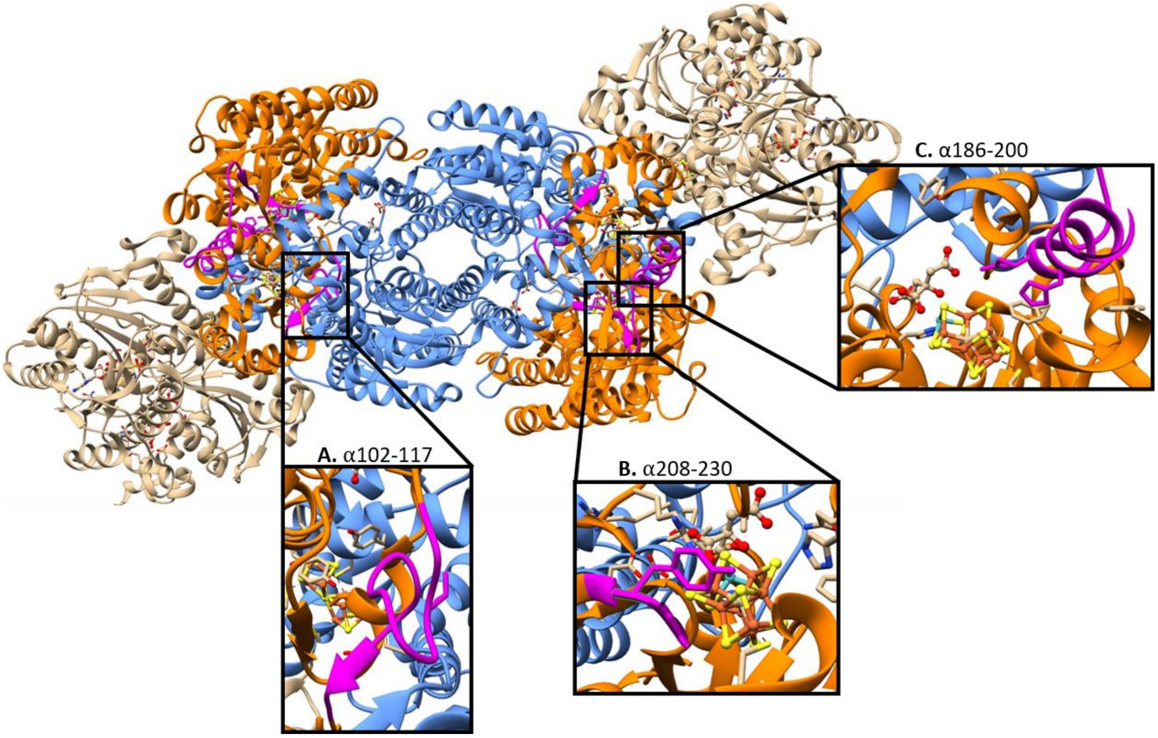

Figure 5.3. Bimodal peptides identified from QF-HDX-MS. The alpha subunit is shown in orange, beta in blue, and the FeP in tan (PDB ID: 4WZB). **A.** α102-117 shows bimodal behavior in the MoFe:FeP 1:1 condition at 10 ms. This region includes αThr104, a residue involved in the formation of a substrate channel allowing N_2 binding to occur, and forms interactions with the beta subunit of the opposite half. **B.** α208-230 shows bimodal behavior in the MoFe:FeP 1:1 and MoFe:FeP 1:2 condition after 10 ms of exchange. This region is near the FeMo-co, and includes the residue αTyr229, which interacts with the FeMo-co. **C.** α186-200 shows bimodal behavior in the MoFe and MoFe:FeP 1:1 conditions at 10 ms. This region is adjacent to the FeMo-co and contains αHis195 which is necessary for N_2 binding and catalysis.

Because this peptide does not interact directly with FeP it is unlikely that the bimodal behavior is caused by a decrease in accessibility at the FeP bound half, exchanging less compared to the free half. Instead the FeP-free half of the MoFeP becomes more dynamic, exchanging more deuterium than the FeP bound half causing the bimodal behavior to appear. The increased dynamics of the α102-117 are likely responsible for the transduction of a signal from one half of the MoFeP, to the other half. Additionally, because of the presence of the αThr104 residue, it is possible that the asymmetric binding of FeP also regulates the binding of N_2 to the FeMo-co.

Another bimodal peptide is the α208-230 region, which is located primarily on the surface of the MoFeP, but also includes residues near the FeMo-co, like αTyr229, that interacts with the cofactor, and influences the protein environment (**Fig 5.3B**)[49]. The α208-230 region shows bimodal exchange behavior in all three conditions at the 10 ms time point. The bimodal behavior suggests that there is structural asymmetry in the MoFeP that is not affected by FeP binding. However, the bimodal behavior is more apparent in the FeP bound conditions, indicating that FeP binding increases the population of MoFeP adopting an asymmetrical structure. The bimodal behavior in the α208-230 region, specifically the αTyr229 residue, likely functions to alter the protein environment around the FeMo-co at the FeP-free MoFeP half when FeP is bound to the other half (**Fig 5.3B, inset**). This alteration of the protein environment supports the hypothesis that negative cooperativity is caused by the asymmetric binding of FeP, and suppresses electron transfer at the FeP free half. Because the bimodal behavior is also observed in the MoFe:FeP 1:2 condition it is possible that the bimodal exchange rate is not influenced by the presence of two equivalents of FeP. Similar to the α208-230 peptide, α186-200 also exhibits bimodal behavior and is adjacent to the FeMo-co (**Fig 5.3C**). In the α186-200 peptide is the αHis195 residue which is involved in the binding of N_2 to the FeMo-co, and necessary for catalysis (**Fig 5.3C, inset**)[50]. Bimodal behavior is only observed in this region in the MoFe and MoFe:FeP 1:1 conditions at the 10 ms time point. The bimodal behavior of the α102-117, α208-230 and α186-200 regions suggests that the asymmetrical binding of FeP influences the protein environment of the FeMo-co, and availability of N_2 to the active site. Additionally, the location of the α102-117 region indicates a possible pathway of communication between the two halves of the MoFeP.

MoFe Dynamics on a Catalytic Timescale To characterize the structural asymmetry of the MoFeP in the context of catalysis, the millisecond time points collected using the quench flow apparatus were used to analyze the state of the MoFeP dynamics during the FeP cycle. The function of the FeP cycle is to deliver electrons to the FeMo-co. The binding of FeP to the MoFeP is regulated by the nucleotides bound to FeP. ATP-bound FeP binds to MoFeP and transfers an electron to the P-cluster which in turn delivers the electron to FeMo-co for substrate reduction. After electron transfer, ATP is hydrolyzed to ADP, causing a conformational change in FeP, reducing the binding affinity with MoFeP. The inorganic phosphate produced from ATP hydrolysis is then released, and FeP dissociates from MoFeP to restart the FeP cycle. Kinetic studies of the FeP cycle have determined the rate constants for each of the steps, which can then be used to determine the time scale each of these steps occurs[8,16]. With the kinetic constants, structural heat maps showing the MoFe:FeP 1:1 vs MoFe (**Fig 5.4**) and the MoFe:FeP 1:2 vs MoFe (**Supp Fig 5.6**) comparisons at the different steps of the FeP cycle. The heat maps reveal regions of the MoFeP that show an increase in exchange (red regions) or decrease in exchange (blue regions) when FeP is present.

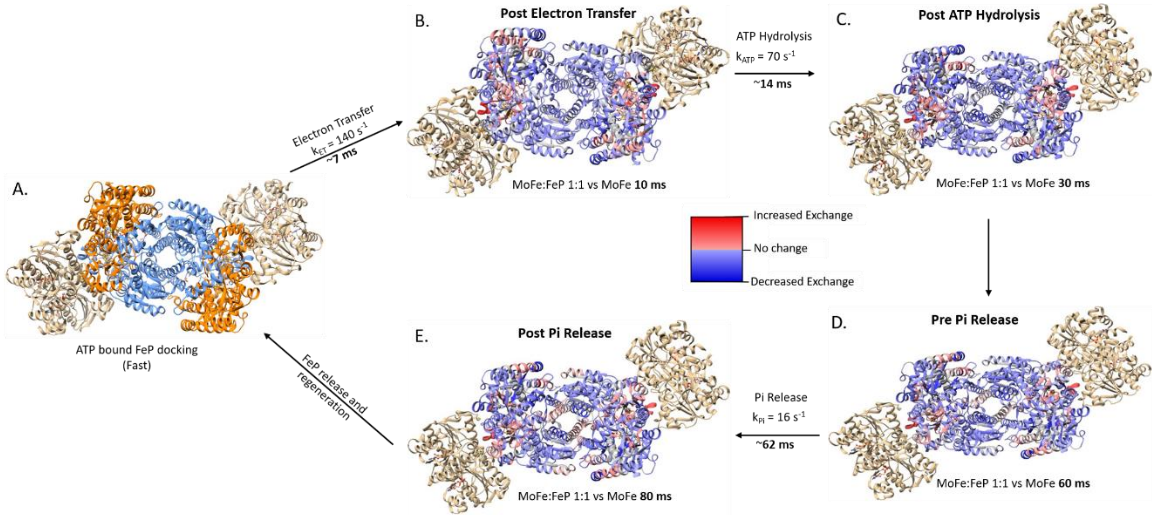

Figure 5.4. Structural heat maps showing the differences in exchange between the MoFe:FeP 1:1 condition and the MoFe condition at the millisecond time points mapped onto the structure of the MoFe protein in accordance with the different steps of the FeP cycle. For all structures, red regions indicate an increase in deuterium exchange in the MoFe:FeP 1:1 condition and blue regions indicate a decrease in deuterium exchange in the MoFe:FeP 1:1 condition. **A.** ATP bound FeP docks with the MoFe protein (PDB ID: 4WZB; AMP-PCP bound FeP shown in tan, α-MoFe shown in orange, and β-MoFe shown in blue). After FeP docking, electron transfer between the two proteins occurs at a rate of k_{ET}= 140 s^{-1} which is approximately 7 ms. **B.** The 10 ms time point captures the state of the MoFe protein shortly after ET. The differences in exchange of the MoFe:FeP 1:1 vs MoFe comparison was mapped onto the AMP-PCP bound FeP-MoFe crystal structure (PDB ID: 4WZB). After ET, ATP hydrolysis occurs at a rate of k_{ATP} = 70 s^{-1}, approximately 14 ms after FeP docking. **C.** After ATP hydrolysis, the ADP bound FeP changes conformation, changing the interactions between the FeP and MoFeP. The difference in exchange for the MoFe:FeP 1:1 vs MoFe comparison is mapped onto the ADP bound FeP-MoFe crystal structure (PDB ID: 2AFI). **D.** Shows the state of the MoFe protein at 60 ms, prior to Pi release for the MoFe:FeP 1:1 vs MoFe comparison. Pi release occurs at a rate of k_{Pi} = 14 s^{-1}, approximately 62 ms after FeP docking. **E.** The protein state at 80 ms reveals the effects Pi release has on the MoFeP structure and dynamics. The differences in exchange of the MoFe:FeP 1:1 vs MoFe comparison is shown.

The FeP cycle begins with ATP bound FeP docking onto the MoFeP quickly (**Fig 5.4A; Supp. Fig 5.6A**). An electron and is then transferred from the [4Fe-4S] cluster of the FeP to the P-cluster of the MoFeP. Electron transfer happens at a rate constant of k_{ET} = 140 s^{-1} which is equal to approximately 7 ms, making it too fast to detect with QF-

HDX-MS[8,16]. However, the 10 ms time point allows the measurement of the MoFeP dynamics immediately after electron transfer. At this time point the MoFe:FeP 1:1 vs MoFe and MoFe:FeP 1:2 vs MoFe (**Supp. Fig 5.6B**) comparisons show a decrease in exchange occurs upon FeP binding. However, there are several areas that show an increase in exchange in the MoFe:FeP 1:1 condition (**Fig 5.4B**). The next step of the FeP cycle is ATP hydrolysis that converts the bound ATP to ADP/Pi. In the ADP/Pi bound state FeP still interacts with the MoFeP, but with a larger distance between the surface of the proteins. The rate constant of ATP hydrolysis is $k_{ATP} = 70\ s^{-1}$, which is approximately 14 ms[8,16]. The earliest time point showing the post-ATP hydrolysis dynamics of the MoFeP is the 30 ms time point. The MoFe:FeP 1:1 vs MoFe (**Fig 5.4C**) and MoFe:FeP 1:2 vs MoFe (**Supp. Fig 5.6C**) comparisons show very little difference from the structures at 10 ms. The next step of the FeP cycle involves the release of the Pi, resulting in another conformational change, and further decreasing the interactions between FeP and MoFeP. The Pi release event occurs at a rate of $k_{Pi} = 16\ s^{-1}$, which is approximately 62 ms[8,16]. Two time points from the QF-HDX-MS experiment capture the dynamics of the MoFeP shortly before Pi release (60 ms) and after Pi release (80 ms). The exchange patterns observed in the MoFe:FeP 1:1 vs MoFe (**Fig 5.4D and E**) and MoFe:FeP 1:2 vs MoFe (**Supp. Fig 5.6D and E**)comparison start to show more differences than the previous time points. Some regions of the MoFe:FeP 1:1 vs MoFe comparison show a decrease in deuterium incorporation. Additionally, both comparisons show an increase in exchange at the $\alpha_1\beta_1$-$\alpha_2\beta_2$ interface at 60 ms. This area shows a decrease in exchange in the MoFe:FeP 1:2 vs MoFe comparison at 80 ms, and continues to show an increase in exchange in the MoFe:FeP 1:1 vs MoFe comparison.

During the course of the FeP cycle, the MoFe:FeP 1:1 condition exchanges more deuterium in some areas than the MoFe condition (**Fig 5.4**), whereas overall the MoFe:FeP 1:2 condition exchange less deuterium than the MoFe condition (**Supp. Fig 5.6**). The more dynamic structure of the MoFeP in the MoFe:FeP 1:1 vs MoFe comparison can be attributed to the asymmetric binding of FeP. Examining the exchange pattern in the MoFe:FeP 1:2 vs MoFe comparison shows that the MoFeP structure incorporates much less deuterium than the other conditions, adopting a protected conformation. As previously stated, this protection is likely due to the protein-protein interactions between FeP and MoFeP which stabilizes the secondary structures, thus decreasing the accessibility of the amide hydrogens for exchange. Because more FeP is present in the MoFe:FeP 1:2 condition, it is expected that a higher degree of protection would be observed, but both conditions would have a similar pattern of exchange when compared to the MoFe condition. While this is observed in the majority of the structure, the MoFe:FeP 1:1 vs MoFe comparison shows that there are some regions where an increase in exchange occurs, indicating that the MoFe:FeP 1:1 condition is more dynamic. The similarities and differences between the MoFe:FeP 1:1 vs MoFe and MoFe:FeP 1:2 vs MoFe comparisons can be used to determine the effects asymmetrical FeP binding has on the structure of the MoFeP and how these effects change throughout the course of the FeP cycle.

The main regions of the MoFeP effected by asymmetric FeP binding are residues at the P-cluster, FeMo-co, and the $\alpha_1\beta_1$-$\alpha_2\beta_2$ interface. When a single equivalent of FeP is bound, the protein environment around the P-cluster is much more accessible to exchange. The increased dynamics of this region are detected immediately after electron transfer (10 ms, **Fig 5.4B**), and is present throughout the entire FeP cycle (**Fig 5.4C-E**). FeP binding is expected to stabilize the P-cluster environment, decreasing exchange. While this is observed in the MoFe:FeP 1:2 condition (**Supp. Fig 5.6**), the increased dynamics in the MoFe:FeP 1:1 condition suggests different behavior is occurring (**Fig 5.4**). As previously mentioned, negative cooperativity in the MoFeP is hypothesized to suppress the electron from FeP to the FeMo-co[24]. The P-cluster plays an integral role in this transfer, because it acts as an intermediary between the FeP and FeMo-co. The integral role of the P-cluster further supports the expected stabilization of the P-cluster protein environment. The areas showing an increase in exchange around the P-cluster include several coordinating Cys residues. This data indicates that when FeP binds to one half of the MoFeP, a signal is being sent from the site of binding, to the P-cluster of the free MoFeP half. This signal results in an increase in exchange around the P-cluster, which likely functions to increase the distance between the P-cluster and FeMo-co, decreasing the rate of electron transfer between these two cofactors.

Investigation of the FeMo-co protein environment reveals dynamic behavior similar to the P-cluster. However, this behavior only appears in the 10 ms time point of the MoFe:FeP 1:1 vs MoFe comparison, and the protein environment around the FeMo-co is more protected during the remainder of the FeP cycle (**Fig 5.4B**). The increased dynamics around the FeMo-co include αVal70, αVal71, and αArg96. These residues are hypothesized to form a substrate channel that allows N_2 to bind to the FeMo-co (αVal70/71) and interact directly with the FeMo-co (αVal70 and αArg96). These residues play an important role in prepping the FeMo-co for nitrogen reduction, and it is likely that the increased dynamics are the result of electron transfer from the P-cluster, and the formation of the substrate channel to allow N_2 to bind to the active site. After electron transfer the protein environment around the FeMo-co shows less exchange in the MoFe:FeP 1:1 vs MoFe comparison, indicating that these regions are more stable. After electron transfer and N_2 binding, the substrate channel will close, decreasing the rate of N_2 diffusion into the active site, and the electron transfer pathway will alter to prevent the loss of electrons bound to FeMo-co.

The mechanism of negative cooperativity in the MoFeP is hypothesized to be controlled by a pathway of communication between the two halves of the complex. For a pathway of communication to function correctly, it must pass through the $\alpha_1\beta_1$-$\alpha_2\beta_2$ interface. Examination of the structural heat maps at 60 and 80 ms provides evidence for a pathway of communication that spans the interface of the MoFeP complex. At 60 ms in the MoFe:FeP 1:1 vs MoFe (**Fig 5.4D**) and MoFe:FeP 1:2 vs MoFe comparison, (**Supp. Fig 5.6D**) the c-terminal regions of the β subunit (β342-362 and β495-523) show in increase in exchange. The structure of the MoFeP reveals that β342-362 and β495-523 of one β subunit interacts with the α-β interface of the other half (i.e. β_1-342-362 and β_1-495-523 interact with $\alpha_2\beta_2$). Any changes in conformation at this region will likely cause a conformational change in the rest of the complex. The increase in exchange prior to Pi release at these regions suggests that the MoFeP switches the activity of each half, prior to the release of ADP-bound FeP. At the 80 ms time point, after Pi release, the MoFe:FeP 1:1 vs MoFe comparison (**Fig 5.4E**) continues to show an increase in exchange at this region, whereas the MoFe:FeP 1:2 vs MoFe comparison (**Supp. Fig 5.6E**) shows a decrease in exchange. A signal sent from the binding site of FeP on one half to the binding site on the other is likely quenched when an ATP-bound FeP interacts with the "newly" active half of the complex. Since the MoFe:FeP 1:2 condition contains two equivalents of FeP for every MoFeP, it is likely that after Pi release there is already an ATP-bound FeP at the other half, quenching the signal. Conversely, in the MoFe:FeP 1:1 condition, since there is only one equivalent of FeP present for each MoFeP, the signal is not quenched with the binding of an ATP-bound FeP, causing the persistent increase in exchange observed at the 80 ms time point.

Conclusions

The present work provides biophysical evidence that supports the presence of a negative cooperativity mechanism within the Mo-dependent nitrogenase system. Using QF-HDX-MS, the structure and dynamics of the MoFeP were tested in three conditions: MoFe (free MoFe), MoFe:FeP 1:1 (1:1 mol ratio of FeP), and MoFe:FeP 1:2 (1:2 mol ratio of FeP). These conditions were used to detail the MoFeP in the absence of FeP (MoFe condition), as well as how the asymmetric (MoFe:FeP 1:1 condition) and symmetric binding of FeP (MoFe:FeP 1:2 condition) effect the structure of the MoFeP. The initial analysis of the QF-HDX-MS data using butterfly plots (**Fig 5.2**) revealed that overall the MoFe condition is more dynamic, as seen by a high amount of exchange, and the MoFe:FeP 1:2 condition is less dynamic. The differences observed in the deuterium uptake of the MoFe and MoFe:FeP 1:2 conditions are supported by the knowledge that protein-protein interactions stabilize protein secondary structures, and decrease the rate of exchange. This analysis helped confirm that differences in deuterium uptake are observed in all conditions, as early as 10 ms.

Examining the MoFe:FeP 1:1 condition revealed that while there are some areas indicating a decrease in exchange, others show an increase, suggesting the MoFeP becomes more dynamic when one equivalent of FeP is present. To better understand this unique exchange pattern, bimodal peptides were sought after to provide evidence of structural asymmetry in the MoFeP when one equivalent of FeP is present. Bimodal exchange indicates a protein is occupying multiple conformations simultaneously. In the MoFeP three bimodal peptides were identified: α82-109, α208-230, and α186-200 (**Fig 5.3**). These peptides all showed bimodal behavior in the MoFe:FeP 1:1 condition at 10 ms, indicating that shortly after the upon FeP binding, the αβ dimers adopt two different conformations. Bimodal behavior was not observed at 60 ms or later. These bimodal peptides are at functionally relevant regions of the protein, and only the α186-200 peptide is near the site of FeP docking. The location of these peptides suggests that asymmetric FeP binding effects the protein environments of the P-cluster and FeMo-co to either enhance or suppress the docking of FeP, and the subsequent electron transfer for N_2 reduction.

The ability to measure the structure and dynamics of the MoFeP on the millisecond time scale, allows the characterization at catalytically relevant time points.

To fully understand the role structural asymmetry has in N_2 reduction, differences in deuterium incorporation were examined in a comparison of the MoFe:FeP 1:1 vs MoFe conditions and MoFe:FeP 1:2 vs MoFe conditions at the millisecond time points (10 ms, 30 ms, 60 ms, and 80 ms). These time points capture the dynamics of the MoFeP during the FeP cycle (**Fig 5.4 and Supp. Fig 5.6**). During the FeP cycle, the MoFe:FeP 1:2 condition shows a steady amount of exchange relative to the MoFe condition, with very subtle changes appearing throughout the FeP cycle. An interesting observation was the noticeable increase in exchange at 60 ms (pre Pi release) at the αβ dimer interface that disappeared at 80 ms (post Pi release) (**Supp Fig 5.6D and E**). On the other hand the MoFe:FeP 1:1 vs MoFe comparison shows several regions where an increase in exchange is observed (**Fig 5.4D and E**). These regions are primarily located around the P-cluster and FeMo-co, further suggesting that asymmetric FeP binding influences the protein environments around the cofactors. Similar to the MoFe:FeP 1:2 vs MoFe comparison, at 60 ms an increase in exchange is observed at the αβ dimer interface, however this increase is still present at 80 ms in the MoFe:FeP 1:1 vs MoFe comparison (**Fig 5.4E**). This "persistent" increase in exchange is likely part of a pathway that sends an allosteric signal from the FeP binding site at one αβ dimer, to the other. This signal likely acts to activate the FeP free half, allowing another equivalent of FeP to bind and allow the FeP cycle to proceed. This is supported by the same region showing a decrease in exchange in the MoFe:FeP 1:2 vs MoFe comparison (**Supp. Fig 5.6E**). The decrease in exchange is likely caused by the presence of an additional equivalent of FeP, quenching the signal after it is sent prior to Pi release.

QF-HDX-MS has provided biophysical evidence that further supports the allosteric regulation of electron transfer from FeP to the FeMo-co. Examining differences in exchange in time points relevant to the FeP cycle reveal areas that show an increase in exchange in the MoFe:FeP 1:1 condition. These areas can be used to connect the FeP binding site, P-cluster, and FeMo-co of one αβ dimer in the MoFeP to the other, revealing the framework of an allosteric signal's transduction pathway. Further analysis with protein dynamic simulations can reveal more information about which amino acid residues are behaving in a similar manner when FeP is present, and can be used to identify the specific residues of the MoFeP that are responsible for transmitting an allosteric signal between the αβ dimers.

References Cited

1. Burgess, B. K. & Lowe, D. J. Mechanism of Molybdenum Nitrogenase. *Chem. Rev.* **96,** 2983–3012 (2002).

2. Sippel, D. & Einsle, O. The structure of vanadium nitrogenase reveals an unusual bridging ligand. *Nat. Chem. Biol.* **13,** 956–960 (2017).

3. Seefeldt, L. C., Hoffman, B. M. & Dean, D. R. Electron transfer in nitrogenase catalysis. *Curr. Opin. Chem. Biol.* **16,** 19–25 (2012).

4. Howard, J. B. & Rees, D. C. Structural basis of biological nitrogen fixation. *Chem. Rev.* **96,** 2965–2982 (1996).

5. Hoffman, B. M., Lukoyanov, D., Yang, Z. Y., Dean, D. R. & Seefeldt, L. C. Mechanism of nitrogen fixation by nitrogenase: The next stage. *Chemical Reviews* **114,** 4041–4062 (2014).

6. Hoffman, B. M., Lukoyanov, D., Dean, D. R. & Seefeldt, L. C. Nitrogenase: A draft mechanism. *Acc. Chem. Res.* **46,** 587–595 (2013).

7. Peters, J. W. *et al.* Redox-dependent structural changes in the nitrogenase P-cluster. *Biochemistry* **36,** 1181–1187 (1997).

8. Yang, Z. Y. *et al.* Evidence That the Pi Release Event Is the Rate-Limiting Step in the Nitrogenase Catalytic Cycle. *Biochemistry* **55,** 3625–3635 (2016).

9. Pence, N. *et al.* Unraveling the interactions of the physiological reductant flavodoxin with the different conformations of the Fe protein in the nitrogenase cycle. *J. Biol. Chem.* **292,** 15661–15669 (2017).

10. Tezcan, F. A. *et al.* Nitrogenase Complexes: Multiple Docking Sites for a Nucleotide Switch Protein. *Science (80-.).* **309,** 1377–1380 (2005).

11. Seefeldt, L. C. *et al.* Control of electron transfer in nitrogenase. *Curr. Opin. Chem. Biol.* **47,** 54–59 (2018).

12. Igarashi, R. Y. & Seefeldt, L. C. Nitrogen Fixation: The Mechanism of the Mo-Dependent Nitrogenase. *Crit. Rev. Biochem. Mol. Biol.* **38,** 351–384 (2003).

13. Duval, S. *et al.* Electron transfer precedes ATP hydrolysis during nitrogenase catalysis. *Proc. Natl. Acad. Sci.* **110,** 16414–16419 (2013).

14. Ryle, M. J. & Seefeldt, L. C. Elucidation of a MgATP signal transduction pathway in the nitrogenase iron protein: Formation of a conformation resembling the MgATP-bound state by protein engineering. *Biochemistry* **35,** 4766–4775 (1996).

15. Thorneley, R. N. F. Nitrogenase of Klebsiella pneumoniae A stopped-Flow Study of Magnesium-Adenosine Triphosphate-Induced Electron Transfer Between The Component Proteins. *Biochem. J.* **145,** 391–396 (1975).

16. Seefeldt, L. C. *et al.* Control of electron transfer in nitrogenase. *Curr. Opin. Chem. Biol.* **47,** 54–59 (2018).

17. Danyal, K., Dean, D. R., Hoffman, B. M. & Seefeldt, L. C. Electron transfer within nitrogenase: Evidence for a deficit-spending mechanism. *Biochemistry* **50,** 9255–9263 (2011).

18. Owens, C. P., Katz, F. E. H., Carter, C. H., Luca, M. A. & Tezcan, F. A. Evidence for Functionally Relevant Encounter Complexes in Nitrogenase Catalysis. *J. Am. Chem. Soc.* **137,** 12704–12712 (2015).

19. Schlessman, J. L., Woo, D., Joshua-Tor, L., Howard, J. B. & Rees, D. C. Conformational variability in structures of the nitrogenase iron proteins from Azotobacter vinelandii and Clostridium pasteurianum. *J. Mol. Biol.* **280,** 669–685 (1998).

20. Tezcan, F. A., Kaiser, J. T., Howard, J. B. & Rees, D. C. Structural evidence for asymmetrical nucleotide interactions in nitrogenase. *J. Am. Chem. Soc.* **137,** 146–149 (2015).

21. Thorneley, R. N. F. & Lowe, D. J. Nitrogenase of Klebsiella pneumoniae Kinetics of the dissociation of oxidized iron protein from molybdenum-iron protein: Identification of the rate-limiting step for substrate reduction. *Biochem. J.* **215,** 393–403 (1983).

22. Hoffman, B. M., Lukoyanov, D., Yang, Z. Y., Dean, D. R. & Seefeldt, L. C. Mechanism of nitrogen fixation by nitrogenase: The next stage. *Chem. Rev.* **114,** 4041–4062 (2014).

23. Maritano, S., Fairhurst, S. A. & Eady, R. R. Long-range interactions between the Fe protein binding sites of the MoFe protein of nitrogenase. *J. Biol. Inorg. Chem.* **6,** 590–600 (2001).

24. Danyal, K. *et al.* Negative cooperativity in the nitrogenase Fe protein electron delivery cycle. *Proc. Natl. Acad. Sci.* **113,** E5783–E5791 (2016).

25. Engen, J. R. J. R. J. R. J. R. J. R. J. R. Analysis of Protein Conformation and Dynamics by Hydrogen/Deuterium Exchange MS. *Anal. Chem.* **81,** 7870–7875 (2009).

26. Englander, S. W. Hydrogen Exchange and Mass Spectrometry: A Historical Perspective. *J. Am. Soc. Mass Spectrom.* **17,** 1481–1489 (2006).

27. Wales, T. E. & Engen, J. R. Hydrogen exchange mass spectrometry for the analysis of protein dynamics. *Mass Spectrom. Rev.* **25,** 158–170 (2006).

28. Woodward, C., Simon, I. & Tüchsen, E. Hydrogen exchange and the dynamic structure of proteins. *Mol. Cell. Biochem.* (1982). doi:10.1007/BF00421225

29. Eyles, S. J. & Kaltashov, I. A. Methods to study protein dynamics and folding by mass spectrometry. *Methods* **34,** 88–99 (2004).

30. Konermann, L., Pan, J. & Liu, Y.-H. Hydrogen exchange mass spectrometry for studying protein structure and dynamics Introduction: protein folding, dynamics, and function. *Chem. Soc. Rev. Chem. Soc. Rev* **40,** 1224–1234 (2011).

31. Walters, B. T., Ricciuti, A., Mayne, L. & Englander, S. W. Minimizing back exchange in the hydrogen exchange-mass spectrometry experiment. *J. Am. Soc. Mass Spectrom.* **23,** 2132–2139 (2012).

32. Woodward, C., Simon, I. & Tüchsen, E. Hydrogen exchange and the dynamic structure of proteins. *Mol. Cell. Biochem.* **48,** 135–160 (1982).

33. Engen, J. R. Analysis of Protein Conformation and Dynamics by Hydrogen/Deuterium Exchange MS. *Anal. Chem.* **81,** 7870–7875 (2009).

34. Englander, S. W., Mayne, L., Bai, Y. & Sosnick, T. R. Hydrogen exchange: the modern legacy of Linderstrøm-Lang. *Protein Sci.* **6,** 1101–1109 (1997).

35. Weis, D. D., Wales, T. E., Engen, J. R., Hotchko, M. & Ten Eyck, L. F. Identification and Characterization of EX1 Kinetics in H/D Exchange Mass Spectrometry by Peak Width Analysis. *J. Am. Soc. Mass Spectrom.* **17,** 1498–1509 (2006).

36. Jaswal, S. S. Biological insights from hydrogen exchange mass spectrometry. *Biochim. Biophys. acta Protein Proteomics* **1834,** 1188–201 (2013).

37. Resetca, D. & Wilson, D. J. Mapping ligand binding using microfluidics-enabled millisecond timescale hydrogen-deuterium exchange. *Int. J. Mass Spectrom.* **420,** 67–73 (2017).

38. Moorthy, B. S., Badireddy, S. & Anand, G. S. Cooperativity and allostery in cAMP-dependent activation of Protein Kinase A: Monitoring conformations of intermediates by amide hydrogen/deuterium exchange. *Int. J. Mass Spectrom.* **302,** 157–166 (2011).

39. Casares, S., Sadqi, M., López-Mayorga, O., Martínez, J. C. & Conejero-Lara, F. Structural cooperativity in the SH3 domain studied by site-directed mutagenesis and amide hydrogen exchange. *FEBS Lett.* **539,** 125–130 (2003).

40. Singh, H., Dai, Y., Outten, F. W. & Busenlehner, L. S. Escherichia coli SufE sulfur transfer protein modulates the SufS cysteine desulfurase through allosteric conformational dynamics. *J. Biol. Chem.* **288,** 36189–200 (2013).

41. Keppel, T. R. & Weis, D. D. Analysis of disordered proteins using a simple apparatus for millisecond quench-flow H/D exchange. *Anal. Chem.* (2013). doi:10.1021/ac4004979

42. Christiansen, J., Goodwin, P. J., Lanzilotta, W. N., Seefeldt, L. C. & Dean, D. R. Catalytic and biophysical properties of a nitrogenase apo-MoFe protein produced by a nifB-deletion mutant of Azotobacter vinelandii. *Biochemistry* **37,** 12611–12623 (1998).

43. Seefeldts, L. C., Morgan, T. V., Dean, D. R. & Mortensonst, L. E. Mapping the

Site(s) of MgATP and MgADP Interaction with the Nitrogenase of Azotobacter vinelandii. *J. Biol. Chem.* **267,** 6680–6688 (1992).

44. Berry, L., Patterson, A., Pence, N., Peters, J. W. & Bothner, B. Hydrogen Deuterium Exchange Mass Spectrometry of Oxygen Sensitive Proteins. *Bioprotocols* **8,** 1–16 (2018).

45. Kavan, D. & Man, P. MSTools - Web based application for visualization and presentation of HXMS data. *Int. J. Mass Spectrom.* (2011). doi:10.1016/j.ijms.2010.07.030

46. Pettersen, E. F. *et al.* UCSF Chimera - A visualization system for exploratory research and analysis. *J. Comput. Chem.* **25,** 1605–1612 (2004).

47. Weis, D. D., Wales, T. E., Engen, J. R., Hotchko, M. & Ten Eyck, L. F. Identification and Characterization of EX1 Kinetics in H/D Exchange Mass Spectrometry by Peak Width Analysis. *J. Am. Soc. Mass Spectrom.* **17,** 1498–1509 (2006).

48. Guttman, M., Weis, D. D., Engen, J. R. & Lee, K. K. Analysis of overlapped and noisy hydrogen/deuterium exchange mass spectra. *J. Am. Soc. Mass Spectrom.* (2013). doi:10.1007/s13361-013-0727-5

49. Owens, C. P., Katz, F. E. H., Carter, C. H., Oswald, V. F. & Tezcan, F. A. Tyrosine-Coordinated P-Cluster in G. diazotrophicus Nitrogenase: Evidence for the Importance of O-Based Ligands in Conformationally Gated Electron Transfer. *J. Am. Chem. Soc.* **138,** 10124–10127 (2016).

50. Kim, C. H., Newton, W. E. & Dean, D. R. Role of the MoFe Protein a-Subunit Histidine-195 Residue in FeMo-Cofactor Binding and Nitrogenase Catalysis. *Biochemistry* **34,** 2798–2808 (1995).

Supplementary Material C

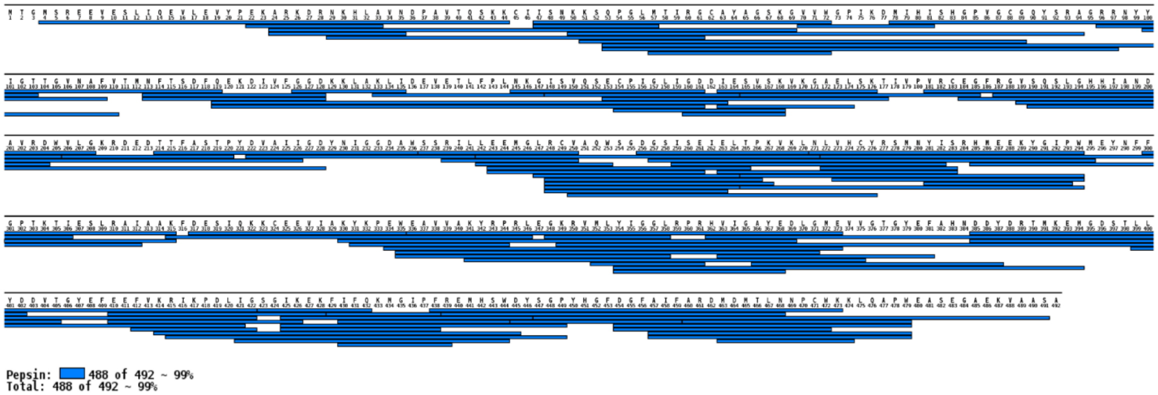

Supplementary Figure 5.1. Peptide coverage map of the α MoFeP subunit. The blue bars represent a peptide identified with LC-MS and LC-MS/MS.

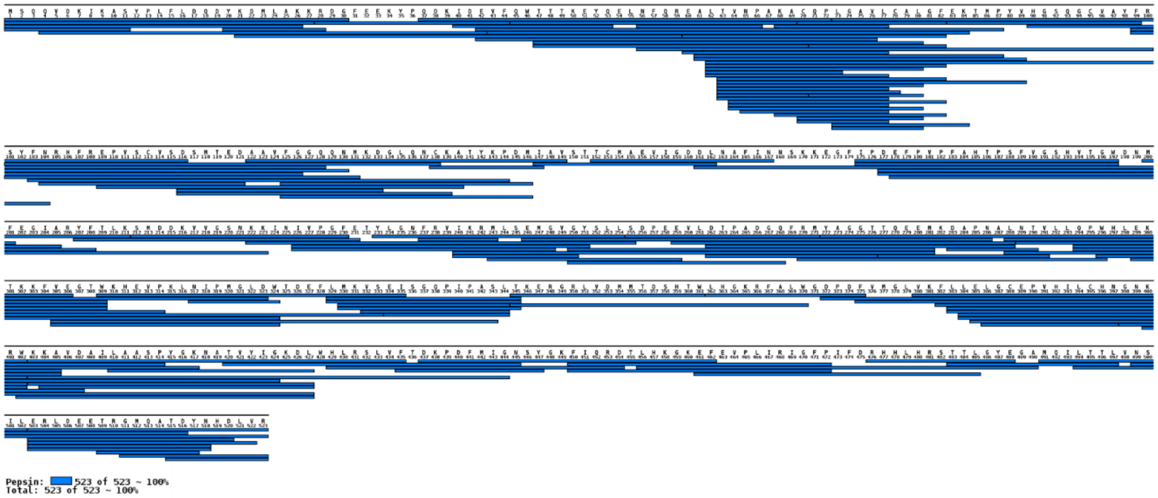

Supplementary Figure 5.2. Peptide coverage map of the β MoFeP subunit. The blue bars represent a peptide identified with LC-MS and LC-MS/MS.

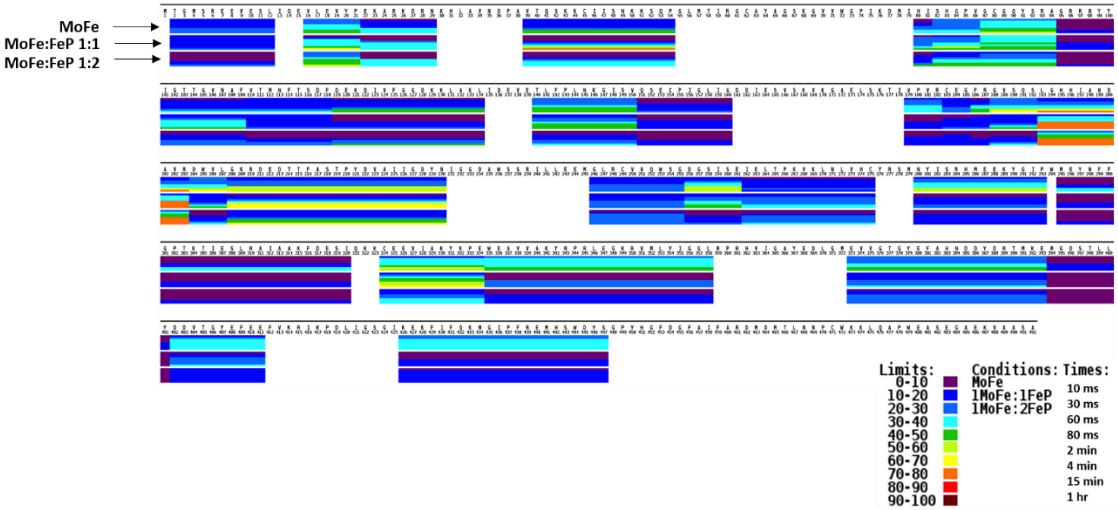

Supplementary Figure 5.3. Comparison of the percent deuterium (%D) incorporated into the 37 peptides from the α subunit showing high confidence scores for deuterium incorporation in the MoFe, MoFe:FeP 1:1, and MoFe:FeP 1:2 conditions over the time course of the experiment. The gradient of the heat map indicates the %D incorporated with purple indicating 0-10% and dark red indicating 90-100%.

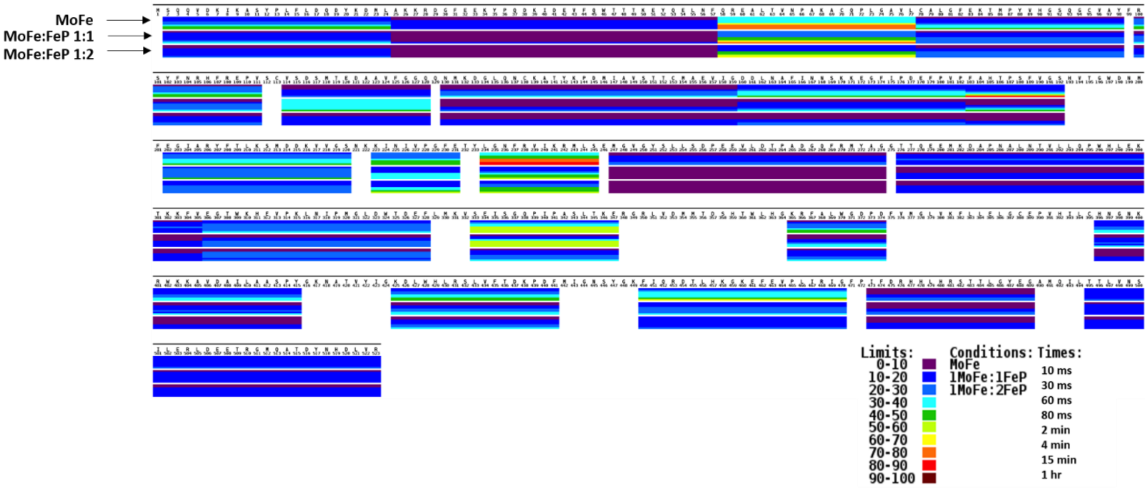

Supplementary Figure 5.4. Comparison of the percent deuterium (%D) incorporated into the 26 peptides from the β subunit showing high confidence scores for deuterium incorporation in the MoFe, MoFe:FeP 1:1, and MoFe:FeP 1:2 conditions over the time course of the experiment. The gradient of the heat map indicates the %D incorporated with purple indicating 0-10% and dark red indicating 90-100%.

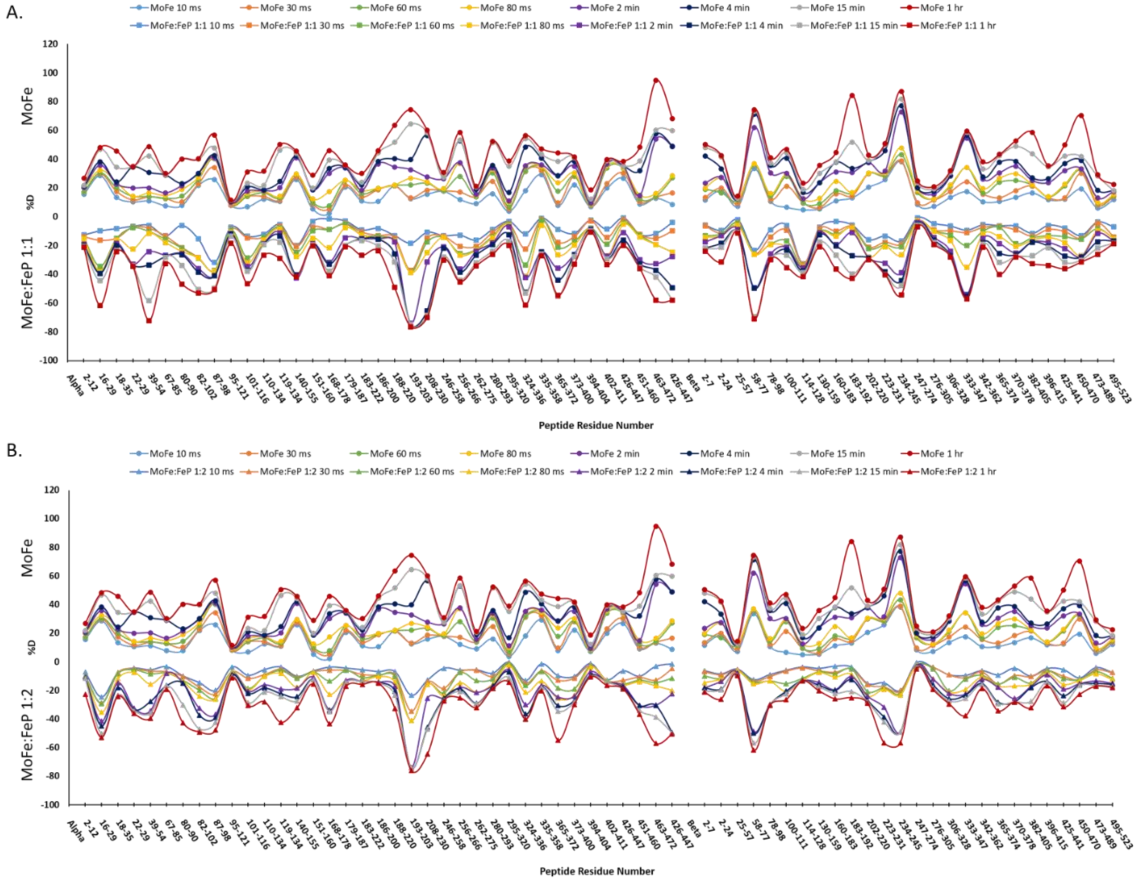

Supplementary Figure 5.5. Butterfly plots showing the percent deuterium incorporated (%D) at all time points (10 ms, 30 ms, 60 ms, 80 ms, 2 min, 4 min, 15 min, and 1 hr) for each of the peptides with high confidence scores from the α (left) and β (right) subunits of the MoFe protein. **A.** Comparison of the MoFe (positive values) and MoFe:FeP 1:1 conditions (negative values). **B.** Comparison of the MoFe (positive values) and MoFe:FeP 1:2 conditions (negative values).

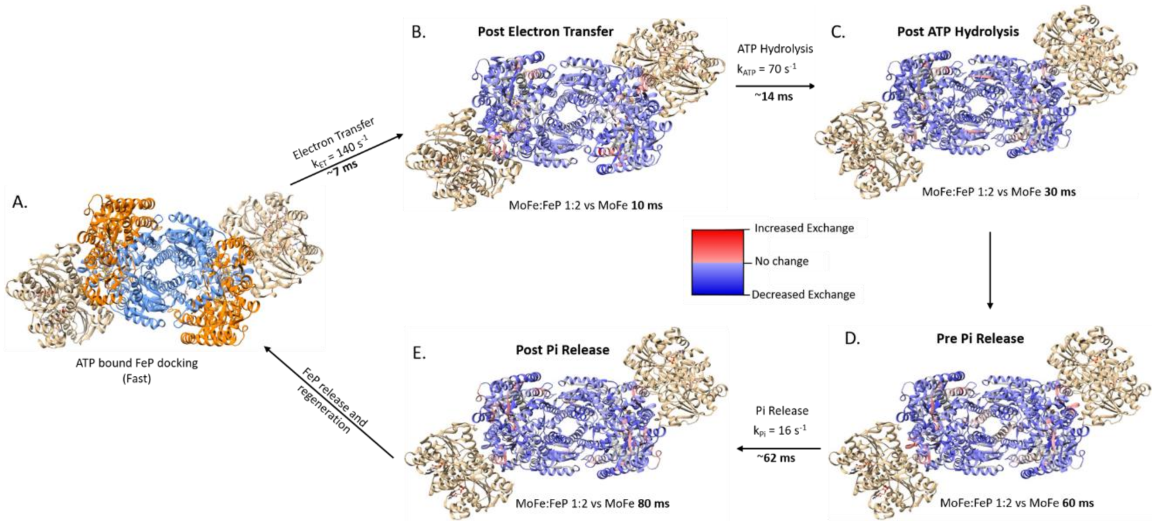

Supplementary Figure 5.6. Structural heatmaps showing the differences in exchange between the MoFe:FeP 1:2 condition and the MoFe condition at the millisecond time points mapped onto the structure of the MoFe protein in accordance with the different steps of the FeP cycle. For all structures, red regions indicate an increase in deuterium exchange in the MoFe:FeP 1:2 condition and blue regions indicate a decrease in deuterium exchange in the MoFe:FeP 1:2 condition. **A.** ATP bound FeP docks with the MoFe protein (PDB ID: 4WZB; AMP-PCP bound FeP shown in tan, α-MoFe shown in orange, and β-MoFe shown in blue). After FeP docking, electron transfer between the two proteins occurs at a rate of k_{ET}= 140 s^{-1} which is approximately 7 ms. **B.** The 10 ms time point captures the state of the MoFe protein shortly after ET. The differences in exchange of the MoFe:FeP 1:2 vs MoFe comparison was mapped onto the AMP-PCP bound FeP-MoFe crystal structure (PDB ID: 4WZB). After ET, ATP hydrolysis occurs at a rate of k_{ATP} = 70 s^{-1}, approximately 14 ms after FeP docking. **C.** After ATP hydrolysis, the ADP bound FeP changes conformation, changing the interactions between the FeP and MoFeP. The difference in exchange for the MoFe:FeP 1:2 vs MoFe comparison is mapped onto the ADP bound FeP-MoFe crystal structure (PDB ID: 2AFI). **D.** Shows the state of the MoFe protein at 60 ms, prior to Pi release for the MoFe:FeP 1:2 vs MoFe comparison. Pi release occurs at a rate of k_{Pi} = 14 s^{-1}, approximately 62 ms after FeP docking. **E.** The protein state at 80 ms reveals the effects Pi release has on the MoFeP structure and dynamics. The differences in exchange of the MoFe:FeP 1:2 vs MoFe comparison is shown.

CHAPTER SIX

SUMMARY AND CONCLUSIONS

Abstract

It was originally thought that electron bifurcation was a unique mechanism only found in the protonmotive Q cycle of the electron transport chain. Recent studies have identified several enzymes that exhibit bifurcating activity in anaerobic organisms. The most studied of these enzymes are the NADH-dependent ferredoxin-NADP$^+$ oxidoreductase (Nfn), the electron transfer flavoprotein (Etf) and the [FeFe]-hydrogenase (Hyd). One of the goals of studying the electron bifurcation mechanism is to determine how electron carriers with a high reduction potential are created under anaerobic conditions. Studies on these systems revealed the diversity of the electron bifurcation reaction, including the different cofactors that act as the site of bifurcation. A major revelation from these studies is that allostery plays a role in the regulation of electron transfer down the endergonic and exergonic branches. These studies also identified the framework of an allosteric communication pathway in the Nfn bifurcating system. To fully understand how electron bifurcation acts as a mechanism of energy conservation, studies on the systems that use the reduced products are also being studied. The most studied are the nitrogenase systems, which are capable of catalyzing the biological reduction of nitrogen, one of the most challenging biological reactions. Three different nitrogenase systems (the Mo-dependent, V-dependent, and Fe-dependent) have been identified that reduce atmospheric nitrogen. Current studies are focused on minimizing the gap in knowledge on the structure-function relationship of the Mo-dependent nitrogenase system, which is the most studied, and the V-dependent and Fe-dependent nitrogenases. Additional studies have provided evidence of negative cooperativity in the Mo-dependent nitrogenase system. Biophysical studies using millisecond time scale H/D exchange measurements are focused on uncovering a pathway of allosteric communication and identifying the mechanistic role of negative cooperativity in the Mo-dependent nitrogenase.

Electron Bifurcation: A New Mechanism of Energy Conservation

After its discovery it was thought that electron bifurcation (EB) was a mechanism for the transfer of electrons that was exclusive to the proton motive Q Cycle found in the electron transport chain of aerobic cellular respiration (**Fig 6.1**)[1,2].

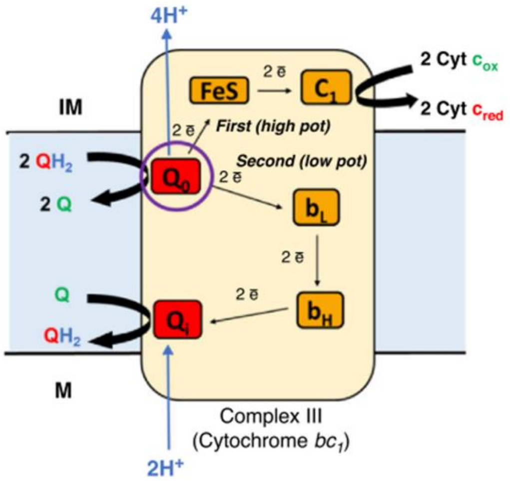

Figure 6.1 Simplified complex III in the ETC. Ubiquinone (Q) accepts electrons from complex I and II, forming the reduced Ubiquinol (QH_2). QH_2 is oxidized to Q, transferring a total of four electrons to Q_0 which bifurcates to the FeS and b_L heme and four protons are transferred into the inner membrane. The 2 electrons from the FeS are transferred to C_1, which reduces cytochrome c. From b_L, the electrons reduce the b_H heme, and then reduce Q_i, which in turn reduces a Q to QH_2, thus regenerating the Q cycle. This figure was adapted from Peters et al, 2018[2].

It was over thirty years later when an enzyme exhibiting activity consistent with EB outside of the electron transport chain was discovered[3]. The basic mechanism of EB involves the coupling of exergonic and endergonic electron transfer events to minimize the amount of free energy lost as heat[4]. Unlike standard oxidation-reduction (redox) reactions found in the “classic” mechanisms of energy conservation (substrate level phosphorylation and oxidative phosphorylation), EB can couple electron transfer reactions that are energetically unfavorable, allowing these reactions to proceed spontaneously[4–6]. Typically electron transfer reactions involve an electron traveling from a more negative to a more positive reduction potential, however with EB, electron transfers from a more positive to a more negative reduction potential are possible[2,4,7,8]. The discovery of EB enzymes outside of cellular respiration revolutionized studies on anaerobic metabolism and energy production. Prior to this discovery it was unknown how anaerobic organisms thrive without access to cellular respiration to produce large amounts of adenosine triphosphate (ATP)[9]. It is now known that through the use of EB anaerobic organisms survive using reduced equivalents of ferredoxin (Fd) as a source of energy[2,4,7,8,10].

Fd is a small monomeric protein that contains a [4Fe-4S] cluster with a highly negative reduction potential (~420 mV)[3,4,7,11]. The reduction potential of Fd indicates that it is more likely to act as an electron donor than an electron acceptor, making the reduction of Fd an energetically demanding process without the use of EB. To reduce Fd, EB enzymes couple an exergonic reduction reaction with the endergonic reduction of Fd using an electron donor with an intermediate reduction potential as a source of electrons. The oxidation of the electron donor leads to a reduced bifurcating center, which first sends an electron down the exergonic reduction branch. The resulting intermediate at the bifurcating center is unstable, but contains a negative reduction potential with sufficient energy to reduce Fd[4,12,13]. The discovery of EB has led to the successful characterization of the bifurcating mechanism in several EB enzymes. The most studied systems are the

NADH-dependent ferredoxin-NADP$^+$ oxidoreductase (Nfn), the electron transfer flavoprotein (Etf), and the [FeFe]-Hydrogenase (Hyd)[2–4,12,14–17]. These enzymes vary greatly from one another based on their size, structure, as well as the cofactors that act as the bifurcating center, and the relay for the electrons to travel down the exergonic and endergonic reduction pathways (**Fig 6.2**) [2–4,12,14–17].

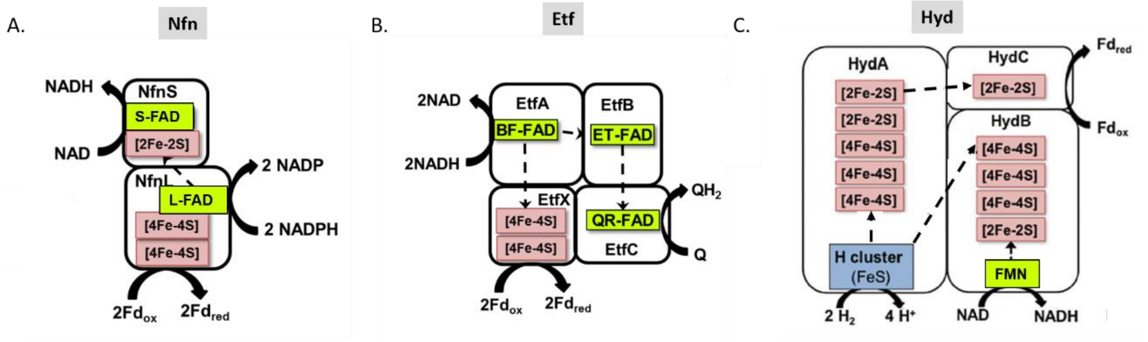

Figure 6.2 Schematic representation of the three model bifurcating enzymes Nfn (**A**), Etf (**B**), and Hyd (**C**). Each schematic details the cofactor and ligand binding sites, while also depicting the hypothesized electron flow for the bifurcating reactions in Nfn, Etf, and Hyd.

The characterization of the EB mechanism has led to the establishment of EB as a third mechanism of energy conservation[2,4,8,10,18,19]. An aspect of EB that remains unknown is how the enzymes regulate the flow of electrons to prevent the transfer of two electrons down the exergonic branch. It has been hypothesized that electron transfer is controlled through a gating mechanism that prevents a second electron traveling through the exergonic pathway[4]. However, biophysical evidence detailing the structure and dynamics of the enzymes during EB is needed to conclusively state if a large-scale conformational change is regulating the flow of electrons, or if more subtle shifts in the protein structure are preventing transfer.

Detailing the Structure and Dynamics of the NADH-Dependent Ferredoxin-NADP$^+$ oxidoreductase

To better understand the regulation of electron flow in the bifurcating enzymes, we characterized the structure and dynamics of the Nfn system using H/D exchange coupled to mass spectrometry (HDX-MS) and statistical coupling analysis (SCA). Amide hydrogens on the peptide backbone freely exchange with hydrogens in solution. By replacing the solvent system with deuterated water (D_2O), deuterium will instead exchange with the amide hydrogens. Using mass spectrometry, the shift in the mass-to-charge ratio (m/z) can be used to determine how much deuterium is incorporated at a given time[20–25]. The structure of a protein heavily influences the rate of deuterium incorporation, primarily through secondary structural elements (alpha helices and beta sheets), which are stabilized by hydrogen bonds involving the amide hydrogens of the peptide backbone[20,26,27]. Stable secondary structures are less likely to unfold, making the amide hydrogens less accessible, whereas more dynamic secondary structures will experience fast local unfolding events that expose the amide hydrogens to exchange. The tertiary interactions of a protein can also influence the rate of exchange due to the surface of a protein's 3D structure being more accessible to fast exchange, while the interior of the protein will take longer to exchange because it is less accessible to the solvent. Additionally, quaternary protein-protein interactions or protein-ligand interactions can also effect the rate of exchange. Binding of a protein or ligand can stabilize the site of binding, decreasing the accessibility for exchange, allowing the site of binding within a protein to be identified. Alternatively, protein and ligand binding can also cause an allosteric conformational change, which in turn would also effect the rate of exchange not just at the site of binding, but at the rest of the protein. This aspect makes HDX-MS an ideal technique for the characterization of the Nfn system's structure and dynamics during the different steps of the bifurcation reaction[28–31].

The goal of this study was to characterize the structure and dynamics of the Nfn system during the bifurcation and confurcation reactions. This was accomplished by measuring the amount of deuterium incorporated into Nfn when the pyridine nucleotide substrates or Fd were present[32]. This led to eight conditions being tested by HDX-MS (As-purified Nfn, Fd bound, NADH bound, $NADP^+$ bound, NADH+$NADP^+$ bound, NAD^+ bound, NADPH bound, and NADPH+NAD^+ bound) at five time points (1 min, 3 min, 15 min, 1 hr, and 3 hrs). Initial analysis of the deuterium incorporation showed that overall the as-purified condition incorporated the most exchange, suggesting it is the most dynamic conformation, and therefore the most accessible to exchange. Examination of the pyridine nucleotide substrates and Fd bound states showed an overall decrease in exchange, with the sharpest decrease appearing at the site of binding for each of the substrates and Fd. These observations are consistent with other HDX-MS studies investigating the binding effects of ligands[33,34]. However, changes in the deuterium incorporation were not only observed at the site of binding, but also at other regions throughout the Nfn structure, suggesting allosteric communication between the pyridine nucleotides and Fd binding sites. To better visualize these changes, six regions that suggested allosteric behavior were highlighted on the structure of Nfn (**Fig. 6.3**).

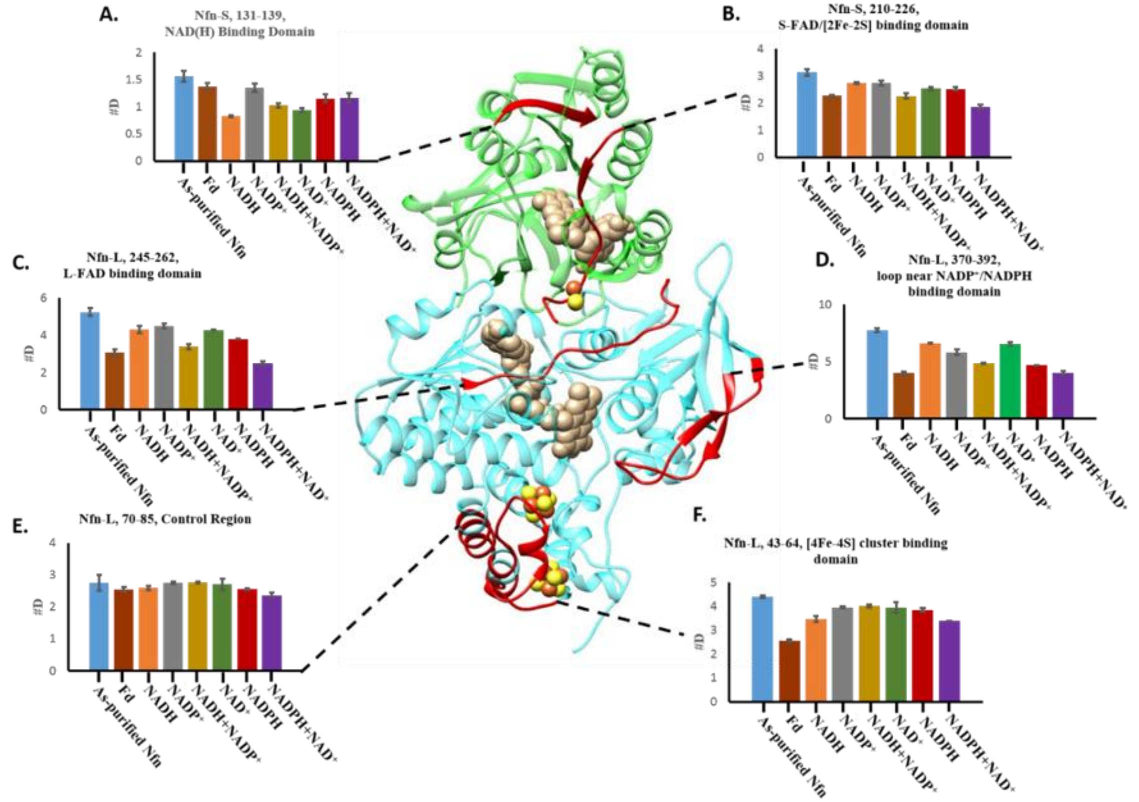

Figure 6.3 Ribbon diagram depicts peptides of interest (**A-F**), as mapped in red, in the Nfn structure from *P. furiosus* (PDB ID: 5JCA). Each histogram plot shows exchange for the indicated peptide after 3 hrs of incubation in deuterated buffer. Each bar represents a different condition: Blue (as-purified Nfn), brown (Fd bound), orange (NADH bound), grey (NADP bound), gold (NADH+NADP bound), green (NAD bound), red (NADPH bound), and purple (NAD+NADPH bound). The peptides indicated are key regions that are thought to be involved in the electron bifurcation reaction. (**A**). Nfn-S (green ribbon structure) residues 131-139 involved in NAD(H) binding. (**B**). Residues 210-226 involved in coordinating the S-FAD and the [2Fe-2S] of Nfn-S are shown. (**C**). Nfn-L (blue ribbon structure) residues 245-262 are near the L-FAD. (**D**). Residues 370-392 are involved in NADP(H) binding. (**E**). Residues 70-85 act as a HDX-MS control region. (**F**). Residues 43-64 are involved in coordinating the two [4Fe-4S] clusters of Nfn-L. Error bars indicate the standard deviation of three replicates.

The deuterium incorporation after 3 hrs of exchange was displayed for each of the eight conditions tested. The regions examined include the NAD(H) binding domain (Nfn-S 131-139**Fig. 6.3A**), S-FAD and [2Fe-2S] cluster domain (Nfn-S 210-226, **Fig. 6.3B**), the

L-FAD binding domain (Nfn-L 245-262, **Fig. 6.3C**), the NADP(H) binding domain (Nfn-L 370-392, **Fig. 6.3D**), and the Fd docking domain (Nfn-L 43-64, **Fig. 6.3F**). Residues 70-85 of the Nfn-L subunit acted as a control region to validate the effectiveness of the HDX-MS reaction (**Fig. 6.3E**).

The presence of allostery was determined by examining the deuterium incorporation when only one pyridine nucleotide, or Fd, was bound. For instance, examining the Nfn-S 131-139 region (**Fig. 6.3A**) revealed that when NAD^+ binds to this region a 30% decrease in exchange is observed (relative to the as-purified condition). Upon examining the deuterium incorporation in the NADPH bound condition (which binds near Nfn-L 370-392, **Fig. 6.3D**), a 20% decrease in deuterium incorporation is observed in Nfn-S 131-139, suggesting this region becomes more protected when NADPH binds to Nfn-L. Examining the site of NADPH binding when NAD^+ is present shows a 20% decrease in exchange (**Fig. 6.3D**). This behavior suggested that pyridine nucleotide or Fd binding causes global conformational changes. These changes are occur at the cofactor and substrate binding sites and act to "prime" the Nfn structure for either the bifurcating or confurcating reaction, depending on which nucleotides are bound.

To further support our evidence of allosteric communication in the Nfn system, and to reveal a pathway of communication throughout the complex, we incorporated statistical coupling analysis (SCA)[35–37]. SCA uses a multiple sequence alignment of a protein of interest with 100+ homologous proteins. Each residue is compared with the sequences of the homologous proteins, and when a mutation is found the remaining amino acid residues in that sequence are compared to the sequence of interest in order to identify another mutation. If another mutated residue is found, these residues are considered to be co-evolving, and possibly involved in pathways of communication throughout a protein complex. SCA on the Nfn complex identified fourteen residues that are potentially involved in communication throughout Nfn: six were identified in Nfn-S and eight in Nfn-L (**Fig. 6.4**).

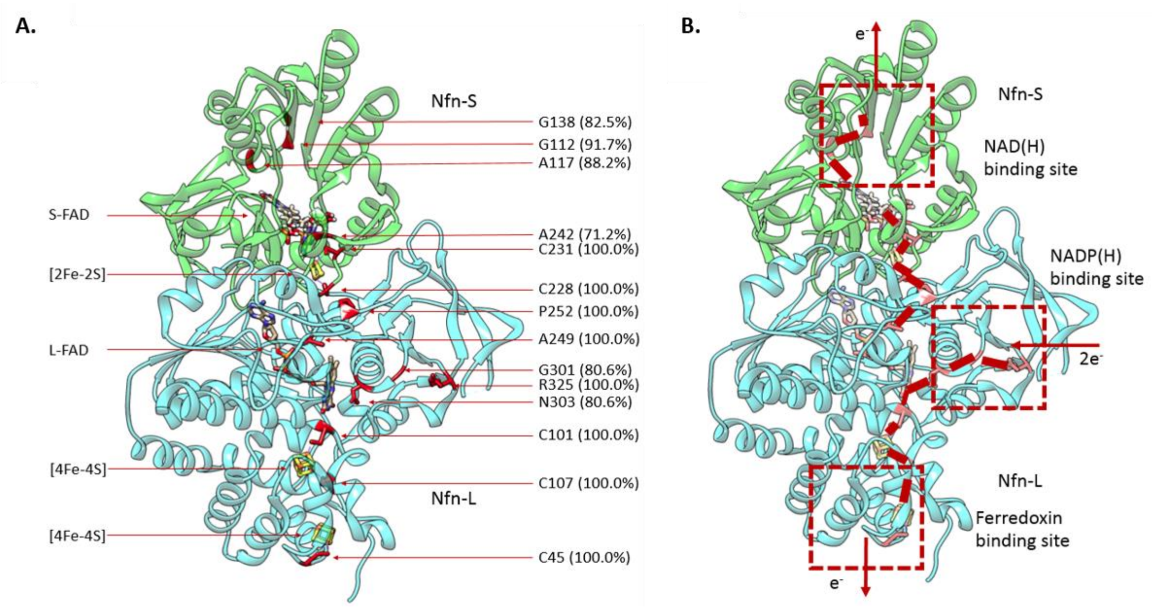

Figure 6.4 (**A**). Structure of Nfn (PDB ID: 5JCA) with residues represented by red sticks that are potentially involved in allosteric communication. All the identified residues along the putative pathway were within 6Å of each other. Here, the small subunit of Nfn (i.e Nfn-S) is represented in green and the large subunit of Nfn (i.e. Nfn-L) is represented in cyan The residues identified in the allosteric communication pathway. Here, the first letter abbreviation is used to denote each residue while the number indicates the position in the structure of *P. furiosus* Nfn (PDB ID: 5JCA). The number in parentheses represents the percent conservation of this residue in our Nfn sequence database comprising 396 Nfn-like homologous sequences. (**B**). Potential pathway of electron transfer between the nucleotide binding and Fd binding sites, coordinating the two [4Fe-4S] clusters of Nfn-L.

Three of the six residues in Nfn-S are present in peptides identified via HDX-MS analysis: Glycine at position 138 within the 131-139 region peptide that interacts with NAD^+/NADH, G112 in peptide 95-113 that interacts with the S-FAD, and G226 that interacts with the [2Fe-2S] cluster. Likewise, eight of the 14 residues were identified in NfnL that connect the L-FAD to the $NADP^+$/NADPH and Fd binding sites. Two of these residues were detected by HDX-MS as being involved in deuterium exchange: Proline at position 252 (P252) in peptide 242-262 that interacts with L-FAD and cysteine at position 45 (C45) in peptide 43-64 that interacts with the distal [4Fe-4S] cluster and Fd.

The identification of an allosteric pathway in the Nfn complex provided new insights into the mechanism of EB. First, the presence of an allosteric pathway suggests a sophisticated means of regulation that controls whether the bifurcating or confurcating reaction will proceed. For instance, binding of NADPH causes a decrease in exchange at the site of binding, but also causes a decrease in exchange at the Fd and NAD^+ binding site, which is the result of these domains becoming more stable. The change in conformation likely alters the binding affinity of the pyridine nucleotide substrates, decreasing the affinity for NADH, while increasing the affinity for NAD^+. Another insight provided by this study is that the originally hypothesized conformational changes to control electron gating are present, however the changes are much more subtle than previously thought. Instead of causing a large scale conformational change that alters the interactions between Nfn-S and Nfn-L, the Nfn system instead experiences smaller changes that alter the distances between the L-FAD and the exergonic reduction branch, in order to decrease the likelihood of a second electron traveling down the exergonic branch.

Characterizing the Similarities and Differences in The Structure-Function Relationship of the Nitrogenase Systems

While the characterization of the EB mechanism is of great interest, another area of focus are the reactions reduced Fd catalyzes. The most well-known reaction is the reduction of atmospheric nitrogen (N_2) to ammonia (NH_3) catalyzed by the nitrogenase systems under standard temperatures and pressures[38–43]. There are three variations of the nitrogenase, each characterized by a unique transition metal present at the active site: the Mo-dependent, V-dependent, and Fe-dependent nitrogenases[41–43]. Of the three nitrogenase systems, the Mo-dependent is the most studied and the Fe-dependent is the least studied. The Fe-dependent nitrogenase, like the Mo-dependent and V-dependent, Uses two proteins to reduce N_2, the FeFe protein (AndDGK) and the Fe Protein (AnfH). The association and dissociation of AnfH with the AnfDGK complexes is known as the Fe protein cycle and describes the transfer of an electron from AnfH to the active site of AnfDGK, the FeFe-cofactor (FeFe-co), and the subsequent ATP hydrolysis and Pi release events that cause the dissociation of AnfH from the AnfDGK complex. Dissociation of AnfH makes it accessible for regeneration so the Fe protein cycle can repeat and transfer the needed number of electrons to the FeFe-co to reduce N_2 to NH_3[44,45]. A major way the V-dependent and Fe-dependent nitrogenases differ from the Mo-dependent nitrogenase is the presence of an additional G subunit[46–49]. While the G subunit is necessary for N_2 reduction, its exact role in catalysis is unknown[50,51]. Using a combination of HDX-MS, chemical cross-linking (XL-MS), and normal mode analysis (NMA) we set out to characterize the structure-function relationship of the AnfDGK protein, and compare it to the MoFe protein (NifDK) to determine the functional role of G subunit, and how the structure-function relationship regulates N_2 reduction.

Our study provided numerous insights into the nature of the interactions in the AnfDGK complex. First, we identified a significant number of high confidence cross-links longer than 30 Å when using the BS3 cross-linking reagent (**Fig. 4.5A**).

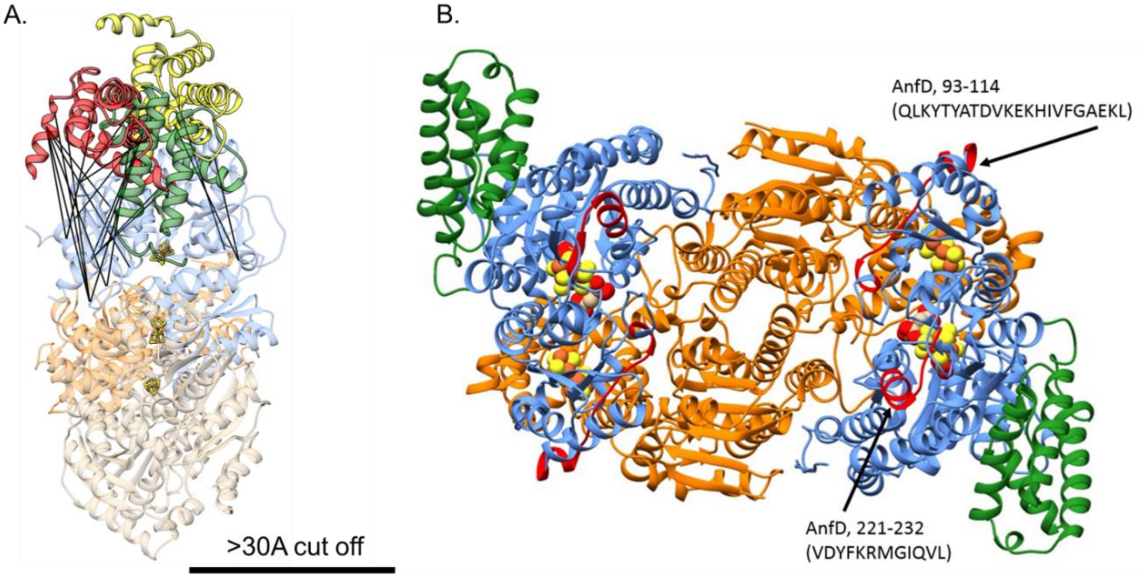

Figure 6.5 Presence of bimodal peptides and long distance cross-links is consistent with the FeFe protein multiple conformations in solution. (**A**) Long distance cross-links between AnfD and AnfG are located mostly in the loop regions and a short helix on AnfD. By rotating the position of AnfG into two alternative positions, as could occur during the Fe protein cycle, all distance constraints can be met. This suggests that the crystal structure of the VFe protein caught only one conformation within the ensemble of FeFe protein. AnfG subunits in red and yellow project alternate docking orientations on AnfD subunit. (**B**) Peptides with bimodal behavior (in red) were found on AnfD and AnfK subunits near P-cluster and FeFe-cofactor.

When examining these cross-links on the homology model of the AnfDGK complex we observed that the cross-linked regions were either part of long loops or short helices, which are secondary structural elements are often involved in protein-protein interactions. Second, detailed examination of the deuterium incorporation in the AnfDGK and NifDK proteins revealed the presence of bimodal peptides in the AnfDGK complex, indicating that these regions are adopting two different conformations simultaneously during the course of the exchange reaction (**Fig. 4.5B**). The presence of extra-long cross-links and peptides with bimodal exchange behavior suggest that AnfDGK is a highly dynamic complex, adopting multiple conformations simultaneously. This dynamic behavior can also be interpreted to mean that the AnfDGK complex adopts an asymmetric conformation, meaning the two AnfDGK trimers are in a different conformation. This behavior has been observed in the NifDK complex of the Mo-dependent nitrogenase, and has been implicated in allosteric regulation of electron transfer through negative cooperativity[52,53]. This behavior was first identified in NifDK pre-steady-state kinetic measurements and was further confirmed using NMA of the NifDK complex. Following the line of reasoning of this previous study, we employed NMA of the AnfDGK homology model. This revealed that at several regions of the AnfDGK complex, such as the P-cluster binding site, AnfH binding site, AnfD-G interface, and the AnfK-K interface there is a distinct asymmetric displacement pattern. However, this was not the asymmetrical behavior that was expected where the AnfD$_1$G$_1$K$_1$ trimer is adopting a similar conformation, and the AnfD$_2$G$_2$K$_2$ trimer is adopting another. Instead the behavior we observed indicated that AnfD$_1$G$_1$K$_2$ subunits are adopting a similar conformation, as seen by the positive correlation at the functionally relevant regions (**Fig. 6.6B**).

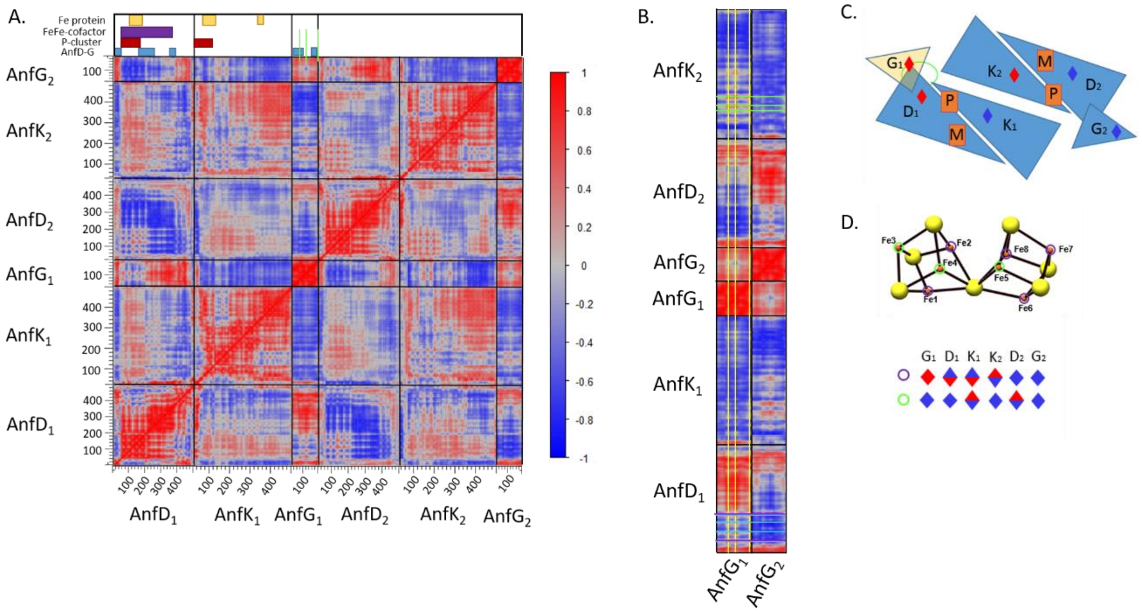

Figure 6.6. Normal mode analysis of the AnfDGK complex. (**A**) Covariance matrix shows the displacement of amino acid residues in Fe-nitrogenase complex. Regions of correlated (in-phase) and anti-correlated (out-of-phase) motions are shown in red and blue, respectively. Axis labels represent approximation of residue numbers at that location. Colored bars at the top represent specific regions of interest within the complex: AnfD-G interactions (blue), P-cluster site (red), FeFe-cofactor (purple), and Fe protein binding site (gold). (**B**) AnfG interaction network. Yellow lines correspond to three main interaction points between AnfG and AnfD. They are positively (movement it the same phase) correlated with the AnfD P-cluster environment (cyan lines), Fe protein binding site (purple lines) and AnfK-K interface (green lines). (**C**) Schematic model highlighting correlations within AnfG interaction network. Red and blue diamonds correspond to regions in- and out-of-phase, respectively. (**D**) The P-cluster interaction network. Green and purple circles distinguish parts of the first coordination sphere showing the same trends of the correlated motions. Red (in-phase) and blue (out-of-phase) triangles correspond only to the differences in the correlated motions between individual subunits. Top/bottom triangle refers to difference in N/C-terminal part of the subunit.

To fully understand the unique dynamics observed in the AnfDGK complex, we developed an ensemble allosteric model (EAM). The framework of the EAM is unique in that it views allostery in terms of ensembles that are dictated by the intrinsic stabilities of conformations for each cooperative substructure in the protein and the interactions between domains[54]. The EAM can also be used to investigate the effects of a thermodynamic architecture of a protein, which describes how energy changes in one part of a protein are manifested at distal sites. This describes the propagation of a signal that is initiated by the binding of a ligand which effects the thermodynamic landscape and how the conformational equilibria in the different regions of the protein are poised prior to ligand binding[55,56]. Investigation of crystal structures of the NifDK and VnfDGK complexes, as well as our homology model of the AnfDGK complex reveal very little structural differences. This does not exclude an allosteric mechanism in the nitrogenase systems, instead it indicates that the process is regulated by thermodynamics, rather than protein dynamics. This indicates that conformational changes result in subtle protein movements rather than large scale rigid body movements. This domain tunability can be modulated by many factors such as covalent modification, protons and cofactors and change in pH. This important feature of an EAM is that the energy landscape can be poised to respond in a "functionally pluripotent manner"[57,58]. Our *in silico* and in solution experiments strongly suggest that dynamic energy landscape defines catalytic activity of Fe-dependent nitrogenase.

Negative Cooperativity and the Regulation of Electron Transfer

Evidence of asymmetric dynamics in the AnfDGK complex fueled the desire to further investigate the Mo-dependent nitrogenase, which is thought to be regulated by a mechanism of negative cooperativity[53,59]. It is hypothesized that upon the binding of one equivalent of Fe protein (FeP) to the MoFe protein (MoFeP), an allosteric signal is sent across the heterodimer interface, suppressing electron transfer on the FeP half of the complex. However, there lacked biophysical evidence to support this hypothesis. Additionally, based on the NMA of the MoFe-FeP complex several potential pathways of allostery have been identified, but the specific pathway of communication in the MoFeP remains unknown.

To obtain biophysical evidence of negative cooperativity we used a quench flow apparatus to perform quench flow HDX-MS (QF-HDX-MS) to measure the dynamics of the MoFeP on the millisecond time scale. To understand the effects FeP binding has on the structure and dynamics of the MoFeP we tested three conditions: free MoFeP, MoFe:FeP 1:1, and MoFe:FeP 1:2. The three conditions were chosen to show the dynamics of MoFeP in the absence of FeP (MoFe condition), and in a 1:1 mixture of MoFeP and FeP (MoFe:FeP 1:1) and in a 1:2 mixture (MoFe:FeP 1:2 mixture). The initial analysis of the QF-HDX-MS data using butterfly plots to compare the %D incorporated into the MoFeP in the presence and absence of FeP revealed that differences in deuterium incorporation can be observed as early as 10 ms (**Fig. 6.7**).

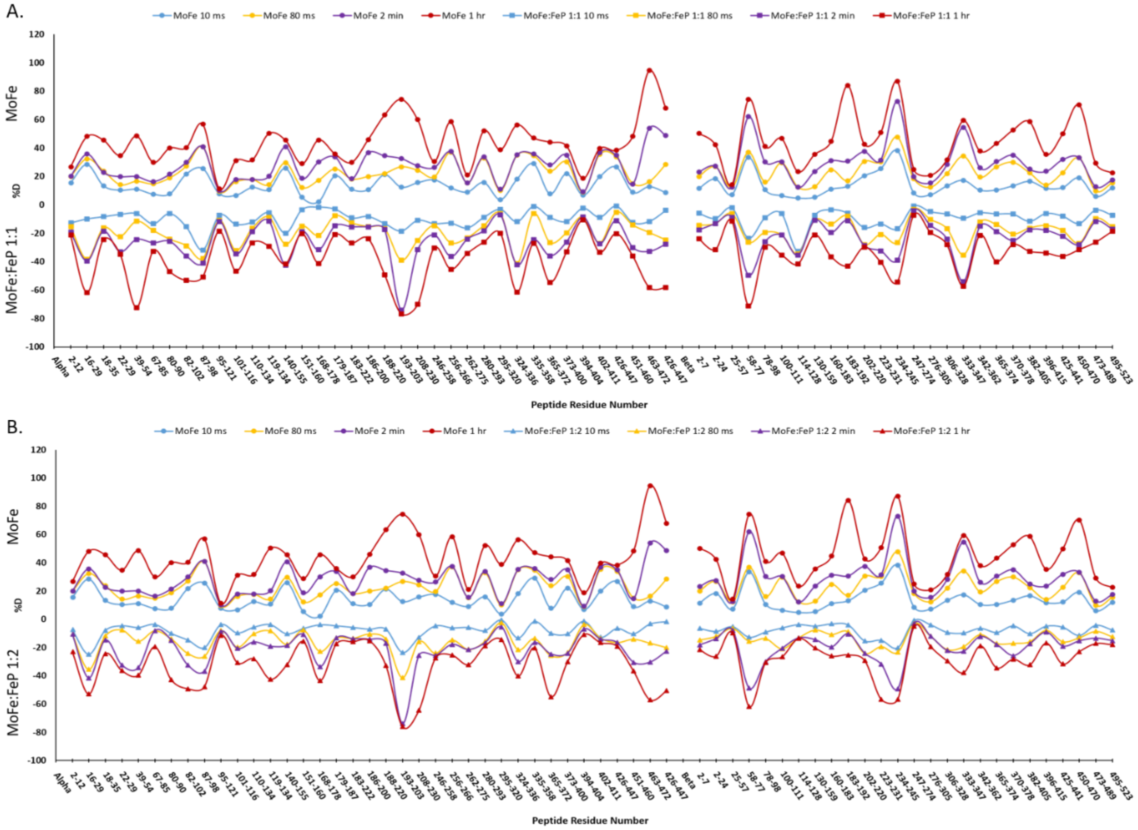

Figure 6.7 Butterfly plots showing the percent deuterium incorporated (%D) at four time points (10 ms, 80 ms, 2 min, 1 hr) for each of the peptides with high confidence scores from the α (left) and β (right) subunits of the MoFe protein. **A.** Comparison of the MoFe (positive values) and MoFe:FeP 1:1 conditions (negative values). **B.** Comparison of the MoFe (positive values) and MoFe:FeP 1:2 conditions (negative values).

Overall the MoFe condition incorporated the most deuterium, and the MoFe:FeP 1:2 condition incorporating the least amount of deuterium. This observation is consistent with the deuterium exchange pattern decreasing after the formation of protein-protein interactions. An interesting observation that emerged from this analysis is that some areas showed an increase in exchange in the MoFe:FeP 1:1 condition. One such region is the β160-183 peptide, which is located on the surface of the β subunit of the MoFeP, and forms part of the surface that interacts with FeP. In the absence of FeP this region exchanges 11% of the maximum possible deuterium at 10 ms. In the MoFe:FeP 1:1 and MoFe:FeP 1:2 conditions, this number decreases to 3%. This trend continues through the full time course, with the MoFe condition incorporating 42%D, MoFe:FeP 1:1 incorporating 36%D, and MoFe:FeP 1:2 incorporating 26%D.

To fully understand the unexpected exchange pattern observed in the MoFe:FeP 1:1 condition, structural heatmaps of the millisecond time points showing the comparison of the MoFe:FeP 1:1 and MoFe conditions was generated (**Fig. 6.8**). The millisecond time points (10 ms, 30 ms, 60 ms, and 80 ms) were chosen because they happen on the time scale of catalysis, specifically during the FeP cycle. The FeP cycle describes the docking of ATP-bound FeP to the MoFeP, and the subsequent electron transfer, ATP hydrolysis, Pi release, and the release of FeP. Because it is hypothesized that it is the asymmetric binding of FeP that triggers the allosteric signal, the millisecond time points can be used to identify a pathway of communication.

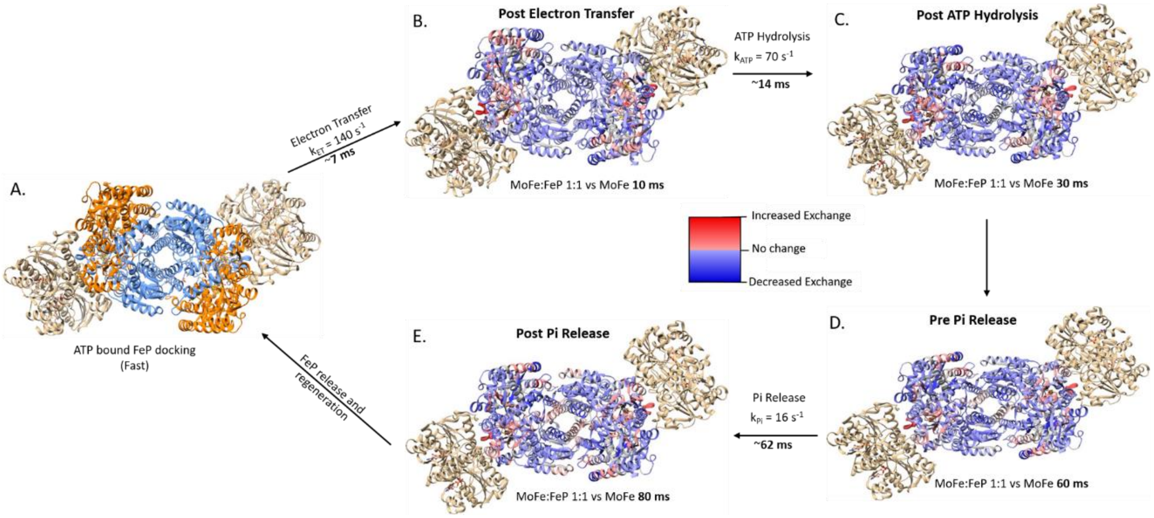

Figure 6.8 But Structural heatmaps showing the differences in exchange between the MoFe:FeP 1:1 condition and the MoFe condition at the millisecond time points mapped onto the structure of the MoFe protein in accordance with the different steps of the FeP cycle. For all structures, red regions indicate an increase in deuterium exchange in the MoFe:FeP 1:1 condition and blue regions indicate a decrease in deuterium exchange in the MoFe:FeP 1:1 condition. **A.** ATP bound FeP docks with the MoFe protein (PDB ID: 4WZB; AMP-PCP bound FeP shown in tan, α-MoFe shown in orange, and β-MoFe shown in blue). After FeP docking, electron transfer between the two proteins occurs at a rate of k_{ET}= 140 s^{-1} which is approximately 7 ms. **B.** The 10 ms time point captures the state of the MoFe protein shortly after ET. The differences in exchange of the MoFe:FeP 1:1 vs MoFe comparison was mapped onto the AMP-PCP bound FeP-MoFe crystal structure (PDB ID: 4WZB). After ET, ATP hydrolysis occurs at a rate of k_{ATP} = 70 s^{-1}, approximately 14 ms after FeP docking. **C.** After ATP hydrolysis, the ADP bound FeP changes conformation, changing the interactions between the FeP and MoFeP. The difference in exchange for the MoFe:FeP 1:1 vs MoFe comparison is mapped onto the ADP bound FeP-MoFe crystal structure (PDB ID: 2AFI). **D.** Shows the state of the MoFe protein at 60 ms, prior to Pi release for the MoFe:FeP 1:1 vs MoFe comparison. Pi release occurs at a rate of k_{Pi} = 14 s^{-1}, approximately 62 ms after FeP docking. **E.** The protein state at 80 ms reveals the effects Pi release has on the MoFeP structure and dynamics. The differences in exchange of the MoFe:FeP 1:1 vs MoFe comparison is shown.

Examining the MoFe:FeP 1:1 vs MoFe comparison revealed that the MoFe:FeP 1:1 condition shows an increase in exchange around the P-cluster and FeMo-cofactor binding sites thorough all time points. This behavior can be attributed to the asymmetric binding of FeP, which causes the FeP free half of MoFeP to adopt a more dynamic conformation, likely increasing the distance between the P-cluster and FeMo-co, and decreasing the rate of electron transfer. Additionally, at the 60 ms time point (**Fig. 6.8D**) the interface between the αβ dimers shows an increase in exchange, becoming more dynamic. A similar behavior is observed in the MoFe:FeP 1:2 condition, however this exchange pattern disappears in MoFe:FeP 1:2 by 80 ms but persists in the MoFe:FeP 1:1 condition. This indicates that the αβ dimer interface is crucial from transmitting an allosteric signal between the two halves, which is "quenched" in the MoFe:FeP 1:2 condition (based on the decrease in exchange at 80 ms) because of the additional FeP present in solution. This is the opposite in the MoFe:FeP 1:1 condition where the increase in exchange is still present at 80 ms. Because an additional equivalent of FeP is not present in this condition we can conclude that the signal is not being "quenched". Using the αβ dimer interface as the starting point, a pattern of increased exchange in the MoFe:FeP 1:1 condition can be traced from the interface through the FeMo-co and P-cluster binding sites, to the FeP binding sites. This pattern presents a framework of an allosteric pathway that sends a signal from the FeP binding site of one αβ dimer to the FeP binding site of the other.

Final Remarks:

The establishment of electron bifurcation as a third mechanism of energy conservation has fueled an increase in the characterization of anaerobic metabolic pathways. This has led to the discovery of several enzymes needed for energy production. The efficiency of these enzymes is much higher than what is typically observed in aerobic energy production pathways. These enzymes serve as ideals targets to characterize the diversity of energy conservation in nature, and potentially leading to the synthesis of similar enzymes with greater efficiency. Before these enzymes can be synthesized a greater understanding of their structure-function relationship is needed. Not only will this knowledge impart a better understanding of how the protein structure influences electron bifurcation, and other types of electron transfer events, but it will also reveal how these enzymes can be improved. With the development of more powerful mass spectrometers, and the increased popularity of mass spectrometry-based techniques, the ability to obtain high resolution biophysical data is becoming increasingly accessible. Detailed in this doctoral dissertation are several examples of what kind of conclusions can be drawn from biophysical data acquired with mass spectrometry-based techniques. These techniques can be used to develop high confidence homology models (XL-MS), detail changes in the structure and dynamics of a protein on the catalytic time scale (QF-HDX-MS), and even identify pathways of allostery (HDX-MS). Additionally, the use of techniques like HDX-MS in the characterization of bifurcating enzymes opens up the possibility for more systems to be characterized, such as enzymes involved in carbon dioxide fixation. Similar to the EB enzymes, a better understanding of the structure-function relationship in other systems can reveal mechanistic details about catalysis, and lead to a better understanding of their mechanism and regulation.

References Cited

1. Mitchell, P. The Protonmotive Q Cycle: A General Formulation. *FEBS Lett.* **59,** 137–139 (1975).

2. Peters, J. W. *et al.* A new era for electron bifurcation. *Curr. Opin. Chem. Biol.* **47,** 32–38 (2018).

3. Buckel, W. & Thauer, R. K. Energy conservation via electron bifurcating

ferredoxin reduction and proton/Na+ translocating ferredoxin oxidation. *Biochim. Biophys. Acta - Bioenerg.* **1827,** 94–113 (2013).

4. Peters, J. W., Miller, A. F., Jones, A. K., King, P. W. & Adams, M. W. W. Electron bifurcation. *Curr. Opin. Chem. Biol.* **31,** 146–152 (2016).

5. Fernie, A. R., Carrari, F. & Sweetlove, L. J. Respiratory metabolism: Glycolysis, the TCA cycle and mitochondrial electron transport. *Curr. Opin. Plant Biol.* **7,** 254–261 (2004).

6. Gnaiger, E., Steinlechner, R., Mendez, G., Eberl, T. & Margreiter, R. Control of Mitochondrial Respiration By Oxygen. *J Bioenerg. Biomembr.* **27,** 583–596 (1995).

7. Buckel, W. & Thauer, R. K. Flavin-based electron bifurcation, ferredoxin, flavodoxin, and anaerobic respiration with protons (Ech) or NAD+(Rnf) as electron acceptors: A historical review. *Front. Microbiol.* **9,** (2018).

8. Buckel, W. & Thauer, R. K. Flavin-Based Electron Bifurcation, A New Mechanism of Biological Energy Coupling. *Chem. Rev.* **118,** 3862–3886 (2018).

9. Thauer, R. K., Jungermann, K. & Decker, K. Energy conservation in chemotrophic anaerobic bacteria. *Bacteriol. Rev.* **41,** 100–180 (1977).

10. Metcalf, W. W. Classic spotlight: Electron bifurcation, a unifying concept for energy conservation in anaerobes. *J. Bacteriol.* **198,** 1358–1358 (2016).

11. Herrmann, G., Jayamani, E., Mai, G. & Buckel, W. Energy conservation via electron-transferring flavoprotein in anaerobic bacteria. *J. Bacteriol.* **190,** 784–791 (2008).

12. Lubner, C. E. *et al.* Mechanistic insights into energy conservation by flavin-based electron bifurcation. *Nat. Chem. Biol.* **13,** 655–659 (2017).

13. Berry, L. *et al.* H/D exchange mass spectrometry and statistical coupling analysis reveal a role for allostery in a ferredoxin-dependent bifurcating transhydrogenase catalytic cycle. *Biochim. Biophys. Acta - Gen. Subj.* **1862,** 9–17 (2018).

14. Schut, G. J. *et al.* The catalytic mechanism of electron bifurcating electron transfer flavoproteins (ETFs) involves an intermediary complex with NAD $^{+}$. *J. Biol. Chem.* jbc.RA118.005653 (2018). doi:10.1074/jbc.RA118.005653

15. Schut, G. J. & Adams, M. W. W. The iron-hydrogenase of Thermotoga maritima utilizes ferredoxin and NADH synergistically: A new perspective on anaerobic

hydrogen production. *J. Bacteriol.* **191,** 4451–4457 (2009).

16. Costas, A. M. G. *et al.* Defining electron bifurcation in the electron-transferring flavoprotein family. *J. Bacteriol.* **199,** (2017).

17. Schuchmann, K. & Müller, V. A bacterial electron-bifurcating hydrogenase. *J. Biol. Chem.* **287,** 31165–31171 (2012).

18. Martin, W. F. Hydrogen, metals, bifurcating electrons, and proton gradients: The early evolution of biological energy conservation. *FEBS Lett.* **586,** 485–493 (2012).

19. Buckel, W. & Thauer, R. K. Energy conservation via electron bifurcating ferredoxin reduction and proton/Na+ translocating ferredoxin oxidation. *Biochim. Biophys. Acta - Bioenerg.* **1827,** 94–113 (2013).

20. Engen, J. R. Analysis of Protein Conformation and Dynamics by Hydrogen/Deuterium Exchange MS. *Anal. Chem.* **81,** 7870–7875 (2009).

21. Englander, S. W. Hydrogen Exchange and Mass Spectrometry: A Historical Perspective. *J. Am. Soc. Mass Spectrom.* **17,** 1481–1489 (2006).

22. Wales, T. E. & Engen, J. R. Hydrogen exchange mass spectrometry for the analysis of protein dynamics. *Mass Spectrom. Rev.* **25,** 158–170 (2006).

23. Woodward, C., Simon, I. & Tüchsen, E. Hydrogen exchange and the dynamic structure of proteins. *Mol. Cell. Biochem.* (1982). doi:10.1007/BF00421225

24. Eyles, S. J. & Kaltashov, I. A. Methods to study protein dynamics and folding by mass spectrometry. *Methods* **34,** 88–99 (2004).

25. Konermann, L., Pan, J. & Liu, Y.-H. Hydrogen exchange mass spectrometry for studying protein structure and dynamics Introduction: protein folding, dynamics, and function. *Chem. Soc. Rev. Chem. Soc. Rev* **40,** 1224–1234 (2011).

26. Woodward, C., Simon, I. & Tüchsen, E. Hydrogen exchange and the dynamic structure of proteins. *Mol. Cell. Biochem.* **48,** 135–160 (1982).

27. Englander, S. W., Mayne, L., Bai, Y. & Sosnick, T. R. Hydrogen exchange: the modern legacy of Linderstrøm-Lang. *Protein Sci.* **6,** 1101–1109 (1997).

28. Jaswal, S. S. Biological insights from hydrogen exchange mass spectrometry. *Biochim. Biophys. acta Protein Proteomics* **1834,** 1188–201 (2013).

29. Moorthy, B. S., Badireddy, S. & Anand, G. S. Cooperativity and allostery in cAMP-dependent activation of Protein Kinase A: Monitoring conformations of intermediates by amide hydrogen/deuterium exchange. *Int. J. Mass Spectrom.* **302,** 157–166 (2011).

30. Casares, S., Sadqi, M., López-Mayorga, O., Martínez, J. C. & Conejero-Lara, F. Structural cooperativity in the SH3 domain studied by site-directed mutagenesis and amide hydrogen exchange. *FEBS Lett.* **539,** 125–130 (2003).

31. Singh, H., Dai, Y., Outten, F. W. & Busenlehner, L. S. Escherichia coli SufE sulfur transfer protein modulates the SufS cysteine desulfurase through allosteric conformational dynamics. *J. Biol. Chem.* **288,** 36189–200 (2013).

32. Berry, L. *et al.* H/D exchange mass spectrometry and statistical coupling analysis reveal a role for allostery in a ferredoxin-dependent bifurcating transhydrogenase catalytic cycle. *Biochim. Biophys. Acta - Gen. Subj.* **1862,** (2018).

33. Sperry, J. B. *et al.* A mass spectrometric approach to the study of DNA-binding proteins: Interaction of human TRF2 with telomeric DNA. *Biochemistry* (2008). doi:10.1021/bi702037p

34. Hamuro, Y. *et al.* Hydrogen/deuterium-exchange (H/D-Ex) of PPARγ LBD in the presence of various modulators. *Protein Sci.* **15,** 1883–1892 (2006).

35. Reynolds, K. A., McLaughlin, R. N. & Ranganathan, R. Hot spots for allosteric regulation on protein surfaces. *Cell* **147,** 1564–1575 (2011).

36. Lockless, S. W. & Ranganathan, R. Evolutionarily conserved pathways of energetic connectivity in protein families. *Science (80-.).* **286,** 295–299 (1999).

37. Halabi, N., Rivoire, O., Leibler, S. & Ranganathan, R. Protein Sectors: Evolutionary Units of Three-Dimensional Structure. *Cell* **138,** 774–786 (2009).

38. Raymond, J., Siefert, J. L., Staples, C. R. & Blankenship, R. E. The Natural History of Nitrogen Fixation. *Mol. Biol. Evol.* **21,** 541–554 (2004).

39. Burris, R. H. & Roberts, G. P. Biological Nitrogen Fixation. *Annu. Rev. Nutr.* **13,** 317–335 (1993).

40. Gruber, N. & Galloway, J. N. An Earth-system perspective of the global nitrogen cycle. *Nature* **451,** 293–296 (2008).

41. Eady, R. R. Structure-function relationships of alternative nitrogenases. *Chem. Rev.* **96,** 3013–3030 (1996).

42. Hu, Y., Lee, C. C. & Ribbe, M. W. Vanadium nitrogenase: A two-hit wonder? *Dalt. Trans.* **41,** 1118–1127 (2012).

43. Burgess, B. K. & Lowe, D. J. Mechanism of Molybdenum Nitrogenase. *Chem. Rev.* **96,** 2983–3012 (1996).

44. Yang, Z. Y. *et al.* Evidence That the Pi Release Event Is the Rate-Limiting Step in the Nitrogenase Catalytic Cycle. *Biochemistry* **55,** 3625–3635 (2016).

45. Pence, N. *et al.* Unraveling the interactions of the physiological reductant flavodoxin with the different conformations of the Fe protein in the nitrogenase cycle. *J. Biol. Chem.* **292,** 15661–15669 (2017).

46. Joerger, R. D., Jacobson, M. R., Premakumar, R., Wolfinger, E. D. & Bishop, P. E. Nucleotide sequence and mutational analysis of the structural genes (anfHDGK) for the second alternative nitrogenase from Azotobacter vinelandii. *J. Bacteriol.* **171,** 1075–1086 (1989).

47. Schüddekopf, K., Hennecke, S., Liese, U., Kutsche, M. & Klipp, W. Characterization of anf genes specific for the alternative nitrogenase and identification of nif genes required for both nitrogenases in Rhodobacter capsulatus. *Mol. Microbiol.* **8,** 673–684 (1993).

48. Chisnell, J. R., Premakumar, R. & Bishop, P. E. Purification of a second alternative nitrogenase from a nifHDK deletion strain of Azotobacter vinelandii. *J. Bacteriol.* **170,** 27–33 (1988).

49. Schneider, K., Gollan, U., Dröttboom, M., Selsemeier-Voigt, S. & Müller, A. Comparative biochemical characterization of the iron-only nitrogenase and the molybdenum nitrogenase from Rhodobacter capsulatus. *Eur. J. Biochem.* **244,** 789–800 (1997).

50. Waugh, S. I. *et al.* The genes encoding the delta subunits of dinitrogenases 2 and 3 are required for Mo-independent diazotrophic growth by Azotobacter vinelandii. *J. Bacteriol.* **177,** 1505–1510 (1995).

51. Schneider, K. & Müller, A. Iron-Only Nitrogenase: Exceptional Catalytic, Structural and Spectroscopic Features. in *Catalysts for Nitrogen Fixation* 281–307 (Springer Netherlands, 2004). doi:10.1007/978-1-4020-3611-8_11

52. Danyal, K. *et al.* Negative cooperativity in the nitrogenase Fe protein electron delivery cycle. *Proc. Natl. Acad. Sci.* **113,** E5783–E5791 (2016).

53. Maritano, S., Fairhurst, S. A. & Eady, R. R. Long-range interactions between the Fe protein binding sites of the MoFe protein of nitrogenase. *J. Biol. Inorg. Chem.* **6,** 590–600 (2001).

54. Wyman, J. *On allosteric models in Current topics in cellular regulation. Volume 6*. (Elsevier, 1972).

55. Goodey, N. M. & Benkovic, S. J. Allosteric regulation and catalysis emerge via a common route. *Nat. Chem. Biol.* **4,** 474–482 (2008).

56. Cui, Q. & Karplus, M. Allostery and Cooperativity revisited. *Protein Sci.* **17,** 1295–1307 (2008).

57. Motlagh, H. N. & Hilser, V. J. Agonism/antagonism switching in allosteric ensembles. *Proc. Natl. Acad. Sci. U. S. A.* **109,** 4134–4139 (2012).

58. Hilser, V. J. & Thompson, E. B. Intrinsic disorder as a mechanism to optimize allosteric coupling in proteins. *Proc. Natl. Acad. Sci. U. S. A.* **104,** 8311–8315 (2007).

59. Danyal, K. *et al.* Negative cooperativity in the nitrogenase Fe protein electron delivery cycle. *Proc. Natl. Acad. Sci.* **113,** E5783–E5791 (2016).

CUMULATIVE REFERENCES CITED

1. Fernie, A. R., Carrari, F. & Sweetlove, L. J. Respiratory metabolism: Glycolysis, the TCA cycle and mitochondrial electron transport. *Curr. Opin. Plant Biol.* **7,** 254–261 (2004).

2. Hatefi, Y. The Mitochondrial Electron Transport and Oxidative Phosphorylation System. *Ann. Rev. Biochem.* **54,** 1015–69 (1985).

3. Marcus, R. A., Sutin, N. & Stojek, Z. Electron transfers in chemistry and biology. *J. Phys. Chem.* **67,** 504 (2002).

4. Marcus, R. A. On the theory of electrochemical and chemical electron transfer processes. *Can. J. Chem.* **37,** (1958).

5. Marcus, R. A. On the theory of oxidation-reduction reactions involving electron transfer. I. *J. Chem. Phys.* **24,** 966–978 (1956).

6. Peters, J. W., Miller, A. F., Jones, A. K., King, P. W. & Adams, M. W. W. Electron bifurcation. *Curr. Opin. Chem. Biol.* **31,** 146–152 (2016).

7. Kemeny, G. Energy Transfer Mechanisms in Mitochondria. *Quantum* **71,** 3669–3671 (1974).

8. Martin, W. F. Hydrogen, metals, bifurcating electrons, and proton gradients: The early evolution of biological energy conservation. *FEBS Lett.* **586,** 485–493 (2012).

9. Gnaiger, E., Steinlechner, R., Mendez, G., Eberl, T. & Margreiter, R. Control of Mitochondrial Respiration By Oxygen. *J Bioenerg. Biomembr.* **27,** 583–596 (1995).

10. Peters, J. W. *et al.* A new era for electron bifurcation. *Curr. Opin. Chem. Biol.* **47,** 32–38 (2018).

11. Mitchell, P. The Protonmotive Q Cycle: A General Formulation. *FEBS Lett.* **59,** 137–139 (1975).

12. Metcalf, W. W. Classic spotlight: Electron bifurcation, a unifying concept for energy conservation in anaerobes. *J. Bacteriol.* **198,** 1358–1358 (2016).

13. Chowdhury, N. P. *et al.* Studies on the mechanism of electron bifurcation catalyzed by electron transferring flavoprotein (Etf) and butyryl-CoA

dehydrogenase (Bcd) of acidaminococcus fermentans. *J. Biol. Chem.* **289,** 5145–5157 (2014).

14. Thauer, R. K., Jungermann, K. & Decker, K. Energy conservation in chemotrophic anaerobic bacteria. *Bacteriol. Rev.* **41,** 100–180 (1977).

15. Buckel, W. & Thauer, R. K. Flavin-based electron bifurcation, ferredoxin, flavodoxin, and anaerobic respiration with protons (Ech) or NAD+(Rnf) as electron acceptors: A historical review. *Front. Microbiol.* **9,** (2018).

16. Buckel, W. & Thauer, R. K. Energy conservation via electron bifurcating ferredoxin reduction and proton/Na+ translocating ferredoxin oxidation. *Biochim. Biophys. Acta - Bioenerg.* **1827,** 94–113 (2013).

17. Peters, J. W., Beratan, D. N., Schut, G. J. & Adams, M. W. W. On the nature of organic and inorganic centers that bifurcate electrons, coupling exergonic and endergonic oxidation-reduction reactions. *Chem. Commun.* **54,** 4091–4099 (2018).

18. Herrmann, G., Jayamani, E., Mai, G. & Buckel, W. Energy conservation via electron-transferring flavoprotein in anaerobic bacteria. *J. Bacteriol.* **190,** 784–791 (2008).

19. Buckel, W. & Thauer, R. K. Energy conservation via electron bifurcating ferredoxin reduction and proton/Na+ translocating ferredoxin oxidation. *Biochim. Biophys. Acta - Bioenerg.* **1827,** 94–113 (2013).

20. Buckel, W. & Thauer, R. K. Flavin-Based Electron Bifurcation, A New Mechanism of Biological Energy Coupling. *Chem. Rev.* **118,** 3862–3886 (2018).

21. Lubner, C. E. *et al.* Mechanistic insights into energy conservation by flavin-based electron bifurcation. *Nat. Chem. Biol.* **13,** 655–659 (2017).

22. Schut, G. J. *et al.* The catalytic mechanism of electron bifurcating electron transfer flavoproteins (ETFs) involves an intermediary complex with NAD $^+$. *J. Biol. Chem.* jbc.RA118.005653 (2018). doi:10.1074/jbc.RA118.005653

23. Schut, G. J. & Adams, M. W. W. The iron-hydrogenase of Thermotoga maritima utilizes ferredoxin and NADH synergistically: A new perspective on anaerobic hydrogen production. *J. Bacteriol.* **191,** 4451–4457 (2009).

24. Costas, A. M. G. *et al.* Defining electron bifurcation in the electron-transferring flavoprotein family. *J. Bacteriol.* **199,** (2017).

25. Schuchmann, K. & Müller, V. A bacterial electron-bifurcating hydrogenase. *J.*

Biol. Chem. **287,** 31165–31171 (2012).

26. Demmer, J. K., Rupprecht, F. A., Eisinger, M. L., Ermler, U. & Langer, J. D. Ligand binding and conformational dynamics in a flavin-based electron-bifurcating enzyme complex revealed by Hydrogen–Deuterium Exchange Mass Spectrometry. *FEBS Lett.* **590,** 4472–4479 (2016).

27. Berry, L. *et al.* H/D exchange mass spectrometry and statistical coupling analysis reveal a role for allostery in a ferredoxin-dependent bifurcating transhydrogenase catalytic cycle. *Biochim. Biophys. Acta - Gen. Subj.* **1862,** 9–17 (2018).

28. Diessel Duan, H. *et al.* Distinct properties underlie flavin-based electron bifurcation in a novel electron transfer flavoprotein FixAB from Rhodopseudomonas palustris. *J. Biol. Chem.* **293,** 4688–4701 (2018).

29. Demmer, J. K., Pal Chowdhury, N., Selmer, T., Ermler, U. & Buckel, W. The semiquinone swing in the bifurcating electron transferring flavoprotein/butyryl-CoA dehydrogenase complex from Clostridium difficile. *Nat. Commun.* **8,** (2017).

30. Beratan, D. N. *et al.* Steering electrons on moving pathways. *Acc. Chem. Res.* **42,** 1669–1678 (2009).

31. Peters, J. W., Beratan, D. N., Schut, G. J. & Adams, M. W. W. On the nature of organic and inorganic centers that bifurcate electrons, coupling exergonic and endergonic oxidation-reduction reactions. *Chem. Commun.* **54,** 4091–4099 (2018).

32. Beratan, D. N. *et al.* Charge transfer in dynamical biosystems, or the treachery of (static) images. *Acc. Chem. Res.* **48,** 474–481 (2015).

33. Cui, Q. & Karplus, M. Allostery and Cooperativity revisited. *Protein Sci.* **17,** 1295–1307 (2008).

34. Motlagh, H. N. & Hilser, V. J. Agonism/antagonism switching in allosteric ensembles. *Proc. Natl. Acad. Sci.* **109,** 4134–4139 (2012).

35. Motlagh, H. N., Wrabl, J. O., Li, J. & Hilser, V. J. The ensemble nature of allostery. *Nature* **508,** 331–339 (2014).

36. Hilser, V. J., Wrabl, J. O. & Motlagh, H. N. Structural and Energetic Basis of Allostery. *Annu. Rev. Biophys.* **41,** 585–609 (2012).

37. Mitternacht, S. & Berezovsky, I. N. Coherent conformational degrees of freedom as a structural basis for allosteric communication. *PLoS Comput. Biol.* **7,** (2011).

38. Daily, M. D. & Gray, J. J. Allosteric communication occurs via networks of tertiary and quaternary motions in proteins. *PLoS Comput. Biol.* **5,** (2009).

39. del Sol, A., Tsai, C. J., Ma, B. & Nussinov, R. The Origin of Allosteric Functional Modulation: Multiple Pre-existing Pathways. *Structure* **17,** 1042–1050 (2009).

40. Goodey, N. M. & Benkovic, S. J. Allosteric regulation and catalysis emerge via a common route. *Nat. Chem. Biol.* **4,** 474–482 (2008).

41. Tsai, C., Sol, A. & Nussinov, R. Allostery: Absence of a change in shape does not imply that allostery is not at play. *J. Mol. Biol.* **378,** 1–11 (2008).

42. Tsai, C. J., Del Sol, A. & Nussinov, R. Protein allostery, signal transmission and dynamics: A classification scheme of allosteric mechanisms. *Mol. Biosyst.* **5,** 207–216 (2009).

43. Reynolds, K. A., McLaughlin, R. N. & Ranganathan, R. Hot spots for allosteric regulation on protein surfaces. *Cell* **147,** 1564–1575 (2011).

44. Lockless, S. W. & Ranganathan, R. Evolutionarily conserved pathways of energetic connectivity in protein families. *Science (80-.).* **286,** 295–299 (1999).

45. Halabi, N., Rivoire, O., Leibler, S. & Ranganathan, R. Protein Sectors: Evolutionary Units of Three-Dimensional Structure. *Cell* **138,** 774–786 (2009).

46. Dobbins, S. E., Lesk, V. I. & Sternberg, M. J. E. Insights into protein flexibility: The relationship between normal modes and conformational change upon protein-protein docking. *Proc. Natl. Acad. Sci.* **105,** 10390–10395 (2008).

47. Fuglebakk, E., Tiwari, S. P. & Reuter, N. Comparing the intrinsic dynamics of multiple protein structures using elastic network models. *Biochim. Biophys. Acta - Gen. Subj.* **1850,** 911–922 (2015).

48. Bahar, I. Normal Mode Analysis of Biomolecular Structures: Functional Mechanisms of Membrane Proteins. *Lang. Dev. crossroads* **110,** 49–59 (1983).

49. Tirion, M. M. Large amplitude elastic motions in proteins from a single-parameter, atomic analysis. *Phys. Rev. Lett.* **77,** 1905–1908 (1996).

50. Danyal, K. *et al.* Negative cooperativity in the nitrogenase Fe protein electron delivery cycle. *Proc. Natl. Acad. Sci.* **113,** E5783–E5791 (2016).

51. Tokmina-Lukaszewska, M. *et al.* The role of mass spectrometry in structural studies of flavin-based electron bifurcating enzymes. *Front. Microbiol.* **9,** (2018).

52. Steiner, R. F., Albaugh, S., Fenselau, C., Murphy, C. & Vestling, M. A mass spectrometry method for mapping the interface topography of interacting proteins, illustrated by the melittin-calmodulin system. *Anal. Biochem.* **196,** 120–125 (1991).

53. Glocker, M. O., Borchers, C., Fiedler, W., Suckau, D. & Przybylski, M. Molecular Characterization of Surface Topology in Protein Tertiary Structures by Amino-Acylation and Mass Spectrometric Peptide Mapping. *Bioconjug. Chem.* **5,** 583–590 (1994).

54. Suckau, D., Mak, M. & Przybylski, M. Protein surface topology-probing by selective chemical modification and mass spectrometric peptide mapping. *Proc. Natl. Acad. Sci. U. S. A.* **89,** 5630–4 (1992).

55. Young, M. M. *et al.* High throughput protein fold identification by using experimental constraints derived from intramolecular cross-links and mass spectrometry. *Proc. Natl. Acad. Sci.* **97,** 5802–5806 (2000).

56. Herzog, F. *et al.* Structural Probing of a Protein Phosphatase 2A Network by Chemical Cross-Linking and Mass Spectrometry. *Science (80-.).* **337,** 1348–1352 (2012).

57. Kaake, R. M. *et al.* A New in Vivo Cross-linking Mass Spectrometry Platform to Define Protein–Protein Interactions in Living Cells. *Mol. Cell. Proteomics* **13,** 3533–3543 (2014).

58. Fernandez-Martinez, J. *et al.* Structure and Function of the Nuclear Pore Complex Cytoplasmic mRNA Export Platform. *Cell* **167,** 1215–1228.e25 (2016).

59. Engen, J. R. Analysis of protein conformation and dynamics by hydrogen/deuterium exchange MS. *Anal. Chem.* **81,** 7870–7875 (2009).

60. Konermann, L., Pan, J. & Liu, Y.-H. Hydrogen exchange mass spectrometry for studying protein structure and dynamics Introduction: protein folding, dynamics, and function. *Chem. Soc. Rev. Chem. Soc. Rev* **40,** 1224–1234 (2011).

61. Percy, A. J., Rey, M., Burns, K. M. & Schriemer, D. C. Probing protein interactions with hydrogen/deuterium exchange and mass spectrometry-A review. *Anal. Chim. Acta* **721,** 7–21 (2012).

62. Walters, B. T., Ricciuti, A., Mayne, L. & Englander, S. W. Minimizing back exchange in the hydrogen exchange-mass spectrometry experiment. *J. Am. Soc. Mass Spectrom.* **23,** 2132–2139 (2012).

63. Woodward, C. K. & Hilton, B. D. HYDROGEN EXCHANGE KINETICS AND INTERNAL MOTIONS IN PROTEINS AND NUCLEIC ACIDS. *Annu. Rev. Biophys. Bioeng.* **8,** 99–127 (1979).

64. Woodward, C., Simon, I. & Tüchsen, E. Hydrogen exchange and the dynamic structure of proteins. *Mol. Cell. Biochem.* (1982). doi:10.1007/BF00421225

65. Englander, S. W., Mayne, L., Bai, Y. & Sosnick, T. R. Hydrogen exchange: the modern legacy of Linderstrøm-Lang. *Protein Sci.* **6,** 1101–1109 (1997).

66. Englander, S. W. & Kallenbach, N. R. Hydrogen exchange and structural dynamics of proteins and nucleic acids. *Q. Rev. Biophys.* **16,** 521–655 (1983).

67. Jaswal, S. S. Biological insights from hydrogen exchange mass spectrometry. *Biochim. Biophys. acta Protein Proteomics* **1834,** 1188–201 (2013).

68. Trabjerg, E., Nazari, Z. E. & Rand, K. D. Conformational analysis of complex protein states by hydrogen/deuterium exchange mass spectrometry (HDX-MS): Challenges and emerging solutions. *TrAC - Trends Anal. Chem.* **106,** 125–138 (2018).

69. Berry, L. *et al.* H/D exchange mass spectrometry and statistical coupling analysis reveal a role for allostery in a ferredoxin-dependent bifurcating transhydrogenase catalytic cycle. *Biochim. Biophys. Acta - Gen. Subj.* **1862,** (2018).

70. Chalmers, M. J., Busby, S. A., Pascal, B. D., West, G. M. & Griffin, P. R. Differential hydrogen/deuterium exchange mass spectrometry analysis of protein-ligand interactions. *Expert Review of Proteomics* **8,** 43–59 (2011).

71. Van Erp, P. B. G. *et al.* Conformational Dynamics of DNA Binding and Cas3 Recruitment by the CRISPR RNA-Guided Cascade Complex. *ACS Chem. Biol.* **13,** (2018).

72. Engen, J. R. *et al.* Partial cooperative unfolding in proteins as observed by hydrogen exchange mass spectrometry. *International Reviews in Physical Chemistry* (2013). doi:10.1080/0144235X.2012.751175

73. Wei, H. *et al.* Using hydrogen/deuterium exchange mass spectrometry to study conformational changes in granulocyte colony stimulating factor upon PEGylation. *J. Am. Soc. Mass Spectrom.* (2012). doi:10.1007/s13361-011-0310-x

74. Burgess, B. K. & Lowe, D. J. Mechanism of Molybdenum Nitrogenase. *Chem. Rev.* **96,** 2983–3012 (1996).

75. Smil, V. *Enriching the earth : Fritz Haber, Carl Bosch, and the transformation of world food production*. (MIT Press, 2001).

76. Haber, F. Über die Darstellung des Ammoniaks aus Stickstoff und Wasserstoff. *Naturwissenschaften* **10,** 1041–1049 (1922).

77. Haber, F. Bemerkung zu vorstehender Notiz. *Naturwissenschaften* **11,** 339–340 (1923).

78. Raymond, J., Siefert, J. L., Staples, C. R. & Blankenship, R. E. The Natural History of Nitrogen Fixation. *Mol. Biol. Evol.* **21,** 541–554 (2004).

79. Burris, R. H. & Roberts, G. P. Biological Nitrogen Fixation. *Annu. Rev. Nutr.* **13,** 317–335 (1993).

80. Gruber, N. & Galloway, J. N. An Earth-system perspective of the global nitrogen cycle. *Nature* **451,** 293–296 (2008).

81. Eady, R. R. Structure-function relationships of alternative nitrogenases. *Chem. Rev.* **96,** 3013–3030 (1996).

82. Hu, Y., Lee, C. C. & Ribbe, M. W. Vanadium nitrogenase: A two-hit wonder? *Dalt. Trans.* **41,** 1118–1127 (2012).

83. Yang, Z. Y. *et al.* Evidence That the Pi Release Event Is the Rate-Limiting Step in the Nitrogenase Catalytic Cycle. *Biochemistry* **55,** 3625–3635 (2016).

84. Seefeldt, L. C., Hoffman, B. M. & Dean, D. R. Electron transfer in nitrogenase catalysis. *Curr. Opin. Chem. Biol.* **16,** 19–25 (2012).

85. Hageman, R. V & Burris, R. H. Nitrogenase and nitrogenase reductase associate and dissociate with each catalytic cycle. *Proc. Natl. Acad. Sci. U. S. A.* **75,** 2699–702 (1978).

86. Seefeldt, L. C., Hoffman, B. M. & Dean, D. R. Mechanism of Mo-dependent nitrogenase. *Annu. Rev. Biochem.* **78,** 701–722 (2009).

87. Hoffman, B. M., Lukoyanov, D., Yang, Z. Y., Dean, D. R. & Seefeldt, L. C. Mechanism of nitrogen fixation by nitrogenase: The next stage. *Chemical Reviews* **114,** 4041–4062 (2014).

88. Schneider, K. & Müller, A. Iron-Only Nitrogenase: Exceptional Catalytic, Structural and Spectroscopic Features. in *Catalysts for Nitrogen Fixation* 281–307

(Springer Netherlands, 2004). doi:10.1007/978-1-4020-3611-8_11

89. Chisnell, J. R., Premakumar, R. & Bishop, P. E. Purification of a second alternative nitrogenase from a nifHDK deletion strain of Azotobacter vinelandii. *J. Bacteriol.* **170,** 27–33 (1988).

90. Luque, F. & Pau, R. N. Transcriptional regulation by metals of structural genes for Azotobacter vinelandii nitrogenases. *Mol. Gen. Genet.* **227,** 481–7 (1991).

91. Harris, D. F. *et al.* Mechanism of N $_2$ Reduction Catalyzed by Fe-Nitrogenase Involves Reductive Elimination of H $_2$. *Biochemistry* **57,** 701–710 (2018).

92. Schneider, K., Gollan, U., Dröttboom, M., Selsemeier-Voigt, S. & Müller, A. Comparative biochemical characterization of the iron-only nitrogenase and the molybdenum nitrogenase from Rhodobacter capsulatus. *Eur. J. Biochem.* **244,** 789–800 (1997).

93. Siemann, S., Schneider, K., Dröttboom, M. & Müller, A. The Fe-only nitrogenase and the Mo nitrogenase from Rhodobacter capsulatus: a comparative study on the redox properties of the metal clusters present in the dinitrogenase components. *Eur. J. Biochem.* **269,** 1650–1661 (2002).

94. Sippel, D. & Einsle, O. The structure of vanadium nitrogenase reveals an unusual bridging ligand. *Nat. Chem. Biol.* **13,** 956–960 (2017).

95. Joerger, R. D., Jacobson, M. R., Premakumar, R., Wolfinger, E. D. & Bishop, P. E. Nucleotide sequence and mutational analysis of the structural genes (anfHDGK) for the second alternative nitrogenase from Azotobacter vinelandii. *J. Bacteriol.* **171,** 1075–1086 (1989).

96. Schüddekopf, K., Hennecke, S., Liese, U., Kutsche, M. & Klipp, W. Characterization of anf genes specific for the alternative nitrogenase and identification of nif genes required for both nitrogenases in Rhodobacter capsulatus. *Mol. Microbiol.* **8,** 673–684 (1993).

97. Waugh, S. I. *et al.* The genes encoding the delta subunits of dinitrogenases 2 and 3 are required for Mo-independent diazotrophic growth by Azotobacter vinelandii. *J. Bacteriol.* **177,** 1505–1510 (1995).

98. Hales, B. J., Case, E. E., Morningstar, J. E., Dzeda, M. F. & Mauterer, L. A. Isolation of a New Vanadium-Containing Nitrogenase from Azotobacter vinelandii. *Biochemistry* **25,** 7251–7255 (1986).

99. Dilworth, M. J., Eldridge, M. E. & Eady, R. R. The molybdenum and vanadium

nitrogenases of Azotobacter chroococcum: effect of elevated temperature on N2 reduction. *Biochem. J.* **289 (Pt 2,** 395–400 (1993).

100. Eady, R. R., Robson, R. L., Richardson, T. H., Miller, R. W. & Hawkins, M. The vanadium nitrogenase of Azotobacter chroococcum. Purification and properties of the VFe protein. *Biochem. J.* **244,** 197–207 (1987).

101. Hales, B. J. Alternative nitrogenase. *Adv. Inorg. Biochem.* **8,** 165–198 (1990).

102. Chan, M. K., Kim, J. & Rees, D. C. The nitrogenase FeMo-cofactor and P-cluster pair: 2.2 A resolution structures. *Science* **260,** 792–794 (1993).

103. Kim, J. & Rees, D. C. Structural models for the metal centers in the nitrogenase molybdenum-iron protein. *Science* **257,** 1677–1682 (1992).

104. Rees, D. C. & Howard, J. B. Structural bioenergetics and energy transduction mechanisms. *J. Mol. Biol.* **293,** 343–350 (1999).

105. Georgiadis, M. M. *et al.* Crystallographic structure of the nitrogenase iron protein from Azotobacter vinelandii. *Science* **257,** 1653–1659 (1992).

106. Toukdarian, A. & Kennedy, C. Regulation of nitrogen metabolism in Azotobacter vinelandii: isolation of ntr and glnA genes and construction of ntr mutants. *EMBO J.* **5,** 399–407 (1986).

107. Christiansen, J., Goodwin, P. J., Lanzilotta, W. N., Lance C. Seefeldt, A. & Dennis R. Dean. Catalytic and Biophysical Properties of a Nitrogenase Apo-MoFe Protein Produced by a nifB-Deletion Mutant of Azotobacter vinelandii†. *Biochemistry* **37,** 12611–12623 (1998).

108. Burgess, B. K., Jacobs, D. B. & Stiefel, E. I. Large-scale purification of high activity Azotobacter vinelandii nitrogenase. *Biochim. Biophys. Acta - Enzymol.* **614,** 196–209 (1980).

109. Peters, J. W., Fisher, K. & Dean, D. R. Identification of a nitrogenase protein-protein interaction site defined by residues 59 through 67 within the Azotobacter vinelandii Fe protein. *J. Biol. Chem.* **269,** 28076–28083 (1994).

110. Yang, Z. Y. *et al.* Evidence That the Pi Release Event Is the Rate-Limiting Step in the Nitrogenase Catalytic Cycle. *Biochemistry* **55,** 3625–3635 (2016).

111. Vaudel, M. *et al.* PeptideShaker enables reanalysis of MS-derived proteomics data sets: To the editor. *Nat. Biotechnol.* **33,** 22–24 (2015).

112. Kelley, L. A., Mezulis, S., Yates, C. M., Wass, M. N. & Sternberg, M. J. E. The Phyre2 web portal for protein modeling, prediction and analysis. *Nat. Protoc.* **10,** 845–858 (2015).

113. Pettersen, E. F. *et al.* UCSF Chimera - A visualization system for exploratory research and analysis. *J. Comput. Chem.* **25,** 1605–1612 (2004).

114. Ledbetter, R. N. *et al.* The Electron Bifurcating FixABCX Protein Complex from Azotobacter vinelandii: Generation of Low-Potential Reducing Equivalents for Nitrogenase Catalysis. *Biochemistry* **56,** 4177–4190 (2017).

115. Lima, D. B. *et al.* SIM-XL: A powerful and user-friendly tool for peptide cross-linking analysis. *J. Proteomics* **129,** 51–55 (2014).

116. Kosinski, J. *et al.* Xlink analyzer: Software for analysis and visualization of cross-linking data in the context of three-dimensional structures. *J. Struct. Biol.* **189,** 177–183 (2015).

117. Wang, J., Shi, Y. & Chait, B. T. CX-Circos: a Web-based Tool for Visualization and Analysis of Chemical Cross-linking Data. in *Proceedings of the 64th ASMS Conference on Mass Spectrometry and Allied Topics* (2016).

118. Berry, L., Patterson, A., Pence, N., Peters, J. W. & Bothner, B. Hydrogen Deuterium Exchange Mass Spectrometry of Oxygen Sensitive Proteins. *Bioprotocols* **8,** 1–16 (2018).

119. Pascal, B. D., Chalmers, M. J., Busby, S. A. & Griffin, P. R. HD Desktop: An Integrated Platform for the Analysis and Visualization of H/D Exchange Data. *J. Am. Soc. Mass Spectrom.* (2009). doi:10.1016/j.jasms.2008.11.019

120. Smith, D., Danyal, K., Raugei, S. & Seefeldt, L. C. Substrate channel in nitrogenase revealed by a molecular dynamics approach. *Biochemistry* **53,** 2278–2285 (2014).

121. Atilgan, A. R. *et al.* Anisotropy of fluctuation dynamics of proteins with an elastic network model. *Biophys. J.* **80,** 505–515 (2001).

122. R Development Core Team. R Development Core Team, 2017. (2017).

123. Wei, T. & Simko, V. R package ‘corrplot’: Visualization of a Correlation Matrix (Version 0.84). (2017).

124. Kelly, L. A., Mezulis, S., Yates, C., Wass, M. & Sternberg, M. The Phyre2 web portal for protein modelling, prediction, and analysis. *Nat. Protoc.* **10,** 845–858

(2015).

125. Merkley, E. D. *et al.* Distance restraints from crosslinking mass spectrometry: Mining a molecular dynamics simulation database to evaluate lysine-lysine distances. *Protein Sci.* **23,** 747–759 (2014).

126. Konermann, L., Pan, J. & Liu, Y. H. Hydrogen exchange mass spectrometry for studying protein structure and dynamics. *Chem. Soc. Rev.* **40,** 1224–1234 (2011).

127. Engen, J. R. *et al.* Partial cooperative unfolding in proteins as observed by hydrogen exchange mass spectrometry. *International Reviews in Physical Chemistry* **32,** 96–127 (2013).

128. Wako, H. & Endo, S. Normal mode analysis as a method to derive protein dynamics information from the Protein Data Bank. *Biophys. Rev.* **9,** 877–893 (2017).

129. Na, H., ben-Avraham, D. & Tirion, M. M. Slow Normal Modes of Proteins are Accurately Reproduced across Different Platforms. 1–31 (2018).

130. Brooks III, C. L., Karplus, M. B. & Pettitt, M. *Proteins: A Theoretical Perspective of Dynamics, Structure, and Thermodynamics*. (J. Wiley, 1988).

131. Hayward, S. *Normal mode analysis of biological molecules*. (M. Dekker,Inc, 2001).

132. Mizuguchi, K., Kidera, A. & Gō, N. Collective motions in proteins investigated by X-ray diffuse scattering. *Proteins Struct. Funct. Genet.* **18,** 34–48 (1994).

133. Van Wynsberghe, A. W. & Cui, Q. Interpreting Correlated Motions Using Normal Mode Analysis. *Structure* **14,** 1647–1653 (2006).

134. Danyal, K. *et al.* Negative cooperativity in the nitrogenase Fe protein electron delivery cycle. *Proc. Natl. Acad. Sci.* **113,** E5783–E5791 (2016).

135. Weis, D. D., Wales, T. E., Engen, J. R., Hotchko, M. & Ten Eyck, L. F. Identification and Characterization of EX1 Kinetics in H/D Exchange Mass Spectrometry by Peak Width Analysis. *J. Am. Soc. Mass Spectrom.* (2006). doi:10.1016/j.jasms.2006.05.014

136. Guttman, M., Weis, D. D., Engen, J. R. & Lee, K. K. Analysis of overlapped and noisy hydrogen/deuterium exchange mass spectra. *J. Am. Soc. Mass Spectrom.* (2013). doi:10.1007/s13361-013-0727-5

137. Maritano, S., Fairhurst, S. A. & Eady, R. R. Long-range interactions between the Fe protein binding sites of the MoFe protein of nitrogenase. *J. Biol. Inorg. Chem.* **6,** 590–600 (2001).

138. Wyman, J. *On allosteric models in Current topics in cellular regulation. Volume 6*. (Elsevier, 1972).

139. Motlagh, H. N. & Hilser, V. J. Agonism/antagonism switching in allosteric ensembles. *Proc. Natl. Acad. Sci. U. S. A.* **109,** 4134–4139 (2012).

140. Hilser, V. J. & Thompson, E. B. Intrinsic disorder as a mechanism to optimize allosteric coupling in proteins. *Proc. Natl. Acad. Sci. U. S. A.* **104,** 8311–8315 (2007).

141. Burgess, B. K. & Lowe, D. J. Mechanism of Molybdenum Nitrogenase. *Chem. Rev.* **96,** 2983–3012 (2002).

142. Sippel, D. & Einsle, O. The structure of vanadium nitrogenase reveals an unusual bridging ligand. *Nat. Chem. Biol.* **13,** 956–960 (2017).

143. Howard, J. B. & Rees, D. C. Structural basis of biological nitrogen fixation. *Chem. Rev.* **96,** 2965–2982 (1996).

144. Hoffman, B. M., Lukoyanov, D., Dean, D. R. & Seefeldt, L. C. Nitrogenase: A draft mechanism. *Acc. Chem. Res.* **46,** 587–595 (2013).

145. Peters, J. W. *et al.* Redox-dependent structural changes in the nitrogenase P-cluster. *Biochemistry* **36,** 1181–1187 (1997).

146. Pence, N. *et al.* Unraveling the interactions of the physiological reductant flavodoxin with the different conformations of the Fe protein in the nitrogenase cycle. *J. Biol. Chem.* **292,** 15661–15669 (2017).

147. Tezcan, F. A. *et al.* Nitrogenase Complexes: Multiple Docking Sites for a Nucleotide Switch Protein. *Science (80-.).* **309,** 1377–1380 (2005).

148. Seefeldt, L. C. *et al.* Control of electron transfer in nitrogenase. *Curr. Opin. Chem. Biol.* **47,** 54–59 (2018).

149. Igarashi, R. Y. & Seefeldt, L. C. Nitrogen Fixation: The Mechanism of the Mo-Dependent Nitrogenase. *Crit. Rev. Biochem. Mol. Biol.* **38,** 351–384 (2003).

150. Duval, S. *et al.* Electron transfer precedes ATP hydrolysis during nitrogenase catalysis. *Proc. Natl. Acad. Sci.* **110,** 16414–16419 (2013).

151. Ryle, M. J. & Seefeldt, L. C. Elucidation of a MgATP signal transduction pathway in the nitrogenase iron protein: Formation of a conformation resembling the MgATP-bound state by protein engineering. *Biochemistry* **35,** 4766–4775 (1996).

152. Thorneley, R. N. F. Nitrogenase of Klebsiella pneumoniae A stopped-Flow Study of Magnesium-Adenosine Triphosphate-Induced Electron Transfer Between The Component Proteins. *Biochem. J.* **145,** 391–396 (1975).

153. Seefeldt, L. C. *et al.* Control of electron transfer in nitrogenase. *Curr. Opin. Chem. Biol.* **47,** 54–59 (2018).

154. Danyal, K., Dean, D. R., Hoffman, B. M. & Seefeldt, L. C. Electron transfer within nitrogenase: Evidence for a deficit-spending mechanism. *Biochemistry* **50,** 9255–9263 (2011).

155. Owens, C. P., Katz, F. E. H., Carter, C. H., Luca, M. A. & Tezcan, F. A. Evidence for Functionally Relevant Encounter Complexes in Nitrogenase Catalysis. *J. Am. Chem. Soc.* **137,** 12704–12712 (2015).

156. Schlessman, J. L., Woo, D., Joshua-Tor, L., Howard, J. B. & Rees, D. C. Conformational variability in structures of the nitrogenase iron proteins from Azotobacter vinelandii and Clostridium pasteurianum. *J. Mol. Biol.* **280,** 669–685 (1998).

157. Tezcan, F. A., Kaiser, J. T., Howard, J. B. & Rees, D. C. Structural evidence for asymmetrical nucleotide interactions in nitrogenase. *J. Am. Chem. Soc.* **137,** 146–149 (2015).

158. Thorneley, R. N. F. & Lowe, D. J. Nitrogenase of Klebsiella pneumoniae Kinetics of the dissociation of oxidized iron protein from molybdenum-iron protein: Identification of the rate-limiting step for substrate reduction. *Biochem. J.* **215,** 393–403 (1983).

159. Hoffman, B. M., Lukoyanov, D., Yang, Z. Y., Dean, D. R. & Seefeldt, L. C. Mechanism of nitrogen fixation by nitrogenase: The next stage. *Chem. Rev.* **114,** 4041–4062 (2014).

160. Engen, J. R. Analysis of Protein Conformation and Dynamics by Hydrogen/Deuterium Exchange MS. *Anal. Chem.* **81,** 7870–7875 (2009).

161. Englander, S. W. Hydrogen Exchange and Mass Spectrometry: A Historical Perspective. *J. Am. Soc. Mass Spectrom.* **17,** 1481–1489 (2006).

162. Wales, T. E. & Engen, J. R. Hydrogen exchange mass spectrometry for the analysis of protein dynamics. *Mass Spectrom. Rev.* **25,** 158–170 (2006).

163. Eyles, S. J. & Kaltashov, I. A. Methods to study protein dynamics and folding by mass spectrometry. *Methods* **34,** 88–99 (2004).

164. Woodward, C., Simon, I. & Tüchsen, E. Hydrogen exchange and the dynamic structure of proteins. *Mol. Cell. Biochem.* **48,** 135–160 (1982).

165. Engen, J. R. Analysis of Protein Conformation and Dynamics by Hydrogen/Deuterium Exchange MS. *Anal. Chem.* **81,** 7870–7875 (2009).

166. Weis, D. D., Wales, T. E., Engen, J. R., Hotchko, M. & Ten Eyck, L. F. Identification and Characterization of EX1 Kinetics in H/D Exchange Mass Spectrometry by Peak Width Analysis. *J. Am. Soc. Mass Spectrom.* **17,** 1498–1509 (2006).

167. Resetca, D. & Wilson, D. J. Mapping ligand binding using microfluidics-enabled millisecond timescale hydrogen-deuterium exchange. *Int. J. Mass Spectrom.* **420,** 67–73 (2017).

168. Moorthy, B. S., Badireddy, S. & Anand, G. S. Cooperativity and allostery in cAMP-dependent activation of Protein Kinase A: Monitoring conformations of intermediates by amide hydrogen/deuterium exchange. *Int. J. Mass Spectrom.* **302,** 157–166 (2011).

169. Casares, S., Sadqi, M., López-Mayorga, O., Martínez, J. C. & Conejero-Lara, F. Structural cooperativity in the SH3 domain studied by site-directed mutagenesis and amide hydrogen exchange. *FEBS Lett.* **539,** 125–130 (2003).

170. Singh, H., Dai, Y., Outten, F. W. & Busenlehner, L. S. Escherichia coli SufE sulfur transfer protein modulates the SufS cysteine desulfurase through allosteric conformational dynamics. *J. Biol. Chem.* **288,** 36189–200 (2013).

171. Keppel, T. R. & Weis, D. D. Analysis of disordered proteins using a simple apparatus for millisecond quench-flow H/D exchange. *Anal. Chem.* (2013). doi:10.1021/ac4004979

172. Christiansen, J., Goodwin, P. J., Lanzilotta, W. N., Seefeldt, L. C. & Dean, D. R. Catalytic and biophysical properties of a nitrogenase apo-MoFe protein produced by a nifB-deletion mutant of Azotobacter vinelandii. *Biochemistry* **37,** 12611–12623 (1998).

173. Seefeldts, L. C., Morgan, T. V., Dean, D. R. & Mortensonst, L. E. Mapping the

Site(s) of MgATP and MgADP Interaction with the Nitrogenase of Azotobacter vinelandii. *J. Biol. Chem.* **267,** 6680–6688 (1992).

174. Kavan, D. & Man, P. MSTools - Web based application for visualization and presentation of HXMS data. *Int. J. Mass Spectrom.* (2011). doi:10.1016/j.ijms.2010.07.030

175. Weis, D. D., Wales, T. E., Engen, J. R., Hotchko, M. & Ten Eyck, L. F. Identification and Characterization of EX1 Kinetics in H/D Exchange Mass Spectrometry by Peak Width Analysis. *J. Am. Soc. Mass Spectrom.* **17,** 1498–1509 (2006).

176. Owens, C. P., Katz, F. E. H., Carter, C. H., Oswald, V. F. & Tezcan, F. A. Tyrosine-Coordinated P-Cluster in G. diazotrophicus Nitrogenase: Evidence for the Importance of O-Based Ligands in Conformationally Gated Electron Transfer. *J. Am. Chem. Soc.* **138,** 10124–10127 (2016).

177. Kim, C. H., Newton, W. E. & Dean, D. R. Role of the MoFe Protein a-Subunit Histidine-195 Residue in FeMo-Cofactor Binding and Nitrogenase Catalysis. *Biochemistry* **34,** 2798–2808 (1995).

178. Sperry, J. B. *et al.* A mass spectrometric approach to the study of DNA-binding proteins: Interaction of human TRF2 with telomeric DNA. *Biochemistry* (2008). doi:10.1021/bi702037p

179. Hamuro, Y. *et al.* Hydrogen/deuterium-exchange (H/D-Ex) of PPARγ LBD in the presence of various modulators. *Protein Sci.* **15,** 1883–1892 (2006).

180. Danyal, K. *et al.* Negative cooperativity in the nitrogenase Fe protein electron delivery cycle. *Proc. Natl. Acad. Sci.* **113,** E5783–E5791 (2016).